Dépôt de couches minces de TiO2 par pulvérisation magnétron et stratégie de dopage à l'azote pour des applications photocatalytiques dans le visible

Houssam Fakhouri

To cite this version:

Houssam Fakhouri. Dépôt de couches minces de TiO2 par pulvérisation magnétron et stratégie de dopage à l'azote pour des applications photocatalytiques dans le visible. Génie des procédés. Université Pierre et Marie Curie - Paris VI, 2011. Français. NNT : 2012PAO66343 . tel-00825830

HAL Id: tel-00825830
https://theses.hal.science/tel-00825830

Submitted on 24 May 2013

THESE DE DOCTORAT

Présentée

À L'UNIVERSITÉ PIERRE ET MARIE CURIE

Spécialité

Génie des procédés et technologies avancées

Présentée par :

Houssam FAKHOURI

Pour obtenir le grade de

DOCTEUR de L'UNIVERSITE PIERRE ET MARIE CURIE (Paris-FRANCE)

Thin film deposition of pure and doped TiO_2 by RF magnetron sputtering for visible light photocatalytic and optoelectronic applications

---

À soutenir le 28 septembre 2012

Encadrement :

Mme. Farzaneh AREFI-KHONSARI	Professeure, LGPPTS, UPMC-Sorbonne Universités
M. Jérome PULPYTEL	Maître de conférences, UPMC-Sorbonne Universités

Rapporteurs :

Mme. Nadhira BENSAADA LAIDANI	Senior Scientist Researcher, FBK, Trento, Italie
M. Laifa BOUFENDI	Professeur, (GREMI), Université d'Orléans

Examinateurs :

M. Mehrdad NIKRAVECH	Professeur, (LSPM-CNRS) Université de Paris 13
Mme. Pascale MASSIANI	Directeur de Recherche-CNRS, (LRS), UPMC-Sorbonne Universités

Invité :

M. Hubert CACHET	Directeur de Recherche-CNRS, LISE, UPMC-SorbonneUniversités

Abstract

Three different ways to dope nitrogen into TiO_2 by means of RF reactive sputtering was compared, and the structural, optical, and photo-active performance of these materials were explored. First, multi-layered thin films of TiO_2 and TiN were prepared by sputtering a titanium target and alternating oxygen and nitrogen reactive gases in the deposition chamber. The total thickness of each multi stack was kept constant while the overall composition of the films (TiN to TiO_2 ratio) was varied between 5% and 30% and the number of TiN/TiO_2 bi-layers was increased from 9 to 45. Secondly, we prepared N-TiO_2 by introducing oxygen and nitrogen reactive gases simultaneously during the depositions. The ratio of oxygen to nitrogen was systematically changed in order to control the concentration of nitrogen incorporation into the films between 0% and 6%. Finally, we prepared TiN thin films and oxidized them at different temperatures and for several time intervals. X-ray photoelectron spectroscopy showed that nitrogen was successfully doped into all of the TiO_2 films in substitutional and/or interstitial sites depending on the deposition conditions. The variance in the concentration and position of the nitrogen doping had a significant effect on the optical, structural and photoactive properties of the three types of N-TiO_2 films. The parameters of sputtering deposition were optimized using both plasma diagnostics and Design of Experiments. This study has shown the desirable ability to control several important physical and chemical characteristics of N-TiO_2 films, with considerable promise for many applications.

Key words: TiO_2 thin film, Nitrogen doping, photocurrent, bi-layer, RF sputtering, photo catalyze, TiN, Oxidation.

Résumé

Nous avons comparé trois méthodes différentes de dopage de TiO_2 à l'azote par pulvérisation cathodique, et avons exploré les propriétés structurelles, optiques et la photo-activité de ces matériaux. Tout d'abord, des films minces successifs de TiO_2 et TiN ont été créés par pulvérisation d'une cible de titane et en alternant les gaz réactifs d'oxygène et d'azote dans l'enceinte de dépôt. L'épaisseur totale de chaque multicouche a été maintenue constante tandis que nous avons fait varier la composition globale des films (rapport TiN/TiO_2) entre 5% et 30% et le nombre de des couches TiN/TiO_2 entre 9 à 45. Deuxièmement, nous avons préparé des couches homogènes de N-TiO_2 par l'introduction simultanée des gaz réactifs d'oxygène et d'azote au cours du dépôt. Nous avons systématiquement fait varier le rapport azote/oxygène afin de modifier d'une façon contrôlée la concentration de l'azote incorporé dans les films de 0% et 6%. Enfin, nous avons préparé des couches minces de TiN et les ont fait subir l'oxydation à des températures différentes pendant plusieurs intervalles de temps. Les mesures d'XPS ont montré que l'azote a été dopé avec succès, dans tous les films de TiO_2, dans les sites substitutionnels et/ou interstitiels en fonction des conditions de dépôt. La variance de la concentration et la position du dopage à l'azote avait une influence significative sur les propriétés optiques, structurelles et photo-actives des trois types des films de TiO_2 dopés. Les paramètres de dépôt par pulvérisation ont été optimisés grâce à des diagnostics du plasma et à un Plan d'Expériences. Cette étude a montré que nous pouvons modifier d'une façon contrôlée et à souhait plusieurs caractéristiques physiques et chimiques importantes des couches de N-TiO_2, qui pourront avoir un grand potentiel pour de nombreuses applications.

Mots clés: couche mince TiO_2, dopage d'azote, photo-courant, bi-couche, RF pulvérisation cathodique, photocatalyse, TiN, Oxidation.

Table of contents

Introduction générale 1
General Introduction 3

Chapter I : State of the art

Abstract 6
Résumé 7
I-1) Introduction 9
I-2) Definitions 10
  I-2-1) Catalysis and photo-catalysis 10
  I-2-2) Band gap 10
  I-2-3) Charge separation 12
  I-2-4) Efforts to enhance the charge separation 13
  I-2-5) Charge transport 15
  I-2-6) Role of adsorbate electrophilicity on charge transport 16
  I-2-7) Reaction steps in heterogeneous photo-catalysis 17
I-3) Titanium dioxide (TiO_2) 20
  I-3-1) Advantages of titania semiconductor 20
  I-3-2) Different crystalline structures of TiO_2 21
  I-3-3) TiO_2 in powder and thin films 23
I-4) Different methods used for TiO_2 production 23
  I-4-1) Solution routes 24
  I-4-2) Gas phase methods 24
I-5) TiO_2 applications 29
  I-5-1) Mechanism of photo-activity of pure and doped TiO_2 29
  I-5-2) Effects of oxygen vacancies 31
I-6) Reviewing the different studies on doping TiO_2 in nano particles and thin films 33
  I-6-1) Nonmetal doping 33
  I-6-2) Photo-activity of N-doped anatase and rutile TiO_2 34
  I-6-3) Nitrogen sites and nitrogen efficiency in the TiO_2 lattice 35
  I-6-4) phase transition in nitrogen doped TiO_2 38
  I-6-5) Nitrogen implantation 38

I-7) TiN oxidation 39
I-8) Photo-induced hydrophilicity and contact Angle Measurements 39
I-9) Conclusion 41
Objective of this study 43
References 44

Chapter II: Plasma diagnostics

Abstract 49
Résumé 50
II-1) Introduction 51
  II-1-1) Experimental set-up for thin film deposition and plasma diagnostic 51
  II-1-2) Applied RF power and the resulted cathode bias voltage 53
  II-1-3) Ex-situ evidence of target poisoning 53
II-2) Optical Emission Spectroscopy OES 54
  II-2-1) Experimental conditions for OES measurements 54
  II-2-2) Emission lines studied in this work 55
II-3) OES measurements in Argon 55
  II-3-1) Relative emission of Titanium lines 55
  II-3-2) Normalization of lines intensities 57
  II-3-3) Effect of argon flow rate at constant pressure and power 57
  II-3-4) Effect of power: correlation between OES and deposition rate (measured by SEM) 58
II-4) OES measurements in Ar/O_2 59
  II-4-1) Parametric study 60
    a) Low pressure and low Argon flow rate 60
    b) High pressure and low Argon flow rate 61
    c) High pressure and high Argon flow rate 62
  II-4-2) Discussions 62
II-5) OES measurements in Ar-N_2 plasmas 63
  II-5-1) Parametric study 63
  II-5-2) Discussion 63
II-6) Electrical measurements used for plasma diagnostic 65
  II-6-1) Langmuir probe measurements 66
    II-6-1-a) Effect of reactive gas at fixed RF power and pressure 66

II-6-1-b) Effect of RF power and pressure 66
II-6-2) Cathode voltage measurements 68
II-6-3) Target voltage and formation of particles 69
II-7) Simple analytical plasma modelling of the sputtering reactor 70
II-7-1) Comparison of Langmuir probe measurements and current measurements 70
II-7-2) Estimation of electron density in the dense plasma ring from current measurements........ 72
II-7-3) Estimation of the electron density in the dense plasma ring from the deposition rate 73
II-7-4) Power balance calculation 75
II-8) Effect of deposition pressure of TiN on the resistivity of the coated thin film 77
II-9) Conclusion 78
References 80

Chapter III: Design of experiments & N doped TiO$_2$ by dual reactive gas sputtering

Abstract 82
Résumé 83
III-1) Introduction 83
III-2) Experimental strategy 84
III-2-1) Design of experiments 85
III-2-2) Thin films preparation 85
III-2-3) Contact angle measurement 86
III-2-4) Film structure and morphology 86
III-2-5) Optical properties and Photo current measurements 86
III-2-6) Photocatalytic activity 87
III-3) Results and discussion 88
III-3-1) Evolution of the surface hydrophilicity 88
III-3-2) Effect of the deposition pressure on the film porosity and deposition rate 89
III-3-3) XRD spectroscopy and crystal size 90
III-3-4) Raman spectroscopy 92
III-3-5) Band Gap Calculation 93
III-3-6) Analyzing the photo-activity and Optimization of the Sputtering Process 94
III-5) Conclusion 96
References 97

Chapter IV: Effect of different nitrogen sites in dual gas sputtering configuration

Abstract 98
Résumé 99
IV-1) Introduction 100

IV-2) Experimental strategy........101
IV-2-1) Thin films deposition........101
IV-2-2) X-ray Photoelectron Spectroscopy........102
IV-3) Results and discussion........102
IV-3-1) Film structure........102
IV-3-1-a) Case of pure TiO_2........102
IV-3-1-b) Case of N doped TiO2........104
IV-3-2) Film morphology........106
IV-3-3) Thin film composition and nitrogen doping........107
IV-3-3-1) N1s peak assignments........107
IV-3-3-2) N 1s peak observation and analysis........108
IV-3-3-3) O 1s Peak Observation and Analysis........110
IV-3-3-4) Ti 2p Peak Observation and Analysis........111
IV-3-4) Valence Band Observation........112
IV-3-5) Optical Properties........114
Band gap estimation........115
IV-3-6) Photoactive Properties........117
IV-3-6-1) Potentiodynamic sweep........117
IV-3-6-2) Intermittent photocurrent measurements........118
IV-3-6-3) Photocatalytic activity........120
IV-4) Conclusion........121
References........122

Chapter V: Nitrogen doping in bi-layer configuration

Abstract........125
Résumé........126
V-1) Introduction........127
V-2) Strategy in this study........128
V-3) Experimental........130
V-3-1) Deposition procedures........130
V-3-2) Thermal transformation and structural study........131
V-3-3) Optical and photoelectrochemical measurements........131
V-4) Results and Discussion........133
V-4-1) Morphology and appearance of TiO2/TiN Bi-layer thin films........133
V-4-2) Crystal Structure of TiO_2/TiN Bi-layer Thin Films........133
V-4-2-1) Crystal size........135
V-4-2-2) Anatase to Rutile ratio........137
V-4-3) Optical Properties........139
V-4-3-1) Transmission and reflection........139

V-4-3-2) Optical band gap 140
V-4-3-3) Main and secondary band gaps 143
V-4-4) XPS surface Analysis 143
V-4-4-1) Ti 2p and O1s Peaks Observation and Analysis 143
V-4-4-2) N 1s Peaks Observation and Analysis 145
V-4-5) Photo-electrochemical properties 146
V-4-5-1) Potentiodynamic Sweep response 147
V-4-5-2) Different features affecting the photo-electrochemical response 148
V-4-5-3) Intermittent Photocurrent in potentiostatic configuration 149
V-4-5-4) Effect of TiN layer thickness on the photo-activity 150
V-4-5-5) memory effect in the electrochemical photo response 152
V-4-6) Photocatalytic activity 153
V-5) Deposition monitoring 153
V-6) Conclusions 155
References 156

Chapter VI : N doped TiO$_2$ via thermal oxidation of TiN

Abstract 158
Résumé 159
VI–1) Introduction 160
VI–2) Strategy of the study 161
VI–2–1) Titanium nitride vs titanium dioxide 161
VI–2–2) Motivations of this work 162
VI–3) Experimental part 163
VI–3–1) Films preparation 163
VI–3–2) Oxidation of TiN thin films 163
VI–3–3) Morphology of as deposited TiN thin films 163
VI–3–4) Crystal Structure 164
VI–4) TiN oxidation kinetic 165
VI–4–1) Dense TiN film deposited at 2 mtorr 165
VI–4–2) Dense TiN film deposited at 3.5 mtorr 167
VI–4–3) TiN film deposited at 5 mtorr 168
VI–4–4) TiN film deposited at 14 mtorr 170
VI–5) Crystal size calculation 171
VI–5–1) Effect of deposition pressure on the crystal size 171
VI–5–2) Dense TiN films deposited at low pressure 172
VI–5–3) Porous TiN Films deposited at high pressure 173
VI–6) X–ray Photoelectron spectroscopy 176
VI–6–1) O1s core level spectra 179
VI–6–2) N1s core level 181
VI–6–3) Ti 2p spectrums 182

VI-6-4) First results of XPS depth profiling:....183
VI–7) Optical Properties....185
VI–7–1) optical absorption....185
VI–7–2) Correlation between structural and optical properties....186
VI–8) Photo electrochemical responses....187
VI–8–1) Linear sweep voltametry....187
VI–8–2) Intermittent Photocurrent in potentiostatic configuration....189
VI–9) Conclusion....193
References:....194
General conclusion 196
Conclusion générale 200
Annexure

Introduction Général

Les semiconducteurs sont des matériaux clés autant pour la production d'énergie solaire que la photodégradation des polluants contenus dans l'eau. Les couches minces à base de dioxyde de titane (TiO_2) sont couramment utilisés dans les cellules photoélectrochimiques de par leur capacité à photodissocier l'eau, permettant ainsi à la production d'hydrogène. Depuis les années 70, de nombreux travaux se sont orientés vers le développement et l'optimisation de nouveaux matériaux possédant notamment une énergie de gap compatible avec les applications photocatalytiques.

Le TiO_2 peut dégrader de nombreux polluants organiques dissouts dans l'eau sous l'action des rayonnements UV. Cependant, à cause de sa largeur de bande d'énergie interdite importante (3,2 eV), ce matériau n'absorbe que très peu la partie visible du rayonnement. De nombreux efforts ont donc été fournis pour permettre l'absorption du spectre visible. En particulier, la stratégie la plus répandue consiste à diminuer l'énergie de gap par dopage.

Les trois caractéristiques principales pour permettre au TiO_2 d'avoir une bonne activité dans le visible sont i) d'introduire des états dans la bande d'énergie interdite permettant ainsi l'absorption de photons visibles, ii) le maximum de la bande de valence (VB) ainsi que les niveaux d'énergie du dopant doivent se trouver au-dessous du potentiel d'oxydation de l'eau (H_2O/O_2) alors que le minimum de la band de conduction (CB) doit se trouver au dessus du poteltiel de reduction (H_2/H_2O), iii) les niveaux d'énergie du dopant doivent se recouvrir suffisamment avec les bandes de TiO_2 afin de permettre un transfert rapide d'électrons.

Le TiO_2 dopé à l'azote a suscité beaucoup d'attention grâce à ses bonnes propriétés photocatalytiques, mais les nombreuses contradictions rapportées dans la littérature font encore l'objet de débats à l'heure actuelle. Dans cette thèse, nous nous sommes focalisé sur la préparation et la caractérisation de différentes couches de TiO_2 dopées azote (TiO_2 :N) par pulvérisation réactive magnétron en vue d'applications liées au traitement de l'eau.

Cette thèse est constituée de 6 chapitres. Dans le premier chapitre, les processus élémentaire entrant en jeu dans la photocatalyse sont décrits, ainsi que l'état de l'art sur l'élaboration des couches de TiO_2 dopées et non dopées. Le second chapitre est dédié aux diagnostics du plasma par spectroscopie optique d'emission (OES) et par sonde de Langmuir, afin de comprendre le procédé de dépôt par pulvérisation. Les phénomènes d'empoisonnement de la cible et d'hystérèse ont été particulièrement étudié, car ces phénomènes peuvent changer fondamentalement les conditions opératoires et ainsi les propriétés des dépôts. Ce chapitre est la base de connaissance principale permettant de sélectionner les paramètres de dépôt étudiés dans les chapitres suivants.

Dans le troisième chapitre, la méthodologie des plans d'expérience a été utilisé afin d'avoir un large aperçu de l'effet des paramètres du procédés sur les caractéristiques physico-chimiques et sur les propriétés photoactives des films de TiO_2 dopés N. L'autre avantage des plans d'expériences consiste à pouvoir faire varier simultanément différents paramètres afin d'observer leurs interactions ; dans ce chapitre la pression et la composition du gaz plasmagène constituent les paramètres étudiés.

Les derniers chapitres sont dédiés à l'étude de trois strategies différents pour produire des films de TiO_2 dopés azote, permettant ainsi d'avoir une bonne compréhension du rôle de la localisation de l'azote dans les films (insertionel ou substitutionnel) dans la maille de TiO_2, ainsi que de la morphologie des films et de la concentration en azote.

Dans le chapitre 4 nous allons étudier le dépôt de couches de TiO_xN_y possédant différentes morphologies et différentes concentrations en azote en introduisant simultanément l'azote et l'oxygène dans l'enceinte de pulvérisation. Des caractérisations poussées par XPS et DRX ont permis de démontrer qu'il est possible de contrôler la localisation de l'azote dans la maille par l'intermédiaire des paramètres du plasma.

Dans le chapitre 5, une nouvelle stratégie jamais rapportée, à notre connaissance, dans littérature a été mise en place. Cette nouvelle approche consiste en l'élaboration de multi-couches de TiO_2/TiN. Les résultats obtenus ont permis de démontrer que les hétérojonctions présentent dans le film permettent une bonne séparation des porteurs de charges et ainsi de meilleures propriétés photoactives.

Enfin dans le chapitre 6, des couches minces de TiN ont été deposes puis oxydées par recuit dans l'air afin de produire des couches de TiO_2:N. Les résultats obtenus montrent que cette stratégie est très intéressante pour produire des couches photoactives dans le visible, bien qu'elle nécessite des traitements post-plasma des dépôts. Dans ce chapitre, les contradictions que l'on trouve dans la littérature sur l'oxydation de TiN seront aussi mises en évidence.

General Introduction

Semiconductors have received considerable attention as a potential solution for clean energy and for photocatalytic degradation of hazardous pollutant in the environment. Titanium dioxide (TiO_2) thin films are used in photoelectrochemical cells, because they have the ability to photo-dissociate water and produce photocurrent for hydrogen production. Since 1970, many efforts have been made to explore suitable materials and to optimize their energy band configurations for photocatalytic applications.

TiO_2 can photodegrade many organic pollutants dissolved in water via UV irradiation. However, due to its large band gap TiO_2 absorbs visible light poorly, and thus has been ineffective for visible-light photocatalysis. Many attempts have been made to improve the photocatalytic activity of TiO_2 under UV and/or visible light irradiation. In particular, the main strategy was to decrease the band gap energy of TiO_2 (around 3.2 eV), in order to absorb visible light, i.e. energies in the range of 1.6–3.0 eV, particularly at 2.5 eV, which corresponds to the solar maximum emission intensity.

Three main characteristics are required to achieve good visible-light activity for $TiO_{2,}$ i) doping should introduce states within the band gap that could be excited by absorbing visible light, ii) the conduction band (CB) minimum and the dopant states must be above the H_2/H_2O reduction level to ensure photoreductive activity, and the valence band (VB) maximum should be lower than H_2O/O_2 oxidation level, iii) sufficient overlap between the doping energy states and band states of TiO_2 is required, in order to provide a fast transfer of the photo-excited carriers to the surface within their lifetime.

Nitrogen doped TiO_2 has received significant attention, but its photoactivity results, reported in the literature, have yielded many contradictions and the efficiency of nitrogen doping sites is still under debate. In this thesis, we will focus on the preparation and characterization of nitrogen doped TiO_2 (TiO_2:N) by RF reactive magnetron sputtering for water purification and water splitting. The thesis is composed of six chapters.

In the first chapter, the fundamental processes involved in photocatalysis as well as the state of the art for intrinsic and doped TiO_2 will be described.

The second chapter is dedicated to plasma diagnostic by Optical Emission Spectroscopy (OES) and by Langmuir probe, in order to understand the plasma deposition process by sputtering. Target poisoning and hysterisis phenomena will be particularly highlighted, because they can dramatically change the process conditions and thus the properties of the coatings. This chapter is the main basis to select the deposition parameters for the different studied films in the following chapters.

In the third chapter, the Design of Experiments (DoE) methodology will be used in order to have an overview about the effect of the different parameters on the physico-chemical characteristics and the photoactivity of N doped TiO_2 films. The advantage of using DoE is to be able to study, simultaneously, the effect of variation of different plasma parameters and to highlight the synergic effects of the most important parameters in the case of the reactive sputtering, which were the pressure and gas composition in the reactor.

The last chapters are dedicated to three different strategies to produce N doped TiO_2 films, that allowed us to have a good overview about the role of both nitrogen doping sites (interstitial or substitutional) in the lattice of doped titania as well as the effect of the morphology and the doping concentration on the nitrogen incorporation and the resulted photoactivity.

Chapter 4, is devoted to the deposition of homogeneous TiO_xN_y films with different morphologies and nitrogen concentrations by the dual gas sputtering process. Extensive studies of the films by XPS and XRD will demonstrate that it is possible to control the position of nitrogen doping (interstitial or substitutional) by controlling the main plasma parameters.

In chapter 5, a new strategy never reported in the literature before will be developed. This new approach consisted in the production of TiO_2/TiN multi-bi-layers. The results will highlight the fact that the heterojunctions obtained in the films can increase the charge separation effect, and thus increase the photoactive properties of the films

Finally, in chapter 6, the production of N doped TiO_2 by oxidizing TiN thin films will be presented. The results will highlight the fact that this strategy is very interesting in order to produce thin films with good photoactive properties. This chapter in particularly emphasizes the contradiction which is found in the litterature survey on the oxidation of TiN.

Chapter I

Chapter I State of the art

Abstract

The utilization of solar irradiation to supply energy or to initiate chemical reactions is already a well established idea. If a semiconductor such as titanium dioxide (TiO_2) is irradiated with light greater than the band gap energy, excited electron–hole pairs are generated that can be utilized in many applications such as solar cells to generate electricity, chemical processes to create or degrade specific compounds, or in producing self cleaning surfaces using the photo-induced super hydrophilicity of TiO_2 films.

TiO_2 shows relatively high activity and chemical stability under ultraviolet light ($\lambda<387$nm), the energy of which exceeds the band gap (3.2 to 3.3 eV) of the anatase crystalline phase. The development of photo-catalysts exhibiting high reactivity under visible light ($\lambda>$ 400 nm) should allow the main part of the solar spectrum to be used, even under the poor illumination of interior lighting. Several approaches for TiO_2 modification have been proposed such as metal-ion implantation using transition, noble, alkaline and rare metals, reduced TiO_x photo-catalysts, non-metal doped-TiO_2 (N, S, C, B, P, I, F), composites of TiO_2 with another semiconductor having a lower band gap energy (i.e. CdS, WO_3, …), sensitizing TiO_2 with dyes, and TiO_2 doped with up conversion luminescence agents.

The morphology effect is less investigated in literature especially in the studies of TiN oxidation to get N-doped or even pure TiO_2. Nitrogen can occupy substitutional (N–Ti–O or Ti–O–N) and/or interstitial (π^* character NO) sites in the titania lattice. This can introduce discrete nitrogen energy states levels at 0.14 eV and 0.73 eV above the top of the valence band, for substitutional and interstitial nitrogen, respectively. Up to now there is no evident explication how to control the presence of one with respect to the other, also, what is the contribution of each nitrogen site on the photo-activity of the doped titania.

In particular, this thesis will primarily focus on the role of nitrogen doping on the photo-activity, morphology, structural, optical, and electronic properties of TiO_2. Three methods utilizing RF sputtering will be used in order to create N-doping within TiO_2; the oxidation of TiN thin films, creating bi-layered TiO_2/TiN films, and the direct dual gas deposition of TiON. By optimizing the experimental conditions, it is possible to achieve nitrogen doped TiO_2 coatings with a desired stoichiometry, concentration and position of doped nitrogen in the TiO_2 lattice. Such coatings can then be used to elucidate the role of substitutional and interstitial doping on the photo-activity of N-doped TiO_2 films.

Résumé

L'utilisation de l'irradiation solaire pour l'approvisionnement en énergie ou pour initier des réactions chimiques est une idée, déjà, bien établie. Si un semi-conducteur, tel que le dioxyde de titane (TiO_2), est irradié par une lumière dont l'énergie est plus grande que l'énergie de bande gap, des paires électron-trou sont générés dans l'état excité, ces paires photo-générés peuvent être utilisés dans de nombreuses applications telles que les cellules solaires (photovoltaïques) pour produire de l'électricité, les processus chimiques afin de créer ou de dégrader des composés spécifiques, ou en produisant des surfaces autonettoyantes à l'aide de la super hydrophilicité photo-induite des couches minces de TiO_2.

TiO_2 montre une photo-activité relativement élevée ainsi qu'une stabilité chimique sous la lumière ultraviolette (λ <387nm) dont l'énergie dépasse la largeur de la bande optique (bande gap) de la phase cristalline anatase (3.2 à 3.3 eV). Le développement de photo-catalyseurs présentant une forte activité sous la lumière visible (λ> 400 nm) devrait permettre d'utiliser la partie principale du spectre solaire, même sous le mauvais éclairage interne. Plusieurs approches ont été proposées afin de modifier le TiO_2, telles que l'implantation ionique et le dopage par des métaux de transition, les éléments nobles, les alcalins et les terre –rares. Par ailleurs on trouve une littérature abondante sur le TiO_2 dopé par les non métaux (N, S, C, B, P, I, F), les composites de TiO_2 avec d'autres semi-conducteurs ayant une plus faible énergie de gap (CdS, WO3, ...), la sensibilisation de TiO_2 avec des colorants, de TiO_2 dopé avec un agent de conversion de luminescence, ou la formation des structures réduites de TiO_x ($x<2$).

L'effet de la morphologie de TiO_2 est moins étudié dans la littérature en particulier dans les études du phénomène d'oxydation de TiN pour obtenir le TiO_2 dopé-N ou même le TiO_2 pur. L'azote peut occuper des sites substitutionnel (N–Ti–O et Ti–O–N) et / ou interstitiel (π* correspondant à N—O) dans le réseau de TiO_2. Ce qui introduirait des états d'énergie discrets, lié à l'azote, situé à 0.14 eV et 0.73 eV au dessus de la band de valence pour l'azote substitutionnel ou interstitiel, respectivement. Jusqu'à maintenant, il n'y a pas eu d'explication claire pour contrôler la présence de l'un ou l'autre, ou encore pour mettre en évidence la contribution de chaque site d'azote sur l'activité photo-induite de dioxyde de titane dopé-N. Cette thèse se concentrera principalement sur le rôle du dopage à l'azote sur l'activité photo-induite, la morphologie, la structure, et les propriétés optiques et électroniques de TiO_2. Trois méthodes basées sur la technique de pulvérisation cathodique RF seront utilisées afin de doper N au sein de TiO_2, l'oxydation des films minces de TiN, la réalisation d'un film mince composé d'un assemblage de plusieurs dépôt des bi-couches de TiO_2/TiN, et enfin par le dopage traditionnel en pulvérisation réactive en utilisant le couple de gaz réactifs d'oxygène et d'azote pour déposer directement les couches de TiON. En optimisant les paramètres expérimentaux, il a été possible de contrôler d'une façon très fine, dans le cas du

dopage des couches de TiO_2 avec l'azote, la stœchiométrie, la concentration et positionnement de l'azote dans la structure de TiO_2. Ces couches donc vont servir pour élucider l'effet de dopage par azote en substitutionnel et/ou interstitiel sur l'activité photo-induite des couches de TiO_2 dopé-N.

I-1) Introduction

Photo-catalytic materials possess unique structural, optical and electronic properties that can be exploited for numerous applications and have been studied extensively for decades. The primary applications of photo-catalysis can be summarized into two major categories; (1) the photo-degradation of organic materials dissolved in water (or another liquid) and (2) water splitting via photolysis in electrochemical cells. The fundamental processes that drive the efficiency of photo-catalysts are governed by their material properties, the incident light intensity, the light frequency and the specific chemical processes of the catalytic reaction. In particular, the properties of the material that can drastically alter the performance of photo-catalysts are the electronic band gap, electron-hole pair generation, recombination dynamics, and finally the transportation of photo-generated charges. Understanding these characteristics individually and how they can be controlled is vital in designing improved and optimized photo-catalysts, which can perform more efficiently and effectively as compared to traditional materials.

The most prominent photo-catalytic material that has been studied is TiO_2, due to its non-toxicity, relative abundance, optical properties, and stability in aqueous solutions. However, TiO_2 by itself can only reach a certain level of photo-catalytic efficiency due to its fast electron-hole pair recombination time, as well as its large band gap energy which only absorbs UV light. Currently, there have been many research efforts exploring ways to improve the efficiency of photo-catalytic materials such as TiO_2 by combining them with other semiconductors or metals to increase the lifetime of the photo-excited electrons and holes, as well as to enlarge the spectral absorbance range to include visible light.

The potential for the applications of the photo-catalytic effects of TiO_2 has attracted considerable interest over the last three decades. The photo-catalytic oxidation of organic compounds in aqueous or gaseous environments has received the most attention, but there is a rapidly increase focus on the oxidation of volatile organic or inorganic compounds in the gas phase, including NO_x and SO_x. The photo-catalytic reduction of organic compounds and metal-containing ions, as well as studies on cell killing and disinfection by illuminated titanium dioxide has also received increase attention.

I-2) Definitions

I-2-1) Catalysis and photo-catalysis

A **catalyst** is a material which accelerates the speed of a chemical reaction without being consumed at the end of the reaction. Its structure or composition can be altered during the reaction but there is no stoichiometric relationship between these alterations and the stoichiometry of the reaction. The **photo-catalytic activity** describes the acceleration of a catalytic reaction by light, and it is associated with the reaction rate.

Heterogeneous photo-catalysis involves photo-reactions at the catalyst surface:

a) if the process of initial photo-excitation occurs on an adsorbed molecule, which then interacts with the catalyst, the process is called **photo-sensitized** reaction.
b) if the initial photo-excitation takes place on the catalyst (photo-excited catalyst) which then acts on an adsorbed molecule, it is called **photo-catalyzed** reaction.

I-2-2) Band gap

The absorption of light is directly dependent on the band gap of the photo-catalyst, which can be explained by the band theory of solids. The band theory classifies materials by their band gap, which is the energy difference between the top of the valence band and the bottom of the conduction band electron orbitals. The **valence band** is also referred to as the highest occupied molecular orbital (HOMO), which is the highest orbital that an electron is naturally found in a material, while the **conduction band** is referred to as the lowest unoccupied molecular orbit (LUMO), because it is the next stable electron orbit that is not already occupied by an electron. The band structures for an insulator, a semiconductor, and a metal are shown in Fig.I-1 to detail the different electronic structures for these distinctively different materials.

Insulators are characterized by their traditionally large band gaps (E_g), which are what give them their intrinsic properties of having poor electron mobility, since the conduction band and valence band are relatively far apart and thus require a large amount of energy to transfer the electrons between bands. Semiconductors have a discrete band gap that is typically much smaller than that of insulators, but is still well defined. Metals have no band gap, but instead have a continuous series of electronic bands throughout the material. This continuum of electronic bands give metals their intrinsic properties of being good electrical conductors, because the conduction and valence bands are so close that electrons are free to move between bands with little or no energy needed.

In order for an electron to be promoted from the valence band to the conduction band level for semiconductors and insulators, it needs to be excited either thermally, electronically, or optically. If a photon with energy greater than or equal to the band gap energy of a material is incident on its surface, an electron in the valence band could absorb this photon and could be excited to the conduction band discretely and becomes a photo-carrier.

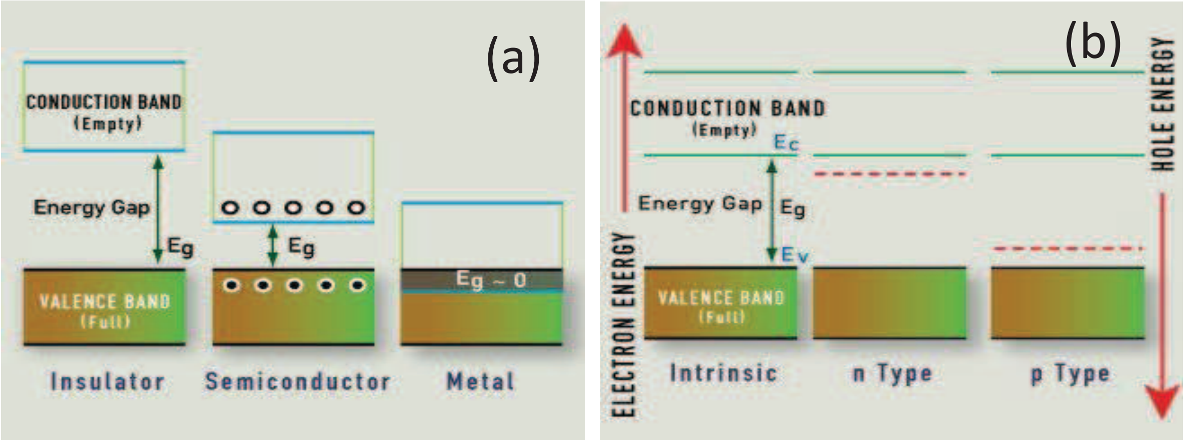

Fig.I-1: Band structures (a) for an insulator, semiconductor and metal & (b) for intrinsic, n type and p type semiconductors.

For example, with TiO_2, the bulk band gap energy in the anatase phase is $E_g = 3.2$ eV ($E_g = 3.0$ eV for the rutile phase), which is the energy between the valence band (corresponding to the O $_{2p}$ orbital), and the conduction band (corresponding to the Ti $_{3d}$ orbital). The energy $E_g = 3.2$ eV corresponds to a wavelength of $\lambda = 388$ nm, which is in the UV region of light.

I-2-3) Fermi level

Another similar and helpful way to characterize different electronic materials is through a description of their Fermi energy level, E_f. For a semiconductor in thermal equilibrium at absolute zero, the Fermi level is defined as the highest filled level of electrons in the ground state. At some finite temperature above this, the electrons gain kinetic energy and can be excited into states above the Fermi level, leaving available openings below that energy (Fig.I-2). We define the Fermi function ***f(E)*** which gives the probability that a given available electron energy state *(E)* will be occupied at a given temperature *(T)*. The Fermi function has the form:

$$f(E) = \frac{1}{e^{\left[{(E-E_f)}/{kT} \right]} + 1} \qquad \text{Eq.I-1}$$

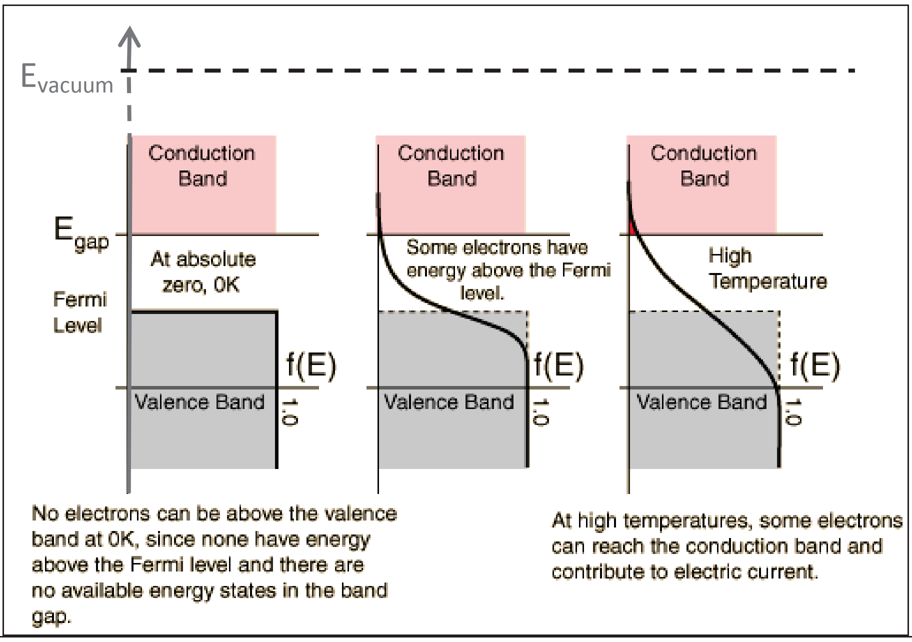

Fig.I-2: Fermi function and Fermi level in a semiconductor as a function of temperature.Note that at hight temperature some electrons can reach the conduction band (in red colore).

The electron population depends on the product of electron density and Fermi function. The Fermi function has a finite value in the gap but electron density is zero in the gap so there is no electron population at those energies (gap). In the conduction band at 0K, there are plenty of available states but there are no electrons because the Fermi function is zero. At high temperatures, both the density of states and the Fermi function could have finite values in the conduction band, so there could be a finite electronic population in the conduction band.

I-2-3) Charge separation

When electron-hole pairs are generated by photo-excitation, they are typically separated for a finite and pre-determined amount of time that is an intrinsic property of the material, and crystalline structure of the material that is being excited. The forward and back transition rates, for electrons going to and from the conduction and valence energy bands, could be described by the equations:

$$k_f(r) = W_f e^{[(R_f - r)/a_f]} \qquad \text{Eq.I-2}$$

and

$$k_b(r) = W_b e^{[(R_b - r)/a_b]} \qquad \text{Eq.I-3}$$

where the subscripts *f* and *b* denote the forward and back processes, *k* is the transition rate, *W* is the transition probability determined by Fermi's golden rule, *r* is the inter-particle distance, *R* and *a* are constants used to parameterize the distance scales of each transition and fall-off of the electronic wave function of the states, respectively. These forward and back transition rates can help to determine the ***probability*** of finding an electron or hole in a particular state via the following relationships,

$$\frac{dp}{dt} = k_f(r)n_f(r,t) - k_b(r)p(r,t) \tag{Eq.I-4}$$

$$\frac{dn}{dt} = -k_b(r)n_b(r,t) \tag{Eq.I-5}$$

where ***p*** is the probability of finding a hole, ***n*** is the probability of finding an electron. From these relationships we can see two trends. First, the change in the probability of finding a hole is dependent on both the forward and backward transitions. This makes sense because the holes are only produced via excitation (the forward reaction), and are then consumed by the backward reaction (recombination). The other trend is for the change in the probability of finding an electron in a given state, which is dependent only on the back reaction kinetics. Again, this makes sense because unlike the photo-generated holes, the electrons are present at all times within the material. The dependence on the back reaction relates to the lifetime of both the electron and holes, because the rate with which the electrons fall back to the initial state will determine the annihilation of holes.

Since the photo-generated holes (and sometimes electrons) are the predominant driving mechanism in photo-catalysis, in type-n semiconductor, it is advantageous to keep the charges separated for as long as possible. While the intrinsic recombination time, τ, is determined by the crystal structure of a material, there are several ways to increase the recombination time by changing the material properties, doping and adding other semiconductors or metals to the primary material. This process is called charge separation.

I-2-4) Efforts to enhance the charge separation

Charge separation initially occurs by photo-excitation, but can be extended by creating hetero-junctions between two materials. For instance, when silver is loaded on titania in a TiO_2-Ag system (Fig.I-3 c), electrons can be excited via photon absorption in TiO_2, and then attracted to Ag due to the difference in Fermi energy levels between the semiconductor and the metal. The difference in the Fermi energy levels and the vacuum energy level characterizes the work function for each material, and is equivalent to an electric potential. The contact between the two materials creates a junction, called a Schottky barrier, where there is an appreciable difference in Fermi energy levels, and thus a difference in the work functions [1]. The difference in the work functions creates an effective electric field that drives electrons toward the metal, and holes toward the semiconductor creating an effective charge separation.

Similarly, if another semiconductor is combined with TiO_2 the differences in the Fermi level of each material creates an electric field due to the different work functions, and also creates an effective charge separation. Using a two-semiconductor system requires the second material to have a higher work function, and thus a lower Fermi energy level than the first material, so each must be chosen carefully to satisfy these conditions. A pictorial representation of the band structure of a single photo-active material as well as a two types of hetero-structures, two semiconductors and one semiconductor and one metal loaded, are shown in Fig.1-3.

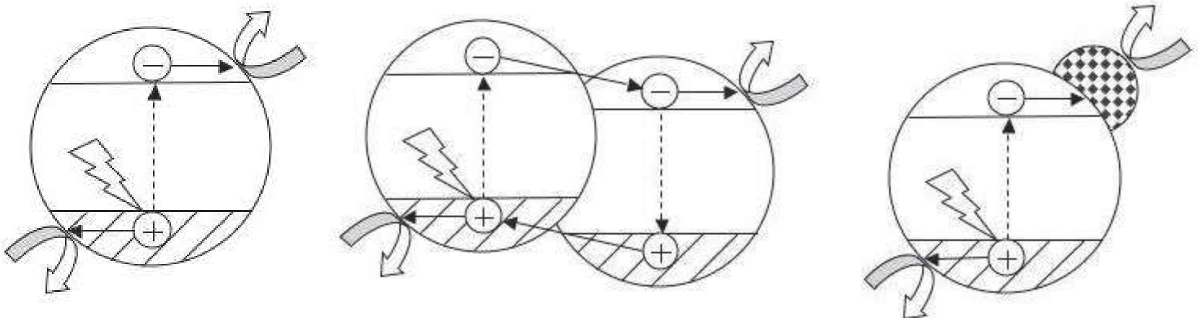

a) single semiconductor b) two semiconductors c) semiconductors + metal

Fig.I-3: Electronic band structure for a single semiconductor, a two semiconductor system, and a semiconductor combined with a metal.

Specifically, the Fermi energy level of the secondary material (metal or semiconductor) needs to be slightly lower than that of the primary material, so that there is a difference in work functions at the junction between the two materials to create an effective electric field. When this is the case, photo-excited electrons in the conduction band of the first material have the ability to transfer to the conduction band of the secondary material (or trapped by the doping metal). This pulls the electrons away from the primary material, and keeps the photo-generated holes free for a longer period of time to continue breaking down reactants, and improve photo-catalytic performance. Effective charge separation can also be achieved through the doping within TiO_2. In the case of TiO_2 prepared in the amorphous state, it has shown poor photo-catalytic activity. This can be explained by the electronic and optical properties of amorphous materials, which dictate that they have no defined band gap. That means that there can be several valence and conduction band energies, with no preference or higher density of one state of energy with respect to others. This, in effect, creates defect energy levels within a defined band gap, so that electrons can be promoted and recombine at several energy levels. With several stable energy levels that are very close together, photo-excited electron-hole pairs are given many opportunities to recombine, and have a shorter distance, or lower amount of energy to travel.

However, when TiO_2 is prepared in the anatase, or even rutile phase, the photo-catalytic performance has shown significant enhancement. The reduction of defects allows the electron-hole pairs to stay apart for a longer time than if there were defects. While the reduction of the latter can remove recombination and trap centers within the band gap, the electron-hole lifetime is still governed by the energy separation in the band gap of TiO_2.

Doped atoms directly inserted into a host lattice, can create bonds with the host atoms, which have different strengths as compared to the initial homogeneous bonds of the host. These new bonds can change the electron/hole conductivity drastically in a local space around the defects, and create a new distribution of electronic energy levels that can keep photo-generated charges apart from each other for a longer period.

I-2-5) Charge transport

Another important characteristic property that determines the performance of photo-catalytic materials is the charge transport of photo-generated charge carriers throughout the material. Since the photo-catalytic reactions occur at the surface of the material, it is important for the photo-generated charges to be able to diffuse to the surface before recombining with each other.

There are two important factors that can affect the transport of charge throughout a material. The first factor is the crystal structure of the material. If an electron-hole pair is created within the bulk of a material, it needs to travel to the surface to complete the chemical reaction. Its path, from the bulk to the surface, is much simpler and easier if the crystal structure of the material is uniform, so that the charge carriers can transfer throughout the lattice easier. The electron mobility is determined by its mean free path, which is larger in an ordered crystal lattice than a defect heavy lattice. This is made easier from a highly ordered crystalline material, because the crystal order corresponds to stable and uniform energy levels surrounding each atom in the crystal lattice. This allows the photo-generated charge carriers to smoothly move from atom to atom by not having to change energy levels and gaining or losing energy. If the crystal structure of the material is not uniform, and has many defects, the mobile charge carriers can be trapped or recombine much more easily as they move throughout the crystal lattice

Another factor that can affect charge transport within a material is the morphology of the structure. For example, for a dense thin film, when electron-hole pairs are created within the bulk material, their motion is determined by a random-walk mechanism. This means that once the charge carriers are generated, they move randomly throughout the thin film, and have no preference to go to the surface, or be extracted in a photo-electrochemical cell.

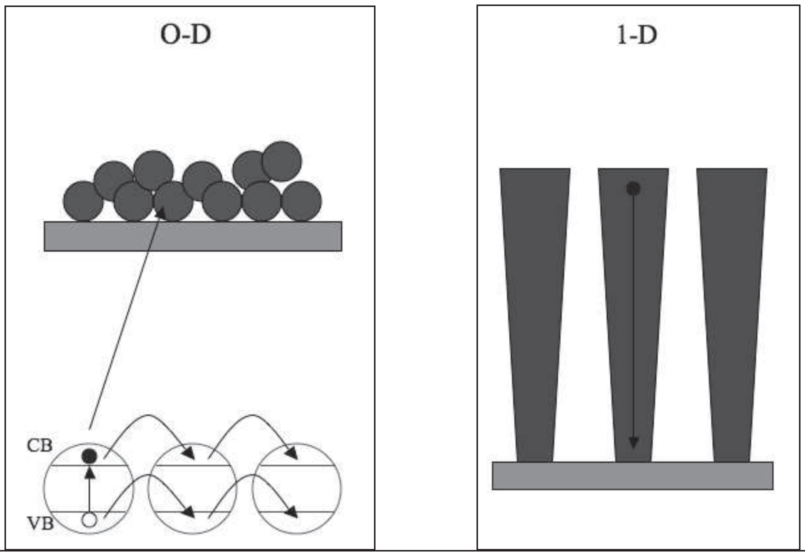

Fig.I-4: Schematic diagram for electron transport in 0-D and 1-D nanostructures

However, if the material is fabricated in a columnar and porous morphology, such as *O-D or 1-D* nanostructures, the charge transport can be improved. An additional issue for films with interconnected zero-dimensional (0-D) nanoparticles in charge transport, is often limited because of the lack of continuous conducting pathways, with electrons moving by a hopping mechanism due to energy barriers between particles [2]. 1-D nanostructures are expected to have improved charge transport properties compared to 0-D nanostructures [3] because of the direct conduction pathways in columns or nanorods compared to electron hopping in nanoparticle systems. A representative scheme showing the electron mobility in *0-D* and *1-D* nanostructures is shown in Fig.1-4.

In a successful utilization of *1-D* nanostructures, Paulose *et al*. [4] demonstrated hydrogen generation utilizing 6 μm long TiO_2 nanotube arrays and attained a hydrogen rate of ~ 180 μLhr^{-1} via photolysis.

I-2-6) Role of adsorbate electrophilicity on charge transport

For polycrystalline TiO_2, it has been shown that electrons could be trapped in the conduction band upon either thermal or photon excitation, where they reside for a long time if the temperature is sufficiently low. The conduction band is depopulated by heating the sample or by charge transfer from the conduction band to adsorbates on the surface. It has been found that efficient charge transfer occurs exclusively between the TiO_2 surface and an adsorbate molecule with an electrophilic moiety. No observable charge transfer occurred with a similar molecule with no hydrophilicity [5].

I-2-7) Reaction steps in heterogeneous photo-catalysis

When an electron is electronically excited from the valence band to the conduction band, it leaves behind a positively charged hole that is also mobile and can move throughout the bulk or surface of a material similar to the way the electrons can move around the conduction band. Both the electron and hole are used to induce the chemical reactions at the surface of the semiconductor material (Fig.I-5). Traditionally, the holes act as an oxidizing agent while the electrons act as reducing agents at the surface of the material. Because the electron-hole pair is very active and initiates most of the reactions on the surface of photo-catalysts, it is beneficial to have a high concentration of these charge carriers at the surface, and to also keep them apart for an extended period of time.

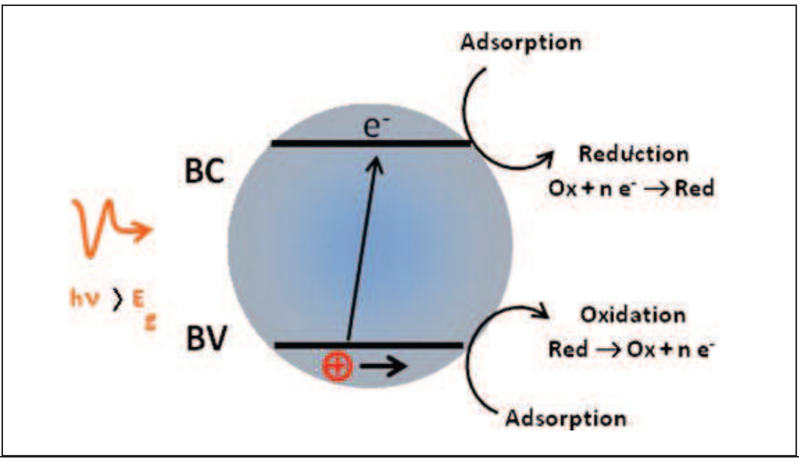

Fig.I-5: Schematic diagram for the reaction steps in heterogeneous photo-catalyse

Heterogeneous photo-catalysis is a complex process that has been the subject of significant research. As with any method including reactions in heterogeneous phases, the photo-catalytic process can be divided into five steps:

1. transfer of reactive molecules dispersed in the solution or gas phase to the catalyst surface
2. adsorption of reactive molecules on the surface of the catalyst
3. reaction on the surface of the adsorbed phase
4. desorption of products
5. elimination of products from the fluid/catalyst interface

The actual photo-catalytic reaction occurs in step 3. When a semiconductor catalyst (SC) of oxide type (TiO_2, ZnO) or chalcogenide (CdS, ZnS) is illuminated by photons of energy equal to or greater than the band gap E_g ($h\upsilon > E_g$), there is absorption of photons and creation of electron-hole pairs. The electron-hole pairs dissociate into free photo-electrons in the conduction band and photo-holes in the valence band. Simultaneously, in the presence of a fluid phase (gas or liquid), adsorption occurs, and depending on the redox potential (or energy level) of each adsorbate, an electron transfer takes place towards molecules of acceptor behavior (A), while the positive photo-holes are transferred to the molecules of donor character (D). Once the reactants are broken down, products are formed at the surface and can be taken away, to free the valuable active surface area needed to continue the reaction effectively. Thus, an important factor in photo-catalysis is that breaking down reactants must deal directly with the diffusion of unreacted particles to the photo-catalyst surface, as well as the diffusion of the reactant products away from the photo-catalyst surface.

The other mechanism for photo-catalysis still involves the photo-generated holes, but only in a secondary manner. This mechanism supposes that the holes break down water molecules into hydrogen (H^+) and hydroxy radicals ($OH^\bullet$) as follows:

$$H_2O + h^+ \rightarrow H^+ + OH^\bullet \qquad \text{Eq.I-6}$$

From there, the hydroxyl radicals, which have a very high oxidation potential, can break down the organic molecules:

$$OH^\bullet + R \rightarrow OH + R^\bullet \qquad \text{Eq.I-7}$$

This reaction scheme is more complicated than the first and requires a two-step process to degrade the dissolved organic materials. While the first mechanism relies on the diffusion of the holes to the photo-catalyst surface as well as the diffusion of the reactants to the surface and the products away from the surface, the second scheme has several more steps. The diffusion of the holes to the surface should be the same as the first scheme, since the photo-catalyst is the same regardless of which reaction scheme we use. However, when the holes break down the water molecules into hydrogen and hydroxyl radicals, these radicals must then find the reactant molecules to break them down. Hydroxyl radicals are not very stable, and have relatively short lifetimes (<1 ms) before forming more stable products such as water or hydrogen peroxide. This scheme requires that the radicals find a reactant molecule and break it down before they become stable themselves, which is a difficult, delicate, and quick process.

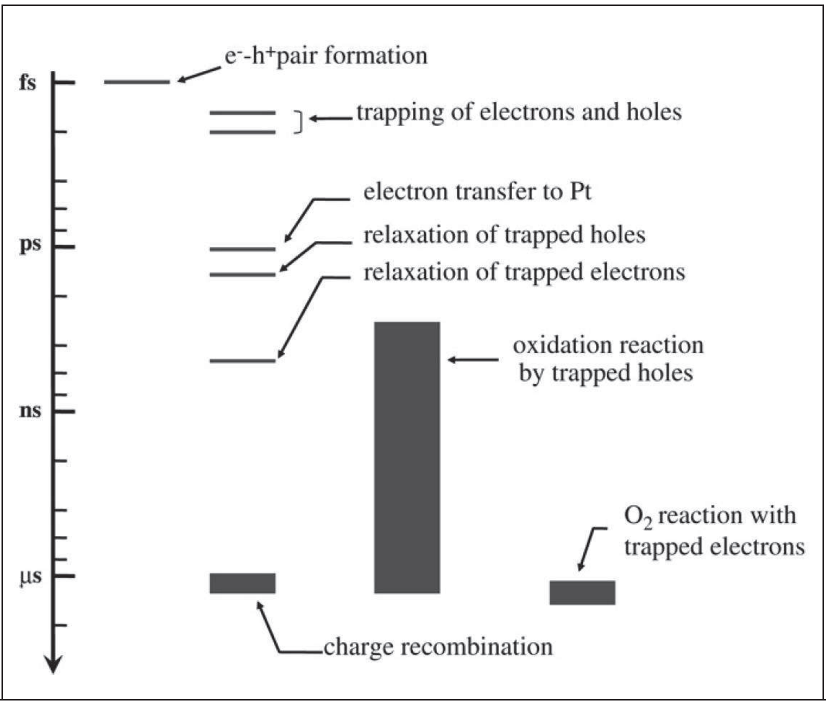

Fig.I-6: Some measured characteristic time scale for primary processes in TiO_2 photo-catalysis after Fujishima et al. [6].

Both of these schemes, i.e. breaking down the pollutants directly or by means of hydroxyl radicals have been used to describe the effect of active photo-catalysts to breakdown organic materials at their surface. While the exact mechanism or number of steps involved is different between the two schemes, there are some similarities that are apparent. Such similarities are that the reaction is driven primarily by the photo-generated holes, and the higher amount of surface area of the photo-catalyst will allow for more holes to reach the surface and either directly breakdown the reactant, or break down water molecules to participate in the degradation reactions. This information is vital for creating optimized photo-catalysts that can take advantage of this mechanism, and a higher performance should be seen in samples with higher surface area. Examples of some measured characteristic times for primary processes in TiO_2 photo-catalysis have been collected in Fig.I-6 and in the annexes of this chapter. [6].

The principles that govern the photo-degradation of pollutants in aqueous solutions and electrochemical water splitting are mostly the same. They include the generation of photo-induced charges, light, and surface reactions. The differences are that the photo-catalytic degradations are localized on the surface of the photo-catalyst, while the photo-electrochemical water splitting reactions transport photo-generated electrons from the photo-catalyst to an anode material to complete the redox reactions.

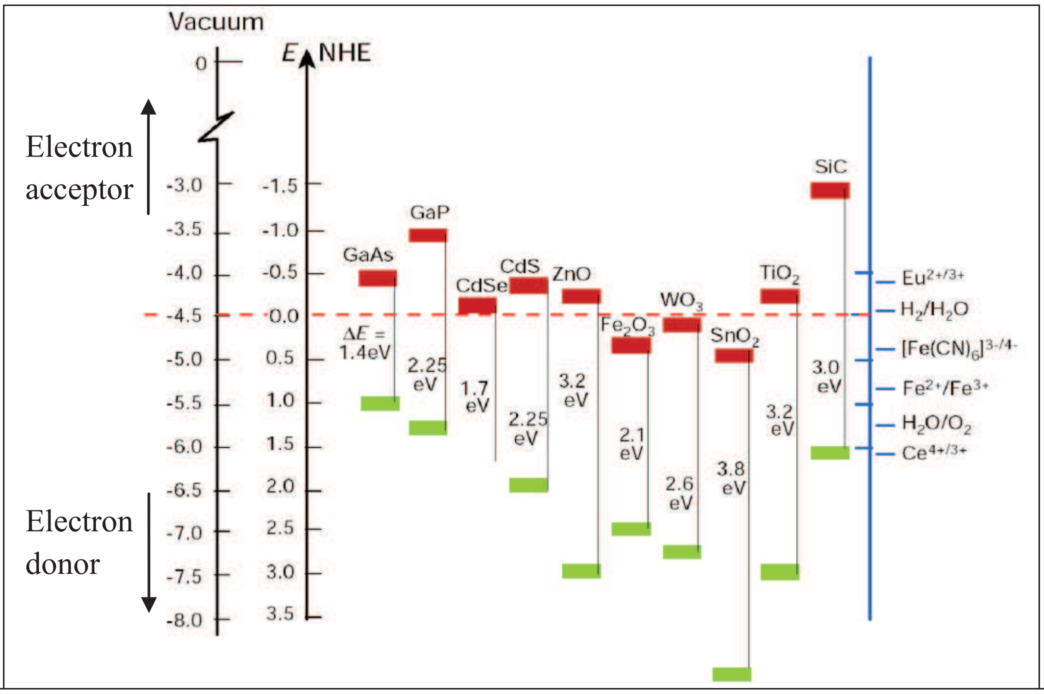

Fig.I-7: Band positions of several semiconductors in contact with aqueous electrolyte at pH 1 [7]

Fig.I-7 presents the Band positions of several semiconductors in contact with aqueous electrolyte at pH=1 (see also [118]), we define the ***electron affinity*** of a semiconductor as the difference between its conductive band minimum and the vacuum energy. A solid which has more positive electron affinity is often called electron acceptor, and the one which has less positive electron affinity is called electron donor, as presented in Fig.I-7. It is useful to note that water splitting could be thermodynamically possible, on the surface of the semiconductor, if the valence band and the conduction band of the semiconductor are lower than O_2/H_2O redox couple and higher than H_2O/H_2 redox couple, respectively. In another words, the valence band should be more positive than V_{O_2/H_2O} and the conduction band should be more negative than V_{H_2O/H_2} (the semiconductor bands cover the water redox voltages).

I-3) Titanium dioxide (TiO$_2$)

I-3-1) Advantages of titania semiconductor

TiO_2 has attracted significant interests for many applications, especially for its high stability and resistivity to corrosion, availability and its low-cost production. Also, this semiconductor has a conduction band CB minimum and dopant states positions above H_2/H_2O level. Sufficient overlap between the intra-gap and band states of the photo-catalyst could provide a fast transfer of photo-excited carriers to the reactive sites at the surface within their lifetime. On the other hand, effective absorption of photons over the visible range (i.e., 1.6–2.8 eV) could be realized with modified TiO_2 (doped or defected titania), and it is possible to get a high surface area with a high density of localized states involving energetic electrons between the conduction band and valence band especially in the case of powders and porous thin films.

I-3-2) Different crystalline structures of TiO_2

Titanium dioxide (TiO_2), also known as titania, is an important photo-catalytic material that exists as two main polymorphs, anatase and rutile having tetragonal coordination. The presence of either or both of these phases has a significant impact on the photo-catalytic performance of the material. Brookite (orthorhombic) is another commonly known polymorph of TiO_2 but it is difficult to produce. Table I-1 summarizes the main physical characteristics of anatase and rutile forms of TiO_2.

Table I-1: main characteristics of anatase and rutile forms of TiO_2.

Property	**Anatase**	**Rutile**
Crystal structure	Tetragonal	Tetragonal
Atoms per unit cell	4	2
Lattice parameters (nm)	a = 0.3785	a = 0.4594
	c = 0.9514	c = 0.29589
Unit cell volume $(nm^3)^a$	0.1363	0.0624
Density (kg m-3)	3894	4250
Calculated indirect band gap		
(eV)	3.23~3.59	3.02~3.24
(nm)	345.4~383.9	382.7~410.1
Experimental band gap		
(eV)	# 3.2	# 3.0
(nm)	# 387	# 413
Refractive index	2.54~2.49	2.79~ 2.903
Solubility in HF	Soluble	Insoluble
Solubility in H2O	Insoluble	Insoluble
Hardness (Mohs)	5.5~6	6~6.5
Bulk modulus (GPa)	183	206

On the other hand, less known but already reported polymorphs could be formed at high pressure [8-9] like TiO_2 II or srilankite (orthorhombic polymorph which has the lead oxide structure), cubic fluorite-type polymorph, pyrite-type polymorph, monoclinic baddeleyite-type polymorph and cotunnite-type polymorph.

Anatase transforms to rutile at elevated temperatures, but this transformation does not have a singular temperature. The transformation temperature depends on the preparation process as well as the post-fabrication annealing and other mechanical methods to inhibit or promote this transformation (ambient pressure, doping, porosity, etc.). It has been reported in many works that the rutile phase is more stable than anatase, which has been confirmed by thermodynamic calculations [10-11]. This difference in stability means that the transition from anatase to rutile is an irreversible process, also rutile TiO_2 can never transform to the anatase phase.

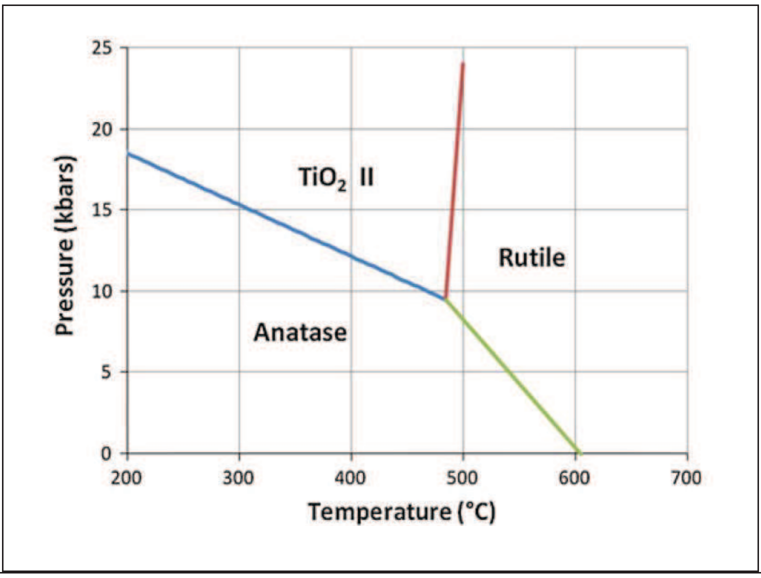

Fig.I-8: Boundaries of phase transitions in TiO_2 vs annealing temperature and pressure [8].

The main differences between anatase and rutile properties are that crystal size of anatase is higher than that of the rutile structure, anatase light absorption is lower than that of rutile and the photo-catalytic activity of anatase is much higher than that of the rutile.

Hanaor et al. [8] have regrouped the main conditions which could promote or inhibit the phase transformation (from anatase to rutile) including the pressure, temperature, morphological effects, and doping elements. Fig.I-8 presents the reaction boundaries of phase transitions in TiO_2 powder versus temperature (within thermal treatment) and working pressure. Over the last 50 years, many studies have been done in order to study the kinetic of anatase to rutile transition, but various values of transition temperature have been reported depending on the preparation technique, the morphology and the structure of the as-deposited TiO_2. As a general conclusion anatase to rutile phase transition could be expected to take place by thermal treatment between 500°C to 750°C (which is discussed in the next section).

Anatase is the preferable structure of titania due to its good photo-activity under UV light irradiation. Rutile phase alone does not have any remarkable photo-activity even though it has a better photo-absorption than the anatase phase (band gap of rutile TiO_2= 2.9 to 3.0 eV). Many explanations are available for this opposite behavior of rutile, the most useful one is the high recombination rate of carriers in the rutile phase. Many authors reviewed the good photo-activity of the anatase-rutile mixtures [12-14], due to the improved charge separation of the two phase mixture and the good photo-absorption of the rutile structure.

I-3-3) TiO_2 in powder and thin films

Using TiO_2 in the powder form presents many major problems such as the need for separation or filtration steps, the problematic use in continuous flow systems and the aggregation of particles (especially at high concentrations). To overcome these disadvantages, thin film fabrication of TiO_2 photo-catalysts has been much more prevalent in recent years. However, the overall photo-catalytic performance of TiO_2 thin films has, in general, shown less activity in comparison with suspended powders in solution [15]. The reason for this is that ***the photo-catalytic process is a surface and not a volume or mass phenomenon*** [68]. Easy access to illuminating light and contaminant material is essential for successful photo-catalytic degradations. In the case of thin films the active surface area is generally planar, while for the TiO_2 powders there is a much larger surface area.

On the other hand, it has been reported that the structural transformation between anatase and rutile as well as the residual strain depend very much on the TiO_2 morphology (powder or thin film) [15-16] as well as the nature of the substrate [17-18] (in the case of thin films). In the work of Martyanov et al. [15], the authors have reported that the nature of the substrate supporting the TiO_2 film is important for the stabilization of the anatase form at high temperature (more than 800°C) compared to anatase powder which could be converted into rutile at 500°C to 600°C.

I-4) Different methods used for TiO_2 production

TiO_2 can be prepared in the form of powders, crystals, or thin films. Both powders and films can have a crystalline structure ranging from a few nanometers to hundreds of nanometers. It should be noted that nanosized crystallites tend to agglomerate depending on the particle size, particle concentration and the ionic strength [19]. If separate nanosized particles are desired, often a deagglomeration step is necessary. However, many novel methods can produce nanoparticles without an additional deagglomeration step [20].

I-4-1) Solution routes

Preparing TiO_2 by a chemical wet process has the advantages of a higher degree of control over the stoichiometry [21], producing homogeneous materials, allowing the formation of complex shapes, and easy preparation of composite materials. However, there are several disadvantages which include expensive precursors, long processing times, and the presence of carbon as an impurity, especially in the case of sol-gel and PECVD. The most commonly used solution routes in the synthesis of TiO_2 are presented in *Table I-2*:

I-4-2) Gas phase methods

For thin film preparation, most fabrication methods are performed in the gas phase, which can be chemical or physical in nature. The main techniques used are summarized in Table I-3. Some of these techniques can also be used to synthesize powders if a method to collect the produced particles is employed.

I-4-2-1) Thermal evaporation

In thermal evaporation, a material is evaporated from a crucible and deposited onto a substrate in a technique called physical vapor deposition (PVD, the stream of material follows a straight line from source to substrate.

I-4-2-2) Electron beam evaporation

In electron beam (E-beam) evaporation, a focused beam of electrons heats the selected material. These electrons in turn are thermally generated from a wire filament (usually tungsten) that is heated by a high current. TiO_2 films deposited by E-beam evaporation have shown superior characteristics over CVD grown films where smoothness, conductivity, the presence of contamination, and crystallinity are concerned, but on the other hand, the production is slower and more laborious. The use of reduced TiO_2 powder (heated at 900°C in a hydrogen atmosphere) is necessary to make it conductive enough (resistivity $\rho \leq 10^{-1} \Omega.cm$) to focus the electron beam in the crucible.

I-4-2-3) Sputtering

This technique is frequently used to produce TiO_2 films with direct current (DC) or radio frequency (RF) currents. The technique uses plasma consisting of argon and oxygen. Accelerated Ar ions hit an electrode made of TiO_2 or Ti and lead to evaporation of a part of the target. The ejected particles can react with any reactive gas introduced in the reactor along with the argon before their deposition on the substrate. This leads to high quality films with good control over the stoichiometry.

Sputtering is the bombardment of an elemental target (titanium) using an inert gas (argon). Reactive sputtering occurs when a gas is purposely added to the sputtering chamber to react with the sputtered material to form a compound. Examples are when oxygen is introduced into the chamber with the sputtering of titanium to form titanium dioxide or when nitrogen is added to form titanium nitride. Since, 1950, reactive sputtering has been used extensively by manufacturers as for coating architectural glass, cutting tools, optical coatings, microelectronic devices and transparent conductive oxides.

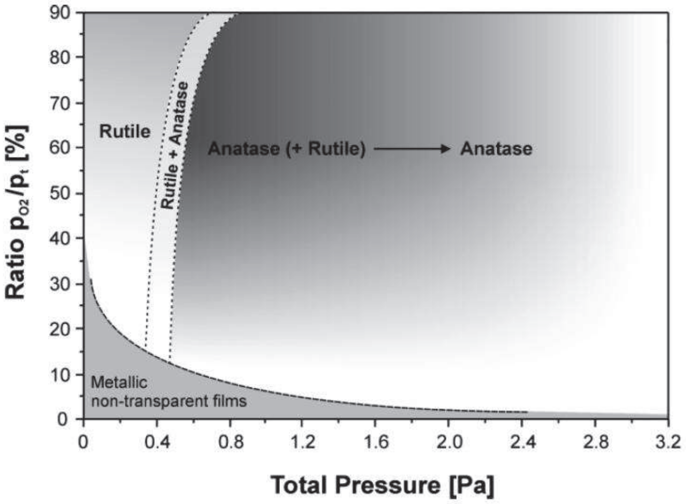

Fig.I-9: Schematic phase diagram for reactive RF magnetron sputtering of TiO_2 films on unheated substrate [23].

It has been reported that the amount of sputtered atoms that reach the substrate and their kinetic energy may decrease with an increase in the sputtering gas pressure [22]. Zeman et al. constructed a schematic phase diagram, based on XRD analyses, for reactive RF magnetron sputtering of TiO_2 films on unheated substrate [23] (Fig.I-9). This diagram summarizes the effect of total working gas pressure and the partial pressure of the reactive gas (oxygen), during the sputtering deposition, on the structure of the deposited TiO_2. The rutile phase is favored at very low sputtering working pressure while higher working pressures could enhance the anatase phase crystallization. Also they concluded a general decrease of the film crystallinity as the working pressure increases.

There has not been much research to investigate the effect of the sputtering working pressure on the film structure [12][24-25], morphology and the resulted photo-activity. In addition, the synergetic effect of pressure, reactive gas and doping level during the sputtering deposition have not been experimentally investigated thoroughly, especially when working before the poisoned mode of sputtered target (detected by the diagnostic of plasma, as will be seen in the next chapter).

When a negative bias is applied to the substrate (-50 to -300V), it can lead to an increase of the energy of the surface atoms resulting in an enhanced surface diffusion, which can result in a better adhesion, nucleation, and crystal structure. Also chemisorbed contaminants could be avoided from the deposited film [26].

A larger bias can be applied to etch the substrate and the deposited film (anti-sputtering), so, the non-uniformities can be reduced. In other words, this reverse bias allows ions to be accelerated towards the substrate rather than the target and the thick points, on the deposited film, will be etched faster (for the same reasons they deposited faster) [26-27]. This process could be also used to clean the surface prior to deposition.

On the other hand, it has been reported that substrate biasing can modify the crystalline phase orientation of thin films [28] and promote the formation of the rutile structure of TiO_2 [29] or even decrease the crystallinity of the deposited film to be amorphous [26-27]. At low pressure, substrate biasing can slightly increase the deposition rate but at higher working pressure the biasing could increase the anti-sputtering of the deposited film [27].

Table I-2: Commonly solution routes used to produce Titanium dioxide.

	Preparation process	Description	Phase structure	Specifications
Solution routes	Hydrolysis & Precipitation methods [30-31]	Precipitation at room temperature from Ti source solutions ($TiCl_3$ or $TiCl_4$) using ($NaOH$, NH_4OH, urea)	amorphous	Non uniform particle size distribution, nanoparticles
	Hydrothermal/Solvothermal methods [32-33][117]	Precipitation of TiO_2 from aqueous or organic solution media at elevated temperatures (>400°C).	anatase, rutile or mixture	More useful to control grain size, particle morphology, crystalline phase, and surface chemistry by regulating the solution composition, reaction temperature, pressure, solvent properties, additives, and ageing time
	Flame pyrolysis [34]	Combustion of $TiCl_4$ with oxygen, temperature reaches about 650°C for a short period (1–2 min).	anatase or mixture	highly crystalline particles of fine/large area. rutile production is difficult as the crystallization time is very short.
	Sol– gel synthesis at room temperature [35-36]	Hydrolysis of $TiCl_4$ or an organometallic compound as TTIP ($Ti[OCH(CH_3)_2]_4$). Thermal treatment (400 to 600°C) is required to remove residual organic materials.	amorphous	Synthesis of thin films, powders, and membranes. Good purity, homogeneity and flexibility in introducing dopants in large concentrations, stoichiometry control over the composition, and the ability to coat large and complex areas
	Electrochemical synthesis [37]	Various Ti compounds have been used, such as $TiCl_3$, $TiO(SO_4)$ and $(NH_4)_2TiO(C_2O_4)_2$. Electrolysis requires both an acidic medium and an oxygen-free environment.	amorphous, anatase, rutile or their mixtures	Reliable control of the characteristic states of the film by controlling the electrolysis parameters as potential, current density, temperature and pH
	Micro emulsion methods [30]	Ti source supported in water & oil microemulsion for synthesis of TiO_2 nanoparticles	amorphous	Very less used

Table I-3: Gas phase methods used to produce Titanium dioxide.

	Preparation process	Description	Phase structure	Specifications
Gas phase methods	Chemical vapor deposition CVD [38-39]	Spraying of Ti-bearing solutions. Compounds (ranging from metals to composite oxides) are formed via a chemical reaction or decomposition of a precursor in the gas phase	amorphous, anatase, rutile or mixture	Film properties depend on the type of precursor, the activation process and on the working pressure.
	Spray pyrolysis deposition (SPD) [40]	An aerosol is formed from a precursor solution (instead of a vapor in CVD). It is directly focused onto the sample in most cases (whereas diffusion is a dominant process in CVD). The heated substrates are at ambient pressure (while in CVD the set-up commonly is under reduced pressure).	anatase, rutile or mixture	Simple deposition technique, low costs, reproducible and can realize deposition on large areas in a short time. BUT, it suffers of reduced film uniformity in most cases, as well as problems in the film smoothness.
	Physical vapor deposition [41-44]	Deposition of evaporated Ti and its subsequent oxidation: - thermal evaporation (1) - electron beam evaporation (2) - sputtering with DC or RF current (3) - ion implantation (4) - dynamic ion beam mixing (5)	amorphous, anatase, rutile or mixture	No chemical transition from precursor to product. Gaseous stream follows a straight line from source to substrate. This leads to shadow effects, which are not present in CVD. It should be realized under reduced pressure to minimize collisions of gas molecules and prevent pollution of the deposited film

I-5) TiO_2 applications

Titania is known to be applicable in a wide range of important technological areas, in energy as electrolysis of water to generate hydrogen [45-46][1]. Also in dye-sensitized solar cells (DSSCs) [47]. For solar cell applications, the anatase structure is preferred over the rutile structure, as anatase exhibits a higher electron mobility, lower dielectric constant, lower density, and lower deposition temperature. Also, TiO_2 has environmental applications for air purification [48][6], water treatment [49-50] as well as built environment for self-cleaning and non-spotting coatings [38][22]. It is used in biomedicine as for self-sterilizing coatings [51], and finally, in optics and optoelectronics.

The electrolysis of water is composed of a complicated series of steps that involves current flowing though an electrolytic solution comprised of water and a charge carrying solute. Traditionally, photo-electrochemical cells (PEC's) are constructed in order to contain all the components to split water including a photo-anode, a cathode, an electrolyte solution, and a load for the current to flow across. The first study of photo-electrochemical water splitting on TiO_2 was reported by Fujishima and Honda in 1972 [52][8].

Titanium dioxide has a high refractive index in both rutile and anatase phases, which results in a high reflectivity from the surfaces. It is therefore used as white pigment in paints, food coloring, cosmetics, tooth pastes and other instances in which white coloration is desired. However, paints utilize polymeric binders to fix the pigment and, when in contact with titania, the oxidation of the polymer may be accelerated by the photo-catalytic effect of TiO_2 when exposed to light. The latter enhances the direct degradation effect of polymers induced by ultraviolet (UV) or solar radiation.

I-5-1) Mechanism of photo-activity of pure and doped TiO_2

Photo-catalytic activity is initiated through the presence of adsorbed radicals on the material surface. These radicals are very oxidative species having free electrons and could be formed via an adsorbed water or oxygen molecule reacting with the photo-generated electrons and holes. Photo-generated carriers are generated when TiO_2 absorbs irradiation having an energy higher than the optical band gap (for pure TiO_2 ~3.2 eV corresponding to UV wavelengths of 290~380 nm). Then electrons are exited from the valence band to the conduction band leaving behind photo-generated holes in the conduction band. Electrons in the valence band act as reducing agents for electron acceptors, and the holes are responsible for the oxidation of electron donors. Therefore, all photo-induced phenomena involve surface bound redox reactions [118].

The following reactions (Eq.I-8 to Eq.I-11) give an example of the most commonly used mechanisms to describe the photo-generation of reactive radicals and their activity, in aqueous solutions or in gaseous environments:

$$TiO_2 + h\nu \longrightarrow h^+ + e^- \qquad \text{Eq.I-8}$$

$$h^+ + H_2O_{adsorbed} \longrightarrow H^+ + OH^\bullet \qquad \text{Eq.I-9}$$

$$h^+ + OH^-_{adsorbed} \longrightarrow OH^\bullet \qquad \text{Eq.I-10}$$

$$e^- + O_{2_{adsorbed}} \longrightarrow O^{-\bullet} \qquad \text{Eq.I-11}$$

Where:

The ***points*** represent the unpaired electrons, $\boldsymbol{h^+}$ represents photo-generated hole in the valence band, and $\mathbf{e^-}$ are the photo-generated electrons in the conduction band.

The generation of positive and negative charge carriers by UV/Visible irradiation is in competition with the recombination tendency. Titania has a relatively slow rate of charge carrier recombination in comparison with other semiconductors, such as Fe_2O_3, because of better hole diffusion in TiO_2 [53]. Carrier separation can be enhanced via the presence of localized states within the band gap of TiO_2 which can trap the photo-generated electrons [54] or the photo-generated holes [55].

Photo-generated electron–hole pair needs a lifetime of at least 0.1 ns to affect the chemical reactions [8]. On the other hand it has been reported that photo-generated electrons and holes could exhibit a lifetime of hours at very low temperatures around 90 K [56]. In the presence of some reactive species adsorbed on the catalyst surface, photo-generated charge carriers may diffuse to these adsorbates and react with them to form radicals rather than recombine [57-59].

The visible light photo-activity of metal-doped TiO_2 can be explained by a valance band shift (band gap reduction) or new energy levels produced in the band gap of TiO_2 as presented in Fig.I-10. The latter levels could be created by doping with metals (Cu, Co, Ni, Cr, Mn, Mo, Nb, V, Fe, Ru, Au, Ag, Pt) [45][49][60-62] in the TiO_2 matrix where electrons can be excited from the defect state to the TiO_2 conduction band by photons with energy equal or higher than $h\nu_2$. Additional benefit of transition metal doping is the improved trapping of electrons to inhibit electron-hole recombination during irradiation. The decrease of the recombination of charge carriers results in enhanced photo-activity. Also, doping with nonmetals (N, S, C, B, P, I, F) [42][49][54-55][47][63-65] can lead to the formation of isolated impurity energy levels above the valence band. So photon absorption having energies higher than $h\nu_3$ excites electrons from this impurity energy level to the conduction band. Some authors reported a hybridation between N_{2p} states and O_{2p} states near the valence band [66]. Of course other codoped semiconductors have been already investigated such as Ta&N doped TiO_2 [67], as well as La&N doped TiO_2 [36].

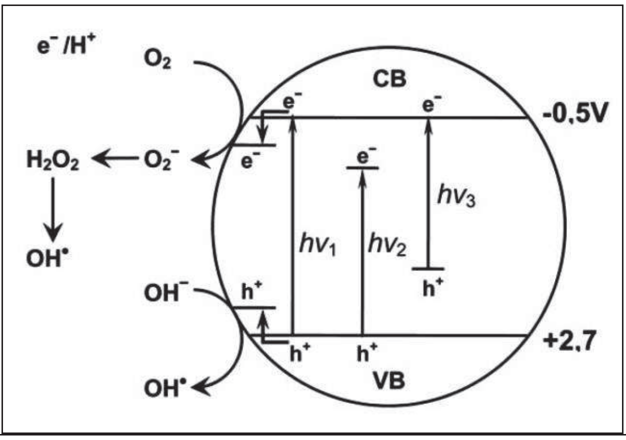

Fig.I-10: Mechanism of TiO_2 *photo-catalysis:* $h\nu_1$*: pure* TiO_2*;* $h\nu_2$*: metal-doped* TiO_2 *and* $h\nu_3$*: nonmetal-doped* TiO_2

I-5-2) Effects of oxygen vacancies

Oxygen deficiencies could introduce other energy states just below the conduction band of TiO_2 [64-65][68-69]. This under-stochiometric TiO_{2-x} should have darker color (light gray to dark color in general). On the other hand, reduced TiO_2 (TiO_2 with oxygen vacancies) has been shown to have a longer lifetime for the holes due to a reduced number of recombination centers [70], but structural imperfections in the TiO_2 lattice could also generate other trap sites which may act as recombination centers, leading to a decrease in the free electron and hole concentration [71]. Trapping of holes at the TiO_2 surface increases its photo-induced reactivity [55].

Wendt et al. [72] provided a comprehensive density functional theory calculation to explain the relationship between the photo-activity of TiO_2 and the reducibility of the oxide. Oxygen vacancies are assumed to cause the Ti_{3d} defect state in the band gap. Using high-resolution scanning tunneling microscopy and photo-electron spectroscopy measurements, they proposed that Ti interstitials in the near-surface region may be largely responsible for the defect state in the band gap and these defect (or donor) sites play a key role in the surface chemistry and reactivity such as providing the electronic charge required for O_2 adsorption and dissociation.

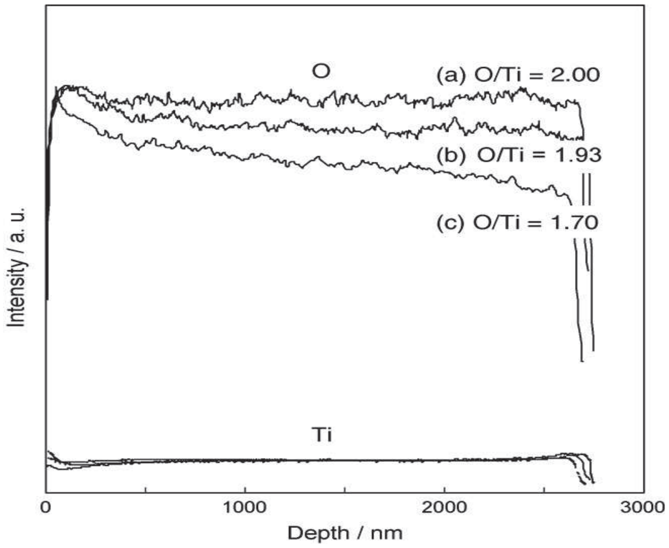

Fig.I-11 : Depth distribution profiles of ^{18}O *and* ^{48}Ti *for: (a) UV grade* TiO_2*, (b) Vis grade* TiO_2 *d=80 mm and (c) Vis grade* TiO_2 *d=70 mm thin films, as determined by SIMS measurements. d : is the distance between the substrate and the target in the sputtering chamber.UV and Visible grade, i.e: photoactive when absorbing UV and visible irradiations, respectively.* [22].

In **sputtering** deposition, many works [22] show a decreased gradient of the O/Ti composition from surface to bulk in the visible grad titania (undoped). Also, as the kinetic energy of the sputtered atoms increases with a decrease in the target/substrate distance, this gradient will be more pronounced if the target/substrate distance decreases. Fig.I-11 presents an example of SIMS depth profiles of UV grade–TiO_2 and Visible grade–TiO_2 (with two different distances of substrate to target) [22]. SIMS investigations revealed that the stochiometrie of O/Ti concentration in both Vis–TiO_2 gradually decreases from the top surface (O/Ti ratio of 2.00±0.01) to the inside bulk, although no significant changes were observed for UV–TiO_2 which is composed of stoichiometric TiO_2. These results clearly indicate that the higher the kinetic energy of the sputtered atoms, the higher the oxygen vacancies formation probability in the TiO_2 thin films, accompanied by a large shift in their absorption band toward visible light regions. Such a unique anisotropic structure was seen to play an important role in the modification of the electronic properties, thus, enabling the absorption of visible light (for this study the authors have used the isotope ^{18}O in the deposition chamber to avoid the role of the oxygen contamination and post-oxidation which takes place with the ^{16}O).

I-6) Reviewing the different studies on doping TiO_2 in nano particles and thin films

In this section we will focus on doping TiO_2 with non metal elements and especially N doped TiO_2. Doping with other elements and more doping techniques are discussed in the annexes of this chapter.

I-6-1) Nonmetal doping

In nonmetal-doped TiO_2 photo-catalyst, the main problem present is that the photo-catalytic activity under visible light is much lower than that under ultraviolet light [22][30][73]. There are several ways to obtain a charge balance if an anion is replaced with a higher valence anion. The three general ways are:

(i) host-cations may oxidize to a higher charge state,
(ii) anion vacancies form that effectively remove negative charges from the crystal,
(iii) cation interstitials form that introduce additional positive charges in the crystal.

The first scenario is not possible in stoichiometric TiO_2 since Ti is already in its maximum valent 4+ charge state. In substoichiometric TiO_2, Ti^{3+} sites can be oxidized by introduction of higher valent anions. The outcome is then identical to scenario (ii). The higher valence of the N-dopants compared to the host O-anions could be compensated by the formation of oxygen vacancies and/or Ti-interstitials [74]. Oxygen vacancies, in the absence of N-dopants, can cause a reduction of Ti^{4+} to Ti^{3+} and occupation of Ti-3d states.

Asahi et al. [63] reported theoretical results from the substitution of C, N, F, P, or S for oxygen atoms in the titania lattice. Results of density of states (DOS) calculations for anatase TiO_2 suggest that substitutional type doping using nitrogen is effective due to the mixing of nitrogen 2p states with oxygen 2p states, thus causing a significant decrease in the width of the overall band gap. Similar calculated results were also obtained for S (sulfur) doping; however, S doping is not commonly employed due to its large ionic radius even though some work found interesting band gap narrowing with sulfur doping [75].

Carbon has recently received considerable interest as a nonmetallic dopant in TiO_2 materials [76][42] as it may act as a photo-sensitizer and could be excited to produce electrons by the visible light with subsequent injection of electrons into the conduction band of TiO_2.

A significantly reduced band gap of 2.32 eV is reported for the Carbon-doped titania [77], forms intra-gap localized levels [49], with good measured photo-current values, compared to 3.0 eV for undoped rutile [77]. The proposed mechanism for this action is band-gap narrowing. However, Tachikawa et al. [78] investigated carbonate-species-doped anatase TiO_2 and found that although UV-induced charge carriers are more generated with carbonate-doped TiO_2, no evidence for enhanced photo-catalytic activity is found. The authors attribute this finding to a possible decrease in the mobility of the photo-generated holes, which participate in the photo-oxidation step. This may be directly related to significant trapping of charge carriers that occurs upon photo-excitation and is directly dependent on the incoming photon flux and the density of impurity sites (which may act as trapping sites) in the surface or the bulk of the semiconductor material [79].

I-6-2) Photo-activity of N-doped anatase and rutile TiO_2

Di Valentin et al. [80] investigated the origin of the difference in photo-activity of anatase and rutile TiO_2 induced by substitutional N-doping using the state-of-the-art density functional theory calculations. In both polymorphs there are N_{2p} localized states just above the top of the O_{2p} valence band. In the anatase phase these states cause a red shift of the absorption band edge towards the visible region. But in rutile, this effect is reduced by the N-induced contraction of the O_{2p} band due to the change in the electronic structure of rutile upon N doping, resulting in an overall increase of the optical transition energy and band gap increase (Fig.I-12).

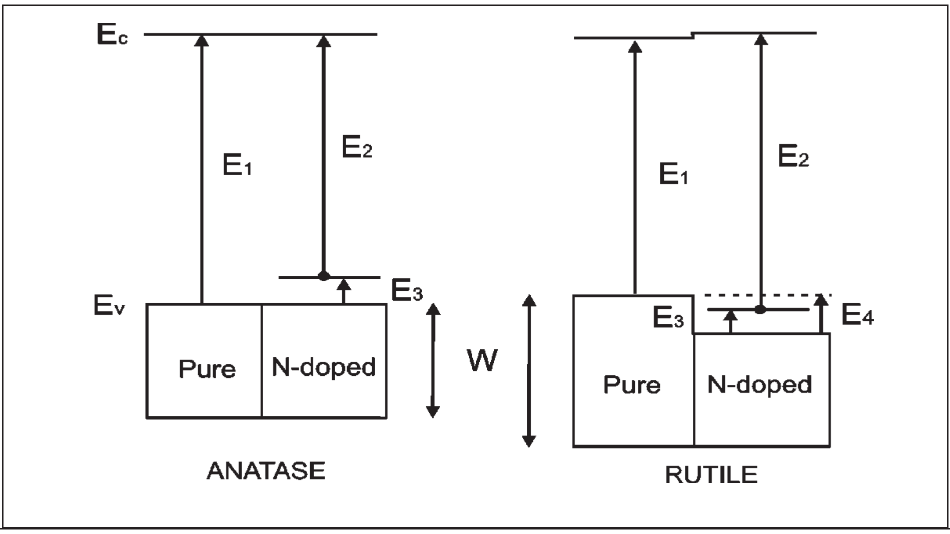

Fig.I-12: schematic presentation of band structure in nitrogen doped anatase and rutile TiO_2.

There are three different major opinions regarding the modification mechanism of TiO_2 doped with nitrogen [118] (which could be generalized for doping with nonmetals); (1) band gap narrowing, (2) new impurity energy levels and (3) new oxygen vacancies. Band gap narrowing has been investigated by Asahi, et al. [63] and it was found that N_{2p} states hybridize with O_{2p} states in anatase TiO_2 doped with nitrogen because their energies are very close, and thus the band gap of N-TiO_2 is narrowed allowing the semiconductor to be able to absorb visible light. Impurity energy levels were investigated by Irie, et al. [81] and it was stated that oxygen sites substituted by nitrogen atom (in TiO_2) form isolated impurity energy levels above the valence band. Irradiation with UV light excites electrons in both the valence band and also in the impurity energy levels. However, visible light irradiation excites electrons in the impurity energy levels only [54].

TiO_2 doped with substitutional nitrogen could have shallow acceptor states just above the valence state. In contrast, TiO_2 doped with interstitial nitrogen have isolated impurity states in the middle of the band gap (about 0.7eV above the valence band). These impurity energy levels are mainly hybridized by N_{2p} states and O_{2p} states [66][82]. Last, oxygen vacancies were investigated by Ihara et al. [83], and they concluded that oxygen-deficient sites formed in the grain boundaries are important to promote visible light activity, and nitrogen doped in parts of oxygen-deficient sites are important as blockers for re-oxidation.

I-6-3) Nitrogen sites and nitrogen efficiency in the TiO_2 lattice

Nitrogen can occupy substitutional (N–Ti–O and Ti–O–N) and/or interstitial (π* character NO) sites in the titania lattice. Fig.I-13 presents the structures of three types of nitrogen centers: (a) substitutional defects, N_s, in which nitrogen atom replaces an oxygen atom. (b) interstitial defects, N_i, in which the nitrogen atom is located in an interstitial place and the oxygen atom is also displaced from its original site. (c) substitutional-interstitial defects, N_{si}, in which the nitrogen atom occupies the same position as in the case of the N_s defect, and the oxygen atom occupies an interstitial place [54].

The difference in the dopant states for substitutional versus interstitial nitrogen impurities in anatase TiO_2 was investigated both theoretically, using DFT (density functional theory) calculations, and experimentally, especially using electron paramagnetic resonance (EPR) spectroscopy, XPS, and photoluminescence measurements [84][73]. The preparation methods and differing experimental conditions are found to drastically affect the nature of the measured XPS signals (more details on the XPS peak assignment of N1s core level are discussed in chapter IV).

In the work of Asahi et al. [63], the films exhibit N_{1s} XPS peaks at 396, 400, and 402 eV binding energies. The authors of this work claim that the nitrogen species responsible for the overall band gap narrowing effect exhibit the **396 eV N_{1s}** binding energy. Similar doped powders that did not show the 396 eV XPS feature also did not show enhanced photo-catalytic activity [63]. This peak is assigned to ***substitutionally*** bonded N^- which is the active dopant in that material. They suggested that substitutional type doping using nitrogen is effective due to the mixing of nitrogen 2p states with oxygen 2p states, thus causing a significant decrease in the width of the overall band gap. However, they reported that interstitial type doping and a mixture of both substitutional and interstitial types were both found to be ineffective. Also, in the work of Sangwook et al. [55] it is concluded that nitrogen atoms in substitutional sites enhance the photo-catalysis of TiO_2 under visible light more effectively than nitrogen atoms in interstitial sites.

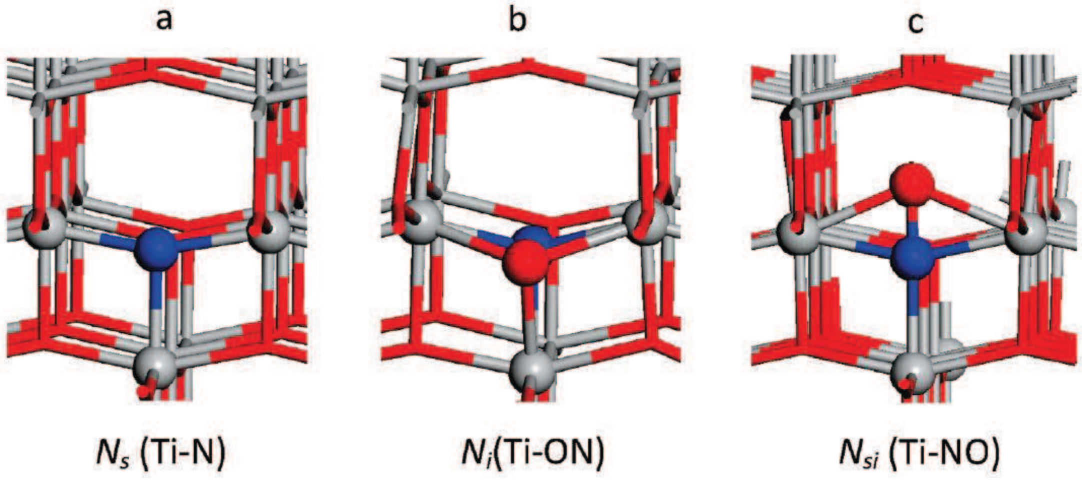

Fig.I-13: Structures of the three types of nitrogen centers (a) substitutional N_s (b) interstitial N_i and (c) substitutional-interstitial, N_{si} [54].

However, Peng et al. [65] found that the synergetic effect of substitutional and interstitial nitrogen of N-doped TiO_2 is able to give the best photo-catalytic activity. Similar results were found by Dong et al. [82]. In one study by Chen et al. it was found that authors attributed the 400 eV N_{1s} XPS peak to substitutional N [85]. Another peak between 399 and 400 eV has been attributed to an N—H complex ***interstitially*** bound in the TiO_2 lattice (if there is a hydrogenated compound during the preparation route of the doped titania) which could also be the active dopant [86-87]. The 402 eV N_{1s} binding electron energy could simply be attributed to interstitial nitrogen in the lattice [55], many authors attributed the 400 eV binding electron energy also to interstitial nitrogen species [88-89].

In the presence of oxygen vacancies, Lee et al. [25] proved that interstitial doping states involving N–Ti–O or Ti–N–O bonds are more effective for photo-catalysis than the substitutional nitrogen doping states, also, Shen et al. [90] found that the presence of interstitial nitrogen is preferable to increase the hydrophilicity of nitrogen doped titania.

Chen et al. also reported that the substitutional type nitrogen species (at around 400 eV in XPS) were responsible for the observed increase in the measured photo-catalytic activity in the visible region due to N—O type bonding (however the reported BE is quite low for N—O species, generally N—O comes out at higher binding energies) [91].

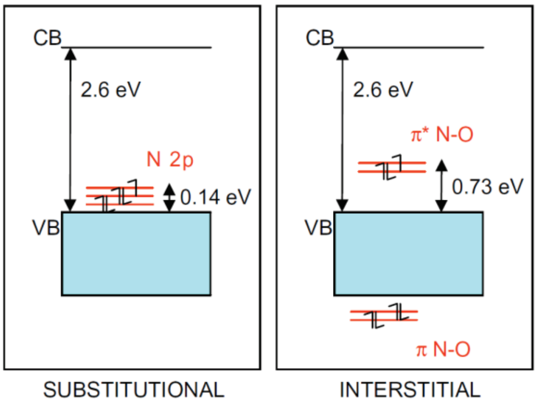

Fig.I-14 Electronic structure computed for substitutional and interstitial models Ref. [92]

Both types of nitrogen impurities are found to add localized states within the band gap. For substitutional type nitrogen, these states are located 0.14 eV above the valence band, and for interstitial type nitrogen species (referred to as N—O), the localized states are calculated to lie 0.73 eV above the valence band [92][82] (Fig.I-14). Also, these calculations have shown a large decrease in the formation energy for oxygen vacancies as a result of additional nitrogen atoms in the lattice. Therefore, oxygen vacancies are most probably induced by nitrogen doping of TiO_2 [84].

Most of nitrogen-doped TiO_2 exhibited visible light absorption as a shoulder in the wavelength range of 400– 600 nm, due to the presence of isolated N_{2p} orbitals above the valence band at lower nitrogen concentration (<2%) that could be doped into the TiO_2 lattice [22][88]. A smooth shift towards visible light regions in the absorption spectra could be achieved in the case of higher doping nitrogen concentration (up to 17%) with the substitutional nitrogen sites [22][92][88][40].

I-6-4) phase transition in nitrogen doped TiO_2

Since nitrogen is only 6% larger than oxygen, then substitution of nitrogen in the oxygen sublattice is possible. Hence, nitrogen is unlikely to destabilize the lattice and so it would be expected to be an inhibitor of the phase transformation from anatase to rutile during any post thermal treatment (Fig.I-8), but it could frequently generate oxygen vacancies in the TiO_2 lattice. It is useful to mention that it is possible to thermally nitride TiO_2 and get N doped titania, only at high pressure (10 to 100 bar) and high temperature (more than 900°C) under nitrogen or ammonia atmosphere [32].

I-6-5) Nitrogen implantation

Batzill et al. studied the effect of nitrogen implantation [74] in the TiO_2 film, when substituting N in the O sites, oxygen vacancies and/or Ti-interstitials could be created to compensate the higher valence of the N-dopant compared to the host O anions. The electron left from these oxygen vacancies should generate (Ti_{3d}) energy states just below the conductive band minimum, but Batzill et al. suggested that Ti^{3+} sites were being oxidized by filling the N_{2p} states (just above the valence band) rather than Ti_{3d} states. These filled states were responsible for the upward shift of the valence band maximum or the band gap narrowing (Fig.I-15).

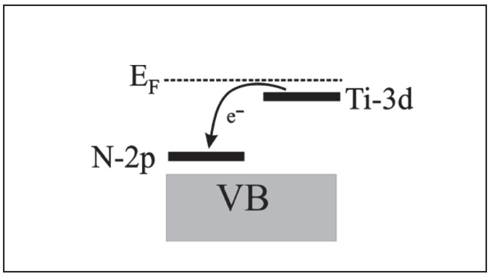

Fig.I-15: Schematic energy diagram of the band gap states induced by Ti^{3+} and N^{3-} defects in the TiO_2 lattice [74].

However, N implantation needs ions accelerated at high energy (0.2 to 200 keV) which can dominate the penetration of N atoms in the bulk (for example, TiO_2 was reported to be penetrated up to 6 nm in depth under bombardment with N ions having energy of 200 eV [74]). Also, a post annealing process was needed to allow diffusion of implanted atoms further into the bulk of the crystal [93] and nitrogen could be mostly present in interstitial sites [41][90].

I-7) TiN oxidation

Titanium Nitride preparation using sputtering technique has been studied in literature [94-95]. Another promising method to stably incorporate nitrogen into TiO_2 is through the oxidation of TiN, which has also yielded very diverse results. For example, Zhu et al. fabricated TiN_x thin films via DC sputtering and then annealed the samples at 450^oC, revealing a pure TiO_2 anatase phase with no traces of TiN left behind [46]. However, Brudnik et al. deposited and then oxidized TiN films using the same method, but achieved a pure rutile phase of TiO_2 when annealed at 300^oC [96], same conclusion found by Lee et al. [76] after oxidation at 450°C. The difference between these two studies was the deposition pressure, which was around 2 Pa for Zhu et al., and 1 Pa for Brudnik et al. ***This leads us to believe that there is a relationship between the sputtering deposition pressure of TiN thin films, and the resulting crystal structure of TiO_2 formed after TiN oxidation*** *(as will be seen in chapter VI).*

In other cases, polycrystalline phases of TiO_2 could be obtained, Lee et al. [76][47] and Wu et al. [97] all obtained a mixed phase of anatase and rutile after annealing TiN nanoparticles in air. While Kowalski et al. reported 300°C as a sufficient temperature to oxidize TiN to TiO_2 [98], many reports explained that the kinetic of TiN oxidation was very slow and it was efficient when annealing temperatures higher than 600°C to 850°C were used [76] to get anatase and/or rutile TiO_2.

While there have been several individual studies which have shown the ability to form anatase, rutile, and mixed phase TiO_2 by oxidizing TiN, a comprehensive method to controllably produce either phase individually, or both phases simultaneously has not been developed. Furthermore, when TiN oxidizes to TiO_2, there is a possibility of creating an intermediary compound of the form TiO_xN_y, which can be interpreted as a partially oxidized TiN layer, or a partially N-doped TiO_2 layer. The ability to manufacture this intermediary layer is vital to improving the visible light absorption and photo-activity of TiO_2, and is a critical challenge in the development of solar-driven photo-catalysts.

I-8) Photo-induced hydrophilicity and contact Angle Measurements

The most commonly utilized method for measuring surface hydrophilicity or hydrophobicity is through analysis of the water contact angle. The sessile drop method involves the placement of a droplet of liquid onto a horizontal surface and measuring the contact angle, either directly or through analysis of a digital image of the droplet on the surface. The solid-liquid interaction at the surface obeys Young's equation as (Fig.I-16):

$$\gamma_{LV} \cos\theta = \gamma_{SV} - \gamma_{SL} \qquad \text{Eq.I-12}$$

where γ_{LV} is the surface tension between the water droplet and the surrounding atmosphere, γ_{SV} is the surface tension between the surface and the surrounding atmosphere, γ_{SL} is the surface tension between the surface and the water droplet, and θ is the contact angle.

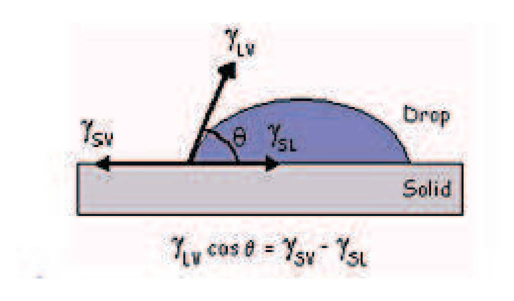

Fig.I-16: Diagram of the vector forces present at the solid- liquid interface. The measured contact angle (θ) is shown.

There are three possible mechanisms which have been proposed for the photo-induced hydrophilicity effect on TiO_2 surfaces. The first is based on ***induced defect production,*** which involves the production of Ti^{3+} ions at the surface as a result of oxygen atom ejection from the lattice. The defects, known as oxygen vacancies or Ti^{3+} sites, when produced on the surface are known to cause water dissociation, and the production of adsorbed OH^- species, which are known to be hydrophilic in nature. Other studies contradict this model [99] and report that the desorption kinetics for undissociated H_2O were essentially identical on two different surfaces with and without O vacancy defects. Second mechanism is based on the ***photo-induced rupture of Ti—OH bonding,*** this model suggests that the photo-induced hydrophilicity effect is due to surface modifications, which lead to an increased surface coverage by Ti—OH groups in the presence of H_2O. –OH groups bound in 2-fold coordination to Ti atoms are converted by H_2O adsorption into two –OH groups that are singly coordinated each to their own Ti atom [100]. Zubkov et al. used IR measurements to prove that no changes occur in the surface-bonding character of Ti-OH groups and of adsorbed H_2O molecules due to UV illumination [101], so, they concluded that the above was not the main model explaining the photo-induced hydrophilicity. The third model consists of the ***photo-oxidation of***

hydrophobic contaminant layer, the produced clean TiO_2 surface is hydrophilic especially if it is prepared by sputtering. The as-prepared surface appears to be clean when investigated using Fourier transform infrared spectroscopy (FTIR) [102]. When it is exposed to the ambient atmosphere, traces of hydrocarbon layers could be detected on the titania surface as measured using SFG (Sum Frequency Generation Spectroscopy) [102]. Photo-catalytic removal of hydrocarbons, from the surface of titania, has been reported to be the explanation for the wettability effect [101].

I-9) Conclusion

Photo-catalytic semiconductors are characterized by a filled valence band, and an empty conduction band. Upon irradiation, valence band electrons are promoted to the conduction band leaving a hole behind. These electron–hole pairs can either recombine or can interact separately with other molecules on the surface. The holes may react either with electron donors in the solution, or with hydroxide ions to produce powerful oxidizing species such as hydroxyl or superoxide radicals. The recombination of the electron and the hole must be prevented as much as possible in order to improve reaction efficiency.

The developments of visible light-responsive TiO_2 photo-catalysts have been investigated by the substitutional doping of metals or nonmetals with the aim of extending the absorption edge into visible light regions and to improve photo-catalytic reactivity. Several works has been carried out in the development of visible light-responsive TiO_2 by the doping of various kinds of anions, such as N, S or C, as a substitute for oxygen in the TiO_2 lattice. For these anion-doped TiO_2 photo-catalysts, the mixing of the *p* states of the doped anion (N, S, C) with the O_{2p} states was reported to shift the resulting valence band edge upwards to narrow the band gap energy of TiO_2. There are several factors that influence the photo-catalytic activity of modified TiO_2 thin films, including the method of doping, the amount of doping, and the annealing temperatures of samples.

N-doping has similar effects on both TiO_2 polymorphs (anatase and rutile). Early studies on N-doping suggested that the N-atoms hybridize with the valence (O_{2p}) band and this consequently results in a delocalization of nitrogen valence electrons and an upward shift of the valence band maximum. *More recent DFT calculation have disputed this claim and suggested the formation of localized N_{2p} states above the valence band of TiO_2.*

Most of nitrogen-doped TiO_2 exhibited visible light absorption as a shoulder in the wavelength range of 400– 600 nm, indicating that the isolated N_{2p} orbitals are formed above the O_{2p} orbitals at lower nitrogen concentration (<2%) that could be doped into the TiO_2 lattice . A smooth shift towards visible light regions in the absorption spectra could be achieved in the case of higher doping nitrogen concentration (up to 17%).

The photo-catalytic activity may be in excellent agreement with the absorbance tendency of the films, but this is not always the case. There is an optimum concentration of the doped element above which the doping element can act as recombination center or also can reduce the surface activation sites of TiO_2 and thus the photo-efficiency decreases. In addition, the space charge region formed in the vicinity of the anatase–rutile interface is thought to be responsible for photo-generated electron/hole separation and high activity of the commercially available TiO_2 Degussa P25.

From the literature it seems that the efficiency of doped-TiO_2 under visible light strongly depends on the preparation method used. In some cases of metal doping, such doped photo-catalysts showed no activity under visible light and/or lower activity in the UV spectral range compared to the non-doped TiO_2 because of the high carrier recombination rates through the metal ion levels. In the nonmetal-doped TiO_2 photo-catalyst, the main problem present is that the photo-catalytic activity under visible light is much lower than that under ultraviolet light. Therefore, development of new and optimized photo-catalysts exhibiting activity under visible light irradiation with surface characteristics insuring improved performance and high chemical and physical stability are crucial before utilization in solar photo-catalytic systems.

Objective of this study

1) Sputtering control and optimization

The sputtering technique has been used for many decades, but there are still many deviations from one system to another. It is important to study the ability of our system to give reproducible depositions with very good morphological and structural control. We used optical and electrical diagnostics to control the plasma in order to understand the different phenomena produced during sputtering to have a better deposition control.

2) Preparation of functional TiO2 under UV and visible light irradiation

In the following chapters we have tried to study and improve the commonly used methods of nitrogen doping in TiO_2 (dual gas sputtering) and to investigate the response of our deposited films according to two main applications: clean energy (photo-current measurements) and the photo-catalytic activity. Secondly, we have tempted to understand and clarify the mechanism of the known TiN oxidation in order to remove the present contradictions found in literature. This study gave us an interesting background and a novel model explaining the mechanism of the TiN oxidation to get different structural mixtures of anatase and rutile nitrogen doped titaniafinally, we have studied a novel method to improve the charge separation in nitrogen doped titania by depositing alternating bilayered films of TiN and TiO_2 which had different compositions and various numbers of bilayers. This study gave a novel understanding of the charge separation in nitrogen doped TiO_2.

References

[1] W Smith, S Mao, G Lu, A Catlett, J Chenb, Y Zhao, *Chemical Physics Letters*, **485** (2010) 171–175.

[2] C Santato, M Ulmann, J Augustynski, *Advanced Materials*, **13** (2001) 511–514.

[3] K Yu, J Chen, *Nanoscale Research Letters*, **4** (2009) 1–10

[4] M Paulose, G-K Mor, O-K Varghese, K Shankar, C-A Grimes, *Journal of Photochemistry and Photobiology A: Chemistry*, **178** (2006) 8–15.

[5] D Panayotov, J T Yates, *Chemical Physics Letters*, **381** (2003) 154.

[6] A Fujishima, X Zhang, D A Tryk, *Surface Science Reports*, **63** (2008) 515–582.

[7] M Grätzel, Review, *Nature*, **414** (2001) 338-344.

[8] D Hanaor, C Sorrell, *Journal of Materials Science*, **46** (2011) 855–874.

[9] P Xiaoyan, C Yi, *Journal of the American Ceramic Society*, **87** (6) (2004)1164–1166

[10] S J Smith, R Stevens, S Liu, G Li, A Navrotsky, J Boerio-Goates, B F Woodfield, *American Mineralogist*, **94** (2009) 236.

[11] J Muscat, V Swamy, N M Harrison, *Physical Review B*, **65** (2002) ID 224112.

[12] S M Marques, C J Tavares, L F Oliveria, A M F Oliveira-Campos, *Journal of Molecular Structure,* **983** (2010) 147-152.

[13] B Sun, A-V Vorontsov, P-G Smirniotis, *Langmuir*, **19** (2003) 3151

[14] D C Hurum, K A Gray, T Rajh, M Thurnauer, *Journal of Physical Chemistry B*, **109** (2005) 977.

[15] I N-Martyanov, K J-Klabunde, *Journal of Catalysis*, **225** (2004) 408–416.

[16] Y Li, M Ma, X Wang, Z Li, *Surface & Coatings Technology*, **204** (2010) 1353–1358.

[17] I Alhomoudi, G Newaz, *Thin Solid Films*, **517** (2009) 4372–4378.

[18] C Giolli, F Borgioli, A Credi, A Di Fabio, A Fossati, M M-Miranda, S Parmeggiani, G Rizzi, A Scrivani, S Troglio, A Tolstoguzov, A Zoppi, Ugo Bardi, *Surface & Coatings Technology*, **202** (2007) 13–22.

[19] Z Allouni, M Cimpan, P Høl, T Skodvin, N Gjerdet, *Colloids and Surfaces B: Bio interfaces*, **68** (2009) 83–87.

[20] O Carp, C L Huisman , A Reller, *Progress in Solid State Chemistry*, **32** (2004) 33–177.

[21] S Bangkedphol, H Keenan, C Davidson, A Sakultantimetha, W Sirisaksoontorn, A Songsasen, *Journal of Hazardous Materials*, **184** (2010) 533–537.

[22] M Kitano, M Matsuoka, M Ueshima, M Anpo, *Applied Catalysis A: General*, **325** (2007) 1-14.

[23] P Zeman, S Takabayashi, *Surface and Coatings Technology*, **153** (2002) 93–99.

[24] K Seon-Hwa, C Yong-Lak, S Yo-Seung, L Deuk Yong, L Se-Jong, *Materials Letters*, **57** (2002) 343–348

[25] S Lee, E Yamasue, K Ishihara, H Okumura, *Applied Catalysis B: Environmental*, **93** (2010) 217–226.

[26] P K Song, Y Irie, Y Shigesato, *Thin Solid Films*, **496** (2006) 121–125.

[27] W Zhou, X Zhong, X Wu, L Yuan, Q Shu,W Li, Y Xia, *Journal of Physics D: Applied Physics*, **40** (2007) 219–226.

[28] M J Jung , K H Nam, L R Shaginyan , J G Han, *Thin Solid Films*, **435** (2003) 145–149

[29] L Chen, M E Graham, G Li, K A Gray, *Thin Solid Films*, 515 (2006) 1176–1181.

[30] A Zaleska, A Review, *Recent Patents on Engineering*, **2** (No.3) (2008) 158-164.

[31] X Qing, W Diana, A Rose, L Dai, L Say, T Timothy, *Nanoscale*, **2** (2010) 1122–1127.

[32] Z Zhang, J B.M- Goodall, D J Morgan, S Brown, R J.H Clark, J C Knowles, N J Mordan, J R.G Evans, A F Carley, M Bowker, J A Darr, *Journal of the European Ceramic Society*, **29** (2009) 2343-2353.

[33] V Sakkas, M Islam, C Stalikas, T Albanis, *Journal of Hazardous Materials* **175** (2010) 33–44.

[34] A Bassi, D Cattaneo, V Russo, C Bottani, E Barborini, T Mazza, P Piseri, P Milani, F Ernst, K Wegner, S Pratsinis, *Journal of Applied Physics*, **98** (7) (2005) 74305.

[35] S Hsiao, J Lin, Y Chin, IEEE SENSORS Conference, (2008) 321-324

[36] Z Liu, Y Zhou, Z Li, Y Wang, C Ge, *Journal of University of Science and Technology Beijing*, **14** (2007) 552.

[37] A Kumar, P Lo, S Chen, *Nanotechnology*, **19** (2008) 255501.

[38] H Szymanowski, A Sobczykguzenda, A Rylski, W Jakubowski, M Gazickilipman, U Herberth, F Olcaytug, *Thin Solid Films*, **515** (2007) 5275–5281.

[39] P McCurdy, L Sturgess, S Kohli, E Fisher, *Applied Surface Science*, **233** (2004) 69–79.

[40] N Raut, T Mathews, S Rajagopalan, R Rao, S Dash, A Tyagi, *Solid State Communications*, **161** (2011) 245–249.

[41] U Helmersson, M Lattemann, J Bohlmark, A P Ehiasarian, J T Gudmundsson, Review, *Thin Solid Films*, **513** (2006) 1–24.

[42] S Battiston, M Minella, R Gerbasid, F Visentin, P Guerrierod, A Leto, G Pezzotti, E Miorin, M Fabrizio, C Pagura, *Carbon*, **48** (9) (2010) 2470–2477.

[43] P Zeman , S Takabayashi, Thin Solid Films, 433 (2003) 57–62.

[44] D Depla, S Mahieu, Reactive Sputter Deposition, Springer New York (2008).

[45] R Dholam, N Patel, A Santini, A Miotello, *International Journal of Hydrogen Energy*, **35** (2010) 9581-9590.

[46] L Zhu, J Xie, X Cui, J Shen, X Yang, Z Zhang, *Vacuum*, **84** (2010) 797-802.

[47] C-P Lee, L-Y Lin, K-W Tsai, R Vittal, K-C Ho, *Journal of Power Sources*, **196** (2011) 1632–1638.

[48] J Taranto, D Frochot, P Pichat, *Industrial & Engineering Chemistry Research*, **48** (2009) 6229–6236.

[49] F Han, V S R Kambala, M Srinivasan, D Rajarathnam, R Naidu, Review, *Applied Catalysis A: General*, **359** (2009) 25–40.

[50] J Suna, L Qiao, S Suna, G Wang, *Journal of Hazardous Materials*, **155** (2008) 312–319.

[51] H Koseki, K Shiraishi, T Asahara, T Tsurumoto, H Shindo, K Baba, H Taoda, N Terasaki, *Biomedical Research*, **30** (2009) 189-192.

[52] A FUJISHIMA, K HONDA, *Nature*, **238** (1972) 37 – 38.

[53] J C Yu, J Yu, W Ho, Z Jiang, L Zhang, *Chemistry of Materials*, **14** (2002) 3808-3816.

[54] S Hamad, J C Gonza, A Barranco, J P Espino, J Cotrino, *Journal of Physical Chemistry C*, **114** (2010) 22546–22557.

[55] S Lee, I Cho, D K Lee, D W Kim, T H Noh, C H Kwak, S Park, K S Honga, J K Lee, H S Jung , *Journal of Photochemistry and Photobiology A: Chemistry*, **213** (2010) 129-135.

[56] T Thompson, J Yates, *Chemical reviews*, **106** (10) (2006) 4428-4453.

[57] H Yu, X Zheng, Z Yin, F Tag, B Fang, K Hou, *Chinese Journal of Chemical Engineering*, **15** (6) (2007) 802-807.

[58] S Biswas, M-F Hossain, T Takahashi, Y Kubota, A Fujishima, *physical status solidi a*, **205** (8) (2008) 2023–2027.

[59] S Woo, W Kim, S Kim, C Rhee, *Materials Science and Engineering*, **449** (2007) 1151-1154.

[60] O Akhavan, E Ghaderi, *Surface & Coatings Technology*, **204** (2010) 3676–3683.

[61] C Karunakaran, G Abiramasundari, P Gomathisankar, G. Manikandan, V Anandi, *Journal of Colloid And Interface Science*, **352** (2010) 68–74.

[62] P Wu, R Xie, J Imlay, J Ku Shang, *Applied Catalysis B: Environmental*, **88** (2009) 576–581.

[63] R Asahi, T Morikawa, T Ohwaki, K Aoki, Y Taga, *Science*, **293** (2001) 269-271.

[64] F Spadavecchia, G Cappelletti, S Ardizzone, M Ceotto, L Falciola, *Journal of Physical Chemistry C*, **115** (2011) 6381–6391.

[65] F Peng, Y Liu, H Wang, H Yu, J Yang, *Chinese Journal of Chemical Physics*, **23** (4) (2010) 437-441.

[66] Z Zhao, Q Liu Q, *Journal of Physics D: Applied Physics*, **41** (2008) 1-10.

[67] K Obata, H Irie, K Hashimoto, *Chemical Physics*, **339** (2007) 124–132.

[68] U G Akpan, B H Hameed, review, *Journal of Hazardous Materials*, **170** (2009) 520–529.

[69] B Liu, L Wen, X Zhao, *Solar Energy Materials & Solar Cells,* **92** (2008) 1–10.

[70] G Liu, F Li, Z Chen, Q Lu, H Cheng, *Journal of Solid State Chemistry*, **179** (1) (2006), 331–335.

[71] K Eufinger, D Poelman, H Poelman, R De Gryse, G B Marin, *Journal of Physics D: Applied Physics*, **40** (2007) 5232–5238.

[72] S Wendt, P Sprunger, E Lira, G Madsen, Z Li, J Hansen, J Matthiesen, A Blekinge-Rasmussen, E Lægsgaard, B Hammer, F Besenbacher, *Science*, **320** (2008) 1755-1759.
[73] A V Emeline, V N Kuznetsov, V K Rybchuk, N Serpone, Review, *International Journal of Photoenergy*, ID 258394 (2008) 1-19.
[74] M Batzill, E-H Morales, U Diebold, *Chemical Physics*, **339** (2007) 36–43.

[75] T Umebayashi, T Yamaki, H Itoh, K Asai, *Applied Physics Letters*, **81**(3) (2002) 454-458.

[76] D Lee, G-Y Kim, J-K Lee, *Metals and Materials International*, **9** (1) (2003) 43-46.

[77] S U M Khan, M AlShahry, W B Ingler, *Science,* **297** (2002) 2243.

[78] T Tachikawa, S Tojo, K Kawai, M Endo, M Fujitsuka, T Ohno, K Nishijima, Z Miyamoto, T Majima, *Journal of Physical Chemistry B,* **108** (2004) 19299.
[79] T L Thompson, J T Yates, *Journal of Physical Chemistry B*, **109** (2005) 18230.

[80] C Di Valentin, G Pacchioni, A Selloni, *Physical Review*, **70** (2004) 085116.

[81] H Irie, Y Watanabe, K Hashimoto, *Journal of Physical Chemistry B*, **107** (2003) 5483-5486.

[82] F Dong, W Zhao, Z Wu, S Guo, *Journal of Hazardous Materials*, **162** (2009) 763–770.

[83] T Ihara, M Miyoshi, Y Triyama, O Marsumato, S Sugihara, *Applied Catalysis B: Environmental,* **42** (2003) 403-409.
[84] C Di Valentin, G Pacchioni, A Selloni, S Livraghi, E Giamello, *Journal of Physical Chemistry B*, **109** (2005) 11414.
[85] X Chen, C Burda, *Journal of Physical Chemistry B*, **108** (2004) 15446.

[86] O Diwald, T L Thompson, T Zubkov, E G Goralski, S D Walck, J T Yates, *Journal of Physical Chemistry B***, 108** (2004) 6004.
[87] H M Yates, M G Nolan, D W Sheel, M E Pemble, *Journal of Photochemistry and Photobiology A: Chemistry*, **179** (2006) 213–223.
[88] J Wang, D N Tafen, JP Lewis, Z Hong, A Manivannan, M Zhi, M Li, N Wu, *The Journal of American Chemical Society*, **131** (2009) 12290-12297.
[89] G He, L D Zhang, G H Li, M Liu, X J Wang, *Journal of Physics D: Applied Physics*, **41** (2008) 045304.

[90] H Shen, L Mi, P Xu, W Shen, P Wang, *Applied Surface Science*, **253** (2007) 7024–7028.

[91] X Chen, Y B Lou, A C S Samia, C Burda, J L Gole, *Advanced Functional Materials*, **15** (2005) 41.

[92] C Di Valentin, E Finazzi, G Pacchioni, A Selloni, S Livraghi, M C Paganini, E Giamello, *Chemical Physics*, **339** (2007) 44–56.
[93] O Diwald, T L Thompson, E G Goralski, S D Walck, J T Yates, *Journal of Physical Chemistry B*, **108** (2004) 52.
[94] N Martin, R Sanjinés, J Takadoum, F Lévy, *Surface and Coatings Technology*, **142** (2001) 615-620.

[95] R Parra, A Arango, P Jose, V Javier, *Dyna,* **163** (2010) 64-74.

[96] A Brudnik, M Bucko, M Radecka, A Trenczek-Zajac, K Zakrzewska, *Vacuum*, **82** (2008) 936–941.

[97] Z Wu, F Dong, W Zhao, S Guo, *Journal of Hazardous Materials*, **157** (2008) 57-63.

[98] A Trenczek-Zajac, K Kowalski, K Zakrzewska, M Radecka, *Materials Research Bulletin,* **44** (2009) 1547–1552.

[99] J M White, J Szanyi, M A Henderson, *Journal of Physical Chemistry B*, **107** (2003) 9029.

[100] Y F Gao, Y Masuda, K Koumoto, *Langmuir*, **20** (2004) 3188.

[101] T Zubkov, D Stahl, T Thompson, D Panayotov, O Diwald, J T Yates, *Journal of Physical Chemistry B*, **109** (2005) 15454.

[102] C Y Wang, H Groenzin, M J Shultz, M, *Langmuir*, **19** (2003) 7330.

[103] J Wang, T Ma, G Zhang, *Catalysis Communications*, **8** (2007) 607-611.

[104] D Kaczmarek, D Wojcieszak, J Domaradzki, E Prociow, *Journal of Physics: Conference Series*, **146** (2009) 012019 1-6.

[105] S Karvinen, P Hirva, T A Pakkanen*, Journal of Molecular Structure: THEOCHEM*, **626** (2003) 271.

[106] T C Kaspar, T Droubay, V Shutthanandan, S M Heald, C M Wang, D Cready, S Thevuthasan, *Physical Review B*, **73** (2006) 155327 1-12.

[107] W D Sproul, D J Christie, D C Carter, Review, *Thin Solid Films*, **491** (2005) 1–17.

[108] X Y Li, P L Yue, C Kutal, *New Journal of Chemistry*, **27** (2003) 1264.

[109] X F Zhao, X F Meng, Z H Zhang, L Liu, D Z Jia, *Journal of Inorganic Materials*, **19** (2004) 140.

[110] S X Wu, Z Ma, Y N Qin, F He, L S Jia, Y Zhang, *Acta Physico-Chimica Sinica*, **19** (2003) 967.

[111] M Okutan, E Basaran, H I Bakan, F Yakuphanoglu, *Physica B*, **364** (2005) 300–305.

[112] V Gombac, L De Rogatis, A Gasparotto, G Vicario, T Montini, D Barreca, G Balducci, P Fornasiero, E Tondello, M Graziani, *Chemical Physics*, **339** (2007) 111–123.

[113] W Smith, Y P Zhao, *Journal of Physical Chemistry C*, **112** (2008) 19635.

[114] W Smith, A Wolcott, R Fitzmorris, J Zhang, Y-P Zhao, *Journal of Materials Chemistry*, **21** (2011) 10792-10800.

[115] J Moon, C Y Yun, K W Chung, M S Kang, J Yi, *Catalysis Today*, **87** (2003) 77–86.

[116] E Piera, M-I Tejedor, M E Zorn, M A Anderson, *Applied Catalysis B: Environmental*, **46** (2003) 671.

[117] Q Chi Xu, D V Wellia, R Amal, D Wei Liao, S C J Loo, T T Yang Tan, *Nanoscale*, **2** (2010) 1122–1127.

[118] H Tong , S Ouyang , Y Bi , N Umezawa , M Oshikiri , J Ye, *Advanced Materials*, 24 (2) (2012) 229-251.

Chapter II

Plasma diagnostics

Chapter II Plasma diagnostics

Abstract

Optical Emission Spectroscopy (OES) and electrical diagnostics were used to characterize the plasma during the sputtering deposition. Deposition pressure, DC bias voltage and the reactive gas concentration in the deposition chamber were found to be the main parameters that affect the plasma and therefore the sputtering deposition. With the variation of oxygen flow rate, significant hysteresis effects were found in the OES intensities with a jump transition from the metallic to the reactive mode of sputtering. These phenomena were less pronounced with nitrogen reactive gas. When the deposition pressure increased, the plasma density increased, but the plasma temperature decreased as well as the negative auto bias voltage of the cathode. Coatings deposited at three different intervals for the variation prassures, between 2 and 14 mtorr, showed significant changes in their physical properties.

Our OES diagnostics showed an important effect of the pumping speed on the working pressure and more dramatically on the target poisoning. Controlling the deposition pressure using the argon flow rate, keeping the pumping speed at the maximum level, was found to be more efficient rather than controlling the pressure by the pumping speed controller. The former can give higher deposition rates and reasonable reproducibility as it can reduce the hysteresis effect and make the transition between the metallic and poisoned depositions more continuous especially with oxygen reactive gas.

Résumé

Nous avons utilisé la spectroscopie d'émission optique et des diagnostics électriques afin de caractériser le plasma pendant le dépôt par pulvérisation cathodique. La pression dans la chambre de de dépôt, la tension DC d’auto polarisation et la concentration de gaz réactif dans la chambre de dépot se sont avérés d’être les principaux paramètres qui modifient les propriétés physiques et chimiques du plasma et en conséquence la nature de la couche déposée par pulvérisation. Sous la variation du débit du gaz réactif d’oxygène, nous avons trouvé un effet d'hystérésis significative au niveau des intensités des spectres de SEO avec une transition brutale du mode métallique vers le mode réactif de pulvérisation. Ces phénomènes sont moins prononcés avec le gaz réactif d’azote. Lorsque la pression de travail augmente, nous avons observé une augmentation dans la densité électronique du plasma, mais la température du plasma diminue ainsi que la tension d’auto polarisation négative de la cathode. Pour étudier le role de la pression sur les propriétés physiques et chimiques des couches déposées, nous nous sommes fixés trois pressions differentes dans la gamme de 2 à 14 mtorr.

Les résultats de la spectroscopie d’émission optique ont montré un effet important de la vitesse de pompage sur la pression de travail et plus dramatiquement sur l'empoisonnement de la cible. Nous avons pu mettre en évidence qu’il est plus judicieux de contrôler la pression dans la chambre de dépôt en jouant sur le débit d'argon, le gaz majoritaire, tout en gardant la vitesse de pompage au niveau maximal, plutôt que de contrôler la pression par le régulateur de vitesse de pompage. Le premier peut donner une vitesse de dépôt plus élevée avec une reproductibilité raisonnable, car elle peut réduire l'effet d'hystérésis et assurer une transition progressive entre le dépôt de type élémentaire (métallique) et empoisonné, surtout en présence du gaz réactif d'oxygène.

II-1) Introduction

The basic issue that must be faced during reactive sputtering is that the reactive gas combines with the target material to form a new compound, changing in this way the surface properties of the target [1-2]. Ideally, this reaction takes place on the surface of the substrate, but in reality it occurs not only at the substrate but also in the reactor volume, on chamber walls and even on the target surface. It is the reaction on the target surface that leads to the classic problem in reactive sputtering called ***"poisoning"*** phenomena. The sputtering rate for the compound material, which forms on the target, is usually significantly less than the rate for the metallic target material especially if this compound is a semiconductor (TiO_2) or an insulator.

Several methods can be applied for magnetron plasma characterization and could be used as control techniques, such as optical emission/absorption spectroscopy [3-5], Langmuir probe measurements and mass spectrometry [6-8]. These three techniques are the commonly used diagnostic means of different types of plasmas nowadays. The measure of the bias voltage at the cathode (V_{bias}) could be also used as a diagnostic alternative [7] but it is less common as compared to the previous three other techniques.

In this chapter we will present some basic equations in sputtering with a brief description of the technique, and then we will compare the main diagnostic results obtained from the Optical Emission Spectroscopy (OES), cathode bias voltage (V_{bias} DC) and Langmuir Probe (LP) measurements.

II-1-1) Experimental set-up for thin film deposition and plasma diagnostic

The major components of the system are presented in Fig.II-1. The objective of the magnetic field is to increase the ionization efficiency by trapping the electrons in the plasma. This allows plasma to be confined at the vicinity of the target surface. An RF source is more efficient than DC source in the case of the reactive sputtering of a semiconductor or insulating material because of charge accumulation on such surfaces in the case of the latter (see target poisoning section below).

The thin films are deposited in a 13.56 MHz RF magnetron sputtering deposition chamber (SPT 120, Plasmionique, Canada), using a balanced magnetron cathode (MAGNION-B). The pumping system includes a turbo molecular pump (300 l/s, Varian TV301 Navigator) and a mechanical pump (ULVAC) for backing the turbo.

The SPT 120 magnetron sputtering reactor has two quartz windows (see Fig.II-1) used as vacuum viewports for optical spectra acquisition. To prevent any contamination on the windows, the viewports are mounted about 10 cm away from the reactor walls using special flanges with additional aluminium foils inside the reactor.

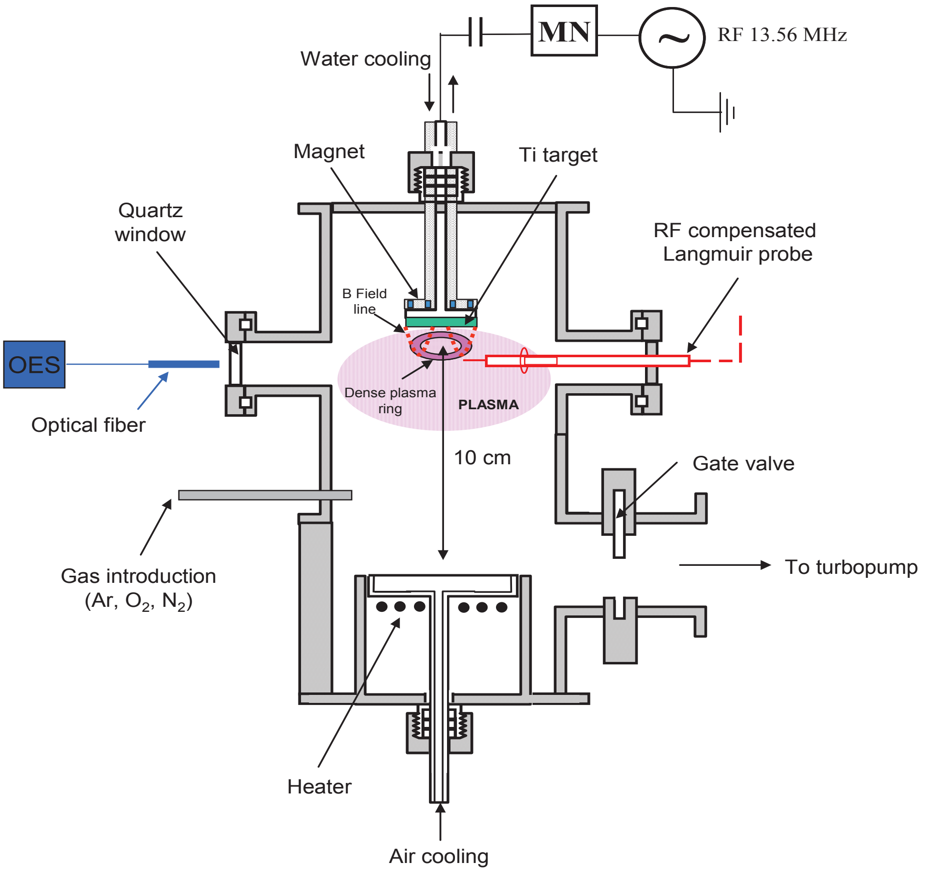

Fig.II-1: General illustration of the sputtering deposition system with diagnostic tools (Langmuir probe and OES).

The background pressure for all depositions was about $P_{b.g.} = 5 \times 10^{-6}$ Torr (6.7×10^{-4} Pa), while the total working pressure was adjusted between 2 to 20 mTorr (0.3 to 3 Pa). All films were deposited using a metallic Ti target (99.95% purity, 2 inch diameter, NEYCO). Prior to each deposition, the target was pre-sputtered in argon atmosphere for 10 minutes to remove any contaminations or "poisoned film" from the Ti surface. Then, the target was sputtered in a reactive gas atmosphere containing Ar + O_2 for TiO_2 films, Ar + N_2 for TiN films or Ar + O_2 + N_2 for TiON films. The typical RF power delivered by the generator was 200 W, corresponding to a typical DC bias ranging from -140 V to -160 V, depending on the target surface conditions (clean target or poisoned target).

The films were deposited on several substrates including electro-polished stainless steel, Si (100) and (101) wafers and ordinary microscope glass slides. Prior to deposition, the non metallic substrates were ultrasonically cleaned with acetone, ethyl alcohol and then de-ionized water for 20 minutes each. The substrate holder was at the floating potential and maintained at 300°C, if there is no other indication. The distance between the substrate holder and the target was fixed to 10 cm.

II-1-2) Applied RF power and the resulted cathode bias voltage

When applying an RF potential on a powered electrode, the voltage oscillates positively and negatively around the 0 offset axe. Because of the higher mobility of the electrons compared to ions, the RF powered electrode can pick up a much greater electron current than ion current for one cycle, and this begins to charge the electrode negatively. The capacitor, in the impedance of the matching box, blocks this DC potential from the power supply, so the cathode charges negatively and the net result after several cycles is a negative cathodic DC potential as shown in Fig.II-2 (a). The difference between the measured AC coupled voltage and the DC coupled voltage is called the ***DC auto bias voltage*** or simply the ***bias voltage*** of the cathode.

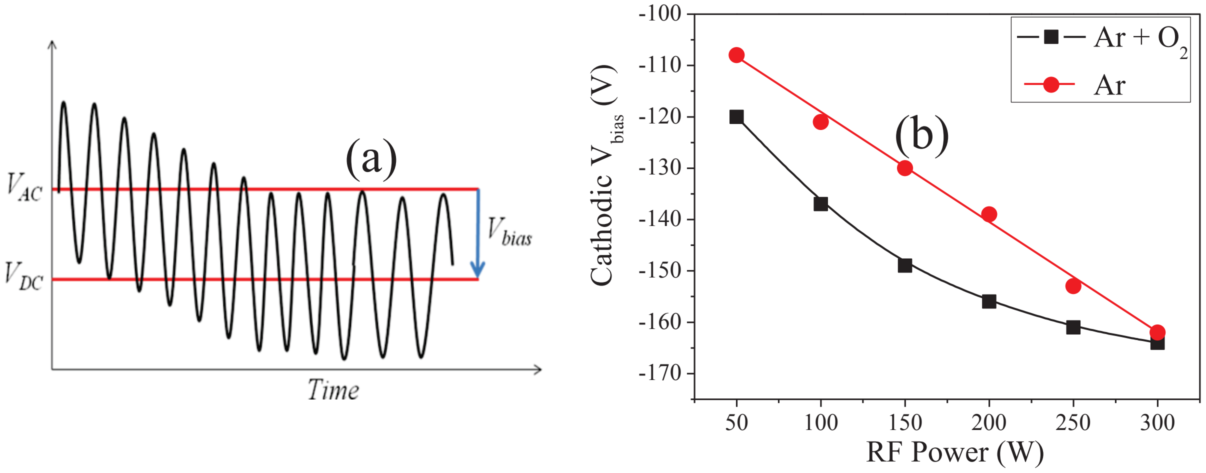

Fig.II-2: Cathode auto-bias voltage for titanium target in argon plasma and argon-oxygen plasma as a function of RF power. Working pressure=5 mTorr.

The cathode bias DC voltage has been measured for different RF powers in (i) pure argon plasma and (ii) in argon-oxygen plasma where O_2/Ar (sccm) = 2/50, as presented in Fig.II-2 (b), the working pressure was 5 mTorr in both cases. DC bias voltage increases linearly as the RF power increases in pure argon plasma. However, in the presence of reactive gas (oxygen) there is no linear dependence between the bias voltage and the RF power, this could be due to the chemical modification of the target surface in the presence of reactive gas, which will be discussed in details later.

II-1-3) Ex-situ evidence of target poisoning

Fig.II-3 shows (a) a pure Titanium target sputtered in Ar atmosphere (on the left) and (b) a poisoned Titanium target sputtered in Ar/O_2/N_2 atmosphere (on the right). As the formation of target compound coverage increases, the deposition rate decreases and the film stoichiometry is modified. Thus, it is of primary importance to perform in-situ diagnostics in order to control or avoid this well known phenomenon.

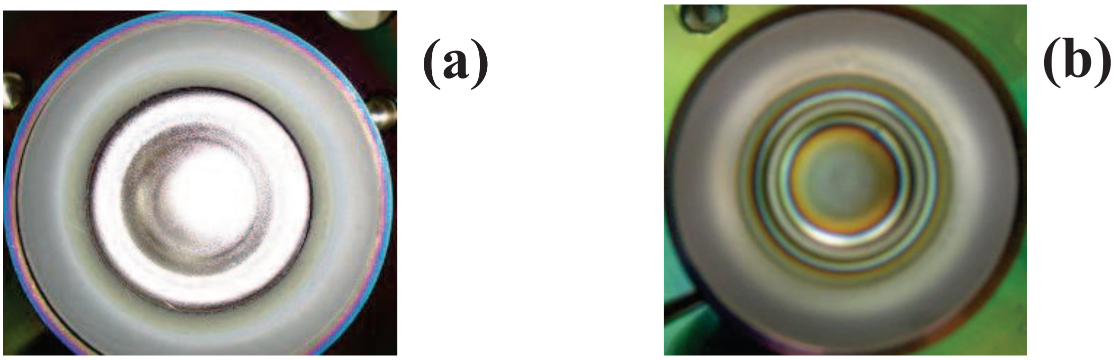

Fig.II-3: (a) Pure Titanium target sputtered in argon atmosphere, and (b) poisoned Titanium target sputtered in Argon/Oxygen/Nitrogen atmosphere

II-2) Optical Emission Spectroscopy OES

In the first part of this chapter, we will focus our study on optical emission spectroscopy (OES). This non intrusive technique is an effective way to understand the influence of different parameters during the sputtering deposition.

II-2-1) Experimental conditions for OES measurements

Fig.II-4 presents a global view of the RF sputtering system with the optical fiber position for the OES measurement. Experiments were carried out under working pressures from 2 to 20 mTorr, which is controlled via two different ways:

1) by changing the Ar gas flow rate with a maximum pumping speed efficiency (gate valve fully open).

2) by changing the pumping speed via the gate valve position with a fixed Argon flow rate.

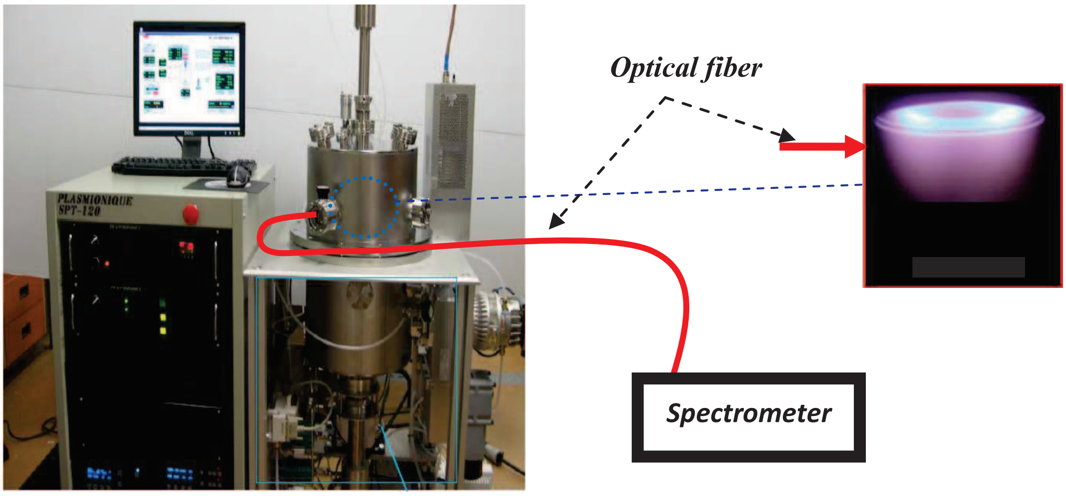

Fig.II-4: Experimental setup for plasma diagnostics by Optical Emission Spectroscopy

The spectra were acquired through optical fiber using two types of spectrometers:

- Mono channel spectrometer (SpectraPro-500i) from Action Research Corporation, with 0.500 Meter Triple Grating Monochromator/Spectrograph and CD detector. It has a wavelength range of 200 to 900 nm, and a resolution of 0.1 nm.
- (Maya 2000+) spectrometer from Ocean Optics using software Spectra Suite. It has a resolution of 0.3 nm, an acquisition range from 200 to 1200 nm and a grating of 300 l/mm.

II-2-2) Emission lines studied in this work

The strongest emission lines for Ti and for Ar are located in the 490–521 nm range and the 690–820 nm range, respectively.

Table II-1: Spectral Optical Emission lines used in the study

Element	Wavelength nm (in air)*	Transition (upper-lower)	Nature of the lower level	Normalized intensity
Ar I	811.5	$3p^{5}(^{2}\mathrm{P}^{\circ}_{3/2})4p \longrightarrow 3p^{5}(^{2}\mathrm{P}^{\circ}_{3/2})4s$	Metastable	1000
	772.4	$3p^{5}(^{2}\mathrm{P}^{\circ}_{3/2})4p \longrightarrow 3p^{5}(^{2}\mathrm{P}^{\circ}_{3/2})4s$	Metastable	400
Ti I	499.1	$3d^{3}(^{4}\mathrm{F})4p \longrightarrow 3d^{3}(^{4}\mathrm{F})4s$	Metastable	600
	517.4	$3d^{2}(^{3}\mathrm{F})4s4p(^{3}\mathrm{P}^{\circ}) \longrightarrow 3d^{2}4s^{2}$	Ground	140
	519.3	$3d^{2}(^{3}\mathrm{F})4s4p(^{3}\mathrm{P}^{\circ}) \longrightarrow 3d^{2}4s^{2}$	Ground	150
	521	$3d^{2}(^{3}\mathrm{F})4s4p(^{3}\mathrm{P}^{\circ}) \longrightarrow 3d^{2}4s^{2}$	Ground	200
N I	746.8	$2s^{2}2p^{2}(^{3}\mathrm{P})3p \longrightarrow 2s^{2}2p^{2}(^{3}\mathrm{P})3s$	Ground	200
O I	777.2	$2s^{2}2p^{3}(^{4}\mathrm{S}^{\circ})3p \longrightarrow 2s^{2}2p^{3}(^{4}\mathrm{S}^{\circ})3s$	Ground	300

** The wavelengths in vacuum (λ_{vac}) are approximately equal to λ_{air} / 1.00027. As a consequence $\Delta(\lambda_{vac}-\lambda_{air}) \sim$ 0.1-0.2 nm.*

We focused our study on eight main groups of emission lines, depending on the sensitivity of the spectrometer used. In particular, we followed the lines which correspond to argon neutrals Ar I (772 and 811 nm) and titanium neutrals Ti I (499, 517, 519 and 521 nm) [3][12][18]. Ti ions spectral lines were too weak to be detected properly and were not investigated. The most intense lines for N and O are located at 746 nm and 777 nm, respectively. All lines used in this study are listed in *Table II-1*.

II-3) OES measurements in Argon

II-3-1) Relative emission of Titanium lines

Argon and titanium have many lines close in energy, especially in the 515-522 nm range. Titanium emission spectra recorded in pure argon plasma for different flow rates at 5 mTorr and 200 W (cathode V_{bias}=142 V DC) are shown in Fig.II-5.

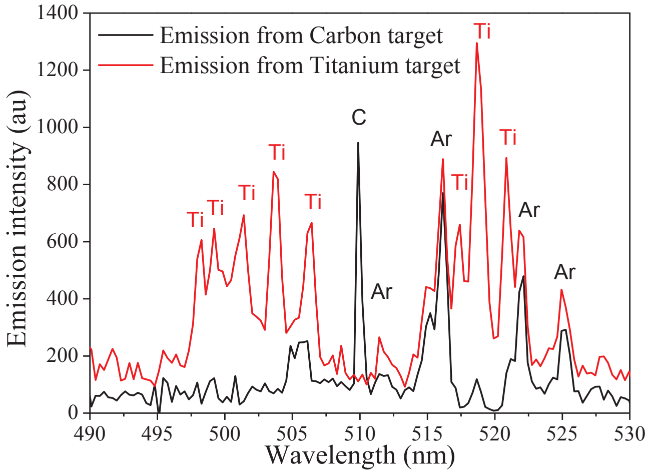

Fig.II-5: Comparison between the emission spectra from titanium and carbon targets at 5 mTorr and 200W.

In order to clearly distinguish Ti lines from argon lines, the emission spectra with 2 different targets: titanium and carbon target were compared. The advantage of using carbon is the very low sputtering rate, approximatly 4 times lower than the titanium one. By comparing the difference between the two spectra shown on Fig.II-5, one can attribute the titanium and argon lines.

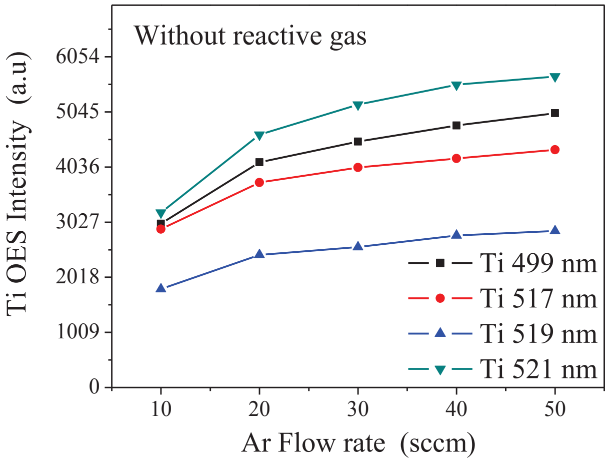

Fig.II-6: Titanium lines in Argon plasma vs Argon flow rate (SpectraPro-500i spectrometer).

Fig.II-6 shows the variation of different Titanium lines in argon plasma as a function of the gas flow rate. The working pressure and the RF power were fixed at 5 mTorr and 200 W, respectively. As shown on figure II-6, the most intense Titanium line measured by the SpectroPro-500i is the line at 521 nm. This result is consistent with the work of Britun et al, [3] on the characterization of Ti-Ar plasma in magnetron sputtering reactor.

However, with the Maya 2000+ spectrometer (not shown on figure II-5), we found that the most intense titanium line is the line at 499 nm, which is consistent with the above standard Table II-1, and the studies of Trenczek-Zajaca et al. [1] and Brudnik et al. [12]. Other Titanium lines have been investigated such as 365.4 nm by Jung et al. [5], 395.8 nm by Musil et al. [19] and 365.3 nm by Perry et al. [20].

II-3-2) Normalization of lines intensities

In many works using OES, emission intensities are normalized. However, there are several methods to normalize OES intensities, depending on the objective of the measurements. Perry et al. [20] used the ratio between the emission line intensity of X species to the intensity at a current of 1 A in DC sputtering. Brudnik et al. [12] and Trenczek-Zajac et al. [1] used the ratio of Titanium emission line (at 500 nm) intensity with reactive gas to the intensity in pure Ar. Vancoppenolle et al. [21], used the ratio between the specific emission intensity to that of Ar (in Optical Emission Spectroscopy and Mass Spectroscopy measurements) [21].

Benien et al. [22] found a linear relationship between the deposition rate and the OES intensity, in the case of chromium sputtering in the nitrogen reactive gas. They used the ratio of Cr emission to the sum of Cr and N intensities, and found a good correlation with the film stoichiometry measured by Auger.

In our study, we define the normalized emission intensity of X as follows:

$$\text{Normalized intensity of X} = \frac{\text{X emission intensity}}{\text{Ar emission intensity}} \qquad \text{Eq.II-1}$$

Where X denotes Ti, O or N. Ar emission intensity is fixed at:

- 811 nm with the (SpectraPro-500i) spectrometer.
- 772 nm with the (Maya 2000+) spectrometer. Indeed, the Ar line at 811 nm, i.e. the most intense line of Ar, was saturated with this spectrometer.

The normalized intensity of Ti emission could give real time indication of the deposition rate.

II-3-3) Effect of argon flow rate at constant pressure and power

In Fig.II-7, the effect of argon flow rate on Ar, Ti and O emission is shown. One can see that even if the pressure and power are fixed, respectively at 5 mTorr and 100 W, a higher argon flow rate can increase the normalized emission of Ti, and thus, the deposition rate of titanium thin films. One can explain this apparently surprising result by taking into account the effect of the gas temperature on the gas density in the sputtering chamber.

Indeed, the relevant parameter in plasma processes is not the gas pressure, but the gas density. For a constant pressure (5 mTorr), with a low total gas flow rate, the residence time of gases is high, so the gas temperature can increase due to electron-molecule elastic collisions, and the gas density will decrease. However, a high total flow rate can keep the gas cooler, so the gas density is higher, as well as the emission lines of Ti and Ar. From Fig.II-7, one can conclude that at constant pressure and power, the sputtering of Ti is enhanced when the gas flow is increased. However, due to the pumping speed limit (125 l/s), we were not able to increase the flow rate above 50 sccm with the same 5 mTorr pressure.

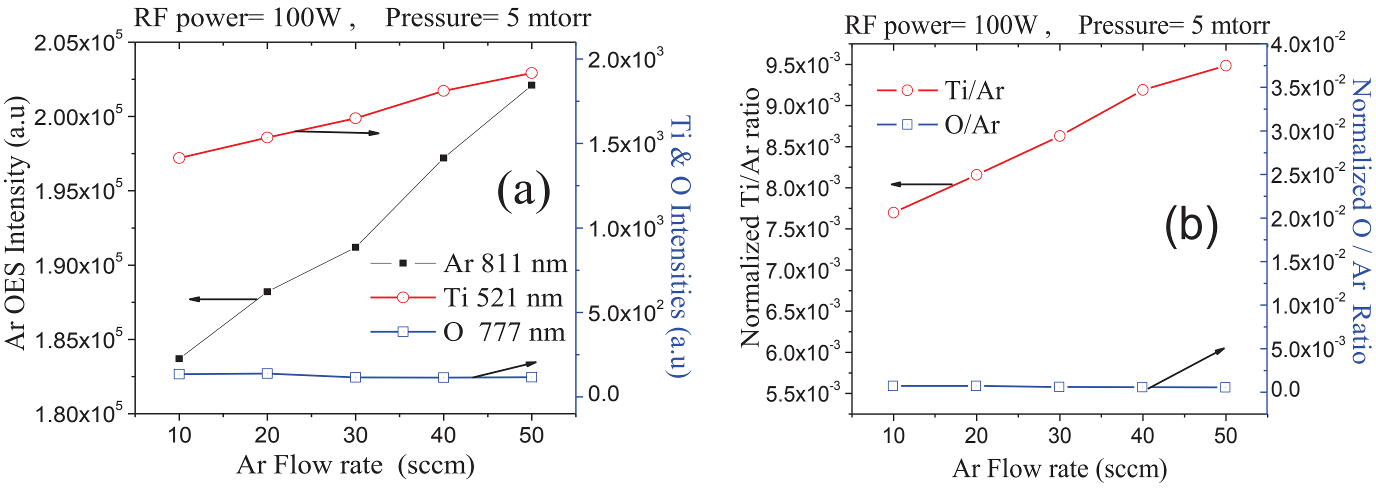

Fig.II-7: (a) Optical Emission lines in Argon plasma vs Argon flow rate & (b) normalized emission intensities vs Argon flow rate. Pressure constant, Rf power=100W.

II-3-4) Effect of power: correlation between OES and deposition rate (measured by SEM)

In Fig.II-8, the pressure and power were respectively fixed to 5 mTorr and 200 W. As compared to figure II-7, the power was increased from 100 W to 200 W. By comparing the normalized Titanium intensities in both figures (II-7-b & II-8-b), it is clear that when the power is doubled, the normalized intensity also is increased twofold (for 20 sccm, Ti/Ar: $8x10^{-3}$ → $1.6x10^{-2}$). These results are consistent with the thicknesses of the films observed by SEM shown on Fig.II-9) where the Titanium deposition rate increased roughly by 2.7 times when the sputtering power increased from 100 to 200 W. Indeed, many works found a quasi linear relationship between the sputtering power and the deposition rate as the work of Brudnik et al. [23].

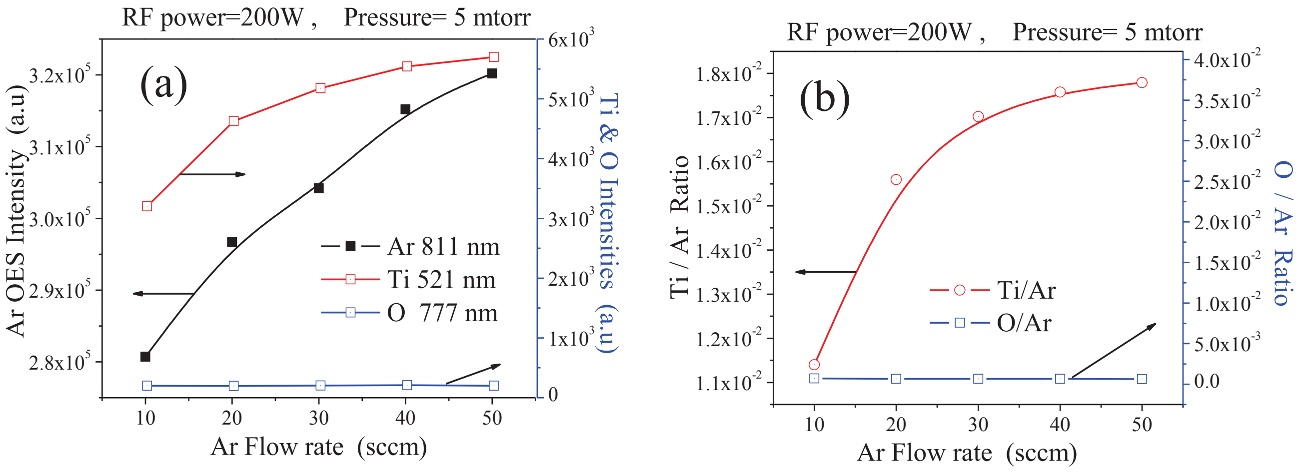

Fig.II-8: (a) Optical Emission lines in Argon plasma vs Argon flow rate & (b) normalized emission intensities vs Argon flow rate (on the right). Pressure constant, Rf power=200W.

Sputtered atoms are characterized by high kinetic energies (3 – 30 eV), as compared to evaporated atoms (0.1 – 0.3 eV) [2]. As the power is increased, the plasma density is increased, and thus the flux of hot sputtered species is increased too, which leads to more energy transferred to the substrate. As a consequence, the films are more crystallized at high power. Indeed, RAMAN spectroscopy measurements show that TiO_2 is well crystallized at high power (200 W), and much less crystalline at low power (100 W) (results not shown).

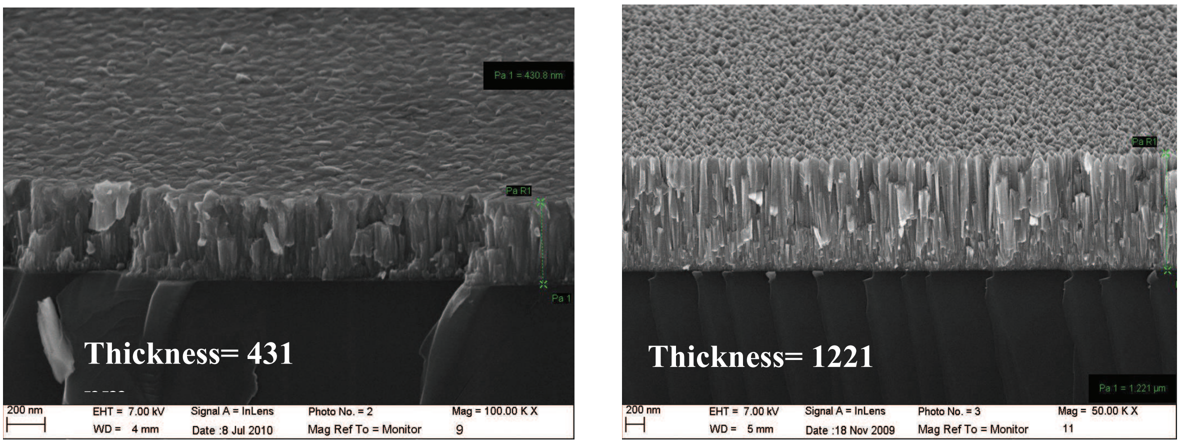

Fig.II-9: SEM images of Titanium film deposited on Silicon wafer at working pressure 3 mTorr and ambient temperature, using different Rf power: 100 W (left) and 200 W (right).

II-4) OES measurements in Ar/O_2

Titanium emission lines in high resolution (0.1 nm) OES in Ar-O_2 plasmas is shown on Fig.II-10. The argon flow rate, working pressure and power were fixed at 50 sccm, 5 mTorr and 200 W respectively. The effect of the oxygen flow rate was studied between 0 to 10 sccm. One can see that i) the intensity of Ti decreases as the partial pressure of O_2 is increased, ii) there is a transition between 1.5 and 2 sccm after which the Ti intensity dramatically falls down; this transition is the so-called poisoning phenomenon.

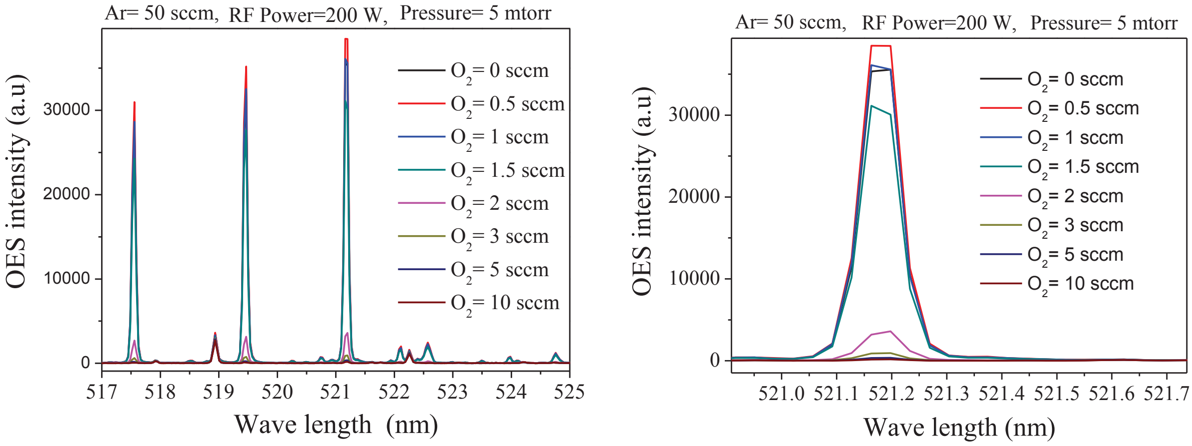

Fig.II-10: Titanium lines in high resolution Optical Emission spectra in Argon-Oxygen plasma for different Oxygen flow rates. Argon=50 sccm, pressure 5 mTorr, power = 200 W.

II-4-1) Parametric study

Titanium OES intensities in argon-oxygen plasma vs oxygen and argon flow rates are presented in Fig.II-11, normalized intensities of Ti/Ar showed the same trend (results not shown). This figure shows that the transition observed previously is always located at the same critical O_2 flow rate, even if the Ar flow rate is varied between 20 to 100 sccm. Based on this observation, one can say that target poisoning is affected by O_2 flow rate, but not by O_2 partial pressure (dilution).

In order to measure the hysteresis phenomenon, O_2 flow rate was increased from 0 to 7 sccm, then decreased for different pressures and Ar flow rates.

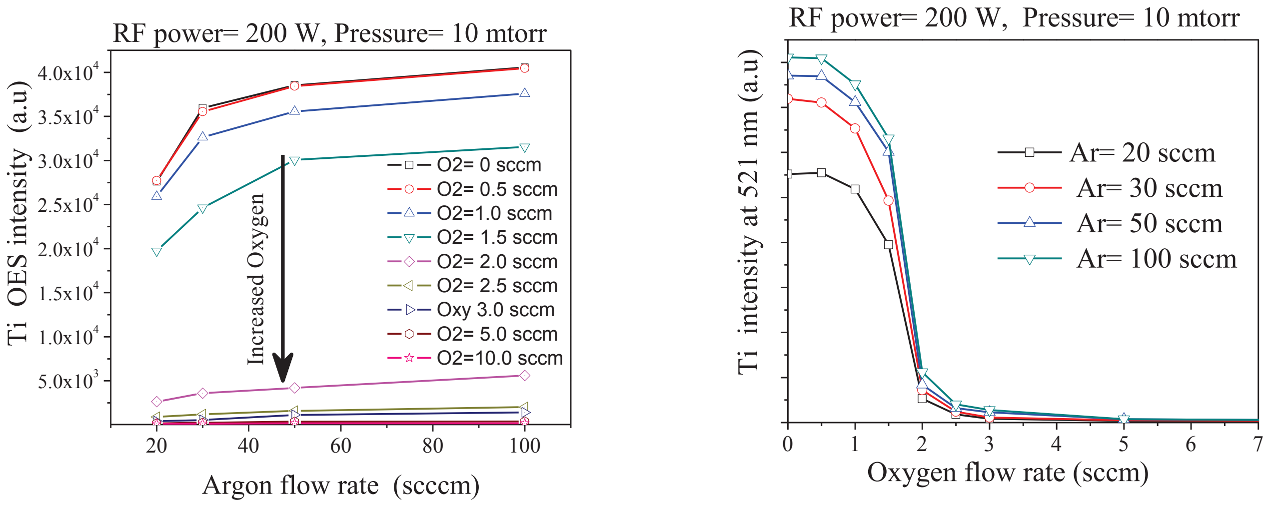

Fig.II-11: Titanium Optical Emission intensities in argon-oxygen plasma vs Oxygen and Argon flow rates. Pressure =10 mTorr, power = 200 W.

a) Low pressure and low Argon flow rate

Fig.II-12 shows the OES intensities, and normalized ones as a function of O_2 flow rate, in Ar-O_2 plasma at low pressure (3.5 mTorr), 200 W power and 35 sccm Ar, gate valve 100% open (full pumping speed = 126.6 l/s).

When the O_2 flow rate is lower than 1 sccm, no O (at 777 nm) emission can be detected in the plasma. This observation may suggest that atomic O is quickly consumed by Titanium, by surface and/or gas phase reactions.

However, when the O_2 flow rate is increased to 2-2.5 sccm, the Ti (499 nm, 519 nm) emissions start to decrease dramatically and O (777 nm) becomes visible. This behavior is the result of target poisoning. Indeed, poisoning will reduce dramatically the flux of sputtered Ti, so excitation of Ti by electron impact and reaction with atomic O will both decrease, as shown on Fig.II-12. In the return part, when O_2 is decreased, the target is still poisoned between 1.5-2 sccm and the metallic mode is recovered below 1 sccm. A hysteresis effect is also observed for Ar (772 nm) and O (777 nm), since the physical and chemical properties of the plasma are strongly dependent on the sputtering of Ti [7].

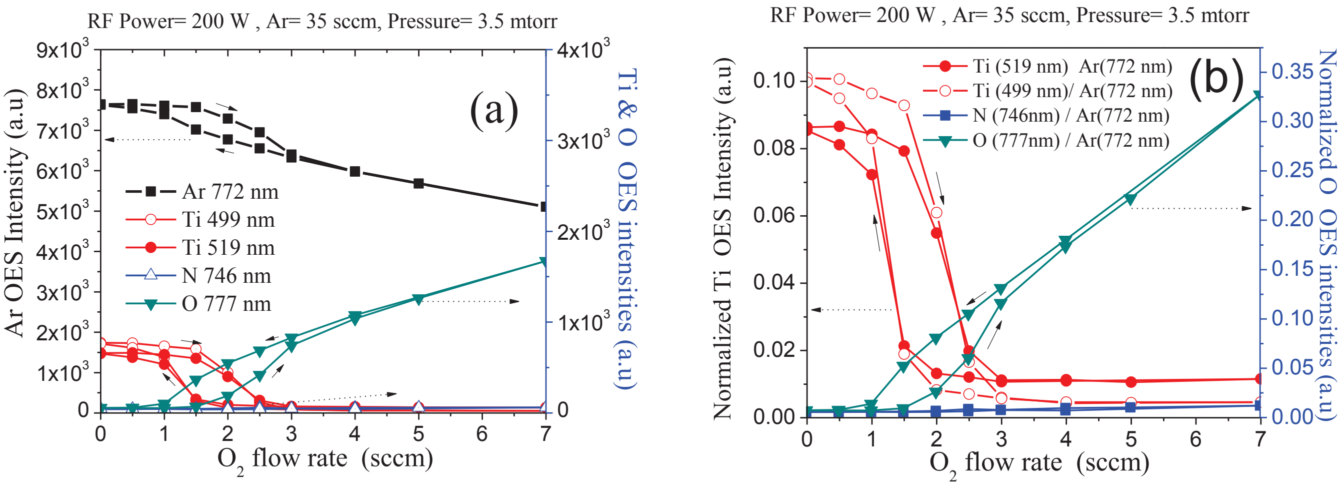

Fig.II-12: (a) Optical Emission intensities (b) Normalized intensities in Argon-Oxygen plasma vs Oxygen flow rate . Argon flow rate 35 sccm, pressure 3.5 mTorr, Rf power 200W. (Spectrometer Maya 2000+).

b) High pressure and low Argon flow rate

Fig.II-13 shows the OES intensities recorded at 14 mTorr. The other parameters are fixed as previously: 35 sccm Ar, 200 W. It is important to note that in order to achieve a pressure of 14 mTorr with a total flow rate of 35 sccm, the gate valve should be opened at 78%. Consequently, as compared to figure II-12, the pumping speed is reduced to 31.6 l/s (126.6 l/s at 100%).

By comparing figures II-12 (3 mTorr) and II-13 (14 mTorr), one can conclude that:

- ✓ An increase of the pressure via a decrease of pumping speed (gate valve), lead to a stronger hysteresis effect.
- ✓ The poisoning effect starts at 2 sccm O_2 approximetly in both cases. However, at high pressure (14 mTorr), the metallic mode is recovered only when O_2 introduction is stopped.
- ✓ As observed previously at 3 mTorr, the presence of O (777 nm) at 14 mTorr is also detected only when the target is poisoned. Thus, O (777) is a good indication of target poisoning.

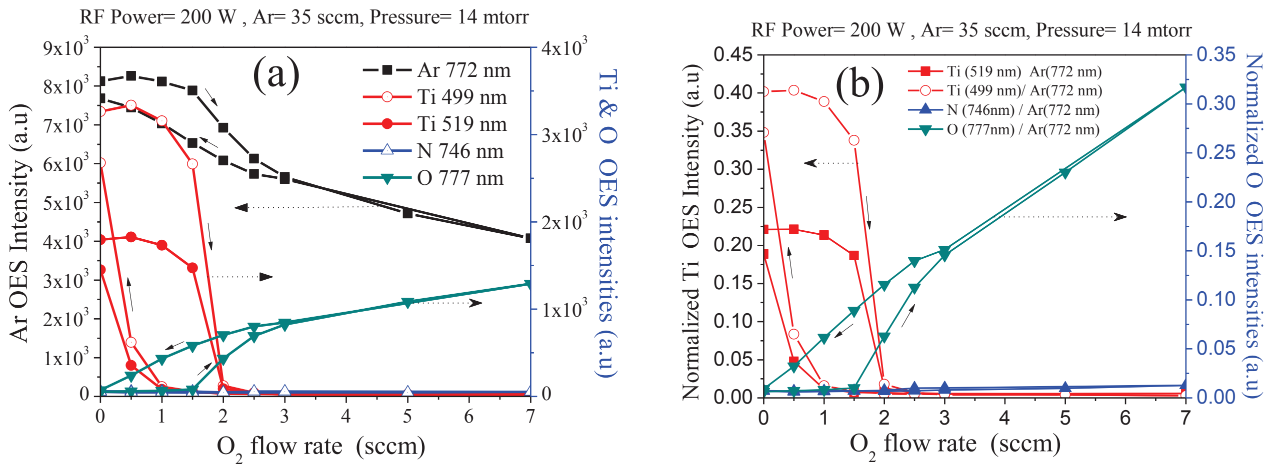

Fig.II-13: (a) Optical Emission intensities & (b) Normalized intensities in Argon-Oxygen plasma vs Oxygen flow rate. Argon flow rate 35sccm, pressure 14mTorr, Rf power 200W. (Spectrometer Maya 2000+).

c) High pressure and high Argon flow rate

Fig.II-14 shows the OES intensities recorded at 14 mTorr and 200 W, with an argon flow rate of 140 sccm. In this case, the gate valve is 100% open, so the pumping speed is the same as in the 3 mTorr / 35 sccm case (126.6 l/s). By comparing figures II-13 (14mTorr, 35sccm) and II-14 (14mTorr, 140sccm) on can conclude that for the same pressure, the hysteresis effect is reduced with a flowrate of 140 sccm, as compared to 35 sccm.

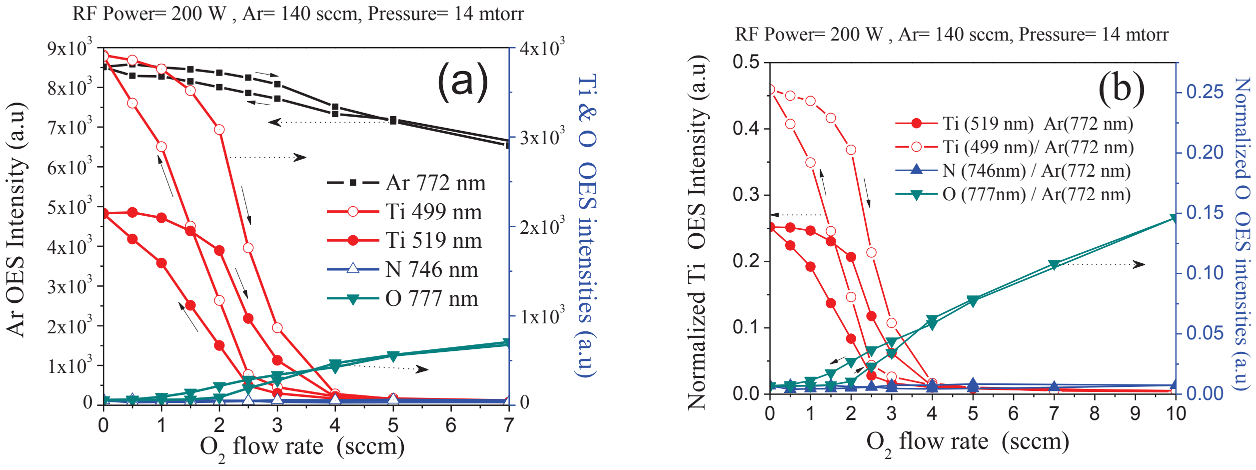

Fig.II-14: (a) Optical Emission intensities & (b) Normalized intensities in Argon-Oxygen plasma vs Oxygen flow rate. Argon flow rate 140 sccm, pressure 14 mTorr, Rf power 200W. (Spectrometer Maya 2000+).

II-4-2) Discussions

In order to clarify the discussion, Fig.II-15 summarizes the normalized OES intensities for Ti (499 nm) and O (777 nm) as a function of O_2 flow rate, pressure and Ar flow rate.

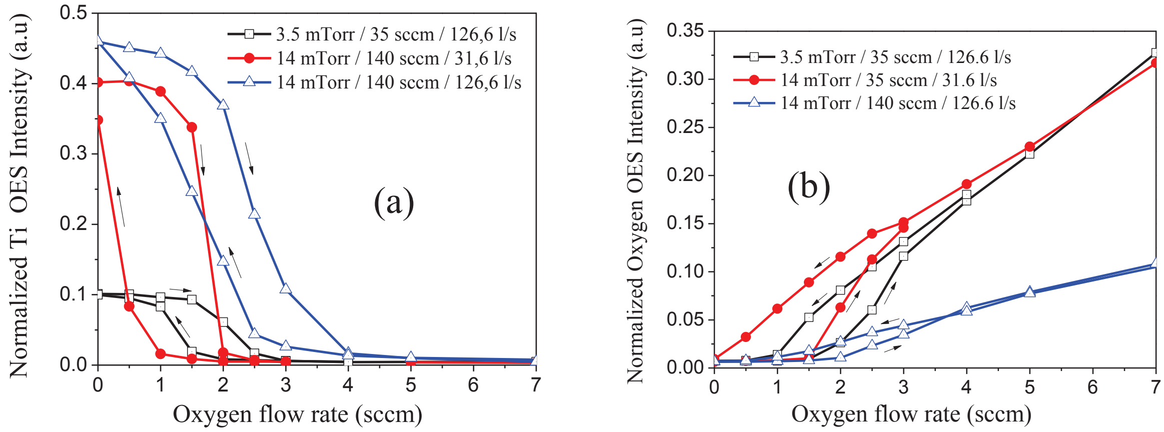

Fig.II-15: summary & comparison of Normalized Optical Emission intensities for (a) Titanium 499 nm and (b) Oxygen 777 nm, from figures.II-12 to II-14. Rf power 200W. (Spectrometer Maya 2000+).

As expected, the normalized Ti (499 nm) intensity at 14mTorr is higher than the one at 3mTorr. Indeed, a higher pressure leads to a higher electron density, and consequently a higher flux of sputtered and ionized Ti. On the other hand, the sheath is still collisionless at 14mTorr, so the ion energy is not disturbed and the sputtering yield will be constant.

Concerning O (at 777nm), by comparing all conditions one can say that (i) this line is a strong indication of target poisoning, (ii) for a O_2 flow rate higher than 3sccm, i.e. when the target is fully poisoned, the normalized O (777) intensity is proportional to O_2 partial pressure (and O_2 flow rate) in the chamber.

Based on figure II-15, it is clear that the hysteresis widths are reduced at higher pumping speed in all cases. This comparison highlights the important role of the pumping speed to perverse the target from poisoning effect. Similarly, Okamoto and Serikawa [24] showed that by increasing the pumping speed, the hysteresis effect is reduced and could be eventually eliminated. Unfortunately, the maximum pumping speed in our PVD set-up is limited to 126.6 l/s, so we are not able to go further.

II-5) OES measurements in Ar-N_2 plasmas

This study is important for the understanding of the deposition of titanium nitride, which finally leads to N doped TiO_2 after thermal oxidation (chapter VI).

II-5-1) Parametric study

The hysteresis effect has been studied in the case of reactive sputtering in nitrogen. Similarly to the previous section, we measured the OES intensities as a function of nitrogen flow rate at different working pressures (2, 3.5, 5 and 14mTorr). All spectra are presented on figure II-16.

As compared to Ar-O_2 plasma, the poisoning effect of nitrogen in Ar-N_2 is easily reversible. Indeed, there is almost no hysteresis effect, especially at 14 mTorr.

II-5-2) Discussion

Fig.II-17 summarizes the normalized optical emission intensities, for titanium 499 nm and nitrogen 746 nm, used from figures.II-16, as a function of nitrogen flow rate in the sputtering chamber. As in the case of the results found with oxygen as reactive gas, the titanium nitride deposition rate (for nitrogen flow rate more than 2 sccm) is much more enhanced when we control the pressure using the argon flow rate rather than the electrical throttle valve. Compare in Fig.II-17(a) below both titanium normalized intensities at 14 mTorr when Ar=140 sccm (control using argon flow rate) and Ar=35 mTorr (control using the throttle valve).

The transition between the metallic state and the poisoned state is continuous in the case of argon nitrogen plasma. As the formed TiN film (deposited progressively on the target) has a good conductivity compared to the case of TiO_2 (using oxygen as reactive gas).

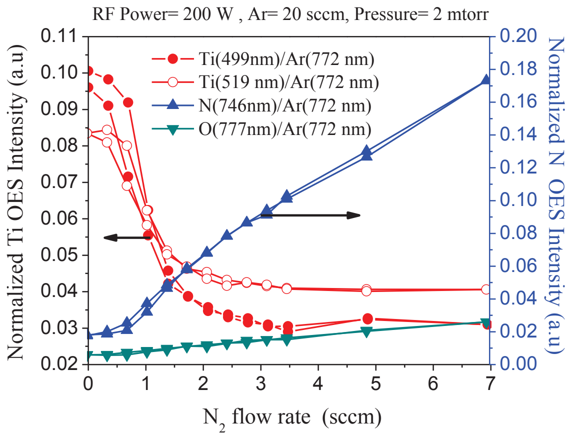

a) Argon flow rate 20sccm, pressure 2 mTorr

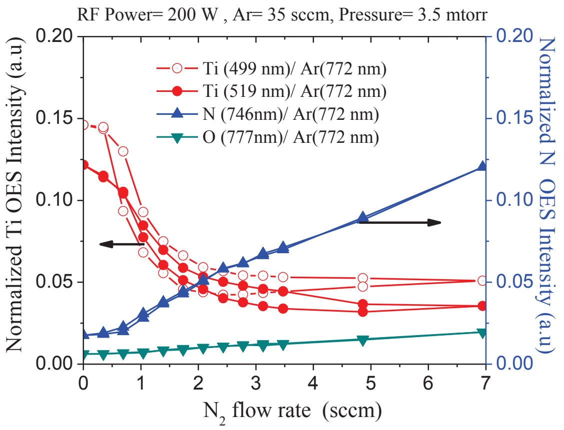

b) Argon flow rate 35sccm, pressure 3.5 mTorr

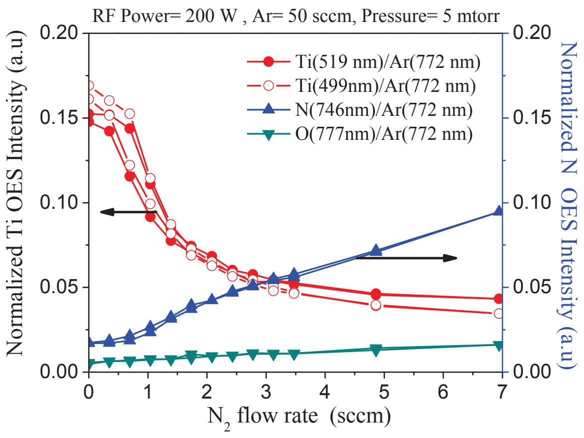

c) Argon flow rate 50 sccm, pressure 5 mTorr

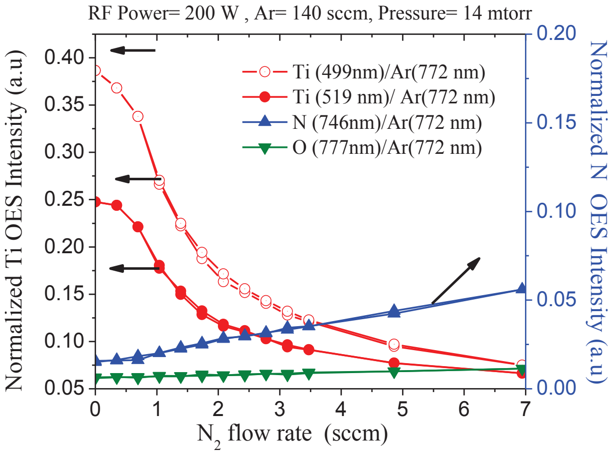

d) Argon flow rate 140 sccm, pressure 14 mTorr

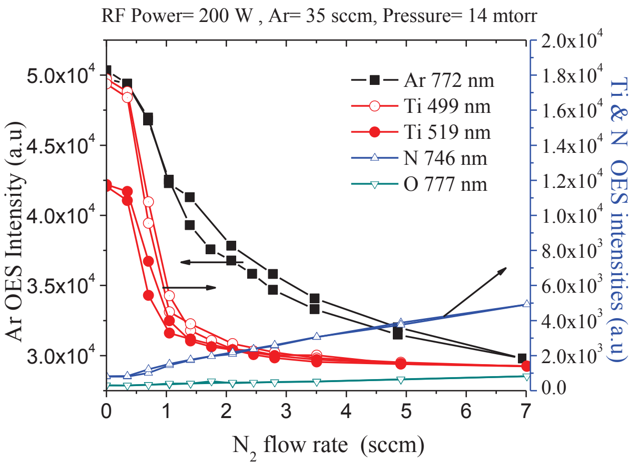

e) Argon flow rate 35 sccm, pressure 14 mTorr

Fig.II-16: Normalized optical emission intensities in argon-nitrogen plasma vs nitrogen flow rate. Pressure was controlled by argon flow rate in (a),(b),(c) and (d), i.e. pumping speed = 126.6 l/s. For (e), pressure was controlled by using the gate valve, i.e. pumping speed =31.6 l/s. RF power 200W. (Spectrometer Maya 2000+).

As the partial pressure of the reactive gas increases, the amount of nitrogen in the film increases, and the deposition rate decreases. There is an optimum operating point along this curve that maximizes both the deposition rate and delivers the desired properties and stoichiometry of the deposited film, this optimum corresponds to a deposition with 0.7 to 1 sccm as nitrogen flow rate at low argon flow rate (20 sccm to 35 sccm), 1 to 1.5 sccm in medium argon flow rate (more than 35 sccm) and 1.5 to 2.5 sccm when working at a higher argon flow rate (140 sccm). This conclusion is independent of the working pressure.

Sproul et al. [7] reported that in order to keep the sputtering in the transition region, the reactive gas partial pressure is usually 3–10% of the total system pressure, the best way to measure the partial pressure is to use the mass spectrometer (MS). We have not done any partial pressures measurements with MS. Also, there is no evident linear relationship between the reactive gas partial pressure, its flow rate and the total pressure

In general, we didn't find any hysteresis in the plot of normalized emission intensities vs nitrogen flow rate in argon-nitrogen plasma even when using the electrical throttle valve to control the pressure. This is the second main difference from the case of argon-oxygen plasma. This is mainly due to the remarkable difference in the conductivity between TiN and TiO_2. Also, the sputtering rate decreases gradually until the poisoned mode in the case of nitrogen reactive gas is reached. But with oxygen, the sputtering rate decreases faster near the poisoned mode.

The decrease in the emission intensity and sputtering rate of titanium is an indication of a decrease in the deposition rate of titanium nitride (at higher nitrogen flow rates), this is mainly due to the low sputtering yield of the TiN film deposited on the target surface compared to the metallic sputtering yield of Titanium (TiN is a very hard ceramic material).

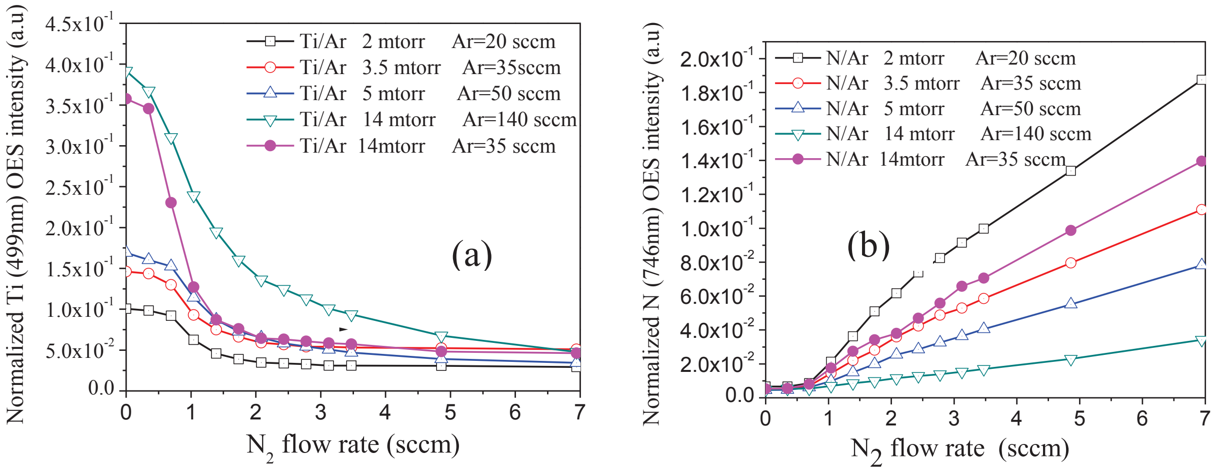

Fig.II-17: Summary & comparison of Normalized Optical Emission intensities for a) Titanium 499 nm and b) Nitrogen 746 nm, from figures.II-16. RF power 200W. (Spectrometer Maya 2000+).

II-6) Electrical measurements used for plasma diagnostic

We will discuss briefly two electrical measurement used for plasma diagnostics in the sputtering reactor:

- ✓ Langmuir probe measurements to estimate the variations of the plasma density and electron temperature.
- ✓ Cathode bias voltage (cathode DC self-voltage).

II-6-1) Langmuir probe measurements

II-6-1-a) Effect of reactive gas at fixed RF power and pressure

Lewis et al. [25] reported that an increase in the reactive gas partial pressure in the plasma could reduce the plasma density due to a subsequent reduction in the ionization collision cross section, which leads also to an increase in the target DC self-bias voltage.

We used the Langmuir probe measurements to estimate the plasma temperature and plasma density under different experimental environments. The Langmuir probe system is an RF compensated Smart probe from Scientific Systems. The target to Langmuir probe vertical distance was about 10 mm. The radial position of the probe tip was 15 mm away from the center of the target.

Fig.II-18 presents the electron density & electron temperature variation near the titanium target, in argon-oxygen and argon-nitrogen plasmas, as a function of reactive gas flow rate. Working pressure, argon flow rate and RF power were 5 mTorr, 30 sccm and 200W respectively.

In argon-oxygen plasmas, the plasma density is highly affected by the reactive gas flow rate rather than the plasma temperature (ΔkT_e=0.4 eV, ΔN_e= 1.53E10 cm^{-3} compared to pure Ar plasma); this is in agreement with [25]. On the contrary in an argon-nitrogen plasma the plasma temperature is the parameter which is mostly affected (kT_e=1.28 eV, ΔN_e= 0.5E10 cm^{-3}).

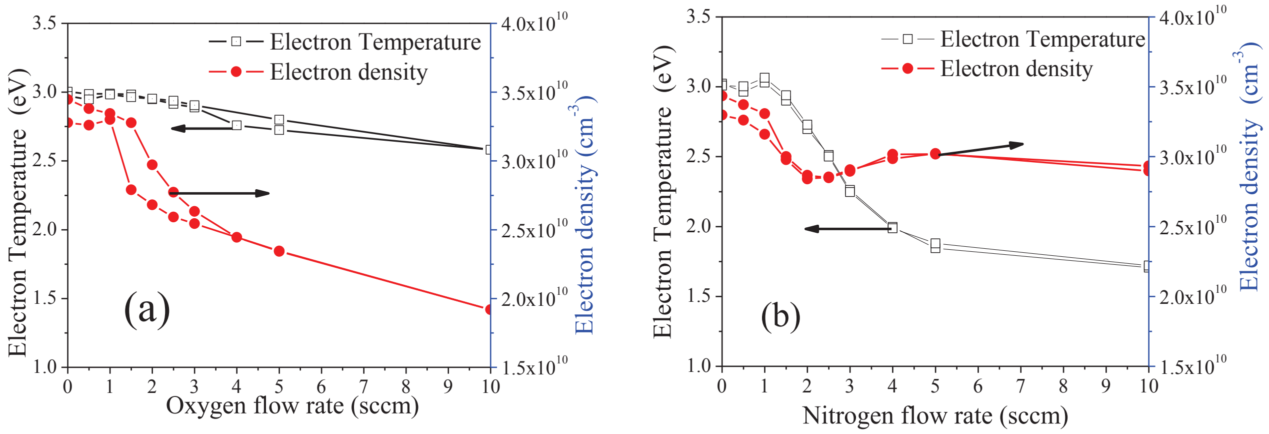

Fig.II-18: Electron Density & Electron Temperature variation near the Titanium target in (a) argon-oxygen plasma and (b) argon-nitrogen plasma, as a function of reactive gas flow rate. Working pressure=5 mTorr, Rf power=200W.

II-6-1-b) Effect of RF power and pressure

Fig.II-19 presents the Electron Density & Electron Temperature variation near the Titanium target, in pure argon plasma as a function of RF power (at a pressure of 5 mTorr) and working pressure (at RF power of 200W). Argon flow rate was 30 sccm in both sets of measurement.

As expected, electron density has a linear relationship with RF power but the electron temperature is not much affected by the electrical power which is a little bit surprising but it still consistent with some reports [37]. However, many works show that the electron temperature decreases with the plasma power, as Nisha et al. [36] who related the T_e decrease to the increase in the ion density. On the other hand, the working pressure is the most relevant parameter which affects both electron density and electron temperature. When the working pressure increases from 3 to 30 mTorr (ten times):

- ✓ Electron density increases from 3E10 to 9E10 (3 times) in a quasi linear trend.
- ✓ Electron temperature decreases from 3.2 eV to 1.8 eV (2 times).

These results concerning the effect of working pressure are not surprising and are consistent with other studies [35].

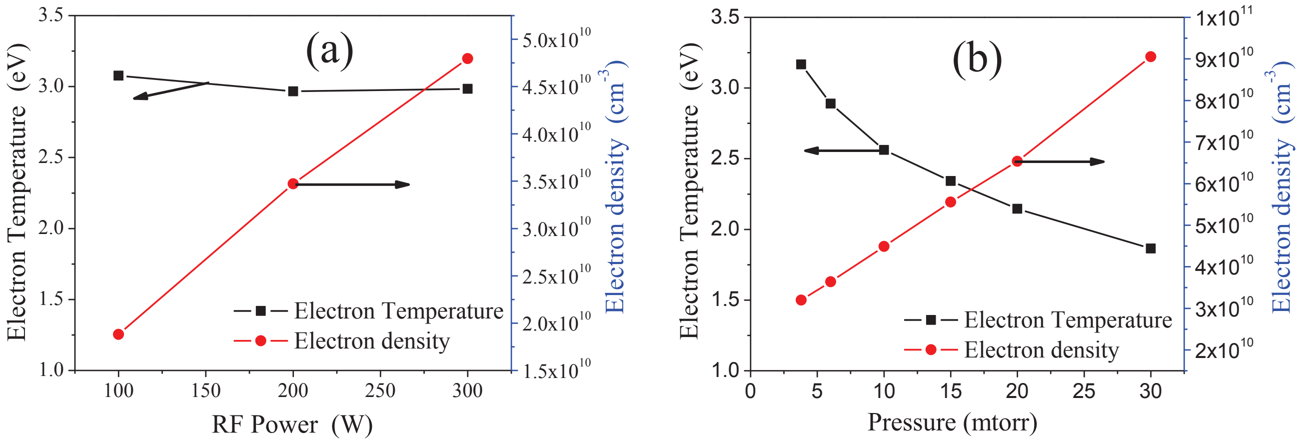

Fig.II-19: Electron Density & Electron Temperature variation near the titanium target in argon plasma (a) vs RF power at 5mtorr and (b) vs working pressure at 200 W.

In order to have a better idea of the effect of the pressure in the reactive mode we repeated these measurements in the presence of oxygen or/and nitrogen in the spurrering chamber (Fig.II-20):

1) With 30 sccm argon & no reactive gas,
2) With 30 sccm argon & 2sccm oxygen
3) With 30 sccm argon & 2 sccm nitrogen
4) With 30 sccm argon & 1sccm oxygen & 1sccm nitrogen

The plasma temperature is more affected by the reactive gas of nitrogen as compared to pure argon and generally decreases with the working pressure, this is due to the increase in the collision probability in plasma. But the electron density increases with the increase in the working pressure, as expected [35], in the case of Ar and its mixtures with the reactive gases. A comparative study between Optical and Langmuir probe diagnostics, in argon plasma, in our RF reactive magnetron sputtering system has been published [39].

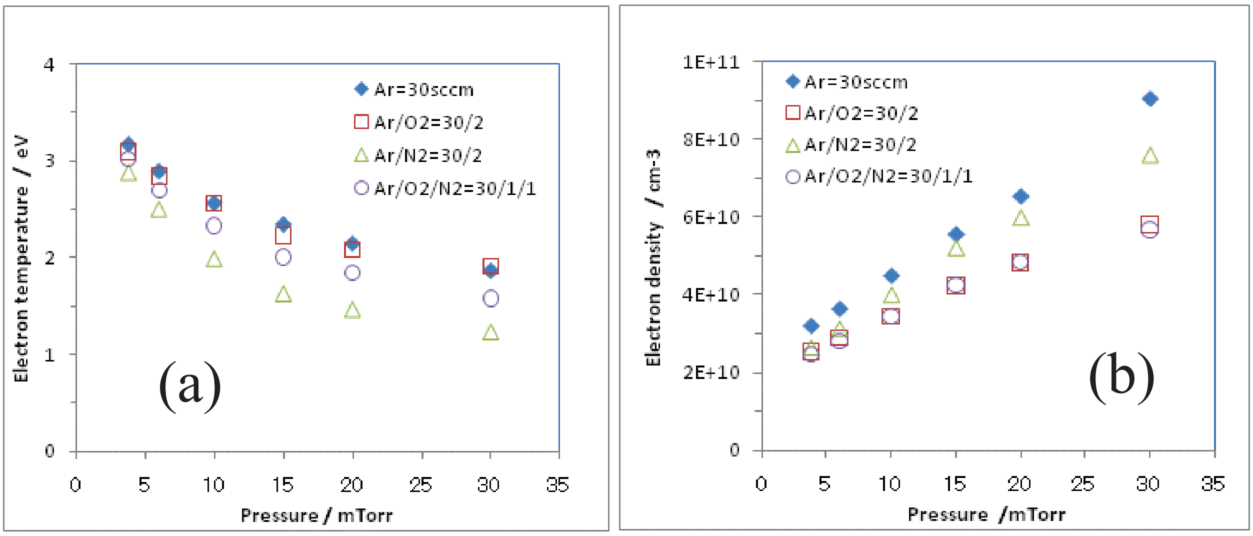

Fig.II-20: (a) Electron Temperature & (b) Electron Density near the Titanium target in argon/oxygen/nitrogen plasmas as a function of the working pressure. RF power=200W.

II-6-2) Cathode voltage measurements

The cathode bias DC voltage changes as the partial pressure of the reactive gas changes. So the measure of the target bias voltage can be a very effective feedback signal for a reactive sputtering process control. Fig.II-21 (a) presents an example of the measured cathode auto-bias voltage for titanium target in argon-oxygen plasma as a function of oxygen flow rate, at 5mTorr and 200W for working pressure and RF power, respectively.

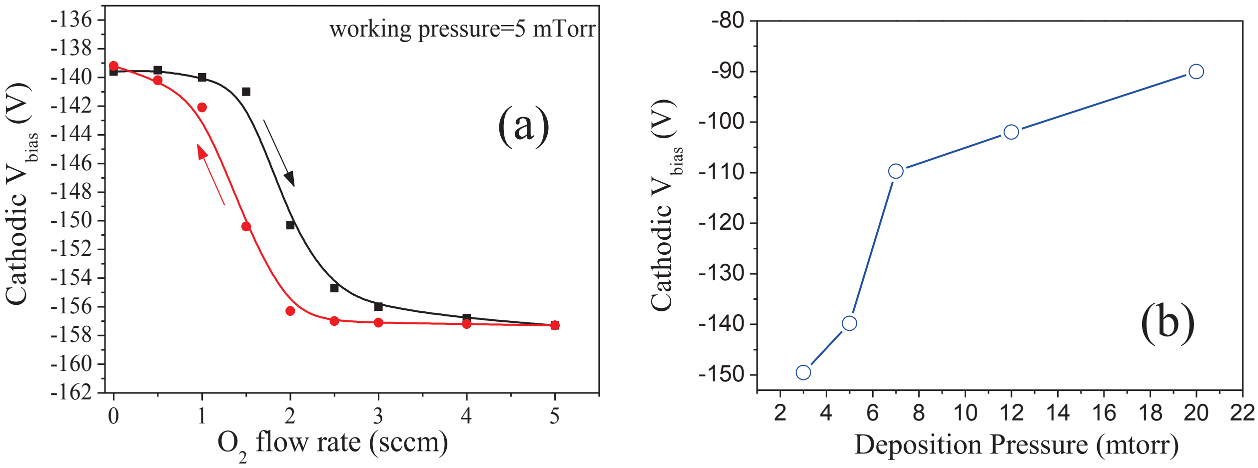

Fig.II-21: Cathode auto-bias voltage for titanium target (a) in argon-oxygen plasma as a function of oxygen flow rate and (b) in pure argon plasma as a function of working pressure. RF power=200W in both cases.

In the TiO_x system, when a constant RF power is applied to the cathode, the cathode DC bias voltage would change according to the reactive gas partial pressure (due to the chemically modified surface state of the target) as shown in Fig.II-21 (a). The cathode voltage is initially stable with the increase of the O_2 flow rate in the range from 0 to 1 sccm, which corresponds to the metallic sputtering region. For further increase in the reactive gas flow rate, a sharp increase of the absolute value in the negative cathode bias voltage takes place, for O_2 flow in the range of 1 to 2 sccm, due to the formation of the dielectric film (titanium oxide) on the surface of the target. This gives rise to the stabilization of the DC bias voltage, when oxygen flow rate exceeds 3 sccm, which is the point where the target becomes completely poisoned. Once the target is poisoned, the cathode voltage levels off at a negative value of about -158 V.

When the oxygen flow is reduced in the return part, the cathode bias voltage remains quite high until the compound layer on the target surface is broken so that the cathode voltage returns to the lower values corresponding to the metallic deposition mode. Note that in the return part (measurements done when the O_2 flow rate is decreased) the DC bias voltages are slightly higher than the initial values. These results correlate well with the electron density measurement (Fig.II-18 (a)).

Note that the cathode DC bias voltage behavior as a function of reactive gas flow rate depends very much on the target material (and on the deposited film):

- ✓ The cathode voltage could decrease as the partial pressure of the reactive gas increases, as the case of reactive sputtering of aluminum in an argon/oxygen atmosphere, as well as the reactive sputtering in aluminum–nitrogen, silicon–oxygen and silicon–nitrogen systems [7]. This decrease in the cathode voltage is due to the compound material which covers the target surface which has a higher secondary electron emission coefficient than the metallic target surface

- ✓ Increases in the cathode DC bias voltage during reactive sputtering for an increase in reactive gas partial pressure have also been observed in the titanium–nitrogen, tantalum–oxygen, and zirconium–nitrogen systems [28][36]. However the cathode voltage can also change for other reasons than the reactive gas partial pressure variation. It could be also affected by a change in the temperature in the chamber, electrical perturbation, and any variation in the working pressure [7] especially when working with dual reactive gases (which will be discussed in chapter IV). So the target DC bias voltage cannot be used as a unique poisoning indicator of the target.

II-6-3) Target voltage and formation of particles

When a semiconductor or an insulating film is formed on the surface of the target, it can charge up. If the charge reaches the breakdown voltage for the insulating film, a spontaneous arc will occur. Arcs usually result in particles being ejected from the target surface, and these particles degrade the film quality.

An arc can be detected by measuring a drop in the absolute value of the DC bias cathode voltage and/or an increase in the cathode current. Once the arc is detected, the power supply to the cathode should be cut off, until the arc is cleared before resuming delivery of power. Fig.II-22 gives an example of the effect of the arcing and particles formation on the TiN deposition.

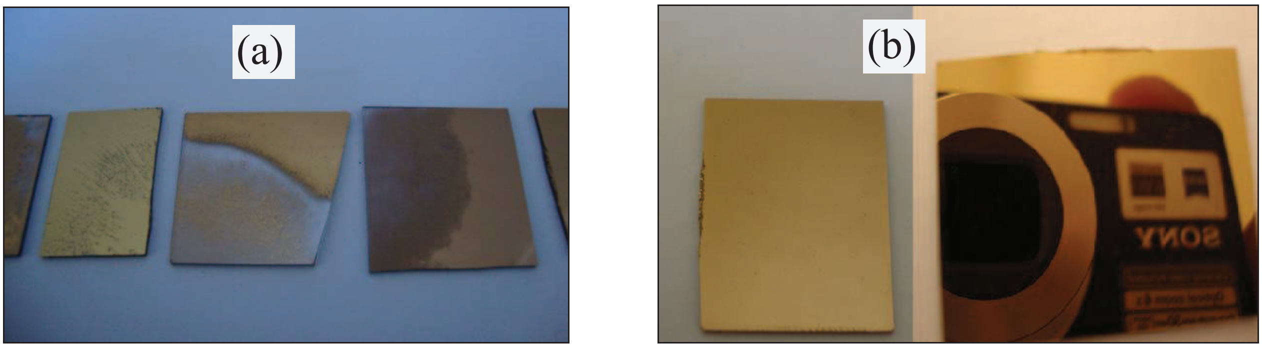

Fig.II-22: (a) Effect of TiN dust particles formation due to arcing during the sputtering deposition. (b) Example of two ideal TiN films deposited on glass substrates, RFpower 200 W, argon 30 sccm and working pressure 3 mTorr.

II-7) Simple analytical plasma modelling of the sputtering reactor

The objective of this section is to use the results of the different plasma diagnostics (Langmuir probe, bias voltage measurements, OES) in order to obtain a simple energy balance in the plasma reactor. An extensive comparative analysis of the discharge by Langmuir probe and OES was performed during the visiting professor position of Pr. S. Mori from Tokyo Institute of technology. Although the results obtained by Mori and al. are not described in this thesis [39].

II-7-1) Comparison of Langmuir probe measurements and current measurements

For a pure argon plasma at a pressure of 5 mtorr and RF power of 200 W, the electron density and electron temperature, measured by Langmuir probe at a distance of z = 2 cm from the cathode, are respectively $n_e = 3.5 \times 10^{16}$ m^{-3} ($3.5x10^{10}$ cm^{-3}) and $kT_e = 2.9$ eV (see Fig.II-19 (a)) .

Outside the sheath, we can assume that the argon ion density is equal to the electron density in our capacitive plasma [38] (see the annex 3):

$$n_{Ar+} = n_e \qquad \text{Eq.II-2}$$

and the ion density at the vicinity of sheath region could be given by the following equation [38]:

$$n_S = e^{-\frac{1}{2}} \cdot n_{Ar+} \qquad \text{Eq.II-3}$$

The argon ion flux density bombarding the cathode can be obtained from the following equation, assuming that the ion speed is equal to the Böhm speed (u_B) [35][38]:

$$\Gamma_{Ar+} = n_S \cdot u_B = n_S \cdot \left(\frac{e \cdot kT_e}{M} \right)^{\frac{1}{2}} \qquad \text{Eq.II-4}$$

$$\Gamma_{Ar+} = 5.6 \times 10^{19} \ \ \mathrm{m^{-2}.s^{-1}} \qquad \text{Eq.II-5}$$

with M = 6.67 x10^{-26} kg is the argon ion mass and e is the electron charge (1.6 x10^{-19} C). The intermediate calculation gives:

Böhm speed **u_B = 2 640 m/s**.

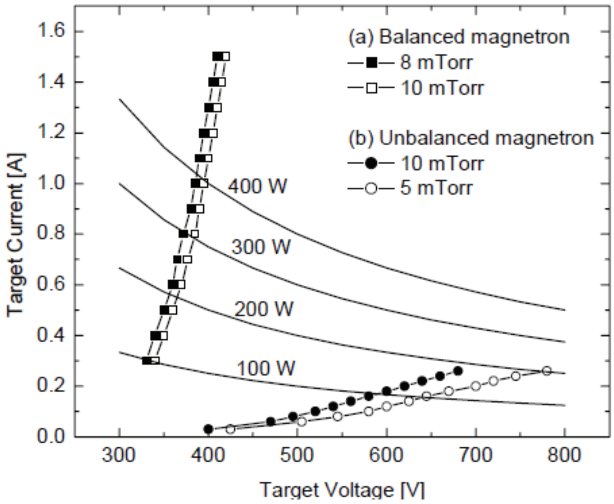

Fig.II-23: Current voltage characteristic of the SPT-120 in argon plasma, from Plasmionique.

The target (cathode) diameter being equal to 2” *(5.1x10^{-2} m)*, the surface of the cathode ($S_{cathode}$) is equal to 2×10^{-3} m² and the argon ion current to the cathode is:

$$I_{(Ar^+)cathode} = S_{cathode} \cdot \Gamma_{Ar+} \cdot e \qquad \text{Eq.II-6}$$

$$\boxed{I_{(Ar^+)cathode} = 0.018 \ A}$$

The cathode current measured by Plasmionique company for our reactor (SPT-120), in the same conditions (Ar, 200 W, balanced cathode) is equal approximately to 0.6 A as shown on Fig.II-23. This current is more than one order of magnitude higher than the current calculated from Langmuir probe measurements.

This difference between the calculated and measured currents can be obviously explained by the role of the magnetic confinement of the plasma (ring shape plasma) which increases the electron density. Indeed, probe measurements were performed at z = 20 mm, i.e. after the high density region. Thus, in order to estimate the correct electron density inside the plasma ring, we will use independently the experimental cathode current and the experimental Ti growth rate.

II-7-2) Estimation of electron density in the dense plasma ring from current measurements

Fig.II-24 presents simple images of target with the plasma ring and its track on the target and an illustration of the torus of plasma. By analysing the image of argon plasma in the SPT-120 reactor with a balanced cathode (Plasmionique) and by measuring the sputtering track dimensions on a Cu target, we can estimate the following dimensions of the plasma ring:

R = 1.9 cm and w = 1 cm

Fig.II-24: (a) Picture of an Argon plasma ring (Plasmionique), (b) Sputtering track on a Cu target, (c) Schematic of a torus.

The surface considered for this calculation, i.e., the surface on which the ion flux is directed, is the following:

$$S_{track} = \pi \cdot \left[\left(R + \frac{w}{2} \right)^2 - \left(R - \frac{w}{2} \right)^2 \right] \qquad \text{Eq.II-7}$$

$$S_{track} = 1.2 \times 10^{-3}\ (\mathrm{m}^2)$$

For an RF power of 200W, the experimental cathode current being equal to 0.6 A (Fig.II-23), we can calculate the argon flux density by using Eq.II-6:

$$I_{(Ar^+)cathode} = 0.6 = S_{track} \cdot \Gamma_{Ar+} \cdot e$$

$$\Gamma_{Ar^+} = 3.1 \times 10^{21} \ \ (\mathrm{m}^{-2}.\mathrm{s}^{-1})$$

By assuming that the electron temperature inside the dense ring is equal to the temperature outside the ring, we can use the previously calculated value of the Böhm ion speed ($u_B = 2640$ m/s). Hence, we can deduce the electron density by combining Eq.II-2, Eq.II-3 and Eq.II-4.

$$\Gamma_{Ar^+} = 3.1 \times 10^{21} = n_S \cdot u_B = n_S \cdot 2640$$

$$n_S = 1.2 \times 10^{18}\ \mathrm{m}^{-3}$$

$$(n_e)_{ring} = 2 \times 10^{18}\ \mathrm{m}^{-3}$$

As compared to the electron density $\boldsymbol{n}_e = 3.5\mathrm{x}10^{16}\ \mathrm{m}^{-3}$ measured at z = 20 mm by Langmuir probe, the electron density in the dense plasma ring should be equal to $(\boldsymbol{n}_e)_{ring} = \boldsymbol{2\mathrm{x}10^{18}\ m^{-3}}$, assuming that the two hypothesis of calculation are satisfied, i.e. i) the ion current to the target comes only from the plasma ring, ii) kT_e inside the ring is equal to kT_e outside the ring.

II-7-3) Estimation of the electron density in the dense plasma ring from the deposition rate

Here we will try to estimate the electron density of the dense plasma by using the measured auto bias voltage of the cathode and the deposition rate of titanium in pure argon plasma. For pure argon plasma at 5mTorr and 200 W, the deposition rate of Ti (G_{Ti}) determined by SEM analysis is 0.13 nm/s. The molar volume of solid titanium is approximately 10.64 $cm^3.mol^{-1}$ at room temperature, giving an atomic density of Ti $(n_{Ti})_{solid}$ of 5.6 x10^{22} cm^{-3}.

By assuming that the sticking coefficient of atomic Ti is 1, i.e. any Ti atom reaching the surface will stick to it, the Ti flux coming to the substrate ($\Gamma_{Ti,substrate}$) is equal to:

$$(\Gamma_{Ti})_{substrate} = G_{Ti} \cdot n_{Ti},_{solid} \qquad \text{Eg.II-8}$$

Ti flux (at the substrate) $(\Gamma_{Ti})_{substrate} = 7.3\times10^{18}\ m^{-2}.s^{-1}$

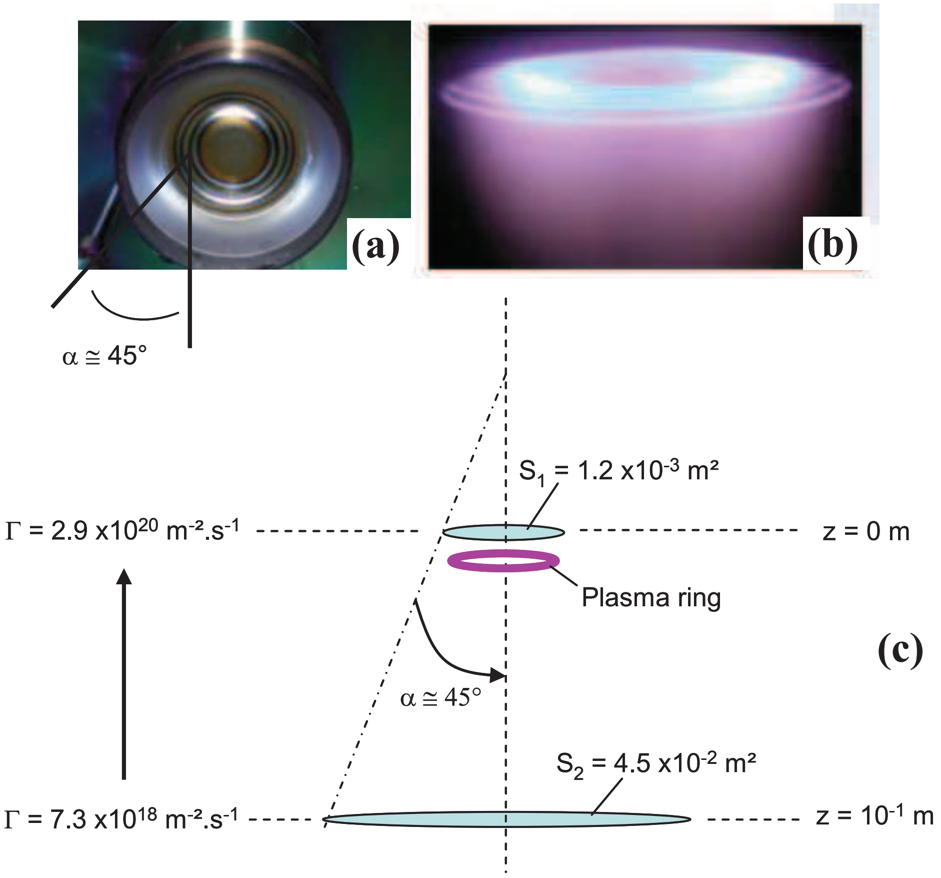

Fig.II-25: (a) Picture of the magnetron cathode showing the target and the anode cone-like shape, (b) Picture of the plasma ring, (c) Schematic of the geometrical construction.

The titanium flux density leaving the cathode surface ($\Gamma_{Ti,cathode}$) is higher than the flux density that reaches the substrate. In order to calculate $\Gamma_{Ti,cathode}$, we will use some geometrical consideration as shown on Fig.II-25.

As calculated previously (Eq.II-7), the sputtered surface on the target is $S_1 = S_{track} = 1.2\times10^{-3}\ m^2$. To simplify the model, we will assume that this surface is circular as show on Fig.II-25. We will also assume that the angular distribution of the sputtered atoms is uniform, but limited to α = 45° due to the shape of the anode.

By using the Thales theorem (if two triangles are similar, the corresponding sides are in proportion), the surface S_2 located at a distance $z = 10^{-1}$ m from S_1 could be easily defined by the following equation:

$$S_2 = \pi\left(\sqrt{\frac{S_1}{\pi}} + z \cdot \tan(\alpha)\right)^2 \qquad \text{Eq-.II-9}$$

$$S_2 = 4.5 \times 10^{-2} \text{ m}^2$$

The conservation of mass principle allows to calculate the density flow of titanium $\Gamma_{Ti,cathode}$ by the following equation:

$$(\Gamma_{Ti})_{cathode} = \Gamma_{Ti},_{substrate} \cdot \frac{S_2}{S_1} \qquad \text{Eq.II-10}$$

$$(\Gamma_{Ti})_{cathode} = 2.9 \times 10^{20} \text{ m}^{-2}.\text{s}^{-1}$$

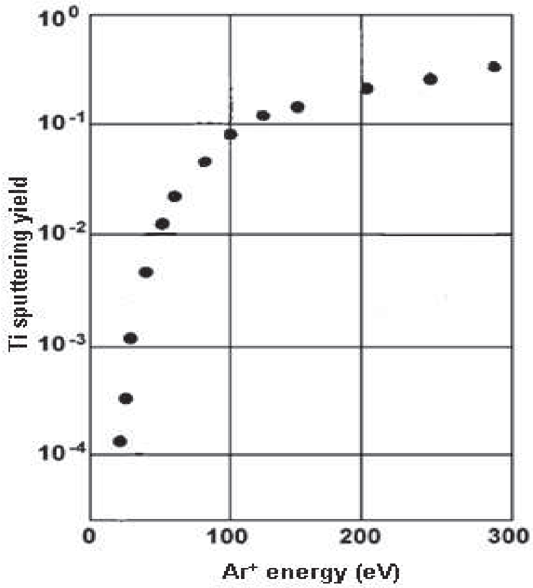

Fig.II-26: Sputtering yield of titanium by Ar$^+$ vs Ar ion energy, from K Wasa et.al. [34].

For the same experimental conditions (Ar, 5mTorr, 200 W), the DC self-bias voltage measured on the cathode is -139 V, as shown on Fig.II-2, and decreases down to -157 V with the introduction of oxygen (target poisoning). By assuming that the sheath is collisionless, the ion energy is then equal to 139 eV, in pure argon plasma, giving a sputtering yield $(\gamma_{Ti})_{Ar^+}$ of approximately 0.1 (Fig.II-26). Thus, in order to ensure a sputtered Ti flux density of 2.9 x10^{20} m^{-2}.s^{-1}, the argon ion flux density on the cathode should be 10 times higher than that of the desired Ti flux density ($1/\gamma_{Ti}$). So one can conclude that argon ion flux density to the target is about $(\Gamma_{Ar+})_{cathode} = 2.9$ x10^{21} m^{-2}.s^{-1}. This value is very close to the value calculated in the previous section from current measurements $(\Gamma_{Ar+})_{cathode} = 3.1$ x10^{21} m^{-2}.s^{-1}). By using Eq.II-2, Eq.II-3 and Eq.II-4, one can obtain an electron density in the plasma ring (***n****e*,ring) equal to 1.9×10^{18} m^{-3}.

II-7-4) Power balance calculation

In chemical engineering, when the electric power is supplied to a system, we should know where this power goes and what it is used for. Generally, a considerable percentage of the power supplied by the generator is lost in the matching and in the cables and thus never goes to the plasma. The other part of electrical power is absorbed by the plasma and is used mainly in a sputtering system to accelerate the ions in the sheath. In this section we will use the previously calculated parameters of the plasma in order to estimate the power balance in our system.

In the previous two sections, we found the following values of electron density and electron temperature of plasma at 200 W and 5 mTorr

- Diffuse plasma region: $\boldsymbol{n_e} = 3.5 \text{ x}10^{16}$ m^{-3}, $\boldsymbol{kT_e} = 2.9$ eV, (Langmuir probe measurement).
- Dense plasma ring : $\boldsymbol{n_{e,\text{ring}}} \sim 2 \text{ x}10^{18}$ m^{-3} (calculated value).

For the cathode, as before, we are going to use 139 eV and 0.6 A, as the argon ion energy and ion current, respectively. So the power dissipated by the ions in the sheath region is $0.6 \times 139 = 83\ W$. The balance sheet of energy which is absorbed by plasma could be given by [38]:

$$\left\{ e \cdot \left(\underset{\substack{\uparrow \\ \text{Ions}}}{V_{dc}} + \underset{\substack{\uparrow \\ \text{Electrons}}}{2(kT_e)} + E_0 + \underset{\substack{\uparrow \\ \text{Collisions}}}{a} \cdot \exp\left(-\frac{kT_e}{b} \right) \right) \cdot 0.61 \cdot \underset{\substack{\uparrow \\ \text{Flux density}}}{n_e} \cdot \sqrt{\frac{kT_e}{M_{Ar}}} \right\} \cdot \underset{\substack{\uparrow \\ \text{Surface}}}{S_1} \qquad \text{Eq.II-11}$$

Where e.V$_{dc}$ and 2.e.kT$_e$ are respectively the energy dissipated by one Ar$^+$ to the cathode and by one e$^-$ to the anode. The term $E_0 + a \cdot \exp\left(-{kT_e}/{b} \right)$ corresponds to the total energy dissipated in the plasma to produce one Ar$^+$–e$^-$ pair. The latter can be significantly higher than the ionization energy of Ar (15.8 eV) when the electron temperature is low. From Lieberman and Lichtenberg [38], one can found E$_0$ = 36 eV, a = 11700 and b = 0.37 for argon, which lead to a total energy to produce one ion-electron pair equal to 40.6 eV for kT$_e$ = 2.9 eV.

The results of the calculations of the different terms in equation Eg.II-11 are presented in Fig.II-27. This model gives a total energy absorbed by plasma $P_{abs} = 115\ W$ for 200 W supplied by the generator.

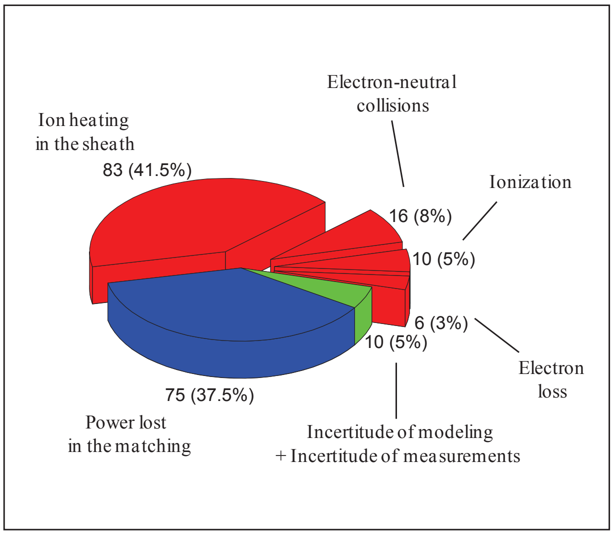

Plasma volume
- Ionization ~ 10 W
- Excitation + gas heating ~ 16 W

Electrodes
- Ions to the cathode ~ 83 W
- Electrons to the anode ~ 6 W

Total ~ 115 W

Fig.II-27: Illustration of power balance calculations in the sputtering system using the power balance equation.

In order to measure the power dissipated in the plasma, we used the method reported by Lieberman et al [38]. The procedure consists in the measurement of the RF power (P_1) and voltage (V_1) during the discharge, this power is the sum of the power absorbed by the plasma and the power lost in the electrical system (matching box, connections, ...). Then, the plasma was switched off by decreasing the pressure, this perturbation leads to a new RF voltage (V_2). The RF voltage V_2 is adjusted in order to be equal to V_1 by changing the power to be P_2, which is the power lost in the electrical system alone and not by plasma. In this case, the electric power which is absorbed by plasma is:

$$P_{abs} = P_1 - P_2 \qquad \text{Eq.II-12}$$

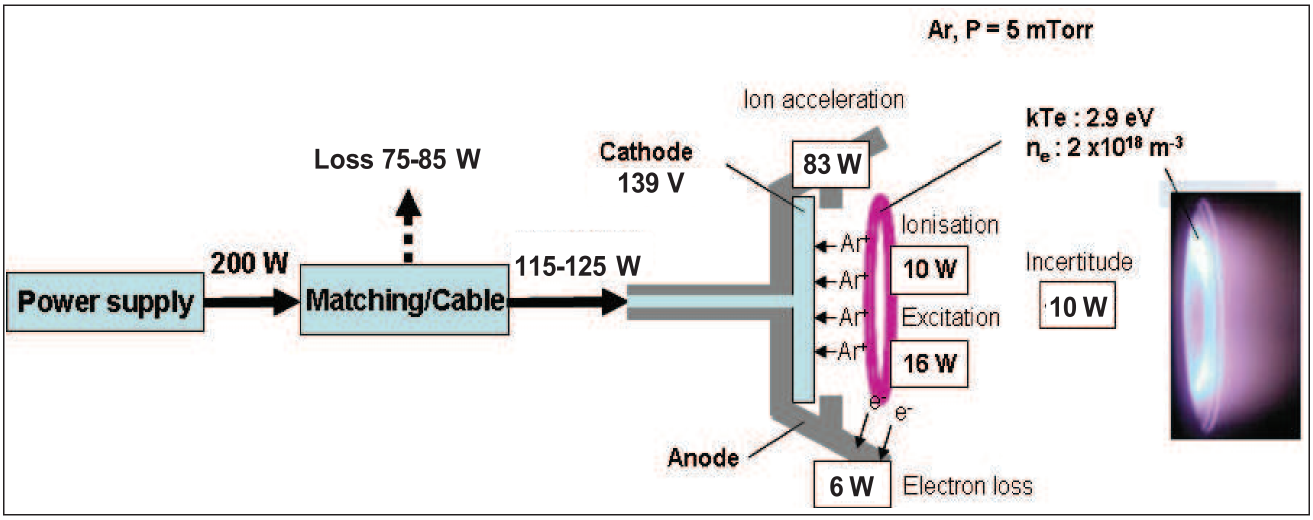

Fig.II-28: Comparison of power balance modeling and power measurements.

Experimentally, in pure argon plasma at a nominal power of 200W and working pressure of 5 mtorr, we found that the electric power absorbed by plasma is (using Eq.II-12):

$$P_{abs} = 200 - 75 = 125\ W$$

This value $P_{abs} = 125\ W$ is very close to the one calculated in the previous model ($P'_{abs} = 115\ W$) using Eq.II-11, thus one can conclude that the power balance model is consistent with the measurement of the power absorbed by the plasma (figure II-28).

Having looked at the different parameters and their effect on the energetic properties of the plasma, we will see in the next paragraph the effect of the most important parameter, which was the pressure, on the macroscopic properties of TiN coatings.

II-8) Effect of deposition pressure of TiN on the resistivity of the coated thin film

We prepared different samples of TiN thin films on glass substrates using the RF reactive sputtering in argon-nitrogen plasma. Before each deposition, Titanium target has been sputtered in argon plasma for about 10 minutes. Then nitrogen reactive gas was introduced in the deposition chamber. TiN films were deposited at the same argon flow rate (2 sccm), a nitrogen flow rate of 1 sccm and a deposition time equal to 150 min. The RF power was 200 W (corresponding to a cathodic V_{bias} = 148±5 V DC). The total deposition pressure was varied between 2 to 14 mtorr and the thickness of the coatings was 700 to 900 nm depending on the deposition pressure.

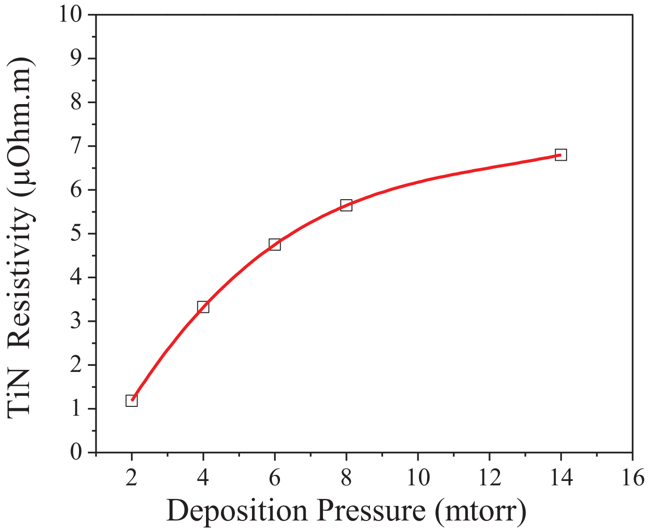

Fig.II-29: Evolution of TiN resistivity as a function of the deposition pressure.

The TiN resistivity has been measured using the 4 points probe setup method, using a current of 1 mA. Fig.II-29 shows the resistivity values of the TiN thin films vs the deposition pressure. The TiN resistivity increases rapidly as the pressure increases from 2 to 9 mTorr, then it increase with lower slope before stabilization for deposition pressures higher than 14 mTorr. The increase in the resistivity could be attributed to the variation of the morphology of the film rather than the stochiometry and the concentration of the defects, because we varied only the deposition pressure and not the reactive gas composition. Increasing the working pressure could lead to an increase in the deposited film porosity and a decrease of the TiN film density. This would induce an increase of the TiN resistivity.

If the working pressure increases too much, the plasma volume should increase in the sputtering chamber, the excited species and electrons in the plasma hit the substrate leading to an “anti-sputtering” of the deposited film so the porosity will not further increase. In another word, at very high pressure, there is a competition between the porosity increase and the “anti-sputtering” phenomena, *the main variation in the morphology could be expected when the films are deposited at pressure between 2 to 14 mTorr in our sputtering process.*

Depending on the deposition pressure, different colors could be obtained for TiN. Compact films deposited at lower pressures had golden color (for stochiometric TiN), more porous films a bronz-brown color, dark films could be obtained when TiN was deposited at pressures higher than 9 mtorr.

II-9) Conclusion

Optical Emission Spectroscopy presents an effective and sensitive technique to detect perturbations during the sputtering deposition. As it is more sensitive to any changes in the plasma composition as compared to the electrical diagnostics, OES can be used as a very good feedback in reactive sputtering control rather than electrical measurements such as cathode DC bias voltage and Langmuir probe measurements. There are three main limitations in the reactive sputtering: first is the hysteresis effect due to the variation in the reactive gas flow rate, second is the jump transition from the metallic to the reactive mode of sputtering, which makes it difficult to achieve the coatings with a certain stoichiometry in this transition region. And the third is the arcing between the target (cathode) and the ground, especially when dielectric coatings are sputtered or when a dielectric film is formed on the cathode.

Reactive gas control during reactive sputtering strongly influences the deposition rate as well as the physical and chemical properties of the coating being deposited. Reactive sputtering is generally carried out in the poisoned mode of the target as it is easier to control, in order to have reproducible properties of the deposited films. However, the deposition rate is low in the poisoned mode compared to the rate from the metallic target. In-situ control of the partial pressure of the reactive gas during a reactive sputtering could eventually help to carry out depositions within the transition region between the elemental and poisoned states of the target, especially if working with oxygen as the reactive gas. An operating point can be chosen that optimizes the desired film properties as well as the deposition rate and a reproducible stoichiometry.

It is easier to control the reactive gas (oxygen, nitrogen, ….) flow rate rather than its partial pressure, the flow rate should be adjusted in a feedback regulation system using optical emission spectroscopy by following the the normalized intensities of the emission lines of the sputtered material (titanium) and/or that of the reactive gas in the deposition chamber. Our results show that it is easier to control the stability and the reproducibility with nitrogen reactive gas rather than oxygen since:

- ✓ In nitrogen reactive gas there is no hysteresis when varring the flow rate up or down.
- ✓ The transition between the metallic and compound mode is more progressive with reactive nitrogen as compared to oxygen.

The deposition pressure is one of the main parameters which can affect the properties of the deposited coating as well as its deposition rate. When the deposition pressure increases, the plasma density increases, but the plasma temperature decreases as well as the negative auto bias voltage of the cathode, this could explain why the deposition rate decreases as the working pressure increases. We distinguished 3 intervals for the variation of the deposition pressure: 2~6 mtorr, 6~14 mtorr and >14 mtorr. Based on the electrical resistivity of the deposited TiN thin films, the physical properties of the deposited films are expected to change only within the first two intervals.

The pumping speed has a significant effect on the working pressure and more dramatically on the target poisoning. Our system could produce a vacuum down to to $2x10^{-6}$ torr (base pressure), other commercialized systems can give a vacuum better then 10^{-8} torr which is more preferable to reduce the poisoning effect and the probability of the formation of solid droplets on the coating. Adjusting the deposition pressure by using the flow rate of the sputtering gas (argon), keeping the pumping speed at the maximum level, is found to be more efficient rather than by changing the pumping speed by the electro-valve. The former can give higher deposition rates and reasonable reproducibility because (i) it can reduce the hysteresis effect and (ii) it can lead to a more continuous transition between the metallic and poisoned depositions.

Increasing the electrical power of the sputtering system can increase the auto bias voltage of the cathode and so the deposition rate depending on the reactive gas flow rate. However, the effect of the electrical power on the plasma temperature and density depend on the type of the reactive gas used (oxygen and/or nitrogen). While the reactive gas flow rate controls the stoichiometry of the deposited film, it also affects the auto bias voltage of the cathode and consequently the deposition rate. Electrical diagnostics of the plasma showed significant differences between the deposition near the metallic mode and the poisoned mode.

References

[1] A. Trenczek-Zajac, M. Radecka, K. Zakrzewska, A.Brudnik, E.Kusior, S.Bourgeois, M.C. Marco de Lucas, L. Imhoff, Journal of Power Sources 194 (2009) 93–103.

[2] U.Helmersson, M.Lattemann, J.Bohlmark, P. Ehiasarian, J.Gudmundsson, Thin Solid Films 513 (2006) 1-24.

[3] N Britun, M Gaillard, L Schwaederlé, Y M Kim, J G Han, Plasma Sources Science and Technology 15 (2006) 790-796.

[4] K.S. Mogensen, S.S. Eskildsen, C. Mathiasen, J. Bøttiger, Surface and Coatings Technology 102 (1998) 41–49.

[5] Min J. Jung, Kyung H. Nam, Leonid R. Shaginyan, Jeon G. Han, Thin Solid Films 435 (2003) 145–149.

[6] J. B. Boffard, Plasma Sources Science and Technology 19 (2010) 065001.

[7] W.D. Sproul, D.J. Christie, D.C. Carter, Thin Solid Films 491 (2005) 1-17.

[8] V Godyak, R Piejak, B Alexandrovich, Plasma Sources Science and Technology 1 (1992) 36–58.

[9] D. Depla S. Mahieu, Reactive Sputter Deposition, Springer Berlin Heidelberg New York 2008.

[10] Y. Yamamura, H. Tawara, Atomic Data and Nuclear Data Tables, 62, Number 2 (1996) 149-253.

[11] J. Lindhard, M. Scharff, Physical Review (1961)124-128

[12] A. Brudnik, M. Bucko, M. Radecka, A. Trenczek-Zajac, K. Zakrzewska, Vacuum 82 (2008) 936–941.

[13] Brudnik A, Jachimowski M, Zendheroud J. Le Vide, Journal of Applied Science and Technology 279 (1996) 273–278.

[14] S. Schiller, U. Heisig, K. Steinfelder, J. Strompfelon, Thin Solid Films, 96 (1982) 235-240

[15] William D. Sproul, James R. Tomashek, U.S. Patent 4,428,811, January 31, 1984.

[16] J. Affinito, R. Parsons, Journal of Vaccum Science & Technology A, 2 (1984) 1275.

[17] E Shidoji, T Makabe, Thin Solid Films, 442 (2003) 27–31.

[18] http://physics.nist.gov/PhysRefData/Handbook/Tables/argontable2.htm

[19] J. Musila, P. Baroch, J. Vlcek, K.H. Nam, J.G. Han, Thin Solid Films, 475 (2005) 208–218.

[20] F.Perry, A.Billard, C.Frantz, Surface and Coating technology, 94 (1997) 681-685.

[21] V. Vancoppenolle, P. Jouan, A. Ricard, M. Wautelet, J.-P. Dauchot, M. Hecq, Applied Surface Science, 205 (2003) 249–255.

[22] H.Benien, J. Maushart, M. Meyer, R. Suchenturk, Materials science and Engineering, A139 (1991) 126-131.

[23] A Brudnik, A Czapla, W Posadowski, Vacuum 82 (2008) 1124–1127.

[24] A. Okamoto, T. Serikawa, Thin Solid Films, 137 (1986) 143.

[25] M.A. Lewis, D.A. Glocker, Journal of Vaccum Science & Technology, A 7 (1989) 1019.

[26] O Novák, J Vlček, Journal of Vacuum Science & Technology, A 29, (2011) 031301+031307.

[27] G. Este, W.D. Westwood, Journal of Vaccum Science & Technology, A 6 (1988) 1845

[28] William D. Westwood, Sputter Deposition, AVS, 120 Wall Street, New York, NY 10005, 2003.

[29] M. Scobey, R. Seddon, J Seeser, R. Austin, P Le Febvre, U.S. Patent 4,851,095, July 25, 1989.

[30] W. Sproul, D. Christie, D. Carter, Society of Vacuum Coaters, 505 (2003) 856.

[31] FUJITSU Scientific and Technical Journal, 46, No.3 (July 2010) 318-326.

[32] F. Perry, A. Billard, P. Pigeat, Measurement 41 (2008) 516–525.

[33] F G Tomasel, D Carter, HWalde, J J Gonzalez, GMcDonough, G A Roche, Plasma Sources Science and Technology 12 (2003) 139–141.

[34] K. Wasa, Thin Film Materials Technology William Andrew, Inc.

[35] R Powell, S Rossnagel**,** *Academic Press* **26** London NW1 7DX/UK (1999).

[36] M Nisha, K Saji, R Ajimsha, N Joshy, M Jayaraj, *Journal of applied physics*, **99** _(2006)_033304.

[37] N Nayan, R Mohamed Ali, I Senain, A Raniah, A Terk, *ISPC* (2011), Philadelphia USA.

[38] M Lieberman, A Lichtenberg, *Wiley international publication*, USA (1994).

[39] S Mori, H Fakhouri, J Pulpytel, F Arefi-Khonsari, *20th International Symposium on Plasma Chemistry,* **ISPC20** (2011) Philadelphia, USA.

Chapter III

Design of experiments & N doped TiO_2 by dual reactive gas sputtering

Chapter III

Design of experiments & N doped TiO_2 by dual reactive gas sputtering

Abstract

Doping nitrogen within TiO_2 is an effective way to enhance visible light photo activity of the doped material due to a direct electron excitation from the N_{2p} states within the band gap. However, nitrogen doping is not always efficient for UV photocatalytic activity. Here, different structures of N-doped TiO_2 (TiO_xN_y) have been prepared by reactive RF (13.56 MHz) magnetron sputtering using dual reactive gas, oxygen and nitrogen, simultaneously in the deposition chamber. A design of experiment was used to optimize the working conditions, oxygen flow rate was kept constant during the deposition, and the nitrogen flow rate and the pressure vere varied to control the nitrogen doping level and morphology of the films, respectively. The morphological, optical, structural, and photocatalytic properties of the films have been studied in order to investigate the competitive effect of the morphology, the chemical composition and the nitrogen state on the efficiency of the photocatalytic activity. Samples prepared at high pressure gave the best photocatalytic activity due to the high specific surface area and the optimal presence of TiO_xN_y crystals in the lattice.

By using the RSM (*Response Surface Methodology)* of the different responses, we achieved a good understanding of the complex processes involved in the sputtering deposition of the thin films especially the effect of the working pressure on the morphology, the structure and the photo-activity of the deposited coatings. The high photocatalytic activity under UV light was found to be due to the high specific surface area, and the introduction of discrete energy levels within the band gap.

Résumé

Le dopage à l'azote de TiO_2 est un moyen efficace pour améliorer l'activité photocatalytique sous rayonnement visible, due à l'excitation directe des électrons provenant des états N_{2p} générés dans la bande interdite. Toutefois le TiO_2 dopéazote n'est pas toujours efficace pour l'activité photocatalytique sous UV. Dans ce travail, nous avons préparé différents films de TiO_2 dopé-N (TiO_xN_y) par pulvérisation cathodique en introduisant simultanément O_2 et N_2 dans l'enceinte. Un plan d'expériences à deux variables, débit d'azote et pression de travail, a été effectué en fixant le débit d'oxygène. Les propriétés morphologiques, optiques, structurelles et photocatalytiques des différentes couches ont été analysées afin d'étudier l'effet compétitif de la morphologie et du taux d'azote sur les couches déposées. Les échantillons préparés à haute pression ont donné la meilleure activité photocatalytique grace à la grande surface spécifique et la présence optimales de cristaux de TiO_xN_y.

En étudiant les Surfaces de Réponse, nous avons obtenu des éléments de compréhension des processus complexes impliqués dans le dépôt des couches minces de TiO_2 dopées azote par pulvérisation, en particulier l'effet de la pression de dépôt sur la morphologie du film déposé, sa structure et ses activités photo-induites. L'amélioration de l'activité photocatalytique sous UV est liée à l'augmentation de la surface spécifique et à l'introduction de niveaux d'énergie dans la bande interdite.

III-1) Introduction

TiO_2 has shown extensive utilization in photocatalysts, dye-sensitized solar cells and smart-surface technologies. However, its use is limited to UV activation, due to its large band gap energy and relatively short electron-hole pair lifetime. Many attempts have been made to address these two issues with varying success [1]. The primary efforts in extending the absorption range in TiO_2 from the UV range to the visible spectrum have focused on doping with non-metals. The band gap energy of TiO_2 could be narrowed by an anion doping due to the mixing of the p states of doped anions (N, S, C) with the O_{2p} states of TiO_2, that could shift the resulted valence band edge upwards [2-3]. Asahi et al. established that nitrogen doping in TiO_2 should be the most effective method to improve visible light photoactivity, due to the small ionic radius of nitrogen (6% higher than that of oxygen) and optimal electronic band positions [2].

The efficiency of doped TiO_2 under visible light strongly depends on the preparation method used. In some cases, such doped photocatalysts showed no activity under visible light [4] and/or lower activity in the UV spectral range compared to the non-doped TiO_2 [4-5]. This may be because of the increase in the carrier recombination rates upon doping [4]. In non-metal doped TiO_2 photocatalysts, the main problem is that the photocatalytic activity under visible light is much lower than that under ultraviolet light [4][6]. Therefore, the development of new and optimized photocatalysts exhibiting visible light activity and improved charge carrier dynamics are necessary.

The study of the individual processing parameters affecting photocatalytic activity is quite complicated due to the abundance of physical and chemical processes that take place, as well as the several parameters in sputtering controls. The response surface methodology, RSM, based on design of experiment is one way to simplify complex processes since it allows multiple physical characteristics to be compared simultaneously. The resolution of the empirical polynomial equation that determines the RSM can be used to understand and predict the optimization of the photocatalytic activity of N-doped TiO_2 by comparing the material properties with the process parameters and functional activity. In this work, we used a Doehlert design to investigate the effect of RF sputtering deposition parameters on the morphological, structural, and optical properties of N-doped TiO_2 thin films with various nitrogen concentrations, and how they affect the UV light photocatalysis of NMP as well as the electrochemical photocurrent under UV and visible light.

This chapter will deal with the traditional method to prepare nitrogen doped TiO_2 by RF reactive sputtering using Ti target and dual reactive gas (oxygen and nitrogen**).** *More particularly, we developed a new study to understand the synergic effect of the deposition pressure and nitrogen flow rate on the physical properties and photoactivity of the deposited films.* Nitrogen doped TiO_2 films were prepared at different deposition pressures, and with different concentrations of nitrogen. The resulting films show a large variance in their optical, morphological, and photoactive properties with significant improvements of the photoactivity observed under UV light irradiation.

III-2) Experimental strategy

We used oxygen and nitrogen as dual reactive gas in the sputtering reactor, to prepare N doped TiO_2 thin films on different substrates, and we worked under different working pressures. In this chapter, the oxygen flow rate was fixed whereas the nitrogen one was variable. Consequently, the ***total reactive gas flow rates was not constant during all experiments*** *(Table III-1).*

***<u>Remark</u>**: in chapter 4, the nitrogen to oxygen ratio was changed while keeping the total reactive gas flow rate constant.*

III-2-1) Design of experiments

For this study, we used the Doehlert design with 2 factors (N_2 flow rate and pressure). The software NEMRODW (2000-D version) has been used to calculate the empirical model for each response. In order to achieve the desired set of data, we used a Doehlert design with 7 experiments [7-8] and 2 more experiments to validate the empirical model. We estimated the optimized conditions by the Response Surface Methodology, **RSM**, based on a second order model. The selected samples for this study are presented in Table III-1.

III-2-2) Thin films preparation

The pure and N-doped TiO_2 thin films were prepared by an RF reactive magnetron sputtering system. A metallic Ti target (50 mm diameter, purity = 99.95%), was sputtered in a reactive gas atmosphere containing Ar, O_2 and N_2. The substrates used were stainless steel, Si (100) wafers, ITO coated glass and ordinary microscope glass slides. Prior to deposition, the non metallic substrates were ultrasonically cleaned with acetone, ethyl alcohol and then de-ionized water for 20 minutes each.

Table III-1: Samples from the Doehlert design (samples 7 and 8 are repeated). X1 and X2 are respectively the reduced coordinate of N_2 and pressure.

N°	Sample ID	O_2 (sccm)	Rf (W)	N_2 [X1] (sccm)	X1	Pr [X2] (mTorr)	X2
1	N0.15 Pr 9 mtorr	1.5	200	0.15	+1	9	0
2	N0.00 Pr 9 mtorr	1.5	200	0	-1	9	0
3	N0.11 Pr 14 mtorr	1.5	200	0.11	+0.5	14	+0.87
4	N0.04 Pr 4 mtorr	1.5	200	0.04	-0.5	4	-0.87
5	N0.11 Pr 4 mtorr	1.5	200	0.11	+0.5	4	-0.87
6	N0.04 Pr 14 mtorr	1.5	200	0.04	-0.5	14	+0.87
7	N0.08 Pr 9 mtorr	1.5	200	0.08	0	9	0
8	N0.08 Pr 9 mtorr	1.5	200	0.08	0	9	0
9	N0.15 Pr 4 mtorr	1.5	200	0.15	+1	4	-0.87

The RF power of the cathode was 200 W (V_{bias}=148±5 V) during all the depositions. The substrate holder was maintained at 300°C. The distance between the substrate holder and the target was fixed at 100 mm. The initial base pressure was between 3 to $7x10^{-6}$ torr, while the total working pressure was varied between 3 to 14 mtorr by cintrolling the pumping speed with the gate valve. The gas flow rates were defined as follow: O_2 : 1.5 sccm (fixed), N_2: 0 to 0.15 sccm and Ar : 30 sccm.

In Table III-1, the TiO_xN_y films are labelled as follows: the nitrogen flow rate (sccm) with the working pressure (mTorr).

III-2-3) Contact angle measurement

Contact angle measurements (Sessile drop) were performed by using deionized water with a volume of 6 µl . Initial tests were performed for each sample without any light irradiation and the contact angle variation was studied over two months. Further tests were conducted for different intervals of illumination with Halogen and UV lamps. A set of three 6 µl droplets were used for each surface, and the average contact angle over time was measured and averaged.

III-2-4) Film structure and morphology

The crystal structure of thin films was characterized by X-ray diffraction (XRD) (X’Pert Pro PW3040-Pro, Panalytical Inc.) using a Cu Kα1 (λ = 1.5418 Å) X-ray radiation source in Bragg-Brentano (θ-2θ) configuration. The average crystallite size was determined by means of standard θ-2θ XRD scans using the *Scherrer Formula*. X’Pert High Score pattern processing was used to collect and process the data. The Raman spectra were recorded in a backscattering geometry using a Renishaw InVia Raman-microscope system and the 633 nm excitation wavelength of a red laser, focused on a spot size of the order of 3µm. Film morphology and thickness were measured by SEM-FEG.

III-2-5) Optical properties and Photo current measurements

Optical measurements (Transmittance and Reflectance) were carried out by a UV-vis spectrophotometer (Varian 6000). The setup of photo-electrochemical measurements is presented in (Fig.III-1). Photo-electrochemical measurements were studied with a potentiostat (Solatron). The reference and counter electrodes used during the PEC measurements were an Ag/AgCl electrode (CHI Instruments/saturated KCl) and a mesh Pt electrode, respectively. Electrochemical cell was filled with an electrolyte of Na_2SO_4, 1 M, (Merk). 125 W white lamp (PHILIPS) has been used to irradiate the samples for the photocurrent measurement and a UV filter has been used to cut off all the UV irradiations in the case of visible light measurements.

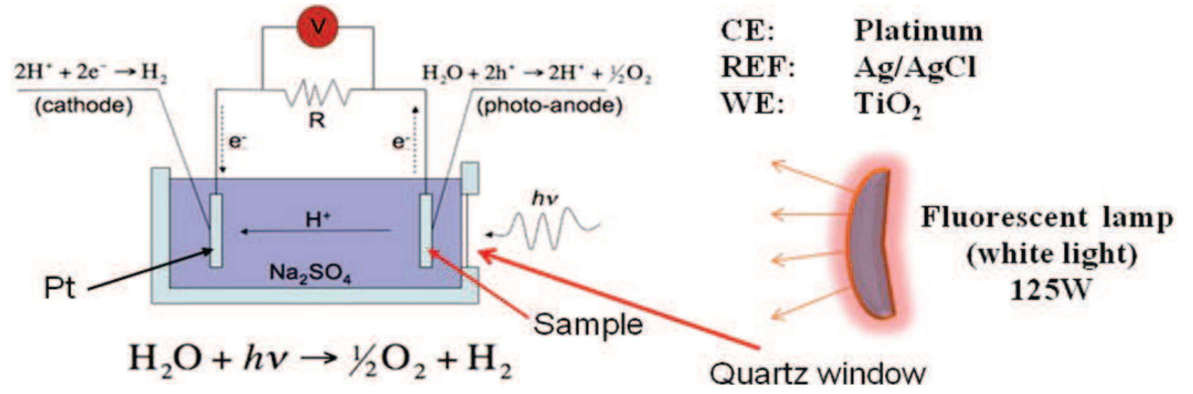

Fig.III-1: Setup for the Photocurrent measurement

III-2-6) Photocatalytic activity

Photocatalytic measurements were realized in collaboration with the *Chemistry and Chemical Engineering Research Center of Iran (Tehran) under* Egide program (GUNDISHAPUR). The photocatalytic activity of the TiO_2 films was evaluated using aqueous solution of NMP (99%, Merck) with an initial concentration of 10 mg/L at room temperature. The treated solution volume is 50 mL. The pH of the solution is adjusted to 3.0 using $HClO_4$ (Sigma-Aldrich, ACS reagent, ≥69% (T)).

Fig.III-2 shows the schematic diagram of the experimental setup. The photocatalytic reactor is a Teflon cylinder unit with an inner diameter of 90 mm. The solution was fed in the reactor by a peristaltic pump (Masterflux, model 7553-75) with a flow rate of 5.2 mL/s. The TiO_2 thin film sample immobilized on a stainless steel plate are placed at the bottom of the reactor. The dimension of each sample was about 50 by 49 mm. The UV source, a 11W UV lamp (Philips TUV low pressure Hg lamp, monochromatic at 254 nm), was placed at a height of 38.7 mm from the bottom of the reactor. The average irradiation intensity inside the reactor measured by using a photodiode (HAMAMATSU model S2281) at a distance of 2.7 cm from the lamp was 28.5 W/m^2. After starting irradiation by the UV lamp, 0.5 ml of the solution was taken every 10 min from a sample port.

The concentration of NMP in the samples was analyzed using High Pressure Liquid Chromatography (HPLC, Shimadzu, Lab solutions) with isocratic elution (3-10% acetonitrile, 97-90% water, flowrate: 1 $ml.min^{-1}$) on a reversed–phase Nucleosil C_{18} column. The detection wavelength was 214 nm.

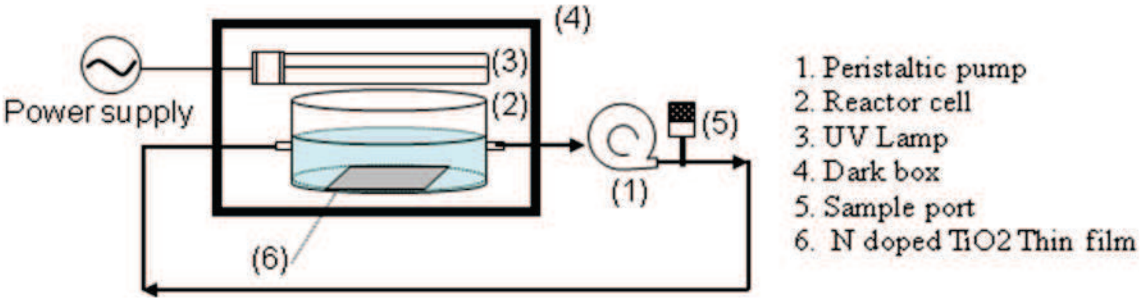

Fig.III-2: Schematic of experimental setup used in the measurement of the photocatalytic activity of different N doped TiO_2 thin films, based on NMP degradation.

III-3) Results and discussion

III-3-1) Evolution of the surface hydrophilicity

Fresh samples (just after deposition) were generally hydrophilic those prepared at very low pressure were even super hydrophilic having contact angle less than 5°. Depending on the deposition parameters, the samples displayed two different behaviours. Fig.III-3 (a) shows the contact angle (CA) variation of two types of samples prepared at high pressure and low pressure. During the storage of the samples under dark conditions, the CA of the low pressure sample increased dramatically from super hydrophilic (< 5°) to 50°. The CA of the high pressure sample was almost stable around 30°. These results are in agreement with literature [9], especially the model proposed by Wang et al. [10] which reported the photo induced change in contact angle of water to be due to the adsorption of hydrocarbon contamination on the surface of the thin film.

Fig.III-3 (b) shows the CA variation after different intervals of illumination with a Halogen or a UV lamp. Under UV irradiation, there is an induction time of about 30 min before the CA decreased, whereas for visible light, this induction time ranges from 60 to 90 min and depends on the deposition pressure. One can also note that under UV irradiation, both samples become super hydrophilic regardless of the deposition pressure. The enhancement of wettability, under irradiation, is due to two phenomena. The first one, is the electron-hole pairs photo-generation under light irradiation, and the degradation of adsorbed hydrocarbons on the TiO_2 surface through the generation of $OH^{\bullet}$ radicals. The second one, is the photo-oxidation (dissociation) of the water droplet, that leads to a larger wettability of the surface.

The response surface of the wettability is shown on figure III-3 (c) as a function of the pressure and of N_2 flow rate. One can identify the region for minimum contact angle. It appears that the N_2 flow rate has less impact on the film wettability as compared to the deposition pressure. This interesting result should be taken into consideration in this chapter but also in the next three chapters.

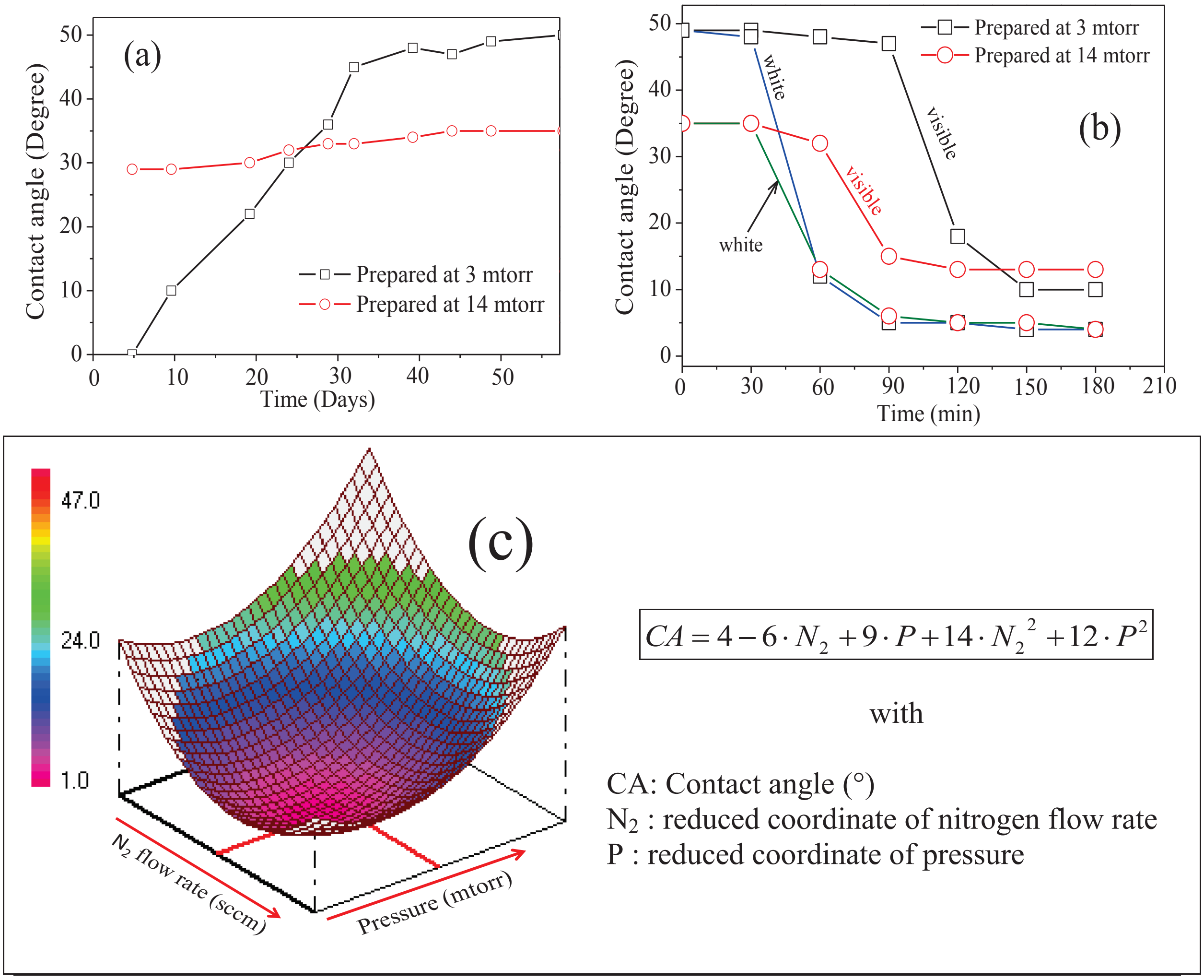

Fig.III-3: (a) Evolution of the contact angle over 2 months during storage in dark conditions, (b) Evolution of the contact angle under visible and UV light irradiation, and (c) Response Surface of the film wettability vs pressure and nitrogen flow rate and corresponding second order equation.

III-3-2) Effect of the deposition pressure on the film porosity and deposition rate

The microstructure of TiO_2 layers has a pronounced effect on the photocatalytic activity. When the pore size is too small the photoactive surface is only the top surface. The sputtering process is able to grow column-like grain structures, and the spacing between columns can be controlled by the sputtering pressure [11]. Fig.III-4 (a) and (b) show the SEM-FEG images of 2 thin films deposited at high (14 mTorr) and low (4 mTorr) pressures, respectively with nitrogen flow rate of 0.04 sccm. Using an image processing software (Visilog 6.7, NOESIS) one can estimate the void fractions respectively equal to 1% and 6% for the low and high pressure sample.

Fig.III-5 shows the RS for the film thickness of TiO_2:N films as a function of deposition pressure and nitrogen flow rate. Since the deposition time was fixed to 5 hr, one can conclude that the deposition rate ranges from 0.3 to1.6 nm/min (in these deposition conditions). The deposition rate decreases quickly with the pressure which is expected due to the decrease of plasma temperature and the auto bias voltage of the target as the deposition pressure increases (see paragraph II-6). But it appears that the nitrogen flow rate has a low impact (a slight decrease) on the deposition rate.

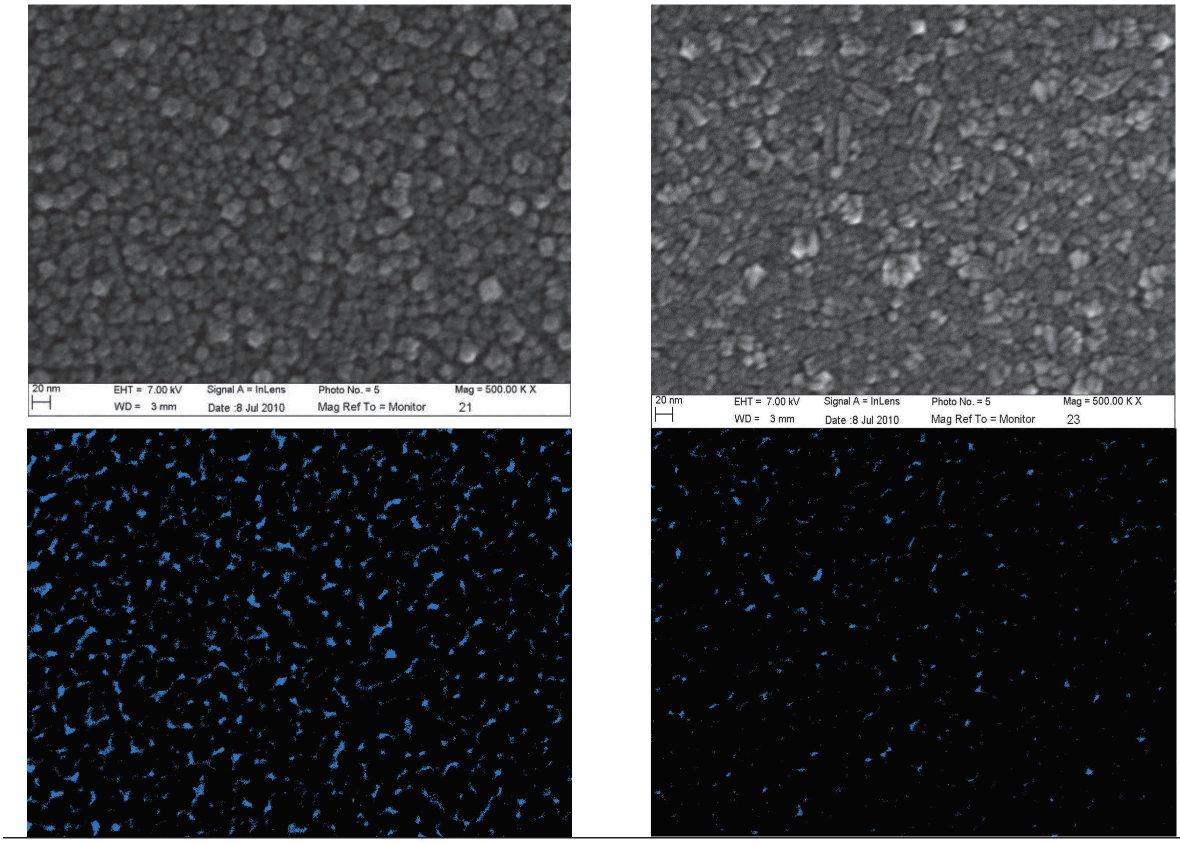

Fig.III-4: SEM-FEG images of N0.04 Pr14 (a) N0.04 Pr 4 (b) and corresponding image treatments showing only the porosities (c) and (d).

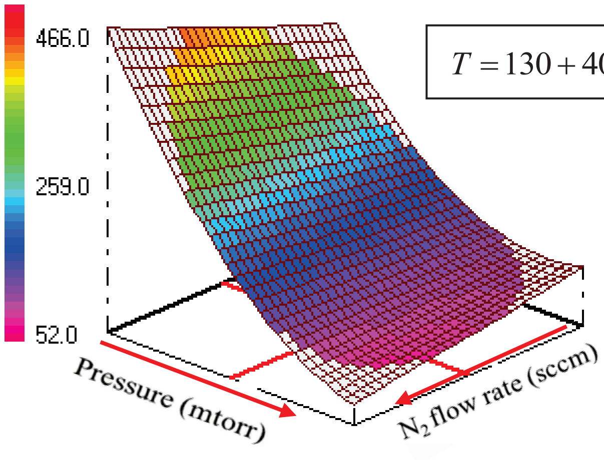

$$T = 130 + 40 \cdot N_2 - 120 \cdot P + 60 \cdot N_2^{\;2} + 130 \cdot P^2 + 35 \cdot P \cdot N_2$$

with

T: thickness (nm)

N_2 : reduced coordinate of nitrogen flow rate

P : reduced coordinate of pressure

Fig.III-5: Surface response of the thickness of N doped TiO_2 thin films. Oxygen flow rate was fixed to 1.5 sccm.

III-3-3) XRD spectroscopy and crystal size

The crystalline phase of TiO_2 remains one of the principal factors which determines the performance of the films; indeed it is well known that anatase is preferable to rutile for the photo-oxidation of organics [12].

X-ray diffraction results (*Fig.III-6*) show that anatase is the primary crystalline phase in the thin films. By changing the N_2 flow rate, a different $N_2:O_2$ reactive mixture ratio is achieved during the sputtering process, there is a slight decrease of the anatase phase. By increasing the sputtering pressure, the anatase peaks, especially (101) and (112), located at $2\theta = 25.4^o$ and $2\theta = 38.0^o$ respectively, become less intense and broader. This indicates that the crystal size and the refractive index are decreased [13]. At the same time, the (103) and (105) orientations of the anatase crystal, located at $2\theta = 37.1^o$ and 54.1^o respectively, disappeared as higher pressure depositions were used. The (105) anatase peak increased by increasing the nitrogen incorporation in the lattice. It is not surprising to see that the anatase (101) decreases rapidly by increasing the N_2 flow rate, since many authors reported a crystal modification when substituting nitrogen into the anatase TiO_2 crystal. The *wide peak* between $2\theta = 41^o$ and 44^o could be attributed to:

1) the presence of the sub stochiometric TiO_2 (TiO_x)

2) or the presence of oxy-nitride phases as TiO_xN_y [14-15].

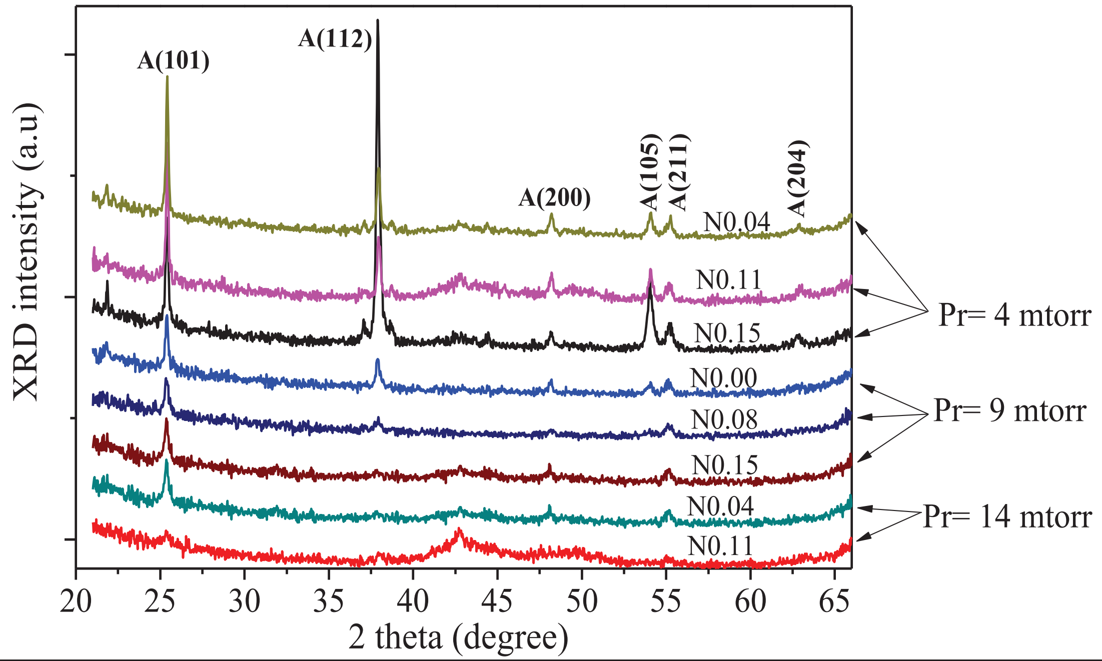

Fig.III-6: XRD data obtained from TiO_2 films prepared at different pressures (Pr) and N_2 flow rates (0.04 to 0.15 sccm).

In the next chapter, XPS measurements will show that the most probable reason for this *wide peak* is the formation of TiO_x (percentage of atomic nitrogen was less than 0.1% in these films). The aveerage crystal size in each film was calculated from the anatase (101) peak using the Scherrer formula,

$$d = \frac{K\lambda}{\beta\cos(\theta)} \qquad \text{Eq.III-1}$$

where d is the crystal size in nm, K is a constant called shape factor (typically equal to 0.9), λ is the apparatus wavelength (λ=0.154 nm), β is the full width at half maximum (FWHM), and θ is the diffraction angle.

The response surface of the crystal size versus both pressure and N_2 flow rate is shown on *Fig.III-7*. One can conclude that the crystal size decreases, from about 45 to 10 nm, by increasing either the N_2 flow rate and/or the deposition pressure. In the literature, Zeman et al. [16] and Eufinger et al. [13] reported the same effect concerning the pressure, but in this study a strong interaction between N_2 and pressure was evidenced which was not reported before.

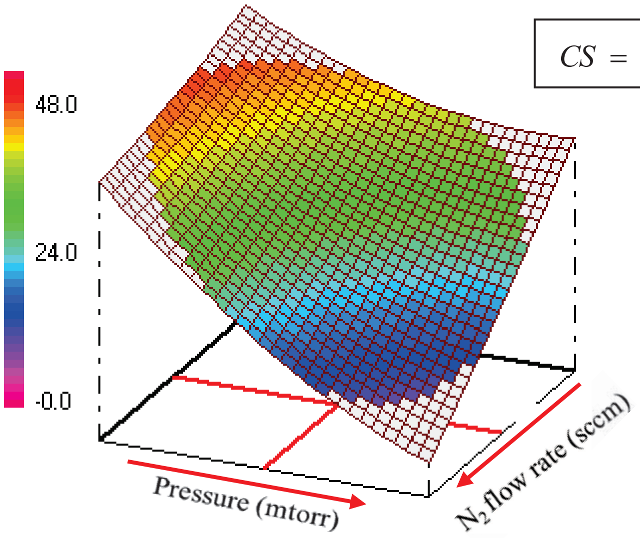

$$CS = 25 - 11 \cdot N_2 - 13 \cdot P + 3 \cdot N_2{}^2 + 2 \cdot P^2 - 8 \cdot P \cdot N_2$$

with

CS: Crystal size (nm)
N_2 : reduced coordinate of nitrogen flow rate
P : reduced coordinate of pressure

Fig.III-7: Surface response of the crystal size versus pressure and nitrogen flow rate

III-3-4) Raman spectroscopy

Raman spectroscopic analysis can provide useful information on the Ti–O bond lengths from the stretching wave numbers which is related to the force constants and lengths of the bonding [17-18]. The Raman shift spectra of some thin films are shown in *Fig.III-8*. All the samples show the typical Raman shift spectra of anatase TiO_2 [19-20], i.e. the main peak at 144 cm^{-1} (E_g, O–Ti–O bending mode) and others at 198 cm^{-1} (B_{1g}/A_{1g}), 398 cm^{-1} (B_{1g}), and 640 cm^{-1} (E_g, Ti–O bond stretching mode). In addition to the optical band modes found by this method, no phonon line shifts were observed.

There is no red shift in the E_g peak at 640 cm^{-1} (stretching vibration) when comparing the pure TiO_2 sample to any of the doped samples. This observation suggests that nitrogen is not incorporated interstitially in the TiO_2 lattice, so the Ti—O bond length is not affected by this doping. The latter will be confirmed by XPS measurements in the next chapter (cf paragraph IV-3-3).

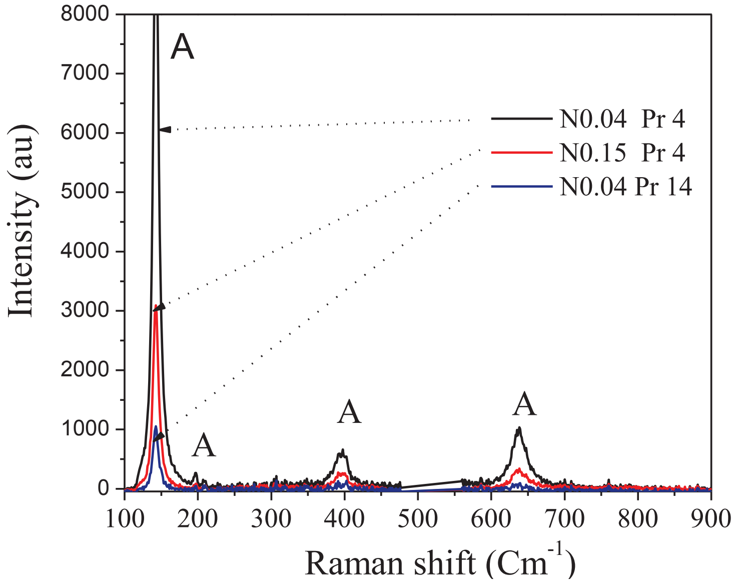

Fig.III-8: Raman spectra of N doped TiO_2 deposited on silicon wafer deposited at N_2=0.04 sccm / 4 mtorr (black), N_2=0.15 sccm / 4 mtorr (red), and N_2=0.04 sccm / 14 mtorr (blue).

III-3-5) Band Gap Calculation

The optical properties of the samples were studied by measuring the transmission and reflectance spectras in the UV-Visible range (210 to 1010 nm). The band gap values were calculated by the Tauc's equation using an indirect allowed transitions (m=2) [21-22],

$$A = \alpha d = \ln\left(\frac{(1-R)^2}{2T} + \left(\frac{(1-R)^4}{4T^2}\right)^{1/2}\right) \qquad \text{Eq.III-2}$$

$$\alpha h\nu = B(h\nu - E_g)^m \qquad \text{Eq.III-3}$$

where A is the absorbance, α is the absorption coefficient, d is the thickness of the sample, R and T are the reflection and transmission spectra, B is a constant called the edge width parameter, $h\upsilon$ is the photon energy, E_g is the optical band gap, and m is a constant which is determined by the optical transition, either direct (m = ½) or indirect (m = 2). The optical band gap is obtained from the extrapolation of the linear plots of $(\alpha h\upsilon)^{1/2}$ vs $h\upsilon$ at the intercept with the $h\upsilon$ axis. The response surface of the band gap is shown in *Fig.III-9*.

The calculated band gap values were estimated between 2.90 and 3.43 eV for the N-doped TiO_2 samples (Theoretical E_g for TiO_2 = 3.2 eV). These variations can be explained by the different nitrogen concentrations in the lattice, as well as by the presence of oxygen vacancies.

Interestingly, the conditions corresponding to the minimum band gap are in the same intervals that display higher hydrophilicity seen in Fig.III-3 (c). This is an interesting correlation, which suggests that the introduction of the intermediate nitrogen energy levels within the band gap can have a substantial effect on the surface active sites of the material, which in turn affect its wettability.

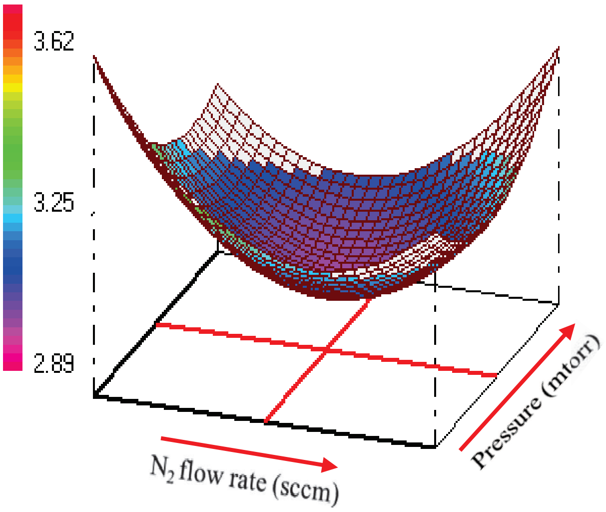

$$E_g = 2.98 - 0.1 \cdot P + 0.24 \cdot N_2^{\,2} + 0.16 \cdot P^2 + 0.12 \cdot P \cdot N_2$$

with

E_g: Band gap (eV)

N_2 : reduced coordinate of nitrogen flow rate

P : reduced coordinate of pressure

Fig.III-9: Modelling of the band gap calculated from the UV-Vis absorption spectra of glass coated by N doped TiO_2.

III-3-6) Analyzing the photo-activity and Optimization of the Sputtering Process

The photo activity of TiO_2 depends on a variety of parameters including the TiO_2 crystalline structure, crystal/particle size, surface morphology and the concentration/nature of the doping element.

In this part, we selected the N-Methyl-2-pyrrolidone (NMP), an industrial pollutant that is found in waste water, and its concentration can be easily controlled by HPLC. Fig.III-10 shows the NMP degradation with different photocatalytic coatings under UV irradiation. It is important to note that the pure TiO_2 has an intermediate effect compared to the other doped samples. This means that in some sputtering conditions, N-doped TiO_2 can enhance the photocatalytic activity under UV irradiation compared to pure TiO_2, while other sputtering conditions can have a negative effect on the photocatalytic reactions under UV illumination. This can reasonably explain the contradictions found in literature about the efficiency of nitrogen doping under UV illumination (see introduction).

The response surface of the time for the complete degradation of NMP is shown in Fig.III- 11 (a). One can distinguish two directions for the minimum NMP degradation time (optimum conditions). The first one, conditions corresponding to higher pressure and lower nitrogen incorporation, which lead to the deposition of porous and thinner films characterized by high active surface sites. The second one, conditions corresponding to lower deposition pressure and higher nitrogen flow rate which lead to the formation of thick films with good photocatalytic activities. At intermediate nitrogen doping and pressure, the mechanism is more complicated

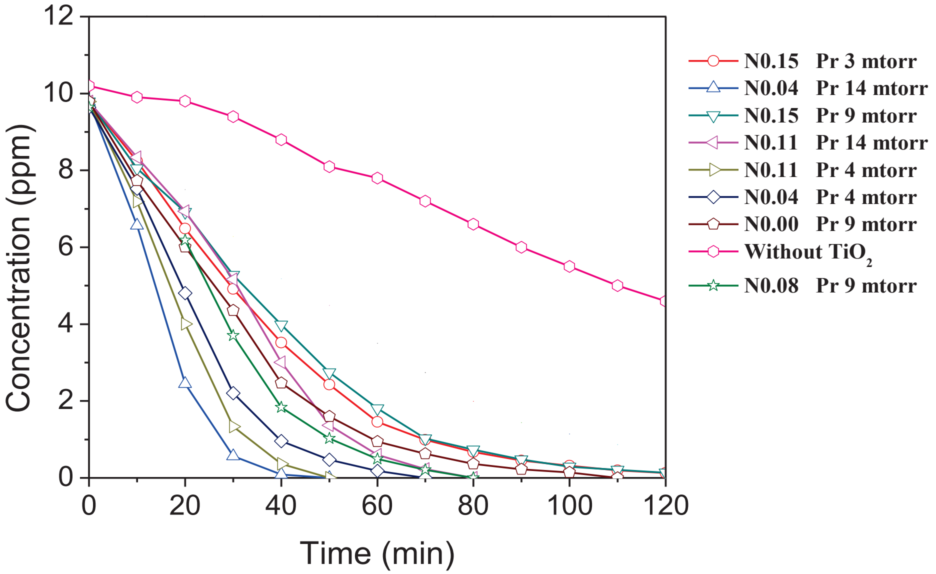

Fig.III-10: NMP degradation time with different deposited TiO_2 samples

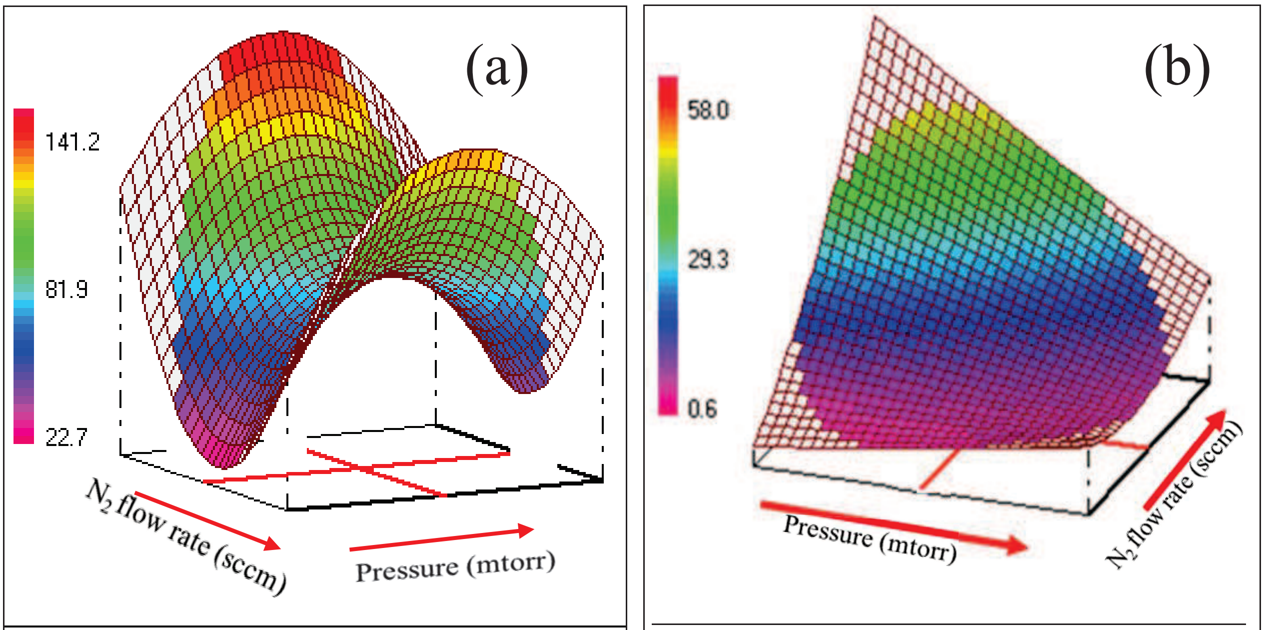

$$Time_{PCA} = 75.97 + 9.94 \cdot N_2 - 50.5 \cdot P + 52.79 \cdot N_2^2 - 44.13 \cdot P^2 + 8.04 \cdot P \cdot N_2$$

$$I_{pc} = 9.96 + 22.13 \cdot N_2 + 3.29 \cdot P + 9.78 \cdot N_2^2 + 33.34 \cdot P^2 + 34.22 \cdot P \cdot N_2$$

Fig.III-11: Modelling of (a) NMP degradation time ($Time_{PCA}$) using the measured time up to total degradation and (b) photo-current generated (I_{pc}) at a bias of 0.5 V/(AgCl/Ag) in 1M Na_2SO_4, using the different samples

To investigate further the presence of these two optima we measured the electrochemical potentiodynamic sweep under white light irradiation (using AgCl/Ag as reference electrode in an electrolyte of Na_2SO_4 1M, pH 7). We measured the generated photocurrent at a bias of 0.5 V/ref. The RSM of the modulated photocurrent at 0.5 V/ref is presented in Fig.III-11 (b). This last plot has only one optimum (maximum photocurrent at

0.5V/ref) at low pressure and high nitrogen flow rate, which is the same as that found in the RSM of photocatalytic activity. From the comparison of the two RSM representation of Fig.III-11 one can conclude that the limiting step for the photocatalytic activity is the charge separation, the charge transport (up to the interface with the pollutant) and the surface morphology of the doped TiO_2. So the porous material with higher developed surface gave a better photocatalytic activity even with less thickness.

III-5) Conclusion

Doping TiO_2 with nitrogen is an effective way to enhance visible light absorption and photoactivity. However, nitrogen doping can also significantly decrease UV photocatalytic activity. Using RF reactive sputtering as a deposition technique, we achieved different structures of N-doped TiO_2 (TiO_xN_y). There is competitive effect of the morphology, the crystalline orientation and the chemical composition on the efficiency of the photocatalytic activity. Samples prepared at high pressure can have an optimized photocatalytic activity, even with lower film thicknesses, but these samples generated very low photocurrents. However, samples prepared at lower pressure were more efficient for photocurrent generation.

The high photocatalytic activity under UV light was found to be due to the higher specific surface area, the optimal presence of anatase crystals in the lattice and the introduction of discrete energy levels within the band gap which lowered the apparent band gap energy.

Overall, this study showed a simple method to produce nitrogen doped TiO_2, which in turn showed increased visible light photoactivity, and improved pollutant degradation. These films showed different behaviors between the photo-electrochemical and the photocatalytic activities.

The use of the design of experiments (with the RSM studies) allowed us to find the optimal deposition conditions which maximize the photocatalytic efficiency of N-doped TiO_2 and other conditions to optimize the electrical and photo-electrochemical responses which can serve as a solid background for further investigations.

References

[1] F Han, V S R Kambala, M Srinivasan, D Rajarathnam, R Naidu, Review, *Applied Catalysis A: General*, **359** (2009) 25–40.

[2] R Asahi, T Morikawa, T Ohwaki, K Aoki, Y Taga, *Science*, **293** (2001) 269-271.

[3] S Khan, M Al-Shahry, W Ingler, *Science*, **297** (2002) 2243-2245.

[4] H Irie, Y Watanabe, K Hashimoto, *Journal of Physical Chemistry B*, **107** (2003) 5483-5486.

[5] B Liu, L Wen, X Zhao, *Solar Energy Materials & Solar Cells,* **92** (2008) 1–10.

[6] H Yu, X Zheng, Z Yin, F Tao, *Chinese Journal of Chemical Engeneering*, **15 (6)** (2007) 802-807.

[7] S Ferreira, W Santos, C Quintella, B Neto, J Bosque-Sendra, *Talanta*, **63** (2004) 1061-1067.

[8] M Bezerra, R Santelli, E Oliveira, L Villar, L Escaleira, *Talanta*, **76** (2008) 965-977.

[9] X Zhao, K Sakka, N Kihara, Y Takada, M Arita, M Masuda, *Microelectronics Journal*, **36** (2005) 549-551.

[10] C Wang, H Groenzin, M Shultz, *Langmuir*, **19 (18)** (2003) 7330-7334.

[11] I Nakamura, N Negishi, S Kutsuna, T Ihara, S Sugihara, K Takeuchi, *Journal of Molecular Catalysis* A: Chemical, **161** (1-2) (2000) 205-212.

[12] A Fujishima, X Zhang, D A Tryk, *Surface Science Reports*, **63** (2008) 515–582.

[13] K Eufinger, D Poelman, H Poelman, R De Gryse, G B Marin, *Journal of Physics D: Applied Physics***,** **40** (2007) 5232–5238.

[14] N Martin, R Sanjinés, J Takadoum, F Lévy, *Surface and Coatings Technology*, **142** (2001) 615-620.

[15] A Trenczek-Zajaca, M Radeckaa, K Zakrzewskab, A Brudnikb, E Kusiorb, *Journal of Power Sources*, **194** (2009) 93-103.

[16] P Zeman, S Takabayashi , *Thin Solid Films*, **433** (2003) 57–62

[17] M Kitano, M Matsuoka, M Ueshima, M Anpo, *Applied Catalysis A: General*, **325** (2007) 1-14.

[18] S Lee, I Cho, D K Lee, D W Kim, T H Noh, C H Kwak, S Park, K S Honga, J K Lee, H S Jung , *Journal of Photochemistry and Photobiology A: Chemistry*, **213** (2010) 129-135.

[19] W Kaiser, A Christensen, G Mullervogt, *Physical Review B*, **17** (3) (1978), 1095-1101.

[20] Z Zhang, J B.M- Goodall, D J Morgan, S Brown, R J.H Clark, J C Knowles, N J Mordan, J R.G Evans, A F Carley, M Bowker, J A Darr, *Journal of the European Ceramic Society*, **29** (2009) 2343-2353.

[21] A Salem, Y El-Gendy, G Sakr, W Soliman, *Journal of Physics D: Applied Physics*, **41** (2008) 025311.

[22] Y El-Gendy, *Journal of Physics D: Applied Physics*, **42** (2009) 115408.

[23] A Mills, J Wang, *Journal of Photochemistry and Photobiology A*, **127** (1999) 123-134.

Chapter IV

Effect of different nitrogen sites in dual gas sputtering configuration

Chapter IV

Effect of different nitrogen sites in dual gas sputtering configuration

Abstract

Different structures of N-doped TiO_2 (TiO_xN_y) have been prepared by reactive RF magnetron sputtering using dual reactive gas, oxygen and nitrogen, simultaneously in the deposition chamber. The morphological, optical, structural, and photocatalytic properties of the films have been studied in order to investigate the competitive effect of the morphology, the chemical composition and nitrogen state on the efficiency of the photo activity of the coatings. Samples prepared at high pressure gave the best photocatalytic activity due to the high specific surface area, the optimal presence of TiO_xN_y crystals in the lattice and the good charge separation thanks to the interstitial nitrogen sites. However, at low pressure, the formation of TiN crystals became most probable, especially at higher nitrogen doping, which acted as recombination centers for the photo-generated charge carriers that should reduce the photocatalytic activity. A good understanding of the complex processes involved in the deposition of the thin coatings by sputtering was achieved. In particularly the effect of deposition pressure on the the photo-activity of the deposited film, as well as the preferential presence of nitrogen sites in the lattice of doped titania was pointed out. Nitride (Ti—N) and substitutional nitrogen speciesappeared when the oxide was not stoichiometric. This suggested that the incorporation of these nitrogen species became favorable in partially reduced titanium oxide networks, conditions which were met when the sputtering deposition was carried out at very low pressure. Interstitial nitrogen sites were detected in N doped titania deposited at high pressure or when there were no oxygen deficiencies. The high photocatalytic activity under UV light was found to be due to the higher specific surface area, the introduction of discrete energy levels within the band gap and the presence of interstitial nitrogen in the lattice rather than the substitutional one. However, the post annealing process did not affect the photocatalytic activity but it improved the charge transfer and the photo-electrochemical response of the porous samples.

Résumé

Nous avons préparé différentes structures de TiO_2 dopé-N (TiO_xN_y) par pulvérisation cathodique en introduisant le couple de gaz réactifs O_2 et N_2 simultanément dans la chambre du dépôt. Les propriétés morphologiques, optiques, structurelles et photocatalytique des différentes couches ont été analysées afin d'étudier l'effet compétitif de la morphologie, la composition chimique et la position d'azote dans le réseau de TiO_2, sur l'efficacité de l'activité photo-catalytic. Les échantillons préparés à haute pression ont donné la meilleure activité photocatalytique grâce à leur grande surface spécifique, la présence optimales des cristaux TiO_xN_y et l'amélioration de la séparation de charge par la présence interstitielle d'azote. Cependant, à basse pression, nous avons dans les conditions d' un taux élevé de dopage d'azote, une grande probabilité de formation des cristaux TiN, qui pourraient agir comme centres de recombinaison des porteurs de charge photo-générés, ce qui devrait réduire l'activité photocatalytique. Nous avons apporté une meilleure compréhension des processus complexes impliqués dans le dépôt des couches minces de TiO_2 dopé azote par pulvérisation, en particulier l'effet de la pression du dépôt et le taux d'azote dans le gaz réactif sur les activités photo-induites ainsi que la présence préférentielle des différents sites d'azote dans le réseau de l'oxyde de titane. Les structures Ti—N apparaissent lorsque l'oxyde est nonstoechiométrique, ce qui suggère que l'incorporation d'azote substitutionnel devient favorable dans les réseaux d'oxyde de titane partiellement réduit en oxygène surtout quand le dépôt s'effectue à très basse pression. Nous avons détecté la présence interstitielle d'azote, dans le réseau de TiO_2 dopé, dans les couches à faible taux de déficits en oxygène surtout si le dépôt est réalisé à plus hautes pressions. L'amélioration de l'activité photocatalytique sous UV a été corrélée à l'augmentation de la surface spécifique, l'introduction de niveaux discrets d'énergie dans la bande interdite et la présence d'azote en positionnement interstitiels dans le réseau plutôt que en substitutionnel. Cependant, les résultats montrent que le processus de post recuit n'affecte pas l'activité photocatalytique, mais il améliore la structure, le transfert de charge et la réponse de photocourant des échantillons poreux.

IV-1) Introduction

Early studies on N-doping within TiO_2 suggested that the N-atoms hybridize with the valence band of the semiconductor, and this consequently results in a delocalization of the nitrogen valence electrons and resulted in an upward shift of the valence band maximum [1]. More recent works have disputed this claim and suggested the formation of localized N_{2p} states above the valence band of TiO_2. Density of state calculations has shown that substitutional N doping could exhibit one isolated impurity level just 0.14 eV above the valence band energy. However, interstitial N doping can also exhibit a localized impurity level at 0.73 eV higher than the valence band top [2]. In addition, interstitial NO and NO_2 doping have exhibited one or two isolated impurity levels in the middle of the band gap between the valence and conduction bands of TiO_2 [2-3] and these impurity levels could be hybridized with N_{2p} and O_{2p} states [4].

The results of nitrogen doped TiO_2 have yielded many contradictions. The Density of State DOS results (Asahi et al. for example) [5] suggest that the substitutional nitrogen doping is more effective than the interstitial one as well as the mixture of both substitution and interstitial due to the introduction of localized N_{2p} states just above the valance band which can mix with O_{2p} states (N—O bonding), allowing the absorption of visible light up to 500 nm. Sangwook Lee et al [3] found that interstitial N doping creates defects at levels deep within the band gap which disturb the charge transfer in the TiO_2 nanoparticles. However, other works found that interstitial N-doping is more effective, for photocatalytic applications, than substitutional doping [3][6]. Diwald et al. found that interstitial doping shows more photoactivity due to the suppressing photo-threshold in opposition of substitutional dopants [7-8]. Other results have been reported which show that a multi-type N doping (interstitial *and* substitutional) gives very good photocatalytic activity in the visible light [9]. Here, we continued the study of the traditional method to prepare nitrogen doped TiO_2 by RF reactive sputtering using Ti target and dual reactive gas (oxygen and nitrogen). *The effect of deposition pressure and nitrogen ratio, in the reactive gas inside the sputtering chamber, was investigated on the total doping level (N_{at} %) and the presence of the different sites of nitrogen within the N doped titania.* Nitrogen doped TiO_2 films were prepared at different deposition pressures, and with different concentrations of nitrogen, but by *keeping constant the flow rate of the total reactive gas* in the deposition chamber. The photo induced electrochemical and catalytic activities have been studied for all the deposited films and have been correlated with the physico-chemical properties. A complex synergy between interstitial and substitutional doping was also observed, having competitive effects on the overall performance of the films.

IV-2) Experimental strategy

IV-2-1) Thin films deposition

Oxygen and nitrogen were used as dual reactive gases in the sputtering reactor, to prepare N doped TiO_2 thin films on different substrates, and under different working pressures, Table *IV-1 shows the different conditions used*. The substrates used for the coatings were stainless steel, Si (100) wafers, ITO coated glass and ordinary microscope glass slides, the substrate holder was maintained at 300°C. The RF power of the cathode was 200 W (V_{bias}=148±5 V) for all thecoating conditions.

Table IV-1: Selected samples for the Dual gas nitrogen doping with fixed total reactive gas (for each pressure) using different ratios of nitrogen in the reactive gas flow rate {$N_2/(N_2+O_2)$}.

Sample ID	Working pressure	N_2 flow rate	O_2 flow rate	Film color
3 mtorr TiO_2	3 mtorr	0 sccm	2.0 sccm	Transparent
3 mtorr 15%	3 mtorr	0.3 sccm	1.7 sccm	Light brown
3 mtorr 25%	3 mtorr	0.5 sccm	1.5 sccm	Green brown
3 mtorr 30%	3 mtorr	0.6 sccm	1.4 sccm	Brown
3 mtorr 35%	3 mtorr	0.7 sccm	1.3 sccm	Black
7 mtorr TiO_2	7 mtorr	0 sccm	2.3 sccm	Transparent
7 mtorr 26%	7 mtorr	0.6 sccm	1.7 sccm	Light brown
7 mtorr 30%	7 mtorr	0.7 sccm	1.6 sccm	Brown
7 mtorr 35%	7 mtorr	0.8 sccm	1.5 sccm	Dark
7 mtorr 48%	7 mtorr	1.1 sccm	1.2 sccm	Black
14 mtorr TiO_2	14 mtorr	0 sccm	2.5 sccm	Transparent
14 mtorr 40%	14 mtorr	1.0 sccm	1.5 sccm	Light brown
14 mtorr 48%	14 mtorr	1.2 sccm	1.3 sccm	Green brown
14 mtorr 60%	14 mtorr	1.5 sccm	1.0 sccm	Brown

The deposition pressure in the chamber has been controlled by the argon flow rate using the maximum pumping speed, as discussed in chapter 2. Argon flow rate was fixed at 30, 70, and 140 sccm in order to deposit coatings at different pressures of p = 3, 7 and 14 mtorr, respectively. Different nitrogen to oxygen ratios were used depending on the working pressure. Using optical emission spectroscopy (OES), we observed the Ti emission lines at 517 and 521 nm, and controlled the TiO_2 deposition parameters in order to have a fixed intensity of the Ti/Ar peaks during the deposition period. The deposition rate was stabilized in the intermediate region between two stable sputtering modes, reactive and metallic. In order to achieve these optimal deposition conditions, the total reactive gas flow rate was fixed at 2.0, 2.3, 2.5 sccm for the samples deposited at 3 mtorr, 7 mtorr, and 14 mtorr, respectively.

IV-2-2) X-ray Photoelectron Spectroscopy

XPS analyses were performed at the university of SURREY (UK) on a Thetaprobe spectroscope (by Thermo Scientific / East Grinstead, U.K.). The source employed was Al Kα monochromated radiation at a power of 140 W.

All the other experimental conditions were the same as those mentioned in chapter 3.

IV-3) Results and discussion

For convenience, we will introduce the definition of the nitrogen ratio in the reactive gas, during sputtering deposition, for each sample to be the ratio of the nitrogen flow rate to the total flow rate of the reactive gases (oxygen and nitrogen). For example, when the nitrogen flow rate is 0.6 sccm, and the oxygen flow rate is 1.4 sccm, then according to the above definition the nitrogen ratio will be 30%, since nitrogen is 30% of the total reactive gas flow rate (2.0 sccm), as mentioned in Table IV-1.

IV-3-1) Film structure

IV-3-1-a) Case of pure TiO_2

Fig.Fig.IV-1 (a) presents the XRD scans for the non doped TiO_2 thin films deposited at three different pressures, 3 mtorr, 7 mtorr and 14 mtorr. Taking into account the ratio between the intensities of the peaks corresponding to the two different anatase orientations of titania i.e. (101) and (112), it is evident that at lower deposition pressure (3 mtorr), the TiO_2 is more crystallized in the preferential (101) orientation rather than the anatase (112), but the latter becomes the preferential orientation as the deposition pressure increases to 7 and 14 mtorr. On the other hand, there is a clear decrease in the anatase XRD intensity at the highest pressure studied (14 mtorr) This could be explained by two facts, (1) a decrease in the TiO_2 crystallinity at higher working pressures which is consistent with the conclusion of Zeman et al. [10], and/or (2) to the reduction in the crystal size (shrinking) when doing the sputtering at higher pressures. As shown in Fig.Fig.IV-1 (b), anatase crystal size increases as the deposition pressure increases from 3 mtorr to 7 mtorr, further increase in the deposition pressure induces a decrease in the crystal size.

Crystal size calculations confirmed also the preferential presence of anatase A(101) at low pressure (3mtorr) and anatase A(112) at high pressure (14 mtorr). However, at an intermediate deposition pressure (7mtorr) there is a competition between both phases accompanied with a general increase in the crystal size.

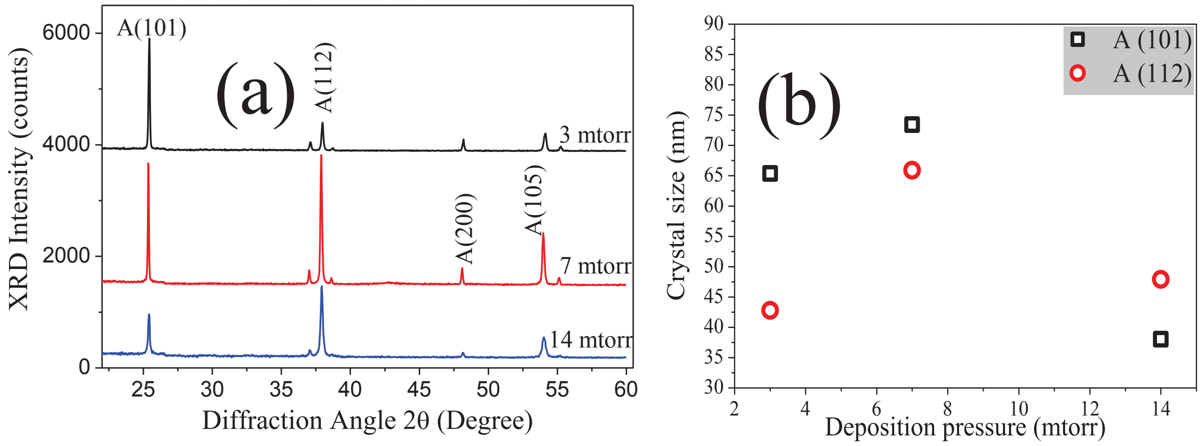

Fig.IV-1: (a) XRD scan of the pure TiO_2 thin films deposited at 3 mtorr (black), 7 mtorr (red), and 14 mtorr (blue).(b) Crystal size of anatase phase (101) and (112) vs deposition pressure, as calculated using Scherrer formula. Samples were post- annealed at 450°C for 1 hour after the deposition.

Comparing the diffraction peaks of A(101) and A(112) between samples deposited at different pressures (Fig.IV-2), a shift in the diffraction angle of both anatase phases of pure TiO_2 is clearly observed when the deposition pressure is changed. This shift could be due to the effect of the variation in the porosity of the films and/or lattice parameters of the resulting coatings deposited at different pressures. In fact, higher deposition pressure could induce some residual microstresses within the TiO_2 films resulting in other strains in the crystal lattice. But also, lowering the deposition pressure results in an increase of the kinetic energy of the TiO_2 particles and this also could induce other deformations in the crystal. On the other hand, microstresses could vary from point to point within the crystal lattice, altering the lattice spacing, broadening and shift in the diffraction peak [11]. Further measurements and calculations are required in order to validate and estimate the residual strains within TiO_2 [11-12].

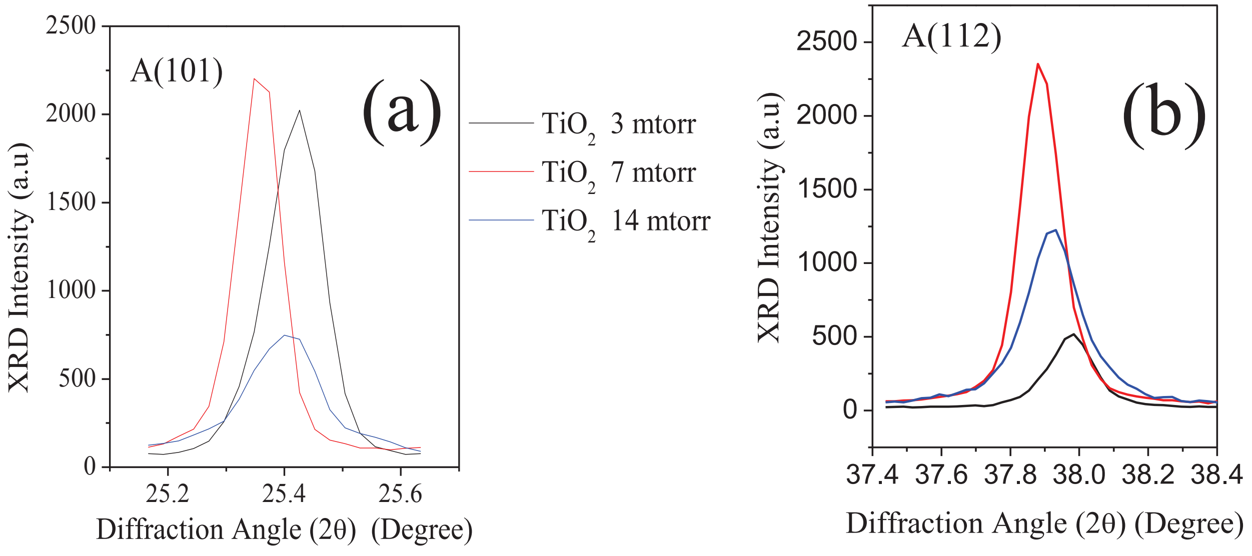

Fig.IV-2: (a) Shift of the XRD diffraction angle in the case of (a) anatase (101) and (b) anatase (112) for the pure TiO_2 thin films deposited at 3 mtorr (black), 7 mtorr (red), and 14 mtorr (blue).

IV-3-1-b) Case of N doped TiO2

The XRD scans for the annealed film prepared at 3 mtorr and 7 mtorr are shown in figures.IV-3 (a) and (b), respectively. These two series have similar trends, the low nitrogen ratio decreases the cristallinity of the anatase phase of TiO_2, but the high nitrogen ratio makes it easier for TiN to form, and the intermediary nitrogen ratios have a competition between the two phases.

Films fabricated at 3 mtorr with the nitrogen ratios of 25% (not presented) and 30% show very similar diffraction spectra. At 3 mtorr, films prepared with nitrogen ratio of 15%, 25%, and 30% all showed diffraction peaks at $2\theta = 25.4^{o}$, and $2\theta = 38^{o}$, corresponding to the (101) and (112) orientations of the anatase phase of TiO_2, respectively. To summarize, the coatings obtained at lower nitrogen ratio (15%) showed a preferred growth in the (101) direction of anatase, while the films deposited at 25% and 30% showed stronger preferred orientation in the (112) direction. The (112) peak may be partially attributed to an increase in nitrogen incorporation within the TiO_2 lattice. This result has never been reported in the literature concerning nitrogen doped TiO_2, and it will be further explored and discussed in the compositional analysis section, using XPS characterization to observe the concentration and nature of N doping in these films (paragraph IV-3-3). When the nitrogen ratio increases above 35% in the reactive gas, a significant destruction of the antase phase took place, with a predominance of the TiN crystals in the deposited films.

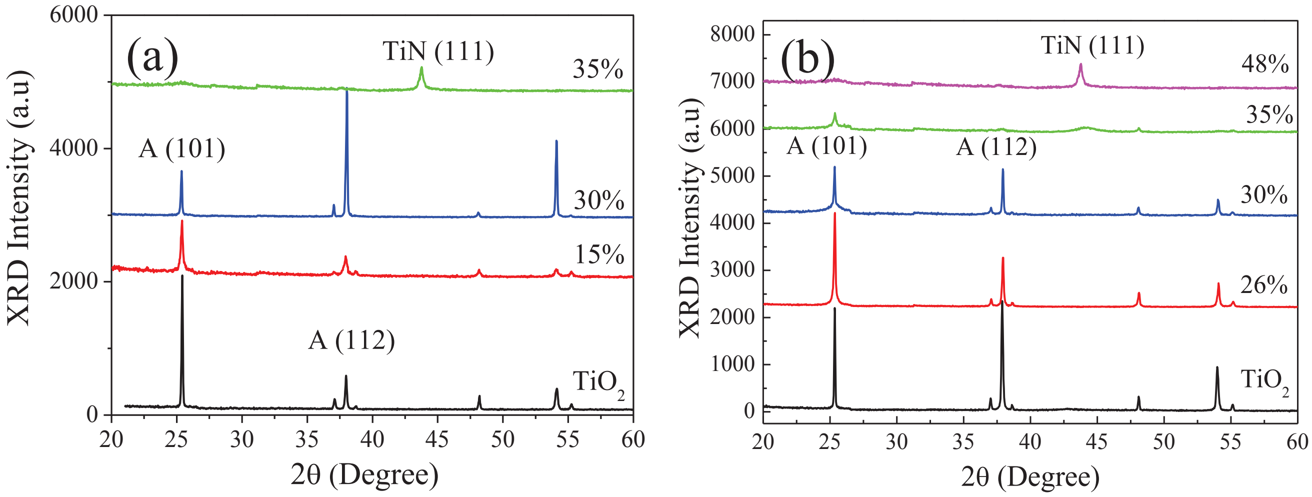

Fig.IV-3: XRD plot of the annealed films deposited at (a) 3 mtorr and (b) at 7 mtorr, with different nitrogen ratio. XRD scans corresponding to pure TiO_2 have been added as reference.

The films deposited at 7 mtorr also showed a difference in their XRD scans as we increased the nitrogen ratio. All of the films deposited with a nitrogen ratio up to 30% showed diffraction peaks at $2\theta = 25.4^{o}$, and $2\theta = 38^{o}$, corresponding to the (101) and (112) orientations of the anatase phase of TiO_2, respectively. Again, as the nitrogen ratio increased, a competition between the (101) and the (112) orientations took place, which may indicate an increase in the nitrogen incorporation into the films. A clear destruction of the anatase phase could be detected when nitrogen ratio reached to 35% in the reactive gas but with no predominance of any TiN phases (unlike samples deposited at 3 mtorr). However, the film deposited at a nitrogen ratio of 48% has a clear peak corresponding to TiN (111) at $2\theta = 43.6^o$ with no anatase diffraction peaks, reflecting a predominance of the TiN crystals rather than titania or titanium oxynitrides in the structure of the coatings.

A different behavior has been observed with the films deposited at 14 mtorr (Fig.IV-4). The pure TiO_2 film showed anatase characteristics, with a high peak intensity found at $2\theta = 38^o$, indicating a preferred orientation in the (112) direction. The introduction of nitrogen did not quench the growth of the anatase crystals of TiO_2. As the nitrogen ratio increased up to 48%, the coating still showed strong anatase characteristics, with dominant peaks found at $2\theta = 38°$, corresponding to the (112) orientations of the anatase phase. Then, when the nitrogen ratio was further increased (60%), we found a surprising increase in the diffraction peak intensity at $2\theta = 25.4^o$ corresponding to a preferential growth in the (101) orientations of the anatase phase rather than the (112) one. That means, there is a change in the nitrogen incorporation sites when the nitrogen ratio increased from 48% to 60%. This result will be analyzed later and correlated with the presence of different nitrogen sites in the doped TiO_2 lattice. (see section IV-3-3).

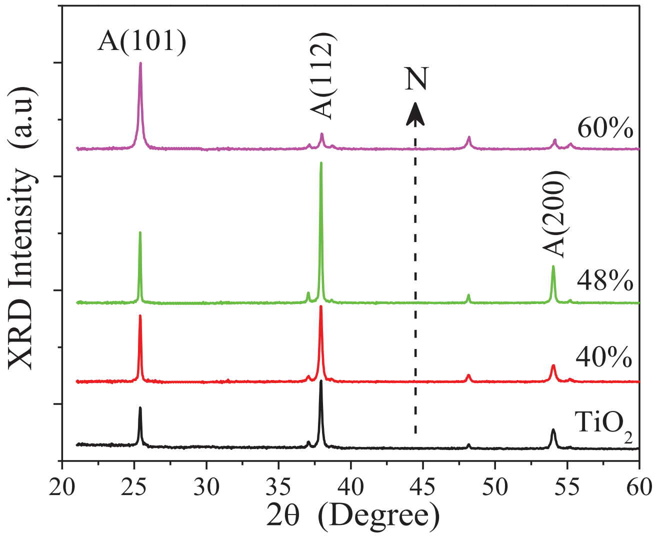

Fig.IV-4 : XRD plot of the annealed films deposited at 14 mtorr with different nitrogen ratios in the reactive gas as well as that of pure TiO_2. Note here that there is no diffraction peaks corresponding to TiN crystals.

We note also that, in all films deposited at 14 mtorr, there is no diffraction peaks corresponding to any TiN structures, which is not the case in samples prepared at lower pressures. The average crystal size was also investigated by using the Scherrer formula Eq.III-1 (chapter 3), not presented here. The overall trend for the samples was similar, showing larger crystal sizes at lower nitrogen ratios, which then decreased as the nitrogen ratio increased for all deposition pressures.

IV-3-2) Film morphology

Fig.IV-5 presents the SEM images of the TiO_2 samples prepared at deposition pressures of 3 mtorr, 7 mtorr and 14 mtorr. The thickness of the films was estimated by the SEM images to be 465 nm, 435 nm, and 460 nm for the films deposited at 3 mtorr, 7 mtorr, and 14 mtorr, respectively. It was observed that the surface roughness drastically increased as the deposition pressure increased. Films deposited at 3 mtorr revealed a relatively smooth surface. For the film deposited at 7 mtorr, the surface roughness increased significantly, with a beginning of a columnar structure with columns which start to be separated. This phenomenon is clearly seen at 14mtorr where the film revealed a columnar structure, with the surface porosity continuing from the film surface throughout the bulk of the coating.

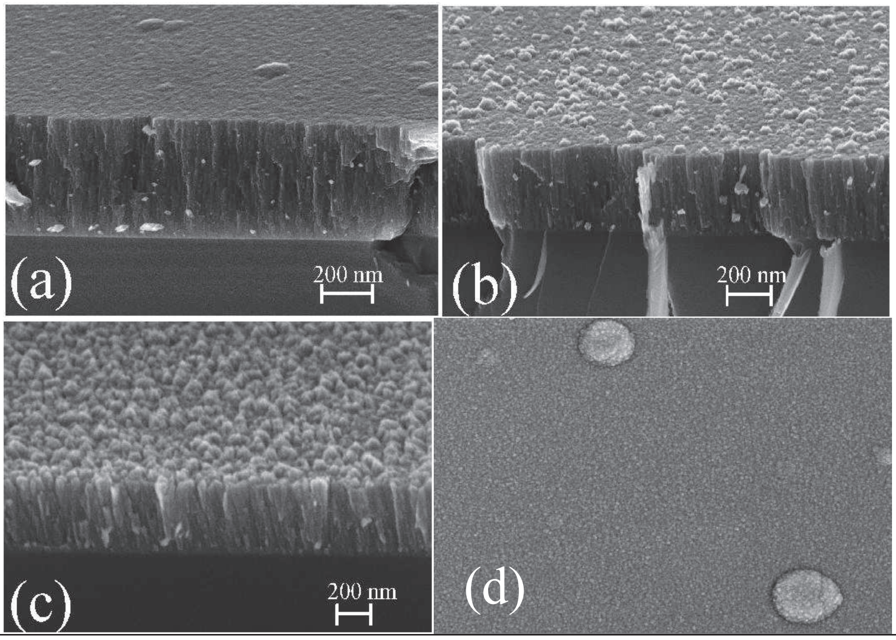

Fig.IV-5: SEM-FEG images of TiO_2 grown at three different pressures (a) 3 mtorr, (b) 7 mtorr, (c) 14 mtorr and (d) example of sample having nanoparticules on the surface.

In addition to the increased porosity, the formation of clusters on the surface of the films was observed beginning from 7 mtorr, and more pronounced at 14mtorr. The clusters were a result of the increased deposition pressure, which can create medium size clusters (about 150 nm) within the plasma phase, and were then subsequently deposited on the surface of the coatings. These clusters should contribute to the formation of a higher specific area of the developed surface. The increase of the porosity of the films by increasing the deposition pressure can be explained by the fact that the kinetic energy of the sputtered particles decreased at higher pressure, and therefore the particles reaching the surface should have less energy, less horizontal mobility and therefore will give rise to more porous films (see also annex 4). By analyzing SEM pictures of some samples, we have detected the presence of nanoparticles (100-300 nm) on the surface of the films as shown in Fig.IV-5 (d). The formation of nanoparticles in RF plasma has been already studied in many reports especially in PECVD [44-50]. An extensive study could be useful in the future to investigate the formation of these nanoparticles in the actual sputtering system.

IV-3-3) Thin film composition and nitrogen doping

In order to better determine the effect of the different deposition parameters in doping of TiO_2 with nitrogen, the composition of each film was determined by XPS. In particular, an emphasis was placed on the nitrogen N 1s energy levels which will be discussed in detail below. In addition, the oxygen O 1s energy levels, the titanium Ti 2p energy levels, as well as the valence band energy corresponding to O 2p have been observed, plotted and discussed in the following sections.

IV-3-3-1) N1s peak assignments

A diverse arrangement in the concentration and nature of nitrogen doping was found throughout the different thin films. In particular two types of doping were found; *substitutional doping*, where N replaced O in the TiO_2 lattice and it was bonded to Ti atoms so that the oxidation state of nitrogen would be (N^{n-}), and interstitial doping, where N was bonded to one or more O atoms, and thus it could be in a negative or positive oxidative state such as NO^-, NO_2^- or NO_3^-. The N 1s core level spectra were determined and deconvoluted into three main distinct peaks: N_s, N_{ch} and N_i, representing substitutional, chemisorbed and interstitial nitrogen, respectively. In Table IV-2 and Fig.IV-6, the most commonly used peaks of the N 1s core level (reported in the literature) and their most significant assignments have been regrouped (more details about these assignments are reported in annex 5).

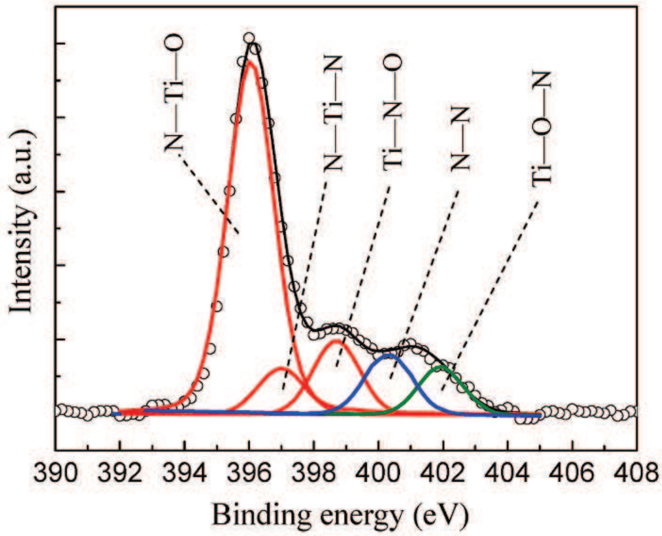

Fig.IV-6: Example of XPS-N 1s core level spectra, after deconvolution, for N doped TiO_2 deposited at 7 mtorr and 35% N_2 ratios in the reactive gas. Interstitial, chemisorbed and substitutional nitrogen are presented in green, blue and red colors, respectively.

The results of deconvolution of the N 1s peaks are regrouped in Fig.IV-7 for the different doped samples, surface composition, including different nitrogen sites with the corresponding BE are presented in Table IV-3. In addition to the two doped nitrogen states (interstitial and substitutional) and the chemisorbed nitrogen, a contribution of another nitrogen state corresponding to TiN crystal around 397 eV was identified [13].

Table IV-2*: Probable nitrogen oxidation states in N doped TiO_2 and the corresponding XPS binding energies.*

Binding Energy		Type of bonding	Nitrogen oxidation state	Ref.
396 (eV)	***substitutional***	N—Ti—O	N^{3-}, N^{2-}	[14-17]
397 (eV)		Ti—N triple bonding in TiN	N^{3-}	[2][17][19-22][23-24]
398 (eV)		N—Ti—O (with electron shift from Ti to N) and/or Ti—N—O	N^{-}	[3][25-26]
400 (eV)	***Chemisorbed***	N_2 and/or NO_x	N^0, N^+	[3][17][24][28]
402 (eV)	***interstitial***	Ti—O—N (or Ti—ON)	N^+, N^{2+}	[16]

IV-3-3-2) N 1s peak observation and analysis

It was observed that nitrogen tends to be incorporated more in interstitial sites at higher working pressures (14 mtorr) rather than at low pressure (3mtorr). At the highest working pressure studied (14 mtorr), the substitutional nitrogen could only be dominant when there was sufficient oxygen deficiencies, i.e: when the nitrogen ratio > 50% in the reactive gas. On the other hand, the interstitial incorporation was preferential for low nitrogen flow rate ratios, regardless of the working pressure values. This could be explained by the low oxygen deficiencies that could not allow the substitutional incorporation of nitrogen in rich oxygen atmosphere conditions. *In short, as the N_2 ratio increased in the reactive gas, the incorporation of nitrogen in the form of substitutional was favored.*

Most of the substitutional nitrogen peaks were located at 396 ± 0.3 eV, which means that the nitrogen was bonded to the titanium cation (Ti—N). An extra N_s peak appeared at 398.1 eV in samples prepared at 3 and 7 mtorr when nitrogen ratio was higher than 30% in the reactive gas. These substitutional (398.1 eV) N1s peaks could be the result of an N—Ti—O configuration in which electron transfer from Ti (having a low electronegativity) to nitrogen atoms in the configuration, which is still consistent with the shift in the Ti 2p towards a lower binding energy [36].

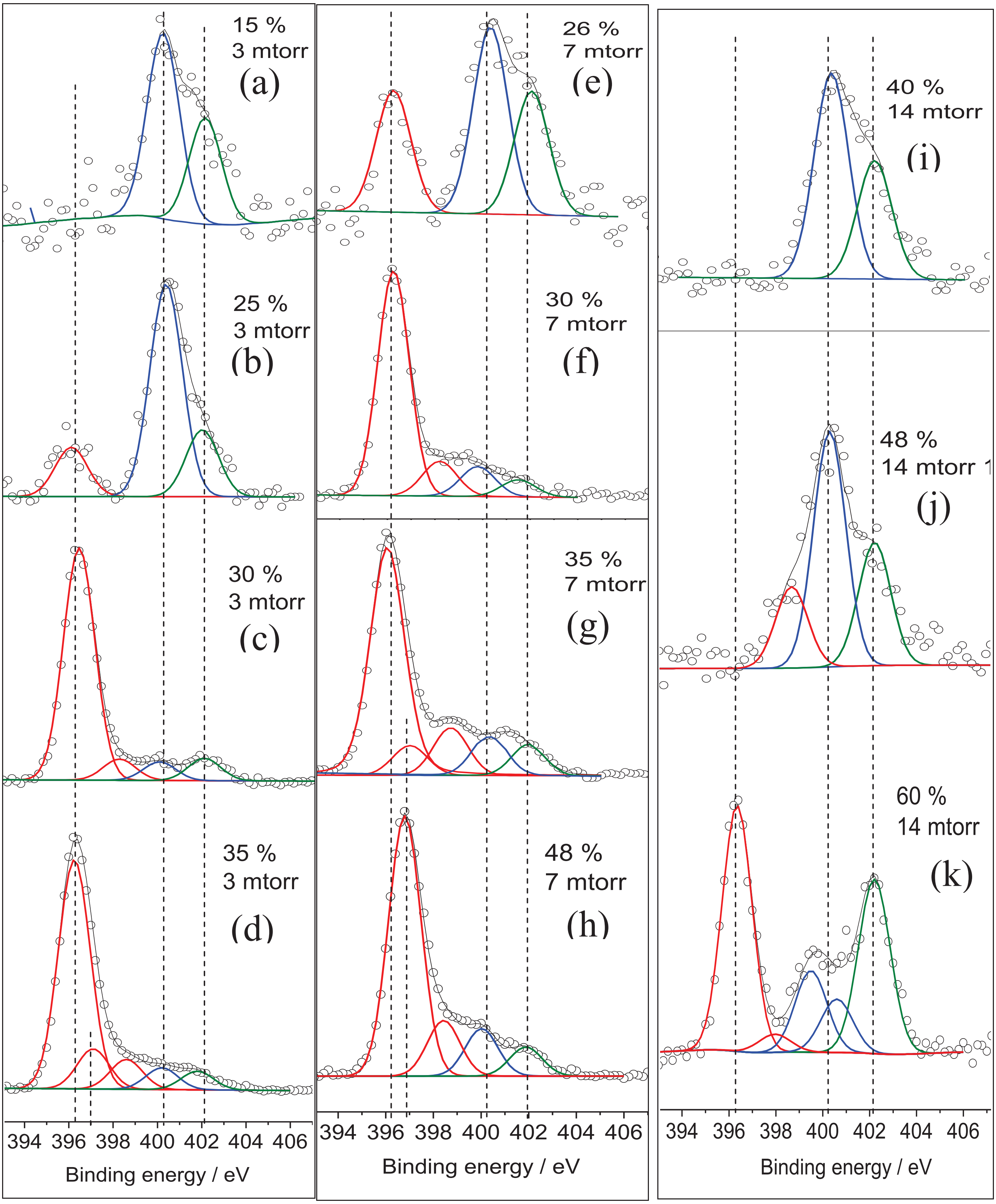

Fig.IV-7: Deconvolution of N 1s core level spectra for different nitrogen flow rate percentages in the sputtering reactive gases for samples deposited at 3 mtorr (left) , 7 mtorr (middle) and 14 mtorr (right). Interstitial, chemisorbed and substitutional nitrogen are presented in green, blue and red colors, respectively.

Pure nitride (nitrogen triple bonded to titanium) was detected in samples prepared at lower pressures (3mtorr and 7 mtorr) when nitrogen ratio exceeded 35% in the reactive gas, while no nitride species were found in samples prepared at high pressure (14 mtorr). These findings are consistent with the XRD data which allowed to identify TiN diffraction peaks in some samples prepared at 3 mtorr and 7 mtorr (in conditions with high nitrogen flow rate ratios), but none at 14 mtorr.

Table IV-3: Surface composition, including different nitrogen sites with the corresponding BE

Sample ID	**Ti**	**O**	**N_{total}**	**N_i (%)** **BE (eV)**	**N_{ch} (%)** **BE (eV)**	**N_s (%)** **BE (eV)**
3 mtorr TiO_2	33.4	66.3	0.3	—	***0.3*** 400	—
3 mtorr (15%)	33.6	65.7	0.7	***0.2*** 402	***0.5*** 400.1	—
3 mtorr (25%)	33.7	65.3	1	***0.2*** 401.9	***0.6*** 400.3	***0.2*** 396.1
3 mtorr (30%)	34.4	62.3	3.3	***0.3*** 402	***0.2*** 400	***0.2+2.6*** 398.2+396.3
3 mtorr (35%)	35.3	58.8	5.9	***0.3*** 401.8	***0.4*** 400.2	***0.5+0.7+4.0*** 398.5+397.1+396.2
7 mtorr TiO_2	33.4	66.3	0.3	—	***0.3*** 400	—
7 mtorr (26%)	33.7	65.2	1.1	***0.3*** 402.3	***0.5*** 400.5	***0.3*** 396.5
7 mtorr (30%)	34.6	61.6	3.8	***0.2*** 401.5	***0.4*** 399.9	***0.5+2.7*** 398.2+396.2
7 mtorr (35%)	35	60.1	4.9	***0.5*** 402	***0.3*** 400.3	***0.6+0.4+3.1*** 398.6+397+396.1
7 mtorr (48%)	35.3	58.7	6	***0.4*** 401.9	***0.7*** 400.1	***0.9 + 4.0*** 398.4+397.0
14 mtorr TiO_2	33.4	66.4	0.2	—	***0.2*** 400.1	—
14 mtorr (40%)	33.6	65.7	0.7	***0.3*** 402.2	***0.4*** 400.4	—
14 mtorr (48%)	33.9	64.3	1.8	***0.5*** 402.1	***1*** 400.2	***0.3*** 398.5
14 mtorr (60%)	34.4	62.3	3.3	***1*** 402.2	***0.4+0.3*** 399.5+400.5	***0.3+1.3*** 398+396.3

IV-3-3-3) O 1s Peak Observation and Analysis

O_{1s} core level spectra are presented in Fig.IV-8 for the three different pressures. In the pure TiO_2 films, the "oxide" peak observed between 530.5 to 531 eV is typically assigned to O—Ti—O bonds. As the working pressure decreased from 14 to 3 mtorr, this peak gradually shifted from 530.6 eV to 531.0 eV. The presence of –OH groups on the surface of the dense samples prepared at lower pressure could have an effect on this shift (in the undoped TiO_2). Contact angle measurement showed that the porous films prepared at 14 mtorr were less hydrophilic than the other samples, which could support the hypotheses of the O 1s peak shift due to the contribution of these –OH groups, on the surface of N doped TiO_2, which have been reported to be the most probable key for the good hydrophilicity of TiO_2 films [37]. The higher binding energy shoulder above 531.0 eV could suggest the presence of surface hydroxyl groups [15] but it could be screened by the C—O contributions. On the other hand, the same observation of peak shift was detected with the Ti 2p spectra in the case of non-doped TiO_2 samples (see next section), i.e: the distance between Ti $2p_{3/2}$ and the main peak of O 1s (71.5 eV) was not changed when working at different pressures. Therefore one can conclude that there is no reduction in the stoichiometry of TiO_2 when we change the deposition pressure, *these BE shifts in the O1s spectra have been attributed to the change in the electronic structure within pure* TiO_2 *when changing the deposition pressure.*

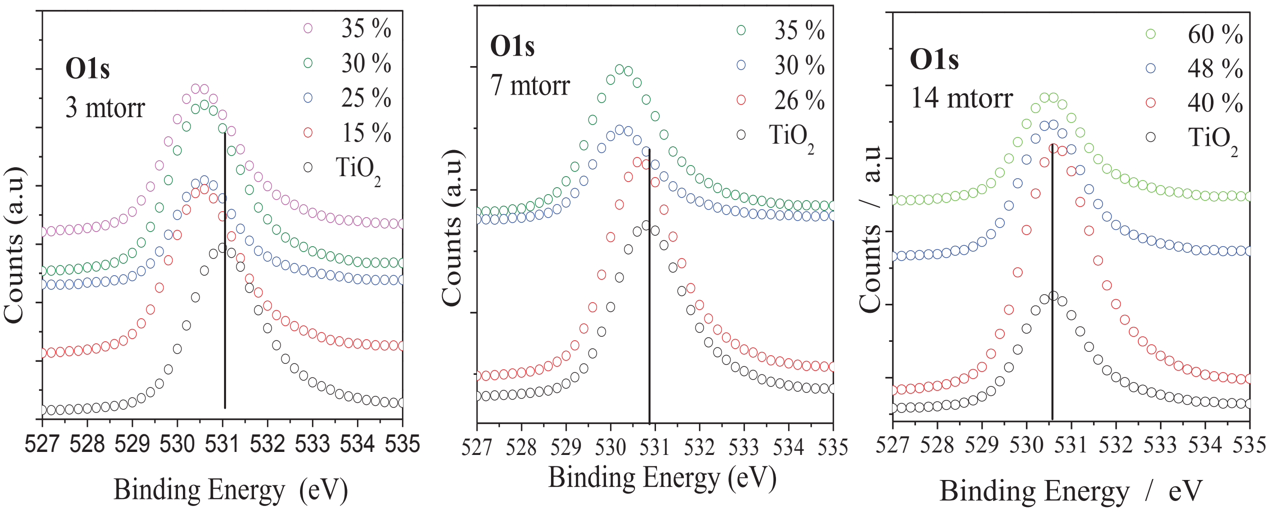

Fig.IV-8: O1S core level spectra for different nitrogen flow rate percentage at three different pressures.

Upon deposition under low (3 mtorr) and medium (7 mtorr) pressures, the incorporation of nitrogen into the TiO_2 anatase lattice induced another shift in the O_{1s} peaks towards lower binding energies due to the Ti—N—O and Ti—O—N—O contributions rather than the O—Ti—O of TiO_2, which is consistent with many reports about N doped TiO_2 [25]. At higher pressure (14 mtorr), no shift in the O_{1s} core level has been detected. This could be due to the dominance of the interstitial nitrogen sites at higher deposition pressure (Fig.V-7 (i), (j) and (k)) in the form of –NO or –NO_2 which could be enhanced by oxygen diffusion within these coatings. The oxygen diffusion could decrease the density of defects in the porous doped samples (deposited at higher pressure) resulting in a decrease in the interstitial sites of N rather than the substitutional sites.

IV-3-3-4) Ti 2p Peak Observation and Analysis

From Fig.IV-9, the spectra of the undoped TiO_2 films exhibited a Ti $2p_{3/2}$ binding energy between 459 to 459.5 eV, depending on the deposition pressure, which is in excellent agreement with the values reported for anatase TiO_2. This indicated that the titanium was in a fully oxidized state of Ti^{4+} (O–Ti–O bonds of anatase) [22][39]. The broadening towards lower binding energies, after nitrogen doping, could indicate a partial reduction of the titanium cations as Ti—N species appeared at lower oxygen ratio i.e. higher nitrogen percentage (as seen above in paragraph IV-3-3-2), this supports that the incorporation of this nitrogen species became favoured in partially reduced TiO_2 networks (to substitute the oxygen vacancies).

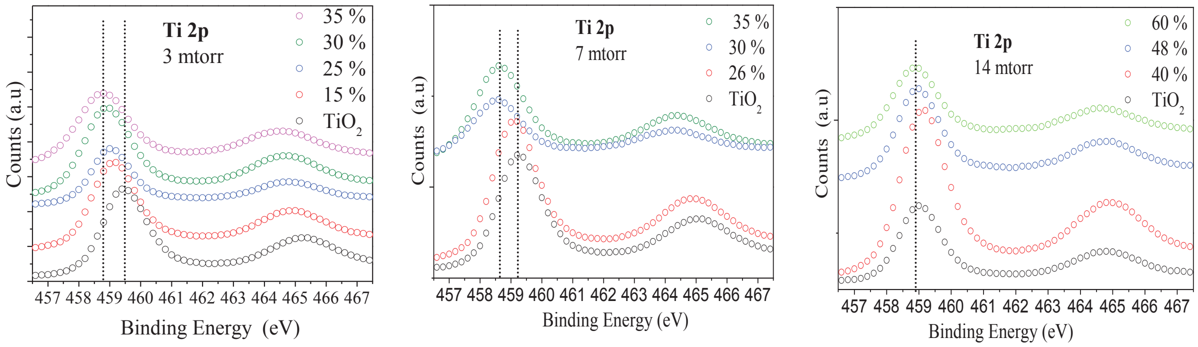

Fig.IV-9: Ti 2P spectra including 1/2 and 3/2 spins for different nitrogen flow rate percentages at three different pressures 3, 7 and 14 mtorr, from left to right respectively.

When depositing at low pressure (3 and 7 mtorr), the shift of the Ti $2p_{3/2}$ binding energies from 459.4 to 458.7 eV is related directly to nitrogen incorporation. However, no shift or shoulders (as compared to pure TiO_2) were observed in the samples prepared at 14 mtorr, as nitrogen was mostly incorporated in interstitial sites which are not directly linked to Titanium.

In summary, the broadening of Ti 2p peaks (towards lower binding energies) is mostly combined with an increase in the N 1s core level intensity, indicating the presence of oxy-nitride bondings and the contribution of the under oxidized Ti 2p peaks [6][13][15][25][39][41]. Substitutional nitrogen in the N-doped TiO_2 is generally accompanied with a shift in the O 1s and Ti 2p energies toward lower binding energies, while interstitial nitrogen doping leads to negligible shifts in the Ti 2p and O 1s BE.

IV-3-4) Valence Band Observation

The difference between the valence band maximum and Fermi level energy can help to describe the electronic structure of pure and doped TiO_2 films by examining the XPS spectra at very low binding energies (near the Fermi level). The valence band O_{2p} XPS spectra for the films deposited at 3 mtorr, 7 mtorr, and 14 mtorr are presented in Figures.IV-9 (a), (b), and (c), respectively. Within the figures, the estimated valence band border from the Fermi level has been extrapolated for all the films, at the intersection between the peak centred at 5.4 eV peak (O_{2p} π-bonding) and the base line [9][35][42]. No signal associated to Ti^{3+} defects states has been observed near the Fermi level (i.e., there were no oxygen vacancy states that could be detected using the present XPS data) [18][41][43]. It was observed that the valance band edge of the *non-doped samples* was at the same position from the Fermi level (2.25 eV) regardless of the deposition pressure.

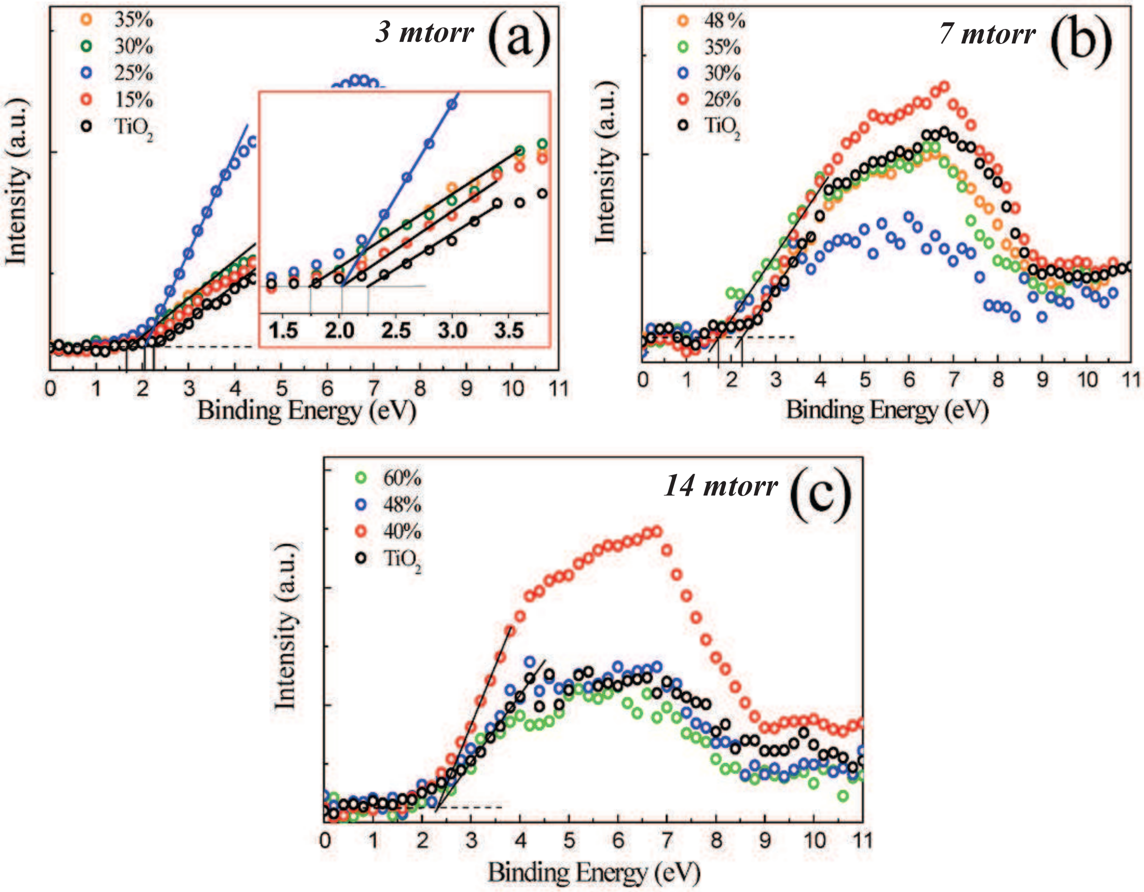

Fig.IV-10: Valence band using O 2p spectra for different nitrogen flow rate percentages at three different pressures.

For the samples deposited at 3 mtorr (Fig.IV-10 (a)), the estimated distance between the valence band edge and Fermi level decreased by 0.23 eV as nitrogen was incorporated in the film. This distance remained constant as the reactive gas mixture was increased up to 25%, corresponding to a nitrogen concentration of 1% within the film. Then as the nitrogen ratio further increased, the atomic concentration of nitrogen increased up to 3.3%, accompanied with an apparent broadening in the valence band up to 0.5 eV compared to that of the undoped film. The latter shift in the valence band edge/Fermi level distance could be due to the domination of substitutional nitrogen doping [16] as mentioned in Table IV-3. The samples deposited at 7 mtorr showed similar trends, with a decrease of the estimated valence band/Fermi level distance as the nitrogen ratio was increased with a change in the decay slope for nitrogen atomic concentrations higher than 3.8%.

The overall trend showed that as more nitrogen was incorporated into the films, the valence band border shifted closer towards the Fermi level, which resulted in a decrease of the energy gap between the valence band and the conduction band. However, the decrease of the valence band/Fermi level energy in the 14 mtorr samples was considerably less than the films prepared at lower pressures, as there was only a very small amount of the nitrogen present in substitutional sites, in agreement with the work of Romero et al. [16].

The decrease in the valence band energy is directly correlated to the decrease of the observed optical band gap energy of the films deposited with low to medium nitrogen doping ($N_{at}< 3.3$ %) (see next section). However, a large difference was seen in films having higher nitrogen concentrations. In particularly the films deposited at 3 mtorr with a nitrogen ratio of 30% (N_{at}=3.3%), the film deposited at 7 mtorr with a nitrogen ratio of 30% (N_{at}=3.8%), and the film deposited at 14 mtorr with a nitrogen ratio of 60% (N_{at}=3.3%) all show significantly decreased band gap energies that do not match with the observed valence band energy shift. The XPS and UV-vis observations (see next section) suggest that at low nitrogen doping (N_{at}<<3.3%) the most significant change in the optical properties is due to the upward broadening of the valence, which results from the overlap of the O_{2p} and N_{2p} orbitals (nitrogen energy states) [27]. However, when the nitrogen doping increases above this critical value, the band gap energies decrease significantly, which is indicative of more intermediary energy levels within the band gap of TiO_2 [2], that could not be detected clearly by the examination of XPS data, as a Fermi level shifting (from vacuum level) could take place at higher nitrogen concentrations within the doped thin film (N_{at}>> 3.3%). In such conditions we might have TiO_2 coatings with TiN islands dispersed in the structure which could explain the very low optical gaps measured.

IV-3-5) Optical Properties

The transmission and reflection spectra were measured, for each sample before and after annealing at 450°C in a closed furnace. The transmission spectra for the annealed films deposited at 7 mtorr are shown in Fig.IV-11 (a), as an example. The trend for the respective spectra for all of the as-deposited and annealed samples was similar, showing a distinct shift of the transmission out to longer wavelengths as the nitrogen incorporation increased. The pure TiO_2 sample showed higher transmission at long wavelengths (above 450 nm), with several oscillations that are from the interference due to the thin film morphology. However, at around λ = 390 nm, the transmission decreases very sharply towards smaller wavelengths, reflecting the absorption edge of the film. The N-doped TiO_2 sample with the smallest nitrogen ratio shows a similar trend, with the sharp decrease in transmission shown to occur at λ = 400 nm, indicating that the introduction of even a small amount of nitrogen during deposition can shift the absorption edge. As the nitrogen ratio increased, the absorption edge shifted out to longer wavelengths, and the sample with the highest nitrogen ratio had an absorption edge begin higher than λ = 500 nm (Fig.IV-11 (a)). The sample deposited at 7 mtorr and with the reactive gas flow rates of N_2 = 0.7 sccm, O_2 = 1.6 sccm (30% N_2) looked similar to the other spectra at higher wavelengths, but around λ = 500 nm, the transmission decreased significantly towards smaller wavelengths. However, at around λ = 450 nm, the slope of the decrease in transmission becomes less sharp. These two slopes may indicate two different electron excitations coming from two different band energy levels. In particularly, the two band transitions may be due to the oxygen 2p orbital excitation from the TiO_2, as well as the introduction of a stable nitrogen (interstitial and/or substitutional) energy level within the band gap. These observations are consistent with other publications showing that most of nitrogen-doped TiO_2 should exhibit visible light absorption as a shoulder in the visible wavelength (> 400 nm) due to the formation of isolated N_{2p} orbitals above the valence band at lower nitrogen doping concentration (N_{at}<2%) into the TiO_2 lattice [29-31]. A smooth absorption shift towards visible light regions could be achieved in the case of higher concentration of nitrogen doping (up to 17%) [30][32].

Band gap estimation

The absorption spectra and the band gap were calculated using equations Eq.III-2 and Eq.III-3.The calculated values of the band gaps for the pure and nitrogen doped TiO_2 films were placed in Table IV-4 as well as Fig.IV-11 (b) for comparison. The as-deposited and annealed pure TiO_2 films showed an estimated band gap energy of $E_g = 3.35 \pm 0.15$ eV, indicative of the anatase phase of TiO_2. However, as nitrogen was introduced into the coatings, different decreasing slopes were observed in the estimated band gap energies, depending on the preparation pressure and the nitrogen percentage in the reactive gas.

There were two clear trends that were present in the estimated band gap energies of the films prepared at different pressures and with increasing nitrogen ratios. First, regardless of the deposition pressure, as the nitrogen ratio was increased, the band gap was found to decrease. This is an expected result, as the introduction of nitrogen, whether substitutional or interstitial, can add stable energy levels within the anatase band gap of TiO_2. Therefore, as more nitrogen was added, the density of nitrogen states within the anatase band gap should increase, and thus more electrons-hole pairs can be excited within the band gap energy of TiO_2. The second observed trend was the effect of deposition pressure on the band gap energies of the thin films.

For films prepared at low pressure, 3 mtorr, the band gap energy decreased from 3.51 eV to 3.18 eV as the nitrogen ratio is increased from 0% up to 25% in the reactive gas. Then, the increase in the nitrogen ratio from 25% to 30% induced a greater decrease in the optical band gap from 3.18 eV to 2.82 eV. Similarly at 7 mtorr, the estimated band gap decreased slowly to 3.25 eV as the nitrogen ratio increased up to 25%, and then it decreased faster, down to 2.6 eV, as the nitrogen ratio was increased from 25% to 34%. After annealing at 450°C the band gap values decreased slightly in general, which could be explained by the enhancement of crystallinity (increase of the crystal size) and electronic transfer, especially for the dense films prepared at lower pressures. For high nitrogen percentages, which leads to low band gap energies one cannot exclude the possibility that we may have deposited a composite TiN/TiO_2 material. The latter has been confirmed by XPS (Fig.IV-7 (d), (g) and (h)).

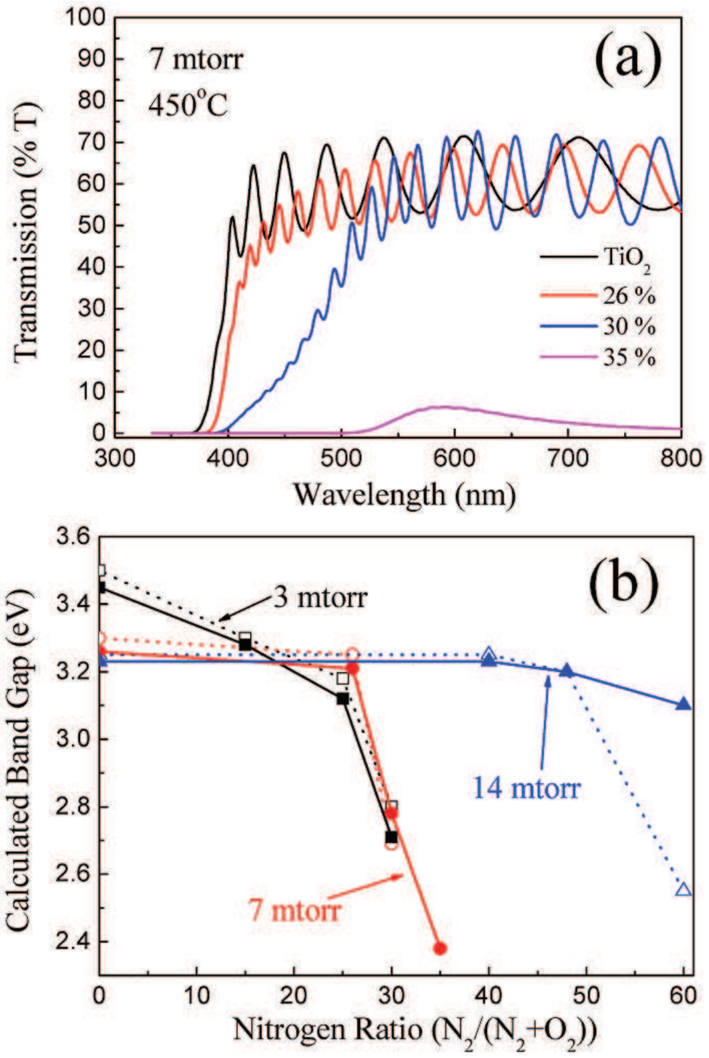

Deposition pressure	$\frac{N_2}{N_2+O_2}$	E_g (eV)
3 mtorr	0%:TiO_2	3.5/**3.45**
	15%	3.3/**3.28**
	25%	3.18/3.12
	30%	2.8/**2.71**
	35%	* / *
7 mtorr	0%:TiO_2	3.3/**3.26**
	26%	3.25/**3.21**
	30%	2.69/**2.78**
	35%	* /**2.38**
	48%	* / *
14 mtorr	0%: TiO_2	3.25/**3.23**
	40%	3.25/**3.23**
	48%	3.2/**3.2**
	60%	2.55/**3.1**

Fig.IV-11: a) UV-vis transmission spectra for nitrogen doped samples prepared at 7 mtorr and annealed at 450°C for 2 hours, b) calculated band gap using Tauc plot for all samples vs N_2 % in thereactive gas {$N_2/(N_2+O_2)$}, before (dotted line) and after annealing (solid line).

Table IV-4: Calculated optical band gaps for as deposited films and ***annealed*** *films (in bold).*
*= Low light transmission

The films prepared at 14 mtorr did not follow the same trends as compared to the coatings deposited at lower pressures. One can note that at this pressure, even when the nitrogen ratio (in the reactive gas) increased up to 40% and 48%, the band gap energy was observed to be 3.25 and 3.2 eV, respectively, which are closer to that of the pure TiO_2 even though they were prepared at a high nitrogen ratio. However, at higher nitrogen percentages in the reactive gas (60%) the estimated band gap energy was found to be 2.55 eV. But after annealing at 450°C, the band gap increased again to 3.1 eV, this increase could be explained by the increase in transmittance accompanied with a loss in nitrogen doping in such porous samples (due to the oxidation of Ti—N bonds in the lattice during the annealing process).

IV-3-6) Photoactive Properties

Two methods were used to test the photoactivity of pure and N-doped TiO_2; the current generation during photoelectrochemical water splitting reactions, and the photocatalytic degradation of NMP.

IV-3-6-1) Potentiodynamic sweep

Fig.IV-12 presents the electrochemical potentiodynamic sweep for N-doped TiO_2 samples deposited at 7 mtorr and irradiated by white light. Films prepared at other pressures have the same overall shape and trends (not shown) as in Fig.IV-12, the only significant difference is the maximum photocurrent density generated, which is discussed later.

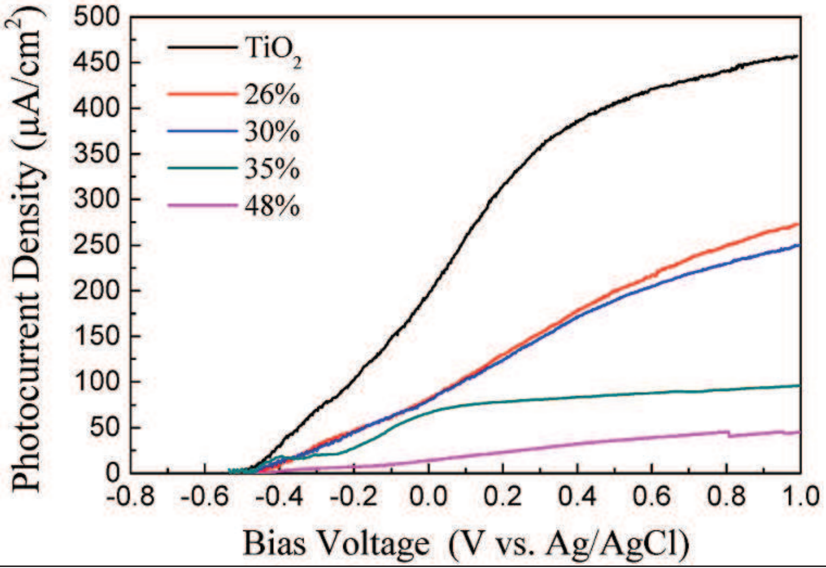

Fig.IV-12: Electrochemical potentiodynamic sweep under white light irradiation using Ag/AgCl as reference electrode in Na_2SO_4 1M, pH 7 for N doped samples deposited at 7mtorr.

The dark current density was approximately 0.3 to 0.6 μA/cm^2 for the positive sweeping bias up to 1.0 V. Upon white light irradiation, the open circuit voltage (V_{OC}) was about -0.5 V for all samples regardless of the deposition conditions. This indicated that the electronic structure was not affected significantly by the surface morphology or the nitrogen incorporation into the TiO_2 films. The photocurrent deviates from the dark current under both white and visible light excitation, although the difference is much greater for white light. This disparity was understandable, because the absorption spectrum for this film showed significantly larger absorbance at UV wavelengths than at visible wavelengths.

IV-3-6-2) Intermittent photocurrent measurements

Fig.IV-13 presents the intermittent photocurrent measured at 0.5 V/(Ag/AgCl) under white light and visible light irradiations for all the samples. The light was allowed to hit each sample in 30-second intervals during these measurements. A UV filter was put into place after 210 second from the beginning of the experiment, so only visible light reached the samples.

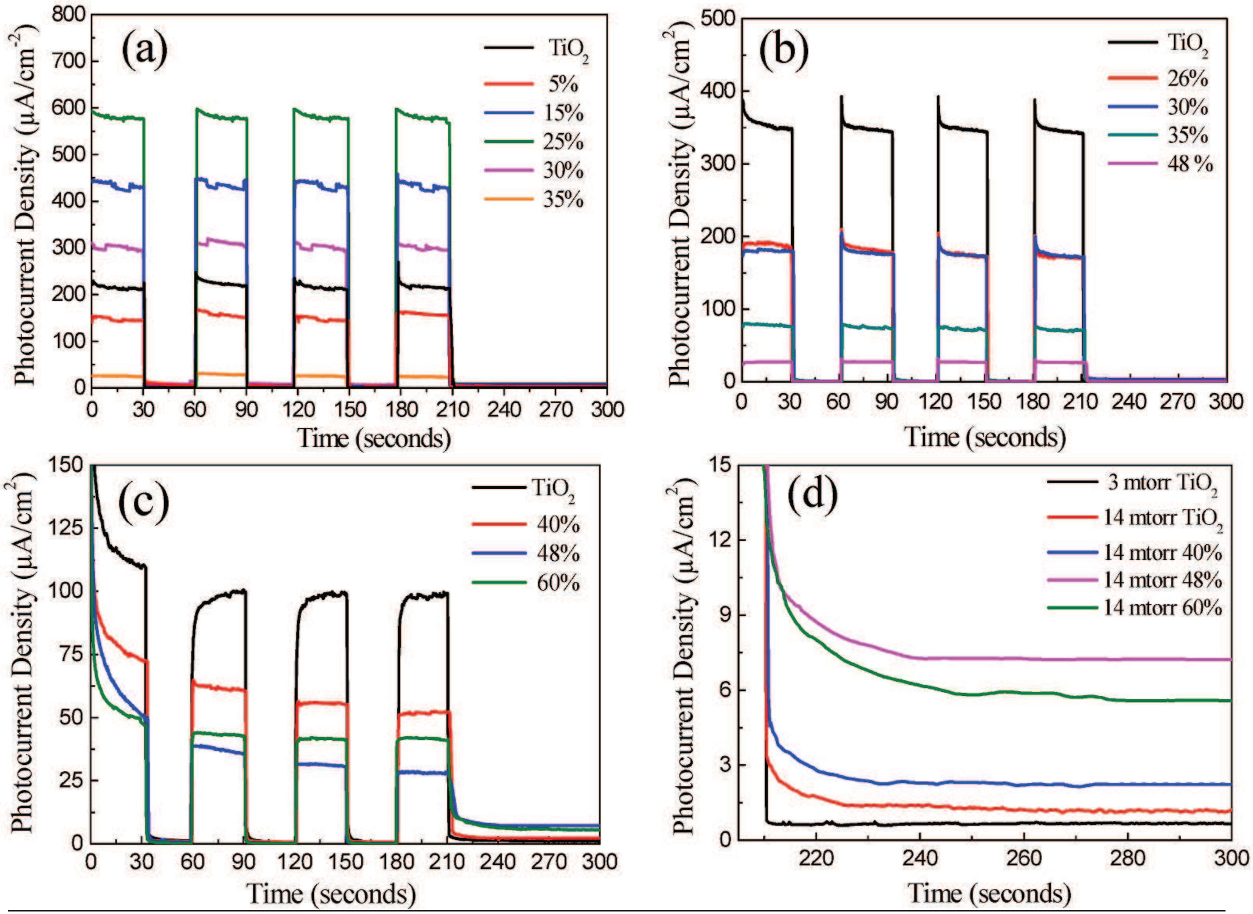

Fig.IV-13: Electrochemical intermittent photocurrent under white light irradiation at a bias voltage of 0.5V/(Ag/AgCl) in Na_2SO_4 1M, pH 7 for all N doped samples deposited at different pressures a) 3 mtorr, b) 7 mtorr and c) 14 mtorr. d) Visible light photocurrent density for samples used in c)

The maximum photocurrent generated, at constant voltage of 0.5 V, under white and visible light was plotted in Fig.IV-14 (a) and (b), respectively. When nitrogen was incorporated in the coatings, it seemed to degrade the photocurrent generated in the samples prepared at 7 mtorr and 14 mtorr under white light irradiation. However, when these samples were irradiated under visible light, the addition of nitrogen was not always destructive to the photoactive performance of these films. In particular, a maximum photocurrent was observed at nitrogen ratios of 30% (8.5 μA/cm^{-2}), 25% (3.8 μA/cm^{-2}) and 48% (7.5 μA/cm^{-2}) for films deposited at 3 mtorr, 7 mtorr, and 14 mtorr, respectively. But, for the samples prepared at 3 mtorr, the incorporation of nitrogen produced more photocurrent under white light and visible light illumination. This may result from the combination of the increased nitrogen percentage and the decreased porosity of these coatings. This trend indicates that the incorporation of nitrogen into the films prepared at pressures above 3 mtorr is destructive to the UV induced photoelectrochemical performance, but enhances the visible light reactivity.

The maximum photocurrent density was found to depend on the deposition pressure as well as the doping level. In general, the samples prepared at 3 mtorr showed the highest photocurrent density, with a peak photocurrent achieved when the nitrogen ratio was 25% (N_{at}=1%) under white light irradiation, and at 30% (N_{at}=3.3%) under visible light irradiation. A maximum white light photocurrent density of 567 $\mu A/cm^{-2}$, 347 $\mu A/cm^{-2}$ and 99 $\mu A/cm^{-2}$ was measured at nitrogen ratios of 25% (3 mtorr), 0% (7 mtorr), and 0% (14 mtorr), respectively.

When interstitial and substitutional nitrogen sites were both observed in the same sample (Fig.IV-7), it seemed to have a synergic effect on the electrochemical properties, especially at lower nitrogen concentrations (N_{at} < 3.3%) where the maximum photocurrent density under UV and visible light irradiation was observed. At higher nitrogen concentrations (N_{at} > 3.3%), the concentration of substitutional nitrogen sites increased, which decreased both visible and UV light photocurrent density regardless of the deposition pressure.

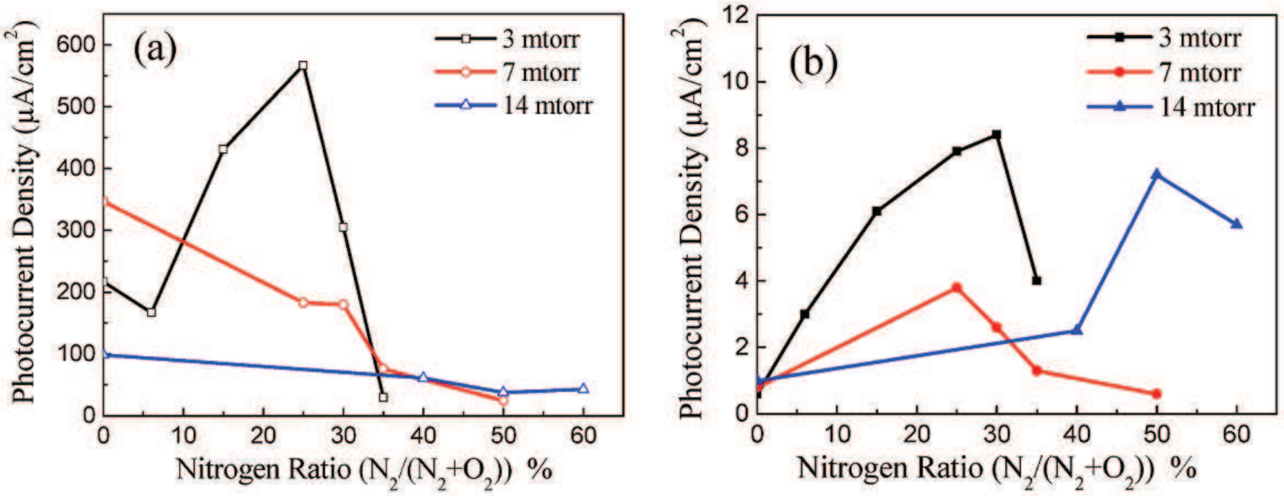

Fig.IV-14: Photocurrent density under a) white light and b) visible light irradiations at a bias voltage of 0.5V/(Ag/AgCl) in Na_2SO_4 1M, pH 7 for all N doped samples deposited at different pressures vs N_2% in the reactive gas.

The photocurrent measurements revealed an apparent memory effect in the films deposited at 14 mtorr which revealed a higher concentration of interstitial doping (interstitial N doping has been confirmed above, cf Fig.IV-7). This memory effect could be seen when the white-light irradiation was switched off or switched to visible light, as shown in Fig.IV-13 (d). It appears that interstitial nitrogen is more efficient to promote charge generation as well as charge separation under visible light compared to substitutional nitrogen. However the latter was found to be more efficient in charge generation and electron transfer but it also increased the recombination rate [33] under light irradiation.

Under visible light irradiation, the decrease of the photocurrent density was observed when substitutional nitrogen was dominant and with the formation of TiN structure which is observed in Fig.IV-7 (c), (d), (f), (g) and (h). The introduction of TiN into the films has two dramatic effects: first, TiN reduced the photo-generation efficiency of the charge carriers due to the destruction of the anatase TiO_2 crystal lattice, and second, they act as recombination centers for the photo-generated electrons and holes.

IV-3-6-3) Photocatalytic activity

The photocatalytic degradation of NMP was carried out under UV light irradiation on samples deposited on stainless steel substrates. For simplicity, the concentrations of NMP as a function of time during the photodegradation with different doped samples deposited at 14 mtorr and pure TiO_2 deposited at 3 mtorr are shown in Fig.IV-15.

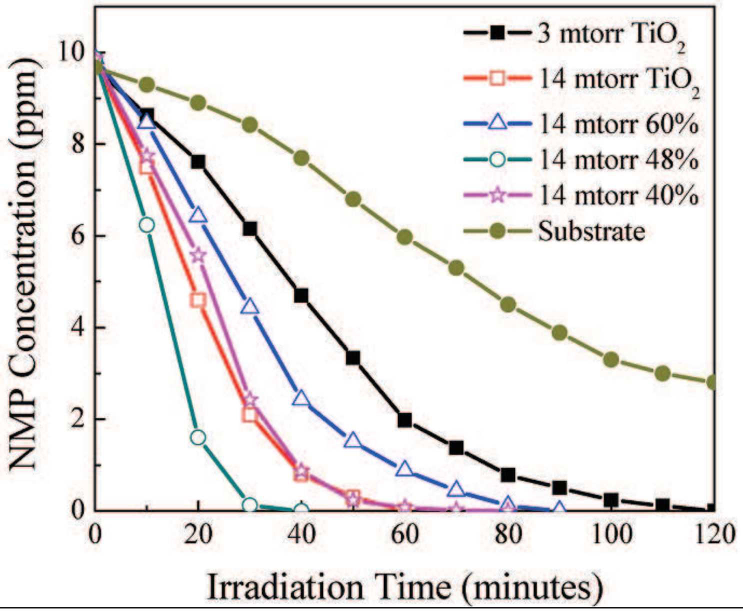

Fig.IV-15: Kinetic of NMP degradation under UV light using some selected N doped samples deposited at 14 mtorr (porous) and 3 mtorr (dense).

It is clear that even with the blank substrate, the concentration of NMP decreases due to photo-bleaching. However, when TiO_2 and N-doped TiO_2 samples were inserted, the degradation kinetics increased significantly. As seen in chapter III, the most efficient photocatalytic activity was found for the samples prepared at 14 mtorr as compared to the films prepared at other pressures [34], specifically the sample prepared with a nitrogen ratio of 48% giving the best photocatalytic activity. The two major characteristics of the coatings which affected the photocatalytic performance were the film morphology and nitrogen doping sites.

As was discussed in previous sections, the deposition pressure had a significant effect on the morphology of the coatings. In particular as the deposition pressure increased, the porosity of the films also increased. The increase in porosity created more active catalytic sites for photocatalysis to take place. The other factor which played a role in the photocatalytic functionality of the films was the nitrogen doping sites. It was observed that as the interstitial nitrogen sites increased, the photocatalytic activity became higher (see Fig.IV-7). Then as the substitutional nitrogen started to become dominant, this activity decreased again as shown by the film prepared at a nitrogen ratio of 60%. This could be a direct result of the change in the photogenerated charge separation, with the porous films having more interstitial nitrogen doping than substitutional nitrogen sites. This is in agreement with what reported by Yates et al. [17] and other works [9][25][38] who found that chemisorbed and interstitial nitrogen doping were more efficient for UV-photocatalytic efficiency rather than substitutional nitrogen doping.

IV-4) Conclusion

The energetic character of the discharge as well as the plasma chemistry in the reactive mode is very sensitive to any change in the reactive gas composition when working at low pressure, unlike working under high pressure where the plasma is more stable and less affected by the reactive gas composition.

Doping nitrogen within TiO_2 is an effective way to enhance the visible light photoactivity. There is a competitive effect of the morphology, the crystalline orientation, nitrogen sites and the chemical composition on the efficiency of the photocatalytic activity. Samples prepared at high pressure had an optimized photocatalytic activity due to the higher specific surface area, the optimal presence of anatase crystals in the lattice, the introduction of discrete energy levels within the band gap and the presence of interstitial nitrogen in the lattice rather than substitutional. However, at low pressure, the formation of TiN crystals became more probable, and acted as recombination centers for the photo-generated charge carriers which reduced the photocatalytic activity. Also, this study showed that *higher deposition pressures enhance the formation of anatase (112) crystal orientation rather than the well known (101) orientation of anatase. The latter could be favored at lower pressure depositions*. These results have been reported for the first time in this work.

The synergic effect of substitutional and interstitial nitrogen sites in dense films are more efficient for photoelectrochemical applications, due to the good light absorption, the good charge transfer in the substitutional doping and the good charge separation in the interstitial nitrogen doping. One can find in the literature that the efficiency of N doping in TiO_2 thin films to improve photocatalytic performancehas aroused much controversy. This study has shown that there is a delicate balance between the concentration and nature of nitrogen doping in TiO_2 that can lead to both improved and deteriorated photo activity. Also, doped films showed different behaviors between the photo-electrochemical and the photocatalytic activities. However, we have shown that there are optimal deposition conditions to maximize the photocatalytic efficiency of N-doped TiO_2 and other conditions to optimize the electrical and photo-electrochemical properties.

References

[1] R Beranek, B Neumann, S Sakthivel, M Janczarek, T Dittrich, H Tributsch, H Kisch, *Chemical Physics*, **339** (2007) 11–19.

[2] C Di Valentin, E Finazzi, G Pacchioni, A Selloni, S Livraghi, M C Paganini, E Giamello, *Chemical Physics*, **339** (2007) 44–56.

[3] S Lee, I Cho, D K Lee, D W Kim, T H Noh, C H Kwak, S Park, K S Honga, J K Lee, H S Jung , *Journal of Photochemistry and Photobiology A: Chemistry*, **213** (2010) 129-135.

[4] A Zaleska, A Review, *Recent Patents on Engineering*, **2** (No.3) (2008) 158-164.

[5] R Asahi, T Morikawa, T Ohwaki, K Aoki, Y Taga, *Science*, **293** (2001) 269-271.

[6] S Lee, E Yamasue, K Ishihara, H Okumura, *Applied Catalysis B: Environmental*, **93** (2010) 217–226.

[7] O Diwald, T Thompson, T Zubkov, E Goralski, S Walck, J Yates, *Journal of Physical Chemistry*, **108 (19)** (2004) 6004-6008.

[8] O Diwald, T Thompson, E Goralski, S Walck, J Yates, *Journal of Physical Chemistry B*, **108 (1)** (2004) 52-57.

[9] F Dong, W Zhao, Z Wu, S Guo, *Journal of Hazardous Materials*, **162** (2009) 763–770.

[10] P Zeman, S Takabayashi, *Surface and Coatings Technology*, **153** (2002) 93–99.

[11] I Ozen, A Gulgun, *Advances in Science and Technology* **45** (2006) 1316-1321.

[12] I Alhomoudi, G Newaz, *Thin Solid Films* **517** (2009) 4372–4378.

[13] A Trenczek-Zajaca, M Radeckaa, K Zakrzewskab, A Brudnikb, E Kusiorb, *Journal of Power Sources*, **194** (2009) 93-103.

[14] N Raut, T Mathews, S Rajagopalan, R Subba Rao, S Dash, A Tyagi, *Solid State Communications,* **151** (2011) 245–249.

[15] Z Zhang, J B.M- Goodall, D J Morgan, S Brown, R J.H Clark, J C Knowles, N J Mordan, J R.G Evans, A F Carley, M Bowker, J A Darr, *Journal of the European Ceramic Society*, **29** (2009) 2343-2353.

[16] S Hamad, J C Gonza, A Barranco, J P Espino, J Cotrino, *Journal of Physical Chemistry C*, **114** (2010) 22546–22557.

[17] H M Yates, M G Nolan, D W Sheel, M E Pemble, *Journal of Photochemistry and Photobiology A: Chemistry*, **179** (2006) 213–223.

[18] M Batzill, E-H Morales, U Diebold, *Chemical Physics*, **339** (2007) 36–43.

[19] A Trenczek-Zajaca, M Radeckaa, K Zakrzewskab, A Brudnikb, E Kusiorb, *Journal of Power Sources*, **194** (2009) 93-103.

[20] R Parra, A Arango, J Palacio, *Dyna* **77** (163) (2010) 64–74.

[21] H Kawasaki, T Ohshima, Y Yagyu, Y Suda, SI Khartsev, AM Grishin, *Journal of Physics Conference Series,* **100** (2008) 012038 1–4.

[22] B Avasarala, P Haldar, *Electrochimca Acta*, **55** (2010) 9024-9034.

[23] M Wong, H Chou, T Yang, *Thin Solid Films*, **494** (2006) 244 – 249

[24] G He, L Zhang,G Li, M Liu, X Wang, *Journal of Physics D: Applied Physics*, **41** (2008) 045304 1-9

[25] F Peng, Y Liu, H Wang, H Yu, J Yang, *Chinese Journal of Chemical Physics*, **23** (4) (2010) 437-441.

[26] J Suna, L Qiao, S Suna, G Wang, *Journal of Hazardous Materials*, **155** (2008) 312–319.

[27] Z Zhao, Q Liu, *Journal of Physics D: Applied Physics*, **41** (2008) 1-10.

[28] A V Emeline, V N Kuznetsov, V K Rybchuk, N Serpone, Review, *International Journal of Photoenergy*, ID 258394 (2008) 1-19.

[29] Y Nakano, T Morikawa, T Ohwaki, Y Taga, *Chemical Physics*, **339** (2007) 20–26

[30] M Kitano, M Matsuoka, M Ueshima, M Anpo, *Applied Catalysis A: General*, **325** (2007) 1-14.

[31] H Irie, Y Watanabe, K Hashimoto, *Journal of Physical Chemistry B*, **107** (2003) 5483-5486.

[32] B Liu, L Wen, X Zhao, *Solar Energy Materials & Solar Cells,* **92** (2008) 1–10.

[33] R Dholam, N Patel, A Santini, A Miotello, *International Journal of Hydrogen Energy*, **35** (2010) 9581-9590.

[34] H Fakhouri, W Smith, J Pulpytel, A Zolfaghari, H Mortaheb, F Meshkini, R Jafari, F Arefi-Khonsari, *Journal of Nano and Electronic Physics*, **3 (1)** (2011) 26-40**.**

[35] J Wang, D N Tafen, JP Lewis, Z Hong, A Manivannan, M Zhi, M Li, N Wu, The Journal of American Chemical Society, 131 (2009) 12290-12297

[36] H Yu, X Zheng, Z Yin, F Tao, *Chinese Journal of Chemical Engeneering*, **15 (6)** (2007) 802-807.

[37] M Simonsen, Z Li, E Søgaard, Applied Surface Science 255 (2009) 8054–8062

[38] H Shen, L Mi, P Xu, W Shen, P Wang, *Applied Surface Science*, **253** (2007) 7024–7028.

[39] H Matsui, H Tabata, *Journal of Applied Physics*, **97** (2005) 123511 _1-8.

[40] J Musil, P Baroch, J Vlcek, K Nam, J Han, *Thin Solid Films,* **475** (2005) 208–218.

[41] S Wendt, P Sprunger, E Lira, G Madsen, Z Li, J Hansen, J Matthiesen, A Blekinge-Rasmussen, E Lægsgaard, B Hammer, F Besenbacher, *Science*, **320** (2008) 1755-1759.

[42] A Fujishima, X Zhang, D A Tryk, *Surface Science Reports*, **63** (2008) 515–582.

[43] C Chusuei, D Goodman, *Journal of surfaces and colloids*, **26** (2010) 921-938.

[44] L Boufendi, J Gaudin, S Huet, G Viera, M Dudemaine, *Applied Physic Letters , **79*** (2001) 4301.

[45] L Boufendi, A Bouchoule, *Plasma Sources Science and Technology, **3*** (1994) 262-267

[46] A Bouchoule, A Plain, L Boufendi, J P Blondeau, C Laure, *Journal of Applied Physics,* ***70*** (4) (1991) 1991.

[47] A Fridman, L Boufendi, T Hbid, B V Potakin, A Bouchoule, Journal of Applyed physics, 79 (1995) 1303

[48] L Boufendi, A Bouchoule, *Plasma Sources Science and Technology,* **11** (2002) A211.

[49] M Cavarroc, M Mikikian, Y Tessier, L Boufendi, *IEEE Transactions on Plasma, Science,* ***36*** (4) (2008) 1016-1017.

[50] J Pulpytel, M Jubault, N Laidani, F Arefi-Khonsari, *11th International Conference on Plasma Surface Enginnering PSE*, Garmisch-Partenkirshen, Germany (2008).

Chapter V

Nitrogen doping in bi-layer configuration

Chapter V

Nitrogen doping in bi-layer configuration

Abstract

Multi-layer thin films of TiO_2 and TiN were deposited by RF reactive magnetron sputtering, and their crystalline, optical, photo-electrochemical properties were measured. The total thickness of each film was kept constant around 500 nm. Firstly, the overall composition of the films (TiN to TiO_2 ratio) was kept constant. The number of layers and thickness of each layer was controlled to create bi-layer thin films which were composed of: 9, 18, 27, 36 and 45 bi-layers. XRD patterns were observed for each film after annealing to measure the grain size and composition of anatase and rutile as a function of temperature. It was found that the phase transition temperature can be substantially controlled (between 550^{o}C and 850^{o}C) for the anatase to rutile transition by varying the number of layers/thickness of each layer. In addition, bi-layer stacking significantly affected the films optical properties by lowering the band gap into the visible light region, and also showed improvement in photo-electrochemical performance under UV and visible irradiation. Secondly different nominal TiN/TiO_2 ratios were attempted within the 9 and 18 bilayers and the photo-activity was found to be enhanced with the 18 bilayers as the TiN/TiO_2 ratio increased up to 30%.

Overall, bi-layer stacking of TiO_2/TiN films has shown a unique and highly desirable control over several important physical characteristics which can be beneficial for many applications such as high-temperature sensors, optoelectronic devices as well as photo-catalytic applications due to the good controlled charge separation within the doped TiO_2.

Résumé

Des couches de TiO_2 dopé azote ont été préparées sous forme de multicouches. Des films minces successifs de TiO_2 et TiN ont été créés par pulvérisation RF cathodique magnétron. Nous avons mesuré la cristallinité, les propriétés optiques, les propriétés photo-électrochimiques de ces couches. L'épaisseur totale de chaque multicouche a été maintenue constante à environ 500 nm. Dans un premier temps, la composition globale des films (rapport TiN/TiO_2 %) a été maintenu constante. Le nombre de couches et l'épaisseur de chaque couche a été fixés de telle façon à créer des multicouches composés de: 9, 18, 27, 36 et 45 bicouches. A partir des spectres DRX, nous avons determiné la taille des grains et la fraction d'anatase et de rutile en fonction de la température de recuit. Nous avons constaté que la température de transition de la phase anatase/rutile peut être contrôlée d'une façon précise (entre 550°C et 850°C) en fonction du nombre des couches et l'épaisseur de chaque couche. En outre, l'empilement des bicouches peut affecter, d'une façon significative, les propriétés optiques en diminuant la bande gap dans la région d'absorption des rayonnements visibles. Aussi, ces couches ont montré une amélioration des activités photo-induites sous irradiation UV et visible.

Dans un second temps, nous avons étudié différents taux nominaux du rapport TiN/TiO_2 dans les 9 et 18 bicouches, l'activité photo induite est trouvée d'être améliorée dans les 18 bicouches en augmentant le rapport TiN/TiO_2 jusqu'à 30%. Globalement, l'empilement des bicouches TiO_2/TiN a montré un contrôle unique et hautement souhaitable de caractéristiques physiques qui peuvent être bénéfiques pour des nombreuses applications telles que les capteurs à haute température, les dispositifs optoélectroniques ainsi que les applications photo-catalytique due à la séparation efficace et contrôlée des charges dans le TiO_2 dopé.

V-1) Introduction

While TiO_2 is a suitable candidate for UV-based photoactive systems, a practical long-term solution requires the use of visible light, and thus the ability to use the solar spectrum to initiate photo-reactions. In addition, the relatively short electron-hole pair lifetime in TiO_2 limits the advancement of its applications. The electrons and holes are used in separate reduction and oxidation reactions at the TiO_2 surface, so extending the lifetime of each charge carrier is vitally important to improving the efficiency of TiO_2 as a functional photocatalyst. It has been reported that anatase has mostly an *indirect band gap* with less electron hole recombination allowing it to be used in solar cells and photocatalysis. Rutile phase has mostly a *direct band gap* making it more useful for optoelectronic devices, but it is not useful for solar cell or photocatalytic applications as it has much more charge recombination.

Several methods have been developed to improve the overall efficiency of TiO_2 by adjusting the structural and morphological properties of the material. For instance, the crystal structure of TiO_2 plays an important role in its optoelectronic performance. When TiO_2 is prepared in the amorphous phase, it has a very poor photocatalytic effect [1]. However, when TiO_2 is in the anatase crystal phase, it has shown a significant increase in the photocatalytic performance [1]. Furthermore, many groups have shown that preparing TiO_2 with a predominant anatase phase (~75%), and having a relatively small amount of the rutile phase (~25%), allows for optimized photocatalytic efficiency [2-5]. In fact, the TiO_2 industrial powder standard, Degussa P25, is prepared respecting the ratio of anatase to rutile, (75% to 25%, respectively) [6]. However, at high temperatures (>550^{o}C), TiO_2 has generally shown rutile dominated crystal phase characteristics [7-8]. While the pure rutile phase of TiO_2 which has a smaller band gap (E_g = 3.0 eV) than the anatase phase (E_g = 3.2 eV), has generally shown significantly worse photoactive properties such as reduced photocatalytic activity, reduced photocurrent generation, and diminished charge transport [2][8]. For these reasons, the ability to tailor and control the crystal phase and composition of TiO_2 is critical in improving its optoelectronic performance.

Other ways to improve the photoactive properties of TiO_2 include coupling it with other semi-conductors or metals [9-12] and doping [13-15]. When TiO_2 is in contact with other semi-conductors which have “similar” conduction and valence band positions, different heterojunction or electronic heterostructures could be formed. These heterojunctions can localize electrons and holes in the conduction and valence bands, extending the lifetime of the photogenerated charge carriers. This can allow photo-generated electrons in the TiO_2

conduction band to travel to the secondary semi-conductor, and allow photo-generated holes to transfer to the TiO_2 valence band. When TiO_2 is in contact with metals, a *Schottky barrier* is formed that is proportional to the difference between the Fermi energy level of TiO_2 and the metal. This barrier is like an electric field that can affect charge carriers in a nearby region and increase the "space charge layer", which can further increase the effective lifetime of the photo-generated electron-hole pairs.

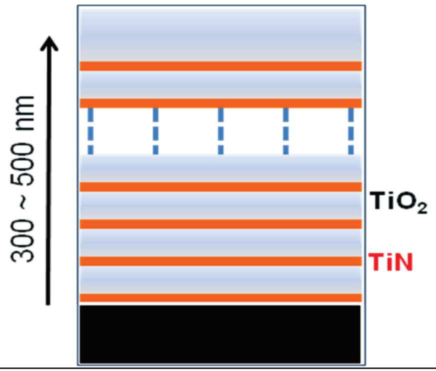

Fig.V-1: Schematic representation of TiO_2/TiN bi-layers.

The increased lifetime of the charge carriers due to TiO_2-semiconductor/metal coupling has shown the ability to significantly increase the photocatalytic and photo-electrochemical properties of these structures. Doping with transition metals can add stable energy levels just below the conduction band while the non-metals can add energy levels above the valence band. In both cases, the band gap can be decreased which can allow for the onset of visible light absorption but not always the photoactivity.

In this chapter, we studied a novel organization of TiO_2/TiN bi-layer (Fig.V-1) thin films created by RF reactive magnetron sputtering. Films were deposited with 9 bi-layers, 18 bi-layers, 27 bi-layers, 36 bi-layers, and 45 bi-layers, with different nominal TiN/TiO_2 ratio and all with the same total thickness (about 500 nm).

V-2) Strategy in this study

Intrinsic TiO_2 is a n-type semiconductor due to its Fermi level which is closer to the conduction band rather than the valance band (Fig.V-2). TiN has a cubic crystal structure and it has a very good advantage to act as a barrier against any metal diffusion. On the other hand TiN has a metallic behavior with electrical resistivity of 18 to70 $\mu\Omega\cdot$cm [16][46], other works found much higher resistivity for TiN [17]. The measured resistivity of our dense TiN films (prepared by sputtering Ti target in a reactive gas of nitrogen) were about 100 to 200 $\mu\underline{\Omega}\cdot$cm (chapter II). These higher values of the resistivity of our TiN could be simply explained by the natural oxidation of the topmost layer on the surface of the TiN thin films.

The Fermi level of TiN should be within its conduction band (TiN is a conductive compound). When stacking TiO_2 in perfect contact with TiO_2, the Fermi level of TiO_2 should shift to be at the same energy level as that of TiN (higher Fermi level, TiN has higher charge density) leading to band bending near the TiO_2/TiN interface and the formation of ***Schottky barrier*** as shown in Fig.V-2 (b). The band bending region within the TiO_2 layer is called the ***space charge*** which is reported to have a width of 2nm to 70nm [18-19].

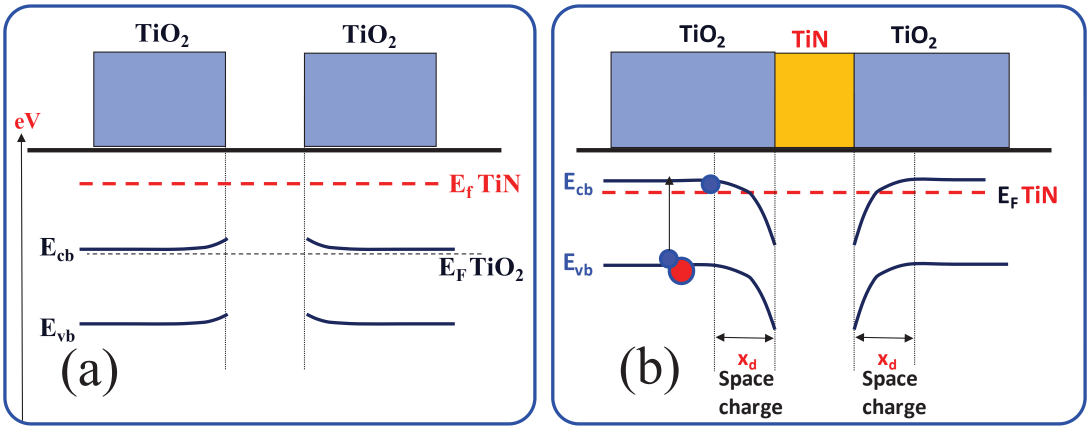

Fig.V-2: Electronic band structure of: a) TiO_2 thin film and b)one bi-layer of TiO_2/TiN showing the formation of two Schottky barriers .

A charge transfer (electronic transfer) takes place at the interface between TiO_2 and TiN to assure the electronic equilibrium. This results in a configuration with the curvature of the electronic bands and the formation of the “space charge” layer (its width is proportional to the difference between the Fermi energy level of TiO_2 and the TiN). In this TiO_2 space charge layer, a static electric field can affect the charge carriers in a nearby region, reducing the probability of electron-hole recombination, which can further increase the effective lifetime of the photo-generated electron-hole pairs.

To determine the best stack configuration we have to:

1) Optimize the number of TiO_2/TiN bi-layers to maximize the space charge width.
2) Optimize the thickness of each TiN layer in order to get the best percentage of nitrogen within the stack.

For a best understanding of the first objective, we can refer to Fig.V-3. In the case (a) the width of the resulted charge space is less than the thickness of the TiO_2 layer. The case (b) presents the ideal condition where the total charge space dimension becomes the same as that of TiO_2 layer, this can give the best separation between the photo-generated electron & hole, the photo-generated electrons will be guided to be trapped in the TiN layer. If the number of bi-layer increases more, there will be a competition between the generated charge spaces in the same TiO_2 layer (Fig.V-3 (c)). In this last case, where the thickness of the TiO_2 coatings becomes even less, and the charge space remains almost the same, the resulted electrical field will be less than that of case (b) due to the overlapping of a part of the charge space regions.

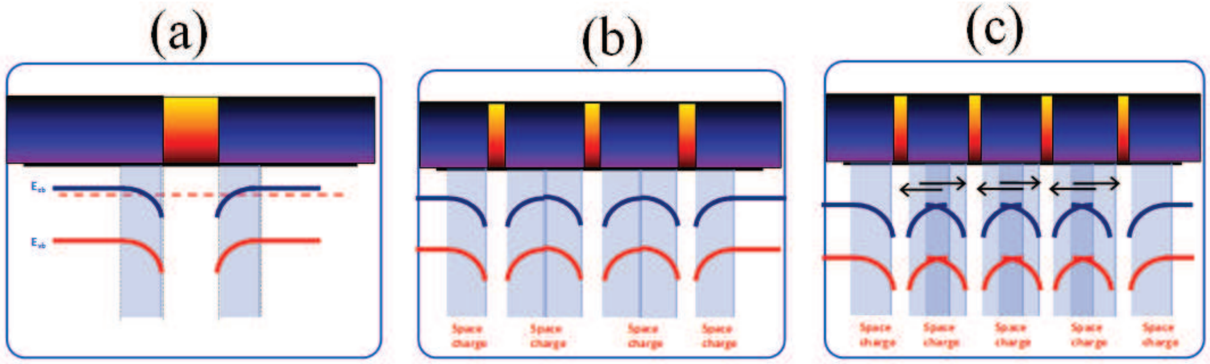

Fig.V-3: Three possibilities of charge space types resulted from the TiO_2/TiN hetero junctions: (a) space charge is less than TiO_2 thickness, (b) space charge equal to the TiO_2 thickness and (c) sum of individual space charge which overlap is higher than the TiO_2 thickness (competition).

V-3) Experimental

TiO_2 films and TiN films were fabricated in the same RF magnetron sputtering deposition chamber (described in chapter II). The depositions for the bi-layer films were carried out successively at the same vacuum and without opening the chamber between depositions, and thus have the same base pressure for both depositions, $p \sim 3$ to 7 x 10^{-6} torr, while the total working pressure was kept constant at 3 mtorr. All films were deposited using a metallic Ti target. The target was sputtered in a reactive gas atmosphere containing Ar + O_2 for TiO_2 films, and Ar + N_2 for TiN films. The argon gas flow rate was fixed at 30 sccm for both depositions, while for TiO_2 deposition the O_2 flow rate was 1.5 sccm , and the N_2 flow rate was fixed at 2 sccm for the TiN films (cf chapter II). The RF cathode power was 200 W (DC bias voltage of about 148 V) for all the depositions in order to minimize the target poisoning effect.

Prior to each multi stack deposition the target was pre-sputtered in argon atmosphere for 10 minutes to remove any contaminations or "poisoned film" from the target surface. The films were deposited on several substrates including electro-polished stainless steel, Si (100) and (101) wafers and ordinary microscope glass slides. Prior to deposition, the non metallic substrates were ultrasonically cleaned with acetone, ethyl alcohol and then de-ionized water for 20 minutes each. The substrate holder was maintained at 300°C and no bias was applied. The distance between the substrate holder and the target was fixed at 100 mm.

V-3-1) Deposition procedures

1) In a first step, we used a fixed composition of TiO_2 and TiN. By designing each film with the particular amount of bi-layers, we were able to create 17, 35, 53, 71, and 89 TiO_2/TiN heterojunctions in each respective sample. The only structural parameters that were

changed were the number of layers, and the thickness of each layer, allowing the ratio of TiO_2 to TiN to remain at a constant 5:1 ratio (20% TiN/TiO_2 thickness ratio) throughout each film. The deposition parameters and flowing time of each reactive gas are all regrouped in Table V-1.

2) Secondly, we optimized the TiN/TiO_2 ratio for the 9 bi-layer and the 18 bi-layer in order to get the best synergic effect of light absorption and charge separation based on the generation of the photo-electrochemical current. Table V-2 presents the deposition parameters for the 9 and the 18 bi-layer optimization, including the flowing time of each reactive gas (O_2 and N_2) in the sputtering reactor.

The structure of the stacked films is completed with the deposition of a TiO_2 layer of 20nm.

V-3-2) Thermal transformation and structural study

The first set of films were then annealed in a closed furnace at different temperatures, from $T_A = 450^oC$ to 950^oC for 2 hours in 100^oC intervals. Then the crystalline structure, of the as deposited and annealed bi-layers, was measured in order to examine the phase transition temperatures for TiO_2 from amorphous to anatase, and from anatase to rutile, depending on the thickness/number of the TiO_2 layers.

The crystalline properties of the films were characterized by X-ray diffraction (XRD) (X'Pert Pro PW3040-Pro, PANalytical Inc.) using a Cu Kα (λ = 1.5418 Å) X-ray radiation source.

V-3-3) Optical and photoelectrochemical measurements

Optical measurements were carried out by a UV-vis spectrophotometer (Varian 6000). Electrochemical measurements were performed at room temperature in a three-electrode cell and the setup of measurement is presented in paragraph II-2-5.

Two different electrochemical interfaces have been used in the electrochemical study:

1) BioLogic EC-Lab V9.00.
2) Solartron SI 1287.

Table V-1: deposition parameters for the different bi-layer deposited at fixed TiN/TiO$_2$ thickness ratio (20%).

bi-layers Nb (or cycles Nb)	TiO$_2$ (nm)	TiN$_2$ (nm)	Hetero junctions	Pressure	Ar	O$_2$	N$_2$	RF Power	Substrate temperature	Estimated total thickness
	O$_2$ flowing time (sec)	N$_2$ flowing time (sec)								
TiO$_2$	**500**	**0**	0	3 mtorr	30 sccm	1.5 sccm	2 sccm	200 W	300°C	500 ± 50 nm
	15600	0								
9	**43**	**11**	17							
	1576	158								
18	**22**	**6**	35							
	788	79								
27	**14**	**4**	53							
	525	53								
36	**12**	**3**	71							
	394	39								
45	**9**	**2**	89							
	315	32								

Table V-2: deposition parameters for 9 and 18 bi-layer deposited at different TiN/TiO$_2$ thickness ratio.

N° bi-layers	TiN / TiO$_2$ nominal ratio	TiO$_2$ (nm)	TiN (nm)	Ar	Pressure	O$_2$	N$_2$	RF Power	Substrate temperature	Estimated total thickness
		O$_2$ flowing time (sec)	N$_2$ flowing time (sec)							
9	30 %	**37**	**16**	30 sccm	3 mtorr	1.5 sccm	2 scccm	200 W	300°C	500 ± 50 nm
		1507	226							
9	20 %	**42**	**11**							
		1576	158							
9	15 %	**45**	**8**							
		1612	121							
9	10 %	**48**	**5**							
		1651	83							
9	5 %	**50**	**3**							
		1691	42							
18	30 %	**19**	**8**							
		754	113							
18	20 %	**21**	**6**							
		788	79							
18	15 %	**23**	**4**							
		806	61							
18	10 %	**24**	**3**							
		825	41							
18	5 %	**25**	**1.5**							
		846	21							

.

V-4) Results and Discussion

V-4-1) Morphology and appearance of TiO2/TiN Bi-layer thin films

The average thickness for all of the thin films was found to be *h* = 500 ± 50 nm. Based on the deposition rate, and the deposition time for each layer, we were able to estimate the thickness of each layer in the multi-layered films (Table V-1). For instance in the 9 bi-layer films with 20% TiN/TiO_2 ratio, the nominal thickness of each TiO_2 layer was h = 46.3 nm, while the thickness of the TiN layer was estimated to be h = 9.3 nm (Table V-1). For the 45 bi-layer films (20% TiN/TiO_2 ratio), the nominal height of each TiO_2 layer was h = 9.3 nm, while the height of the TiN layer was estimated to be h = 1.9 nm.

Different bi-layered thin films, deposited on glass slides, are presented in Fig.V-4. The transparency of the films is very much affected by the thickness of the TiN layers in the bilayes, i.e. the increase of the thickness of the TiN layer (from 1.9 nm to 9.3 nm) leads to a gradual decrease in the total transparency of the films.

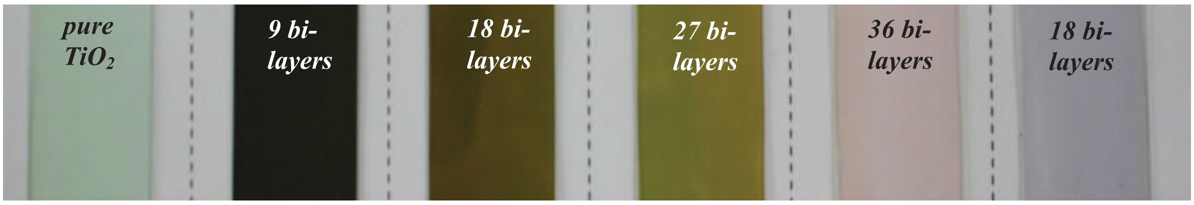

Fig.V-4: Photograph of the as-deposited films showing the range of colors produced for the different samples.

V-4-2) Crystal Structure of TiO_2/TiN Bi-layer Thin Films

The crystallographic properties of the as-deposited and annealed bi-layer samples (at T_a = 450°C, 550°C, 650°C, 750°C, 850°C, and 950°C) were determined by X-ray diffraction (XRD). Each sample was annealed for 2 hours at the above mentioned temperatures. In order to most effectively demonstrate the differences in the TiO_2 crystallinity as a function of the temperature for the bi-layer films, the calculated crystal size of the anatase and rutile crystals in each bi-layer and single layer TiO_2 thin film after various post-deposition annealing temperatures have been presented in Table V-3. The films with the fewest number of bilayers (9 bi-layers) and the highest number (45 bi-layers), are discussed in detail.

The XRD patterns for the as-deposited and annealed 9 and 45 bi-layer films are shown in Fig.V-5. The as-deposited films showed a very small and wide bump centered around 2θ= 25.4°, corresponding to the (101) orientation of the anatase crystal phase. This peak is very weak due to small crystal size and/or poor crystallinity in the as-deposited sample.

Table V-3: The calculated grain size of the anatase and rutile crystals in each bi-layer and single layer TiO_2 thin film at various post-deposition annealing temperatures.

Sample	***TiO_2***		***9 bi-layer***		***18 bi-layer***		***27 bi-layer***		***36 bi-layer***		***45 bi-layer***	
	A (nm)	R (nm)	A (nm)	R (nm)	A (nm)	R (nm)	A (nm)	R (nm)	A (nm)	R (nm)	A (nm)	R (nm)
As-dep	22.0	…	13.0	…	9.4	…	…	…	…	…	…	…
450^{o}C	43.0	…	21.9	…	15.8	…	35.1	…	37.4	…	45.3	…
550^{o}C	48.1	54.9	29.4	47.61	32.3	45.9	37.2	44.5	41.4	39.2	51.4	36.8
650^{o}C	62.9	68.9	42.3	66.24	42.9	60,7	50.7	58.7	52.1	54.2	60.7	44.5
750^{o}C	63.2	71.8	…	69.52	…	70.1	…	60.7	61.3	63.4	62.2	49.7
850^{o}C	63.2	78.0	…	74.80	…	74.5	…	65.4	61.8	65.6	62.5	59.5
950^{o}C	…	87.3	…	84.22	…	82.9	…	73.3	…	67.4	…	65.2

After annealing the 9 bi-layer film at T_a = 450^{o}C, the film showed a stronger peak at 2θ = 25.4^{o}, in addition to new small peaks at 2θ = 35.3^{o}, and 54.5^{o}, corresponding to the (004), and (200) orientations of the anatase phase of TiO_2, figureV-5 (a). When the film was annealed at T_a = 550^{o}C, the (101) anatase peak became much taller and thinner, showing a drastic increase in the anatase crystallinity. The intensity of the secondary anatase peaks at 2θ = 35.3^{o}, and 54.5^{o} also increased. In addition to the growth of the heights of the anatase peaks at this temperature, a small peak could be seen at 2θ = 27.5^{o}, corresponding to the (100) orientation of the rutile phase of TiO_2, showing that there was a mixed anatase/rutile phase composition of the film at this temperature. When this film was further annealed at T_a = 650^{o}C, the original (101) anatase peak at 2θ = 25.4^{o} became a barely noticeable bump in the pattern and the diffraction peak at 2θ = 27.5^{o} for the (100) rutile phase became dominant, increase its peak height several hundred times over the previous temperature. The peak is much narrower compared to the previous peak, which is due to an increase in the crystal size. After annealing at T_a = 750^{o}C, 850^{o}C, and 950^{o}C, the overall shape of the pattern remained the same, only showing the rutile phase diffraction peaks. The only change in the pattern is that the (100) rutile peak becomes taller and thinner as the temperature increases, again indicating an increase in crystal size. No diffraction peaks for TiN are present at any annealing temperature, perhaps due to the small thickness of the TiN layers.

The XRD patterns for the 45 bi-layer film annealed at the same temperatures are shown in Fig.V-5 (b). Again no peaks are seen for TiN due to the thinness of the layers. After annealing at T_a = 450^{o}C, the film revealed relatively strong peaks at 2θ = 25.4^{o}, 35.3^{o}, 48.2^{o}, and 54.1^{o}, corresponding to the (101), (004), (200) and (211) orientations of the anatase phase of TiO_2. After annealing at T_a = 550°C, all of the anatase peaks present at T_a = 450°C became more pronounced, increase their peak height. In addition, three new peaks arise at 2θ = 27.5°, 44.4°, and 54.4°, corresponding to the (100), (210), and (211) orientations of the rutile phase of TiO_2. This phase transition is identical to the 9 bi-layer films when annealed from T_a = 450°C to T_a = 550°C, which also changed from the pure anatase phase to an anatase dominated phase with a small amount of rutile. However, the 45 bi-layer film shows a different trend for the phase transition at higher temperatures. When this film was annealed at T_a = 650°C and 750°C, the XRD spectrum revealed a pattern that was very similar to the previous one, which was dominated by anatase and showed only a small amount of rutile.

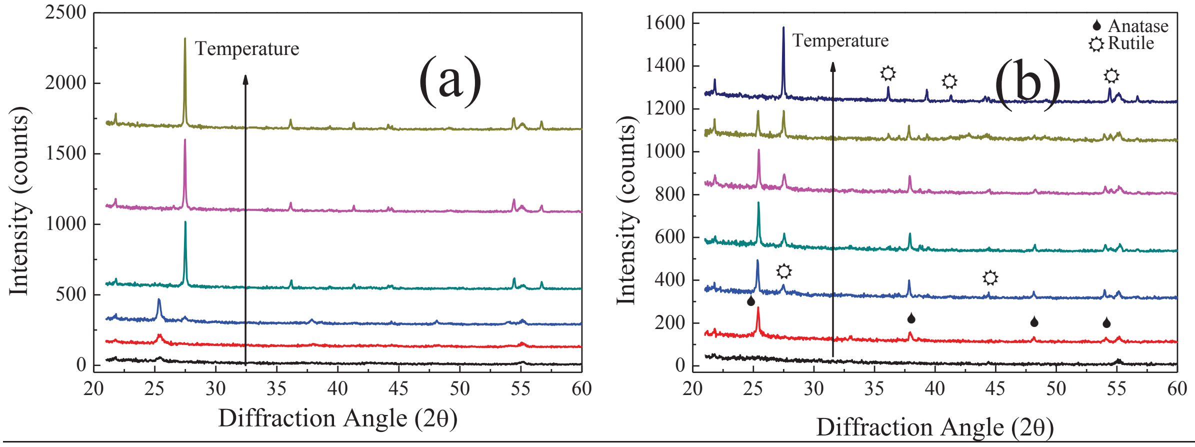

Fig.V-5: XRD patterns of (a) the 9 bi-layer film and (b) the 45 bi-layer thin films deposited on silicon. The patterns were taken of the as-deposited sample (bottom), and after annealing for 2 hours from T_A = 450°C to T_A = 950°C, in 100°C intervals.

After annealing at T_a = 850°C, the (101) anatase peak began to shrink, and the (100) rutile peak started to grow. In fact, at this temperature, the peak height for the (101) anatase peak and the (100) rutile peak were almost identical, revealing an almost uniformly equal composition of the two crystal phases. When this film was annealed at T_a = 950°C, the anatase peaks completely disappeared, and the XRD pattern was dominated by the rutile peaks, specifically the (100) peak which became very tall and very thin. The other bi-layer samples were analyzed similar to the above films, with the crystalline peaks and phase composition being observed accordingly.

V-4-2-1) Crystal size

From the XRD patterns, it is also possible to determine the crystal size of the anatase and rutile crystals using the Scherrer formula (Eq.III-2, chapter 3). For the anatase crystal, the (101) peak located at 2θ = 25.4° was used, while for the rutile crystal, the (100) peak located at

$2\theta = 27.4^o$ was considered. The crystal size for the anatase and rutile phases at each annealing temperature were calculated for each of the bi-layer films, as well as for the pure TiO_2 film using Eq.III-1, the values of crystal sizes obtained are shown in Table V-3. There are several trends, versus annealing temperature, which are apparent for all the samples depending on the number of layers. To further highlight these changes, the anatase and rutile crystal size were plotted with respect to the post-deposition annealing temperature and number of bi-layers in Fig.V-6 (a) and (b), respectively.

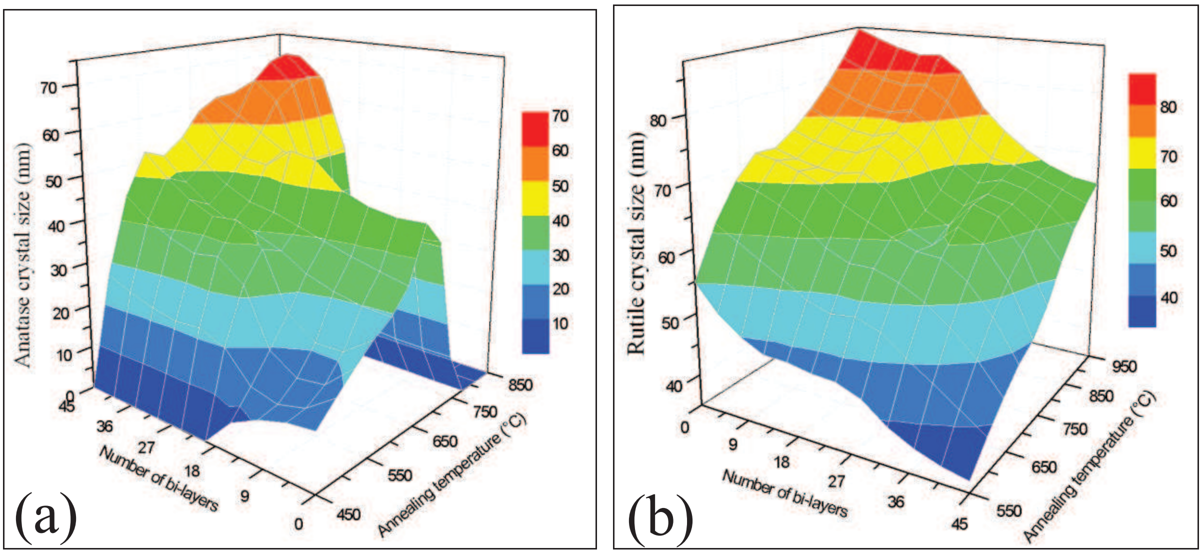

Fig.V-6: The crystal size as calculated from XRD as a function of the number of bi-layers and annealing temperature for (a) the anatase crystals and (b) the rutile crystals (note that the bi-layers order is reversed between (a) and (b)).

Regardless of the number of layers, as the post-deposition annealing temperature increased, so did the crystal size (without taking into account the emergence or disappearance of each crystal phase). This trend is consistent with previous literature regarding the crystal size of TiO_2 at high temperatures [20]. It is interesting to note that as the number of layers increased, the average size of the ***anatase*** crystals also increased, at fixed annealing temperature and before the appearance of rutile phase (< 550°C). This is an unusual trend because as the number of layers increased, the thickness of each TiO_2 layer decreased, giving less vertical space for the crystals to form. This pattern suggests that as the TiO_2 layer thickness decreased,

- either the anatase crystals grew along the horizontal axis parallel to the substrate,
- and/or the anatase crystals span several layers.

This latter possibility would be very interesting, because it would effectively place the thin TiN layers in the middle of a larger TiO_2 crystal, which could then act as an original nitrogen-doped

TiO_2 crystal. Such films should thus have a significant impact on the optical properties, the electronic structure as well as the photo-activity of the films.

In the as deposited films, the crystallization of the anatase phase seemed to be dependent on the thickness of the TiO_2 layers as well. The as-deposited pure TiO_2 thin films showed an anatase crysal size of d = 22 nm, the only other films which showed an as-deposited anatase crystal structure were the 9 bi-layer, and 18 bi-layer, which have TiO_2 layer thicknesses of 46 nm and 23 nm respectively. This suggests that the ***anatase formation during deposition requires at least 23 nm space to form****, which is consistent with the crystal size of the TiO_2 film (22 nm), and which is very close to the thickness of TiO_2 in the as deposited 18 bi-layer film (23nm).*

<u>V-4-2-2) Anatase to Rutile ratio</u>

In order to calculate the phase content of each sample, the peak intensities for the rutile peak (100) and anatase peak (101) can be compared. The fraction of anatase in each sample, f_A, can be calculated using the following equation (Yan's method) [2]:

$$\boxed{f_A = \frac{1}{1 + \frac{1}{K}\frac{I_R}{I_A}}} \qquad \text{Eq.V-1}$$

where K is a constant (K = 0.79 for $f_A > 0.2$, and K = 0.68 for $f_A \leq 0.2$), I_R is the height of the (100) rutile peak, and I_A is the height of the (101) anatase peak. It is straight forward to calculate the fraction of rutile, f_R, in each sample,

$$f_R = 1 - f_A \qquad \text{Eq.V-2}$$

Using Equation (Eq.V-1) and Equation (Eq.V-2) it is possible to examine how the fraction of anatase and rutile change for each bi-layer sample as a function of temperature. The percentage of anatase for each of the bi-layer samples as well as the pure TiO_2 film is calculated in Table V-4 and plotted in Fig.V-7 as a function of the annealing temperature. The general trend for each sample is that the anatase phase emerges predominantly after annealing at T_A =450°C, which is consistent with prior experiments and literature [20]. After annealing at T_A =550°C, the rutile phase emerges for each bi-layer sample, and thus the percentage of anatase begins to decrease. The pure TiO_2 film shows the most stable anatase phase at high temperatures, and is dominated by anatase up to T_A = 850°C. The 45 bi-layer film shows the closest trend to the pure TiO_2 film, remaining predominantly anatase up to T_A=750°C (Table V-4).

A possible explanation for the large variance in the phase change temperatures can be ascribed to the TiN films that border the TiO_2 layers. TiN is a hard barrier material which could prevent material diffusion [21-23][47], and can possibly make it harder for the anatase TiO_2 crystals to increase their size close to the TiO_2/TiN boundaries. When the film layers are very thin, this boundary effect may not be large enough to affect the whole TiO_2 layer because it could be easily oxidized to form TiON, while in the thicker TiN films this boundary effect can be felt throughout the entire surrounding TiO_2 layers. However, thin films of TiN begin to oxidize to rutile TiO_2 between T_A = 650°C and 750°C, this oxidation process is developed in more detail in the next chapter.

Table V-4: The fraction of rutile (f_R) calculated by the Yan method [2]. *The value of f_R was used to calculate the fraction of anatase (f_A).*

T_A	9 bi-layers	18 bi-layers	27 bi-layers	36 bi-layers	45 bi-layers	TiO_2
450°C	0	0	0	0	0	0
550°C	30	29.6	28.9	28.6	25.3	0
650°C	93.7	65.8	47.7	31.2	27.2	5
750°C	96.8	97.6	92.8	37.4	32.6	10
850°C	100	100	100	100	56.9	35
950°C	100	100	100	100	100	100

The overall trend for the bi-layer films is that as the number of layers decreases, the anatase to rutile phase transition shifts to lower temperatures (from 850°C to 550°C). For instance, the 9 bi-layer film is only dominated by the anatase phase (anatase>50%) up to T_A=550°C, but the 45 bilayer film can be dominated by the anatase phase up to 800°C.

After annealing at T_A = 850°C, all of the bi-layer films became rutile, with no discernable peaks for TiN present. For the bi-layer films with a thicker layer of TiN, i.e. the 9 layer film, the rutile phase arises and is dominant at T_A = 650°C. At this temperature, the deep TiN layers were supposedly not-oxidized and should show no peaks for rutile TiO_2, meaning the origin of the rutile peaks can be attributed to the phase change within the TiO_2 layer, and not the TiN layer (we didn't observe any diffraction peaks for TiN even with the 9 bilayers, because the maximum TiN thickness was still less than the detection limit of our diffractometer. Maybe by using grazing angle XRD, TiN diffraction peaks could be detected. For the films with thinner TiN layers, i.e. the 45 layer film, a rutile diffraction peak was found beginning at T_A = 650°C to 750°C, which could be from:

- the oxidation of the thin (2 nm) and dense TiN film leading to Rutile TiO_2 at elevated temperature (see chapter V).
- the thermal transformation of the dense TiO_2.

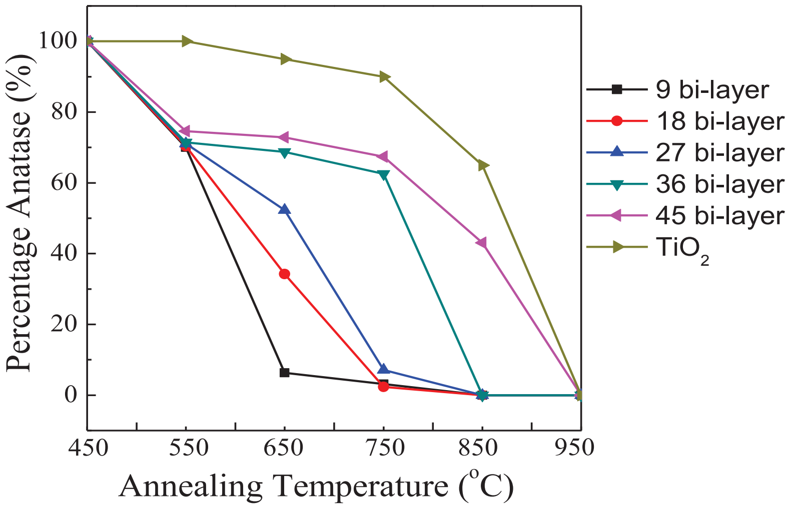

Fig.V-7: Plot of the Anatase phase percentage estimated by the method of Yan et al.[2]*, for different number of bi-layers vs post- annealing temperature.*

It seems more reasonable to assert that the variance in the phase transition temperature found in the TiO_2 layers is due to either the spatial confinement of the TiO_2 layers, the thickness of these layers, possible boundary effects from TiN, or from a small amount of nitrogen doping present at the boundary layers. Arbiol et al. reported that doped TiO_2 films showed distinct changes in their crystallography and phase transition temperatures due to the effects of doping, which are consistent with our results [24].

V-4-3) Optical Properties

V-4-3-1) Transmission and reflection

A predominant aspect of the bi-layer films was their change in color and transparency which were both a function of the number of layers and TiN/TiO_2 thickness. From the photograph in Fig.V-4. The pure TiO_2 film is almost completely transparent compared to the films with different layers of TiN. The films with thicker TiN (smaller number of layers) appear to be the darkest, and the films got progressively lighter as the TiN layers became thinner. This description of the color change in the samples is only subjective, but it is used to provide quantitative agreement with the optical properties measured by spectroscopy.

The optical properties for the TiO_2 and bi-layer thin film samples were measured before and after annealing at T_a = 450°C. The transmission and reflection spectra for each sample were measured directly, and the spectra for the annealed films are shown in Fig.V-8. The TiO_2 single layer film showed high transmission at longer wavelengths with distinct interference oscillations, then a sharp decrease began around λ = 380 nm toward smaller wavelengths. The transmission spectra looked very similar for the 45- and 36 bi-layer thin films, with a very small increase in the transmission onset, shifting further out to longer wavelengths by several nanometers. However, the transmission spectra for the 9-, 18-, and 27 bi-layer films differ greatly from the previous films. The 27 bi-layer films showed a similar trend to the previous samples, but the transmission onset at lower wavelengths had shifted out to λ = 391 nm, and showed a slightly lower overall transmission at higher wavelengths. The 9- and 18 bi-layer films showed small transmission at higher wavelengths, with the 9 layer films showing the lowest overall transmission. The transmission for both films significantly decreases at around λ = 466 nm, a marked shift out to the visible range from the TiO_2 film and bi-layer films with 36 or more layers.

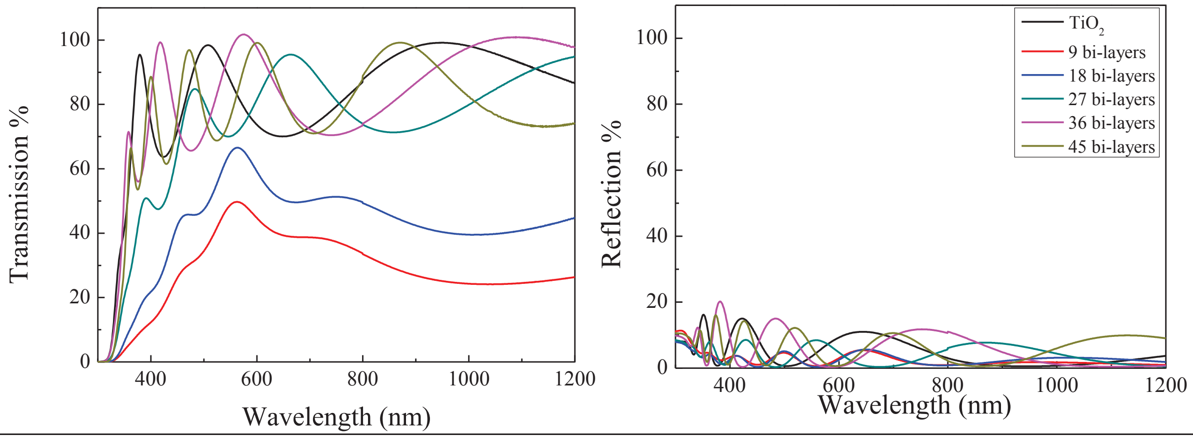

Fig.V-8 : Transmission (a) and reflection (b) spectra for the pure TiO_2 (black), 9 bi-layer (red), 18 bi-layer (blue), 27 bi-layer (green), 36 bi-layer (pink), and 45 bi-layer (gold) films as shown in Fig.V-4.

The reflection spectra for all the samples showed similar trends, with only slight differences in the number and height of oscillations (Fig.V-8 (b)). Each film showed distinct oscillations beginning at longer wavelengths, and they continue to shorter wavelengths. The only noticeable difference in all of the samples is that the 9 and 18 bi-layer films had a slightly decreased reflection throughout the spectra, but the overall shapes of the spectra remain very similar.

V-4-3-2) Optical band gap

In order to obtain the effective optical band gap of the single layer and bi-layer films, we have calculated the absorption spectra using the following equation [25-27]:

$$A = \alpha d = \ln\left(\frac{(1-R)^2}{2T} + \left(\frac{(1-R)^4}{4T^2} \right)^{1/2} \right) \qquad \text{Eq.V-3}$$

where A is the absorbance, α is the absorption coefficient, d is the thickness of the sample, and R and T are the reflection and transmission spectra. The calculated absorbance spectra for the annealed samples are shown in Fig.V-9. The TiO_2 film showed very low absorbance at visible light wavelengths, and the absorption increased drastically for $\lambda \leq 360$ nm. Similarly, the 45- and 36 bi-layer films showed very low absorbance at higher wavelengths, and their absorption on-set shifted out to $\lambda = 365$ nm and $\lambda = 376$ nm, respectively.

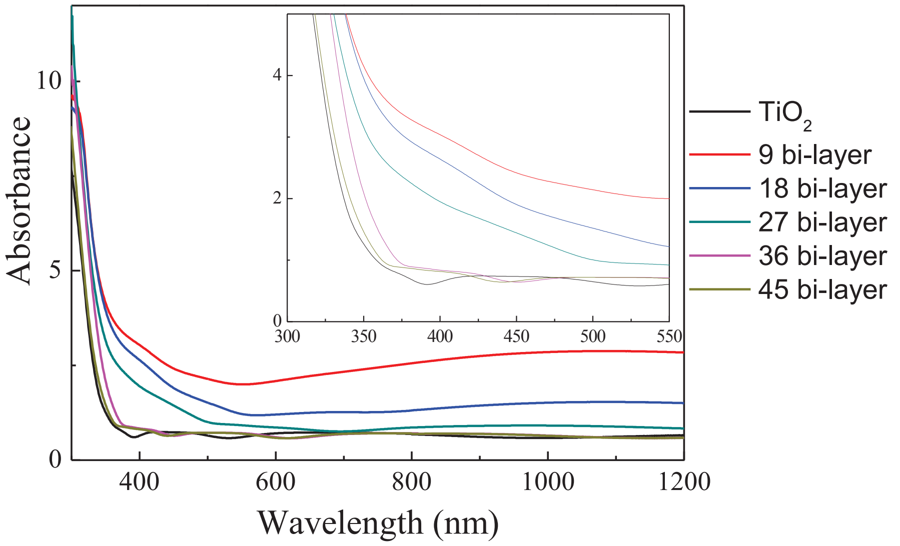

Fig.V-9 : Calculated absorbance spectra for the pure TiO_2 (black), 9 bi-layer (red), 18 bi-layer (blue), 27 bi-layer (green), 36 bi-layer (pink), and 45 bi-layer (gold) films. The insert in the figure shows a zoomed in view of the absorption onset region, between $\lambda = 300$ nm and $\lambda = 550$ nm.

The 27 bi-layer film showed a drastic change in the shape of its absorption spectra. The absorption was very low at higher wavelengths, but began to increase steadily at around $\lambda = 500$ nm, then dramatically at around $\lambda = 369$ nm. The 9- and 18 bi-layer samples both showed higher absorption at higher wavelengths, with the 9 bi-layer sample showing the highest absorption. In addition, the absorption onset for the 18 and 9 bi-layer samples shifted out to around $\lambda = 550$ nm for both samples. The shift in the absorption spectra for the samples with 9, 18, and 27 bi-layer samples could be due to the effect of the TiN layers within the thin films:

The thin TiN layers, imprisoned between the larger TiO_2 layers, could have some light absorption, but also TiN could involve many light reflections (within the film) which then will be absorbed **again** by the TiO_2 layers, this could multiply the light pathway and so the light absorption. This effect could be pronounced in the 9, 18 and 27 bi-layer samples due to the thickness of the TiN layers, whereas this phenomenon is not seen in the samples with 36 and 45 bi-layer because the TiN layer is too thin.

Also, there is a possibility that the interface between the TiO_2 and TiN layers could allow for a small amount of nitrogen diffusion into the TiO_2, creating a layer of nitrogen-doped TiO_2. N-doped TiO_2 has shown the ability to effectively absorb visible light.

The effective optical band gaps were also calculated for each sample. In order to obtain the band gap for the thin films, we plotted $(\alpha h\nu)^{1/2}$ vs. hν, shown for the annealed samples in Fig.V-10. The band gap energy can be obtained by following the linear portion of this plot through the x-axis, the calculated values were placed into Table V-5 for comparison. There are several interesting trends that can be seen from this table.

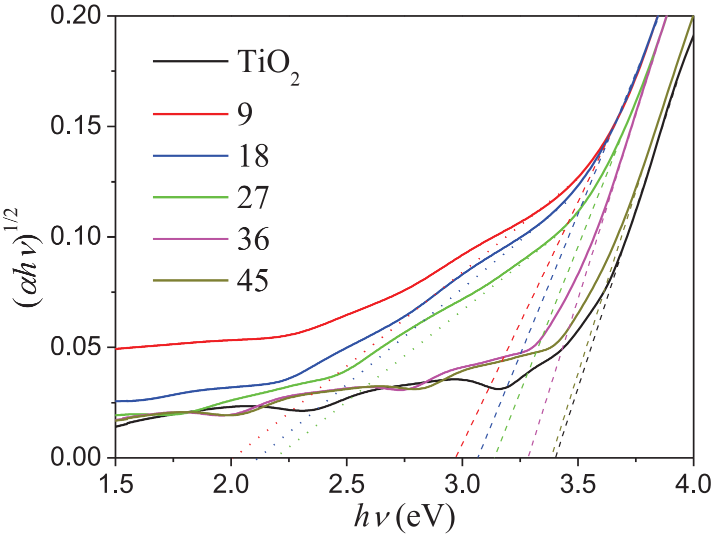

Fig.V-10: Tauc plot used to extract the band gap energy for the pure TiO_2 (black), 9 bi-layer (red), 18 bi-layer (blue), 27 bi-layer (green), 36 bi-layer (pink), and 45 bi-layer (gold) films.

The pure TiO_2 films showed a band gap of E_g = 3.40 eV which is within the experimentally reported values for TiO_2 in literature [28][48]. The samples with 45 and 36 bi-layers showed a band gap energy closest to the pure TiO_2 before and after annealing. This can be due to the small thickness of the TiN layers in these films. It is possible that the TiN layers were so thin that they had a very small or negligible effect on the optical properties of TiO_2, similar to how these samples were the closest to the pure TiO_2 in crystallinity found in the XRD patterns. However, as the thickness of the TiN layers (and TiO_2 layers) increased, the band gap appreciably decreased. A minimum band gap energy is achieved in the 9 bi-layer sample, showing an energy close to E_g = 2.96 eV (after annealing), which corresponded to a wavelength of λ = 419 nm. The main decrease in the band gap may result from the interface between the film layers, which can create an N-doped TiO_2 layer, which has shown the ability to shift the absorption of TiO_2 from the UV range to the visible.

Post annealing process seems to decrease the apparent band gap for the stacks with a low number of layers (9 to 18 layers). The band gap decreased after the post annealing due to the enhanced crystallinity and the increase in the crystal size (up to 22 nm). However the annealing process has an “apparent” minor effect on the band gap in the case of stacks composed of a higher number of layers (36 and 45 layers) as well as the pure TiO_2. This difference in the annealing effect, could be explained by the higher increase in the crystal size of the pure TiO_2

film, the 36 and the 45 bilayer (about 43 nm). In fact, it seems that the crystal size has a positive effect decreasing the band gap when the former increases up to 22 nm. Then, if the crystal size further increases, the band gap increases again which is consistent with the conclusion found in chapter 3 (see Fig.III-7 and III-9).

Table V-5. Calculated band gap energy for different bi-layers and single layer TiO_2 thin film before (as-deposited/A.D.) and after (450^oC) annealing.

Sample	TiO_2		9 layer		18 layer		27 layer		36 layer		45 layer	
	A.D	450^oC	A.D	450^oC	A.D	450^oC	A.D	450^oC	A.D	450^oC	A.D	450^oC
E_g (eV)	3.42	3.40	3.08	2.96	3.16	3.07	3.17	3.13	3.30	3.28	3.40	3.39

V-4-3-3) Main and secondary band gaps

In addition, secondary band gap energies can also be estimated for the 9, 18, and 27 bi-layer samples, because they exhibit an extra shoulder of absorbance, with a second linear portion that can also be extracted to the zero-point. If these areas are extracted, the band gap energies correspond to E_g = 2.01 eV, 2.12 eV, and 2.20 eV for the 9, 18, and 27 bi-layer samples, respectively. These energies correspond to visible light absorption at λ = 617 nm, 585 nm, and 563 nm, which are slightly higher than the initial absorption edges seen in the absorbance spectra for these samples (Fig.V-9).

The secondary reduced band gap could result from the heterogeneous junctions between the film layers, which can create other defects and doping states within the gap of the N-doped TiO_2 layer, that could promote the electron excitation from the valance band to the intermediate states and then to the conduction band.

V-4-4) XPS surface Analysis

Theoretically, as the upper layer of each multi stack film is a 20 nm of pure TiO_2, the XPS data should provide only the characteristics of this thin layer, but it can show the influence of the deeper layers on the superficial TiO_2 one (as nitrogen diffusion to the surface, the change in the electronic structure on the surface,... etc).

V-4-4-1) Ti 2p and O1s Peaks Observation and Analysis

Fig.V-10 presents the different trends of the O 1s core level spectra as well as in the Ti 2P spectra for samples prepared at fixed TiN ratio (20%) within the stack, as we change the number of layers.

Other than the Ti 2p$_{1/2}$ peaks, the spectra of the pure and stacked TiO$_2$ films exhibited a Ti 2p$_{3/2}$ peak at binding energies between 458.4 and 459 eV, which is in agreement with the values reported for anatase TiO$_2$ [29-33]. This indicated that the titanium was in a fully oxidized state of Ti^{4+} in the stacked films (O–Ti–O bonds of anatase) [34][20].

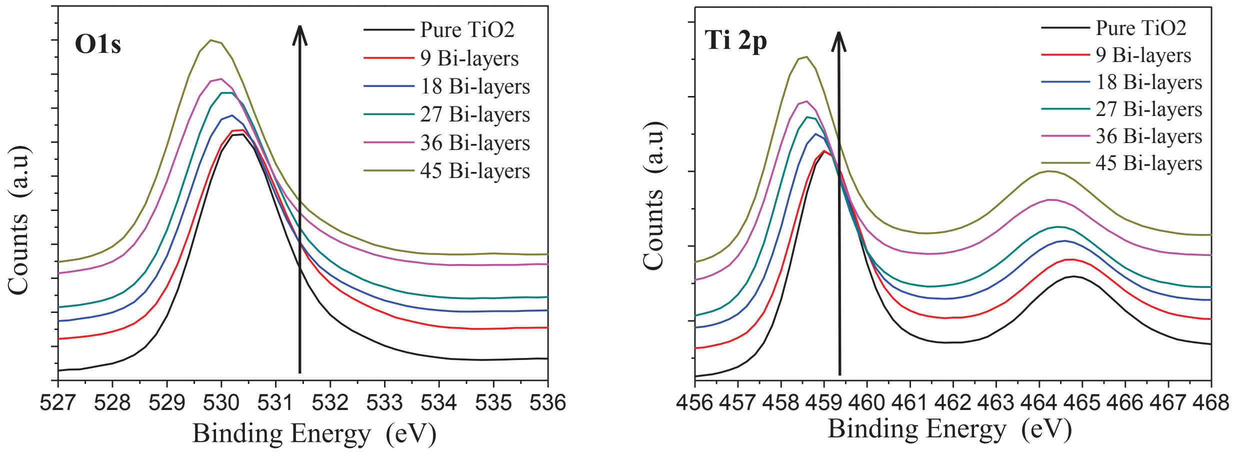

Fig.V-10: XPS O1$_s$ core level spectra and Ti 2p spectra including 1/2 and 3/2 spins, for different bi-layers (9 to 45) with fixed TiN ratio (20%).

On the other hand, as the number of layers increased, the Ti 2p peak shiftd towards lower binding energies (459 eV to 458.4 eV) which means that there is a change in the chemical environment for the titanium. This shift could be explained by many reasons:

- *partial reduction of the titanium cations and the formation of oxygen vacancies within the lattice.*
- *the bonding of Ti with lower electronegative species than oxygen, such as the formation of Ti—N bonds within the TiO$_2$.*
- *or the change of the electronic affinity of the stacked TiO$_2$/TiN material.*

The electrostatic charging has been already corrected by setting the C 1s spectrum at 285 eV and applying the resulted shift to all the other spectra. However, the partial reduction of Ti could be excluded as the same shift has been detected in the O 1s peaks. Indeed, energy shift between Ti 2p$_{3/2}$ and O 1s is about ***71.4 eV*** which is the same for all the bi-layer films, this means that the stoichiometry of the topmost TiO$_2$ layer is the same for all of the analysed samples. Also, the incorporation of nitrogen species could become favoured only in partially reduced titanium oxide networks, so the Ti—N species could appear only when the oxide is defective. But the presence of Ti—N bonds could be also excluded since the N 1s spectra (Fig.V-11) present a broad nitrogen peak centred at about 400 eV corresponding to trapped chemisorbed nitrogen molecules [35-38]. Indeed titanium nitride (Ti—N) bondings are usually detected at 397eV [37] [39-44].

So, ***the change in the electronic affinity is the main reason for the shift in Ti 2p peak as the number of layers increases.*** The electronic affinity of pure TiO_2 is supposed to be slightly higher than 4.2 eV as the conduction band of TiO_2 is at 4.2 eV (as compared to the vaccum level). As the number of bi-layers increases, the thickness of each TiN layer in the stack decreases and the space charge capacity should change. The variation in the charge space affects the total electronic affinity of the stacked TiO_2/TiN film. Laidani et al. [45] already proposed that the shift in binding energy could result from the variation of the position of Fermi level with respect to the core lines in the case of TiO_2 having intrinsic defects.

It is useful to mention that, the photo-emitted electrons that have escaped into the vacuum of the XPS instrument are those that originate from a maximum of the top 10 nm of the material. All of the deeper photo-emitted electrons, which were generated as the X-rays penetrated 1– 5 micrometers in depth of the material, are either recaptured or trapped in various excited states within the material.

The same samples also exhibited a main O 1s peak at 529.8 eV to 530.4 eV (assigned to O—Ti—O bonds) which are reported to be the typical oxide peak in titania [32-33]. The same reasoning, as seen with the Ti 2p shift could be applied for the shift observed towards lower binding energies (530.4 eV to 529.8 eV).

V-4-4-2) N 1s Peaks Observation and Analysis

Fig.V-11 (a) presents an example of XPS spectrum of O 1s core for the 18 bi-layer sample after deconvolution. Fig.V-11 (b) presents the XPS spectrum of N 1s core level for the samples prepared at fixed TiN/TiO_2 ratio as the number of layers changes from 9 to 45. The presence of the O 1s shoulder at higher binding energy, between 531.5 eV and 532 eV, (Fig.V-11(a)) suggests:

- the presence of hydroxyl (–OH) groups on the surface of these samples (contribution of Ti—OH bonds) [21].
- And/or the presence of C—O bonds (531.5 eV) and C=O bonds (533 eV) as a surface contamination [45].
- and /or the formation of Ti—O—N bonds on the surface of TiO_2 due to interstitial incorporation of nitrogen [33].

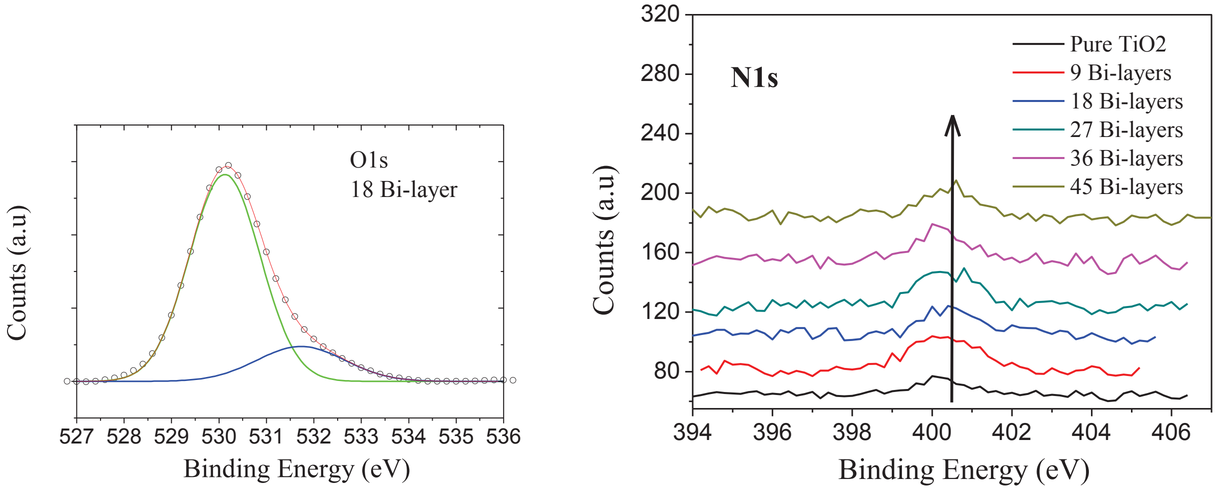

Fig.V-11 (a) An example of fitted O 1s spectra for the 18 bi-layer and (b) N 1s core level spectra for different number of layers with fixed TiN ratio (20% as compared to TiO2 thickness).

The last suggestion concerning the attribution of the chemical shift of O1s can be excluded as no peaks, in the N 1s core level spectrum, corresponding to interstitial N (at 402 eV) or even substitutional N (at 396~398 eV) were detected on the surface of the bilayer coatings (cf Table IV-2). The presence of hydroxyl groups and also the hydrocarbon contamination are both possible especially as the N 1s spectra (Fig.V-11 (b)) presents a large nitrogen peak centred at about 400 eV, corresponding to trapped chemisorbed nitrogen molecules N_2 or some O—N bonds, due to nitrogen contamination from the residual nitrogen gas in the sputtering reactor or from the ambient atmosphere.

V-4-5) Photo-electrochemical properties

A white lamp (125 W, PHILIPS) has been used as illumination source. In all the Photo-electrochemical measurements (the emission spectra of the lamp is presented in annex 6).

Potentiodynamic sweeps of the bi-layers films and the single TiO_2 film were measured under white light (UV and visible irradiations), as presented in Fig.V-12. For simplicity, we restricted the study here for fixed TiN ratio in the films (20% as compared to the thickness of the TiO_2 layer) and we studied the effect of changing the number of layers (from 0 to 45).

To investigate the photolectrochemical activity under different irradiation condutions (dark, UV light and visible light) the photocurrent response has been measured at fixed DC bias (0.5 V/ref) in intermittent way (30 sec white irradiation and 30 sec dark) for 210 seconds. From that point (210 sec to 300 sec), a UV filter was used (to cut the UV irradiations of the white light) in order to measure the photocurrent generated under visible irradiation from the same lamp (Fig.V-13). These measurements have been done for all the samples using (AgCl/Ag) as reference electrode.

V-4-5-1) Potentiodynamic Sweep response

The linear sweep voltammograms (Fig.V-12 (a)) show a similar trend for the different bi-layer films. The open circuit voltage (OCV) is about -0.5 to -0.6 V/ref, that means ***there is no significant change in the upper electronic structure*** between the different bi-layer films. In the cathodic part, the photocurrent is in the order of 1 µA when the voltage is between -0.5 down to -0.6 V/(AgCl/Ag), then the cathodic current increases significantly between -0.7 and -0.8 V/(AgCl/Ag) due to the increase in hydrogen generation (on the TiO_2 film).

As the anodic biasing increases, the positive photocurrents increase and the increase rate is more significant for biasing values higher than -0.1 V/(AgCl/Ag) before reaching the quasi-stationary photocurrent which corresponds to the maximum charge separation. At higher biasing/(AgCl/Ag), this stationary current is limited by the flux of the photons and their energy reaching the surface of the studied film. The measurements were stopped at 1.0 V/(AgCl/Ag) to prevent any etching on the films due to the high oxygen generation rate at higher biasing voltage.

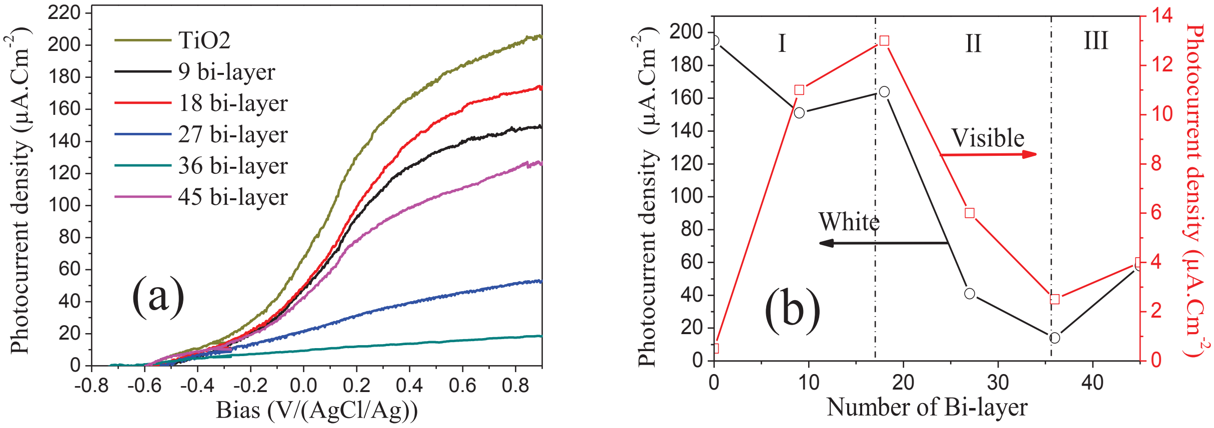

Fig.V-12: a) Linear sweep voltammograms under white light irradiation and b) measured photocurrent density at 0.5 V/(AgCl/Ag) under white and visible irradiations, for pure and different bi-layer thin films, see also Fig.V-13.

Fig.V-12 (b) presents the measured values of the photocurrent density at fixed bias of 0.5V/(AgCl/Ag) as a function of the number of layers, at fixed TiN/TiO_2 ratio (20%). The pure TiO_2 presents the highest photocurrent under white light and negligible photocurrent under visible light, due to the efficient UV light absorption but not for the visible wavelengths. So, the addition of thin TiN layers has shown a remarkable ability to absorb visible light and create mobile electron-hole pairs. This supports the UV-Vis data, which showed the bi-layer samples shifted their absorbance bands out to the visible light region.

Also, in the bi-layered films, the white light photocurrent is 15 time higher than the visible light one. This disparity is understandable, because the absorption spectrum for this film shows significantly larger absorbance at UV wavelengths than at visible wavelengths. ***This can lead us to propose that the visible light absorption (photo-activity) is due to the presence of new energy states in the gap of TiO_2 rather than the valence band shift, in addition to the efficient charge separation which will be seen in the section (V-4-5-4).***

V-4-5-2) Different features affecting the photo-electrochemical response

In Fig.V-12 (b) we can distinguish three regions:

Region I: Initially, as the number of layers increases from 9 to 18, the photocurrent increases. This can be due to the increase in the number of hetero-junctions that promote effective charge separation. The 18 bi-layer films has almost the double of the amount of TiO_2/TiN junctions as the 9 bi-layer films, so it is straightforward to assume that the increase in junctions is directly related to an increase in charge separation due to the addition of more ***charge space*** in the TiO_2 layers (Fig.V-3 (b)).

Region II: However, the 27 bi-layer films show a sharp decrease in photocurrent generation as compared to the 18 bi-layer films. While the 27 layer film has more heterojunctions than the 9 and 18 bi-layer films, it produces significantly less photocurrent under UV and visible irradiations. This can be the result of overlapping in the charge space regions, which can have a destructive effect on the charge separation. If the photogenerated carriers are free to move within the TiO_2 layer after excitation, they can feel an equal and opposite pull toward the opposing TiN layers (Fig.V-3 (c)). When two such regions overlap, the result is that the charge carriers (electron-hole) will not separate efficiently, leading to the decreased lifetime as electrons will be more likely to recombine with holes. As this effect was seen in the transition from the 18 to 27 bi-layer films, we can assume that the critical effective charge separation region is a distance in between the thickness of the TiO_2 layers for these two films. Furthermore, since the effective space charge region is close to the TiO_2/TiN interface, and there are two of these interfaces in each TiO_2 layer, we can assume that the effective charge space is half of the thickness of these TiO_2 layers. ***Using this, we can assume that the effective charge space region is between 12 nm and 22 nm*** (half of the thickness of TiO_2 layer in the 18 and 9 bi-layers, respectively, see Fig.V-3) for our films (Table V-1). However, the thickness of the TiN layer may also be a factor in the depth of the space charge region, so further experiments with various TiN thicknesses have been carried out (see the next section).

Regions III: further increase in the number of bi-layer results in a slight re-increase in the UV photo electrochemical efficiency, this increase is less pronounced in the visible light response. This is not surprising as the increase in the number of bi-layers at the same total thickness leads to a reduction in the thickness of TiN which could diffuse in the TiO_2 layers to form a homogeneous film of TiO_xN_y. Assuming this hypothesis, the space charge modelling is more difficult and the proposed model in (Fig.V-3) is no more applicable.

V-4-5-3) Intermittent Photocurrent in potentiostatic configuration

Fig.V-13 (a) presents the performance of different bi-layer films prepared at fixed TiN thickness ratio (20% as compared to TiO_2 layers in the stacked films) and irradiated with intermittent white light (t_{on}= t_{off}= 30 sec) the photocurrent was measured at a bias of 0.5 V/(AgCl/Ag). Dark photocurrent (no light irradiation) was less than 1 µA for all theses samples. This figure can give us a clear idea about the evolution of the electrochemical photo-activity under the different illumination conditions, white light, dark, and visible light (the UV irradiations were stopped during the last 90 seconds in Fig.V-13 (a)).

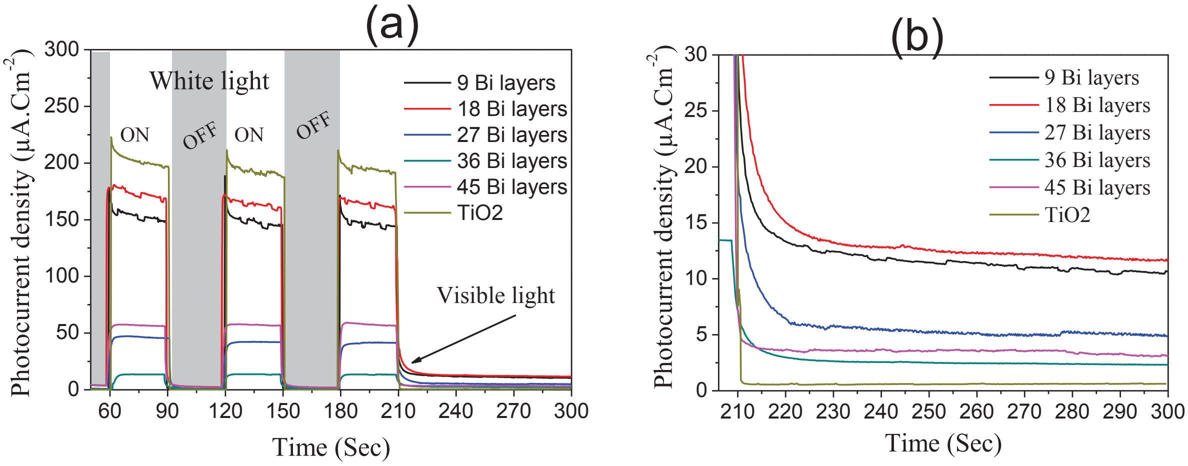

Fig.V-13: Photocurrent generated at 0.5V/(AgCl/Ag, under (a) intermittent white light/dark irradiations and (b) visible light irradiations for each of the bi-layer films and that of TiO_2 single layer.

Fig.V-13 (b) presents the evolution of the measured photocurrent when we switched from the white to visible irradiations. A small memory effect could be recognised with the bi-layered films, as the stabilization of the visible light photocurrent (and also dark one) takes place within 10 to 20 sec after cutting off the UV irradiations. This supports that the recombination rate of the charge carriers could be reduced when dealing with bi-layered films due to the electron trapping and transfer in the TiN layer. The 9 and 18 bi-layers give the nearest performance to TiO_2 under UV light with more efficiency under visible irradiations; this encouraged us to look at the effect of increase the TiN percentage within these films, as discussed in the next paragraph.

V-4-5-4) Effect of TiN layer thickness on the photo-activity

We restricted this study only to the case of 9 and 18 bilayers (Table V-2). Nominal TiN ratio has been varied between 5% to 30% (loaded TiN in the TiO_2 film). We measured the photo-induced electrochemical current using the same standardized setup as before.

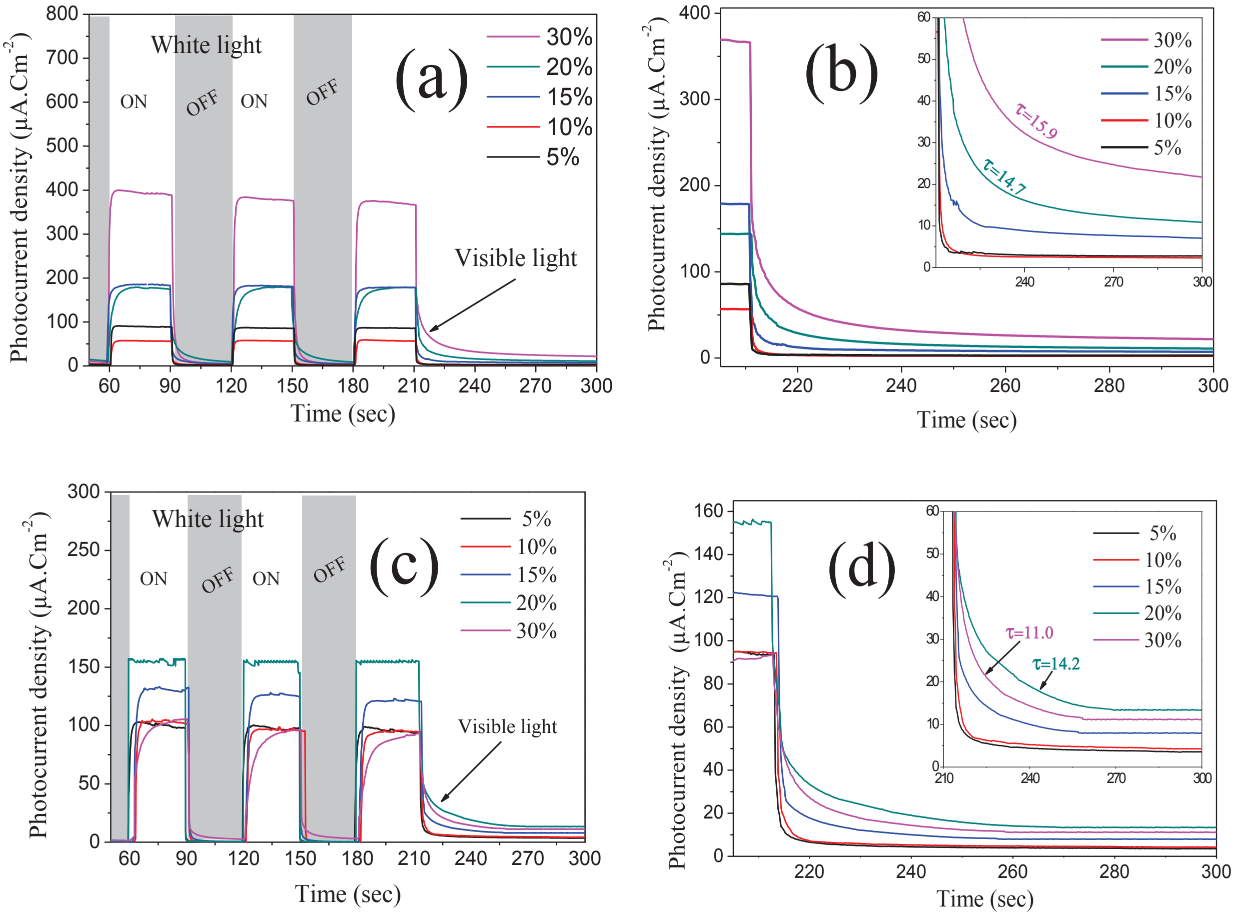

Fig.V-14: Photocurrent generated at 0.5V/(AgCl/Ag) for the 18 bi-layers (a)&(b,)and the 9 bi-layers ((c)&(d) with different TiN ratios of loaded layer within the photoactive film (τ is a transient time constant which will be discussed in section V-4-5-5).

Fig.V-14 summarize the measured photocurrents under a bias of 0.5V/(AgCl/Ag):

18 bi-layers under intermittent white light

18 bi-layers under visible light (when adding the UV filter)

9 bi-layers under intermittent white light

9 bi-layers under visible light (when adding the UV filter)

Fig.V-15 shows the experimental values of the photocurrent at 0.5 V/(AgCl/Ag), after the stabilization period, measured under white light (black) and visible light (red) irradiations for both type of bi-layers (9 and 18) vs the TiN ratio in the films. In the case of the 18 bi-layers, the photo-induced current increased steadily (up to 400µA in the white light and 23 µA in the visible light) as the TiN ratio increased up to 30%. But with the 9 bi-layers, the photo-generated current showed a maximum (154 µA in white light and 13.5 µA in visible light) for TiN ratio of 20%, further increase in the TiN ratio (thickness) leads to a dramatic decrease in this photo-activity.

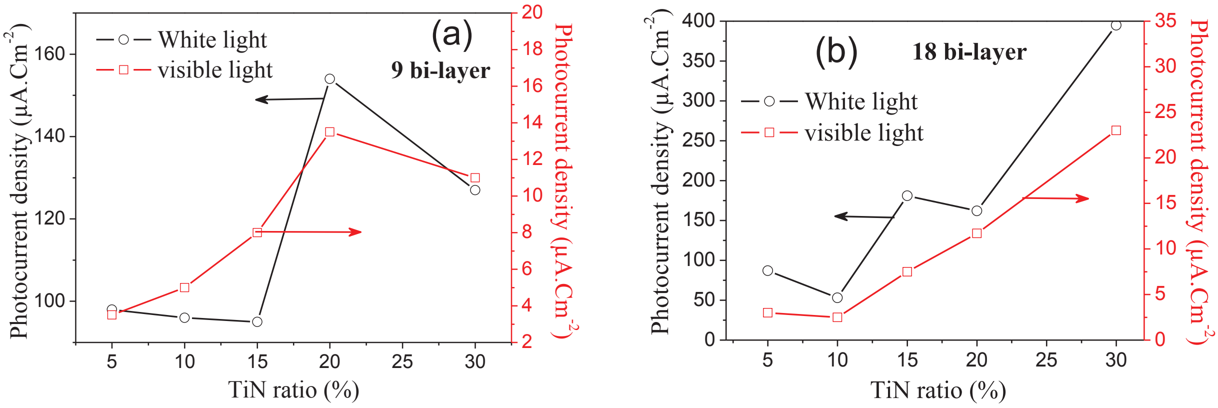

Fig.V-15: Photocurrent generated at 0.5V/(AgCl/Ag) for the 9 bi-layers (a)and the 18 bi-layers (b), vs TiN loaded layer ratio, under white (black) and visible (red) irradiations.

Table V-6: Nominal TiN layer thickness in the 9 and 18 TiN/TiO$_2$ stacked thin films (nm).

	5%	10%	15%	20%	30%
9 bilayer	3	5	8	11	16
18 bilayer	1.5	3	4	6	8

In a global view, the 18 bi-layers multistack is still more efficient to generate higher photocurrents than the 9 bi-layers under white light (UV) as well as visible light irradiations. The 18 bi-layers could generate a photocurrent up to 2.5 times higher than that generated by the 9 bi-layers. Many reasons could be behind this dramatic decrease in the photo-activity of 9 bi-layers. We believe that the TiN layer thickness is the main reason. Indeed the thickness of TiN increases with the increase of TiN ratio, but it is the opposite for that of TiO$_2$. Table V-6 presents the calculated nominal thickness of each TiN layer within the 9 and 18 multi-stack for the different TiN/TiO$_2$ ratios.

The maximum TiN thickness in the 18 bi-layers (TiN ratio 30%) is 8 nm which is still much thinner than the 11 nm of the 9 bi-layers (TiO_2 ratio 20%) after which the photocurrent decreases. ***This means that there is a critical thickness for TiN layer which should be between 11 nm and 16 nm***. If the TiN thickness exceeds this critical value, there should be a dramatic reduction in the photo efficiency. We can suppose that the TiN layer could have the following effects:

- ✓ the ratio of TiN (in the bi-layer film) affects the charge space region.
- ✓ the increase of the TiN ratio (more than the critical values) decreases the UV and visible light absorption within the TiO_2 layers.

In fact, the photoactive materials (in the bi-layer film) are the TiO_2 layers, the increase in the thickness of the TiN layer is accompanied with a decrease of the TiO_2 layer one. Thicker TiN layers could induce the electron-hole recombination leading to a reduction in the photoactivity.

V-4-5-5) memory effect in the electrochemical photo response

The most interesting remark in the bi-layer design is the evident photocurrent relaxation in dark and when switching from UV to visible irradiations (at 210 sec) as shown in Fig.V-14 (b) and (d). This is a direct reflection of the charge separation efficiency of the bi-layer array. With the 9 bi-layers, the visible light photocurrent is stabilized after 50 seconds from the instance of the UV filters insertion (for samples having 20% TiN ratio). This relaxation time is even higher in the case of the 18 bi-layer with the samples having up to 30% TiN ratio. Here again, the charge recombination rate was found to be efficiently reduced with the 18 bi-layers as the TiN ratio increased; the dark photocurrent (*after a white light illumination*) is increased from 1μA up to 9 μA when the TiN ratio increased from 5% to 30% (cf Fig.V-14 (c) and (d)).

The relaxation of the measured photocurrent could be modulated in the following equation:

$$\zeta = \frac{I(t) - I_{st}}{I_0 - I_{st}} = e^{\left(-t/\tau\right)} \qquad \text{Eq.V-4}$$

Where τ is a transient time constant which depends on the recombination rate between the photogenerated electron-holes, ***I(t)*** is the measured current at time ***t***, I_{st} is the stationary current after stabilization, I_0 is the initial current when we stopped the irradiation (or switched from white to visible light). The values of $\ln(\zeta)$ *were plotted vs time* and we used a linear fitting to extrapolate and find the slope of the resulted plot which is the inverse of τ . Table V-7 illustrates the calculated values of the transient time τ for the 9 and 18 bilayers at different TiN ratios.

Table V-7: Calculated values of the time constant τ for *different ratios of TiN in the 9 and 18 bi-layers (sec).*

	5%	10%	15%	20%	30%
9 bilayer	2.1	2.0	9.9	14.2	11.0
18 bilayer	1.6	2.5	8.7	14.7	15.9

It is clear that when the TiN thickness is below the critical values (*11 to 16 nm*), the transient time is increased when the TiN ratio increases. This means that the recombination time is reduced when the TiN thickness increases but remains below the critical thickness. *The 18 bi-layers multistack having 30% of TiN/TiO$_2$ thickness seems to reduce 10 times the recombination between the photo-generated carriers (increase the transient time 10 times).*

V-4-6) Photocatalytic activity

These measurements are still under process, but the first results showed a surprising enhancement of the 9 bi-layers giving the highest photocatalytic performance on the degradation of NMP, MB and carbamazepine (CBZ) especially with 30% TiN/TiO$_2$ ratio, rather than the 18 bi-layers which are more efficient for the photocurrent generation. This means that the ***limiting steps*** in the photocatalytic reactions (using the photoactive TiO$_2$ bilayers) are different than that in photo-electrochemical responses. The same conclusion has been found also in the case of the dual gas sputtering (chapters III and IV). Photo Hall effect measurements, in different irradiation conditions, could help to understand why photocatalytic and photocurrent measurements do not present the same trend for the different multistack layers.

V-5) Deposition monitoring

We monitored the plasma behavior during the bi-layer deposition using optical emission spectroscopy. Emission lines of titanium (500 nm), oxygen (777 nm) and nitrogen (746 nm) have been normalized to the argon emission lines (772 nm). The normalized emission lines vs time are presented in Fig.V-16. It is important to remember that when an increase in the reactive gas (oxygen or nitrogen) emission line was detected, it means that the total quantity of sputtered titanium atoms had reacted with the reactive gas and so the emission of reactive gas measured was that in excess. For this reason, when both gases were suddenly and simultaneously introduced in the reactor (when we switch from one gas to the other) a sudden increase in the reactive gas emission intensity should be detected (Fig.V-16).

In this plot, the deposition begins in an O_2 atmosphere (TiO_2) deposition. At time t = 295 seconds, the O_2 gas is turned off, and N_2 gas is introduced. When this change in the reactive gases occured, it was clearly observed that the nitrogen emission intensity increased very sharply at first, then stabilized within ~12 seconds. In addition, the titanium emission line stabilized almost instantly, within 6 seconds. This tells us that the TiN deposition plasma has reached a steady-state equilibrium within approximately 12 seconds after we switch from O_2 to N_2 gas introduction. Although the emission lines are not an exact image of what is happening at the surface of the substrate, we assume here that after the plasma reaches this steady-state equilibrium (t>12 seconds), the thin film deposition will be stoichiometric TiN. There is also a possibility that a mixed TiN_xO_y phase may be deposited during the transition period due to the residual oxygen gas in the deposition chamber.

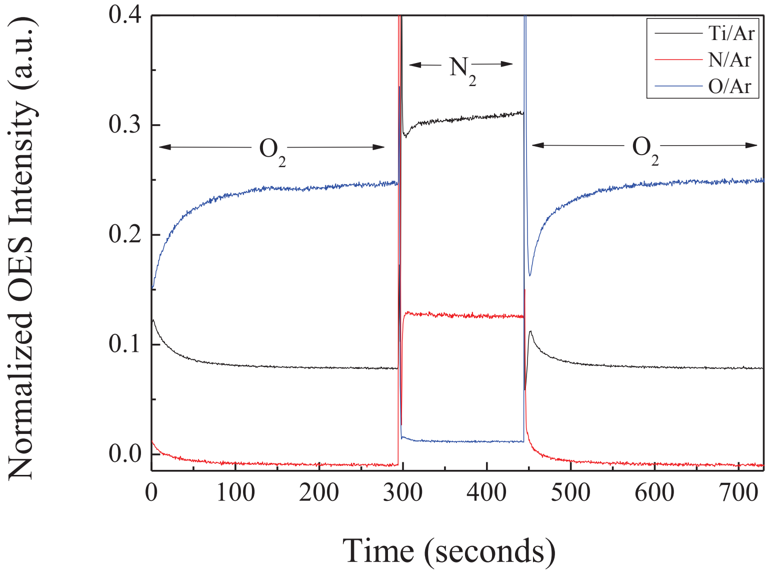

Fig.V-16: Plot of the normalized optical emission spectra for Ti, N, and O as a function of time when the two gases are introduced separately.

It is important to note the stabilization time for TiN depositions (<12 second) and to compare the latter to the deposition time used for each of the bi-layered arrangements. In particular, for the 45 bi-layer films with the thinnest layer of TiN, the N_2 gas introduction time is t = 30 seconds. For the films with less bi-layers, and larger layer thicknesses, the N_2 gas introduction time increases to t = 37, 48, 75, and 150 seconds for the 36, 27, 18, and 9 bi-layered films, respectively (if the nominal TiN ratio is kept constant at 20%). So far, we were able to deposit TiN (having shorter deposition time) since the stabilization time is much lower than the nominal deposition times as mentioned in Tables V-1 and V-2.

When the N_2 gas is turned off and the O_2 gas is turned on at t =445 seconds, we see a dramatic decrease in the emission intensity from nitrogen and titanium, and a large increase in the oxygen peak. Compared to the nitrogen stabilization time, the oxygen takes much longer,

longer than 50 seconds to become stable that means the poisoned mode with O_2 gas is reached 4 times slower than the case with N_2 reactive gas. Again, here we will assume that when the plasma displays stabilized emission lines for the respective components that the film deposited will be stoichiometric TiO_2. It is also possible that during the transition period that a mixed titanium oxynitride layer be deposited before the plasma is stabilized. We assume that for each of the arrangements of bi-layers, that a definite layer of TiN and TiO_2 are formed, albeit very thin for the 45 bi-layered film.

V-6) Conclusions

Thin film stacks of TiO_2/TiN bi-layers were fabricated and characterized to determine their crystalline, optical, composition and photoactive properties. Deposition parameters have been chosen to produce stoichiometric TiN/TiO_2 bi-layers with well defined *Schottky barriers*. The crystalline properties were found to be dependent on the annealing temperature and the thickness of each TiO_2 layer. In particular, the phase transition temperature from anatase to rutile can be easily controlled by changing the thickness and number of the TiO_2 and TiN layers. The optical properties also show a great variance in the absorption and band gap of the materials even with fixed TiN/TiO_2 ratio and by varying the number of sub-layers. All the bi-layer coatings show a shift to visible light absorption as compared to pure TiO_2, with the largest shift seen in the 9 and 18 bi-layer samples. The photo-electrochemical results gave very interesting results, showing that the number of layers and thickness of the layers play an important role in the charge generation, charge separation and transport properties within each film, as well as the emergence of visible light photo-activity, which is not seen in TiO_2 alone. As we found with the dual gas sputtering (chapter III and IV), there are again some deviations between the photo-catalytic activity and the photo-electrochemical activity. Experimentally, we estimate that we can reduce the recombination rate between the photo-induced electron-holes up to 10 times using this design, but the thickness of each TiN layer should not exceed a limiting value of 11 to 16 nm.

References

[1] Y He, Z Zhang, Y Zhao, *Journal of Vacuum Science and Technology B*, **26** (2008) 1350–1358.

[2] M Yan, F Chen, J Zhang, M Anpo, *Journal of Physical Chemistry B*, **109** (2005) 8673–8678.

[3] R Bickley, T Gonzalez-Carreno, J Lees, L Palmisano, J Tilley, *Journal of Solid State Chemistry*, **92** (1991) 178–190.

[4] A Datye, G Riegel, J Bolton, M Huang, M Prairie, *Journal of Solid State Chemistry*, **115** (1995) 236–239.

[5] T Ohno, K Sarukawa, K Tokieda, M Matsumura, *Journal of Catalysis*, **203** (2001) 82–86.

[6] D Hurum, A Agrios, K Gray, T Rajh, M Thunauer, *Journal of Physical Chemistry B*, **107** (2003) 4545.

[7] B O'Regan, M Gräzel, *Nature,* **353** (1991) 737–740.

[8] L Kavan, M Gräzel, S Gilbert, C Klemenz, H Scheel, *Journal of American Chemical Society,* **118**, (1996) 6716-6723.

[9] S Higashimoto, N Kitahata, K Mori, M Azuma, *Catalysis Letters*, **101** (2004) 49–51.

[10] W Smith, Y Zhao, *Journal of Physical Chemistry C*, **112** (2008) 19635–19641.

[11] Z Wu, D Lee, M Rubner, R Cohen, *Small*, **3** (2007) 1445-1451.

[12] W Smith, Y Zhao, *Catalysis Communications*, **10** (2009) 1117–1121.

[13] W Choi, A Termin, M Hoffman, *Journal of Physical Chemistry*, **98** (1994) 13669–13679.

[14] T Umebayashi, T Yamaki, S Yamamoto, Q Miyashita, S Tanaka, T Sumita, K Asai, *Journal of Applied Physics,* **93** (2003) 5156–5160.

[15] H Tong , S Ouyang , Y Bi , N Umezawa , M Oshikiri , J Ye, *Advanced Materials*, 24 (2) (2012) 229–251.

[16] O Pierson, Handbook of refractory carbides and nitrides: properties, characteristics, processing, and applications. *William Andrew* (1996) Westwood New Jersey.

[17] R Andrievski, Z Dashevsky , G Kalinnikov, *Technical Physics Letters*, **30** (11) (2004) 930–932.

[18] T Cai, Y Liao, Z Peng, Y Long, Z Wei, Q Deng, *Journal of Environmental Sciences*, 21 (2009) 997–1004.

[19] H Haick, Y Paz, *Journal of Phusical Chemistry B*, **107** (2003) 2319–2326.

[20] B Avasarala, P Haldar, *Electrochimca Acta*, **55** (2010) 9024–9034.

[21] Z Zhang, J Goodall, D Morgan, S Brown, R Clark, J Knowles, N Mordan, J Evans, A Carley, M Bowker, J Darr, *Journal of the European Ceramic Society*, **29** (2009) 2343–2353.

[22]. U Helmersson, M Lattemann, J Bohlmark, A Ehiasarian, J Gudmundsson, *Thin Solid Films*, 513 (2006) 1–24

[23] R Parra, A Arango, P Jose, V Javier, *Dyna*, **163** (2010) 64–74.

[24] J Arbiol, J Cerda, G Dezanneau, A Cicera, F Peiro, A Cornet, J Morante, *Journal of Applied Physics*, **92** (2002) 853–861.

[25] J Pankove, *Optical Processes in Semiconductor*, (1975) New York: Dover.

[26] A Salem, Y El-Gendy, G Sakr, W Soliman, *Journal of Physics D: Applied Physics*, **41** (2008) 025311.

[27] Y El-Gendy, *Journal of Physics D: Applied Physics*, **42** (2009) 115408.

[28] P McCurdy, L Sturgess, S Kohli, E Fisher, *Applied Surface Science*, **233** (2004) 69–79.

[29] D Won, C Wang,H Jang, D Choi, *Applied Physics A*, **73** (2001) 595–600.

[30] M Wong, H Chou, T Yang, *Thin Solid Films*, **494** (2006) 244–249

[32] Y Li, M Ma, X Wang, Z Li, *Surface & Coatings Technology,* **204** (2010) 1353–1358.

[33] G He, L Zhang,G Li, M Liu, X Wang, *Journal of Physics D: Applied Physics*, **41** (2008) 045304 1–9

[34] H Matsui, H Tabata, *Journal of Applied Physics*, **97** (2005) 123511 1–8.

[31] J Liao, H Chen, C Chang, S Chiu, Z Chen, *Thin Solid Films,* **515** (2006) 176–185.

[35] S Lee, I Cho, D K Lee, D W Kim, T H Noh, C H Kwak, S Park, K S Honga, J K Lee, H S Jung , *Journal of Photochemistry and Photobiology A: Chemistry*, **213** (2010) 129–135

[36] A V Emeline, V N Kuznetsov, V K Rybchuk, N Serpone, Review, *International Journal of Photoenergy*, ID 258394 (2008) 1–19.

[37] G He, L Zhang,G Li, M Liu, X Wang, *Journal of Physics D: Applied Physics*, **41** (2008) 045304 1–9.

[38] H M Yates, M G Nolan, D W Sheel, M E Pemble, *Journal of Photochemistry and Photobiology A: Chemistry*, **179** (2006) 213–223.

[39] C Di Valentin, E Finazzi, G Pacchioni, A Selloni, S Livraghi, M C Paganini, E Giamello, *Chemical Physics*, **339** (2007) 44–56.

[40] A Trenczek-Zajaca, M Radeckaa, K Zakrzewskab, A Brudnikb, E Kusiorb, *Journal of Power Sources*, **194** (2009) 93–103.

[41] M Wong, H Chou, T Yang, *Thin Solid Films*, **494** (2006) 244 – 249

[42] H Kawasaki, T Ohshima, Y Yagyu, Y Suda, SI Khartsev, AM Grishin, *Journal of Physics Conference Series*, **100** (2008) 012038 1–4.

[43] R Parra, A Arango, J Palacio, *Dyna* **77** (163) (2010) 64–74.

[44] B Avasarala, P Haldar, *Electrochimca Acta*, **55** (2010) 9024–9034.

[45] N Laidani, P Cheyssac, J Perrière, R Bartali, G Gottardi, I Luciu, V Micheli, *Journal of Physics D : Applied Physics*, **43** (2010) 485402 (11pp)

[46] M Birkholz, K Ehwald , P Kulse , J Drews , M Fröhlich , U Haak , M Kaynak , E Matthus , K Schulz, D Wolansky, *Advanced Functional Materials*, **21** (2011) 1652–1656

[47] E Aubry, M Ghazzal, V Demange, N Chaoui, D Robert, A Billard, *Surface & Coatings Technology*, **201** (2007) 7706–7712

[48] D Hanaor , C Sorrell, *Journal of Materials Science*, **46** (2011) 855–874.

Chapter VI

N doped TiO_2 via thermal oxidation of TiN

Chapter VI

N doped TiO_2 via thermal oxidation of TiN

Abstract

Thin films of TiN were prepared via reactive RF magnetron sputtering at various deposition pressures. After deposition, TiN thin films were oxidized in a closed furnace at several different temperatures for different time intervals, which revealed the formation of different phases of N doped TiO_2. The resulting TiN/TiO_2 thin films showed drastic changes in their composition, crystal structure, optical properties, and photoactivity. By examining how the deposition pressure and post–oxidation conditions affected the TiN films, samples were prepared to optimize visible light absorption and photocurrent generation. A model for the oxidation process was proposed which described the structural change from TiN to TiO_2 through optical, morphological, and crystalline characterization. This study has systematically shown the ability to tailor the optical, morphological, and crystalline properties of TiO_2 by tailoring the intrinsic properties of TiN thin films and subsequent oxidation, in order to get an effective visible light photo–active titanium oxide coating. .

Résumé

Dans ce dernier chapitre, nous avons étudié les dépôts de couches minces de TiN par pulvérisation magnétron RF à différentes pressions de travail. Ces couches ont été ensuite oxydées par recuit dans l’air en faisant varier la température et le temps de recuit, afin d’obtenir des films de TiO_2 dopé N possédant différentes structures. Les couches minces qui en résultent sont caractérisées par des changements drastiques de composition, de structure cristalline, de propriétés optiques, et propriétés photoactivités. En examinant les effets de la pression de travail durant le dépôt et des conditions de post–oxydation sur les films de TiN, nous avons préparé des échantillons dans le but d’optimiser l'absorption de lumière dans le visible et la génération de photocourant. En se basant sur les caractéristiques optiques, morphologiques et cristallines, nous avons proposé un modèle pour décrire l’oxydation de TiN. Cette étude a montré qu’il est possible de systématiquement adapter les propriétés optiques, morphologiques et cristallines de TiO_2 dopé N en jouant sur les propriétés intrinsèques des couches minces de TiN et sur leur oxydation, afin d'obtenir des couches minces d’oxyde de titane dopé azote photo actives dans le visible.

VI–1) Introduction

The photocatalytic efficiency of TiO_2 can be enhanced when it is in contact with a material that has a higher Fermi energy level than itself, because it helps to create effective charge separation which can extend the lifetime of photo–generated electron hole–pairs [1–3]. When the lifetime of electron–hole pairs is extended, it is possible to improve the functionality of the photocatalyst. Nitrogen can be incorporated into the crystal lattice of TiO_2 either substitutionally or interstitially. The nature and concentration of the doping can play a large role in the overall effectiveness of TiO_2 to absorb visible light, through the reduction of the band gap, the introduction of stable energy levels within the band gap, or the prevalence of oxygen vacancies [4–8]. These studies suggest that the fabrication techniques used to create N–doped TiO_2 films play a critical role in the electronic and optical properties of the doped films.

A promising method to stably incorporate nitrogen into TiO_2 is through the thermal oxidation of TiN, which has yielded very diverse results. For example, Zhu et al. fabricated TiN_x thin films via DC sputtering and then oxidized the samples at 450^{o}C, revealing a pure TiO_2 anatase phase with no traces of TiN left behind [9]. However, Brudnik et al. deposited and then oxidized TiN films using the same method, but achieved a pure rutile phase of TiO_2 when oxidized at only 300^{o}C [10]. The difference between these two studies was the deposition pressure, which was around 2 Pa for Zhu et al., and 1 Pa for Brudnik et al. Therefore there should be a probable dependence between the sputtering deposition pressure of TiN thin films, the oxidation temperature and the resulting crystal phase of TiO_2. Also, a pure phase of TiO_2 could be formed upon oxidizing TiN thin film at suitable temperatures, Lee et al. [11] and Wu et al. [12] both obtained a mixed phase of anatase and rutile after oxidation of TiN nanoparticles in air.

While Kowalski et al. reported 300°C as sufficient temperature to oxidize TiN to TiO_2 [13], many reports explain that the kinetics of TiN oxidation is very slow and it is only efficient for oxidation temperatures higher than 600°C to 850°C [11] to transform TiN into anatase and/or rutile TiO_2.

Furthermore, when TiN oxidizes to TiO_2, there is a possibility of creating an intermediary compound of the form TiO_xN_y, which can be interpreted as a partially oxidized TiN layer, or a partially N–doped TiO_2 layer. The ability to manufacture this intermediary layer is vital to improve the visible light absorption and photoactivity of TiO_2, and is a critical challenge in the development of solar–driven photocatalysts. While there have been several individual studies which have shown the ability to form anatase, rutile, and mixed phase TiO_2 by oxidizing TiN, a comprehensive method to produce in a controlled manner either phase individually, or both phases simultaneously has not been developed.

Recent researches reported that anatase (101) is not the most efficient crystalline structure of TiO_2 for photocatalytic applications. Selloni et al. found that anatase (001) is more reactive, on the surface of which, water can go through dissociative adsorption rather than the molecular adsorption on anatase (101) [14]. So it could be interesting to produce and characterize other anatase crystals of TiO_2 rather than anatase (101).

VI–2) Strategy of the study

<u>VI–2–1) Titanium nitride vs titanium dioxide</u>

The most stable structure for titanium nitride is a cubic face centered crystal (cf8) with octahedral coordination geometry having a lattice parameter of 4.24 Å [15]. Titanium dioxide has more stable structures (Fig.VI–1), especially:

1) rutile phase which has a tetragonal primitive structure (tp6).
2) Anatase crystal which has a tetragonal structure but it is much longer and less dense than rutile.

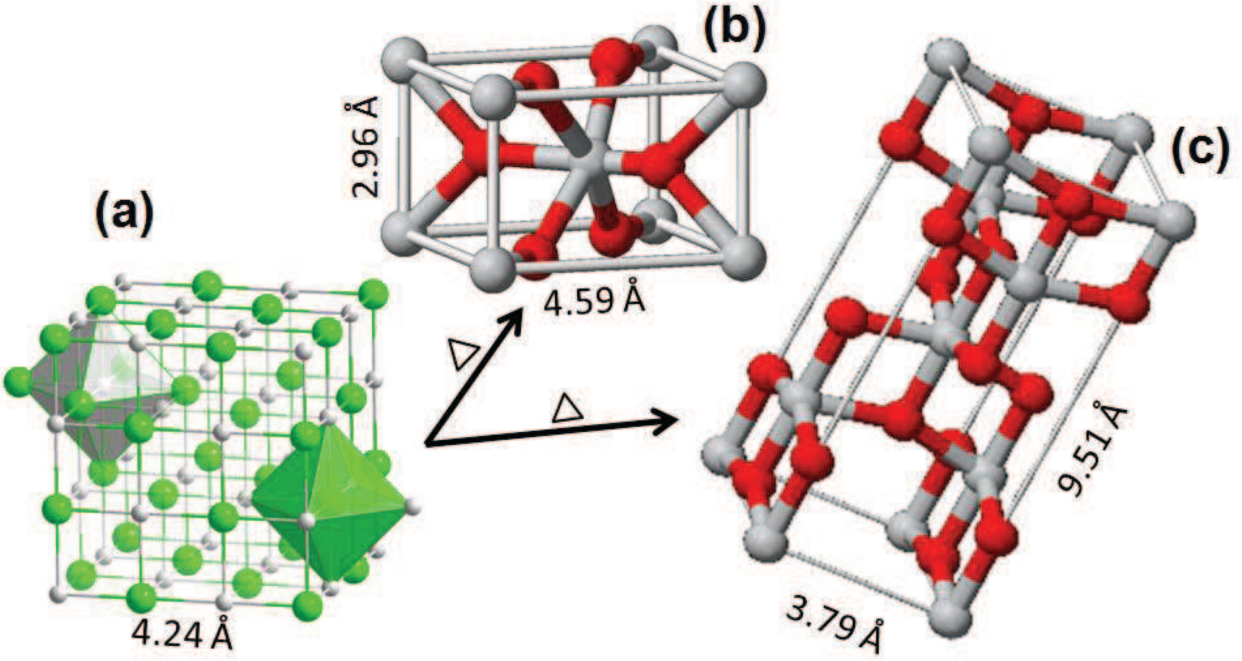

Fig.VI–1: (a) TiN crystal structure with octahedral coordination geometry, b) tetragonal rutile and c) tetragonal anatase TiO_2, with the mentioned unit cell dimensions. Titanium atoms are in grey.

It is clear that TiO_2 rutile phase has the nearest cell volume to TiN. But anatase is about two times bigger, as it has double number of atoms per unit cell compared to rutile

(Table I–2, chapter I). That means, anatase phase needs more space, than rutile, to be formed via the oxidation of TiN.

VI–2–2) Motivations of this work

In this chapter, we studied the oxidation of TiN films having different morphologies. Initially, the TiN films were prepared by RF reactive sputtering, the films density could be perfectly controlled by the deposition pressure during the sputtering process. So different TiN thin films having the same thickness but different porosities could be achieved. Then, thermal oxidation at various temperatures and different oxidation times could reveal the oxidation kinetics for each TiN film, as well as the transition between the different phase structures as TiN, anatase TiO_2 and rutile TiO_2.

The TiN deposited at low pressure were oxidized to the rutile phase of TiO_2, but the oxidation of the coatings deposited at high pressure gave rise predominantly to anatase TiO_2, if anatase phase had enough space to be formed. The films deposited at moderate pressures were expected to show both anatase and rutile characteristics.

Intermediary layers of TiON were formed during the oxidation process especially from the dense TiN films deposited at low pressures (Fig.VI–2 (a)). So, the optical properties of the oxidized film revealed different absorption efficiencies in the visible light region, which can shift closer to the UV spectrum as the oxidation time and temperature increased.

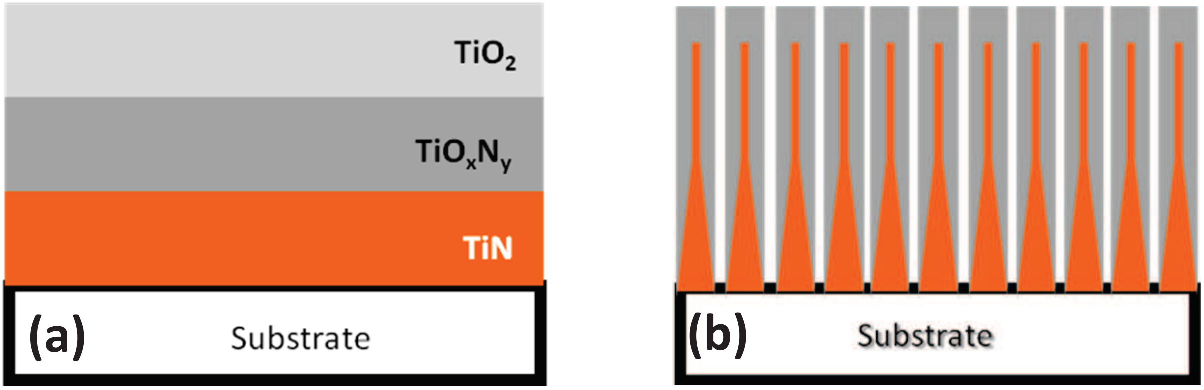

Fig.VI–2: Proposed models for TiN oxidation, (a) from dense TiN film and (b) from porous TiN film.

In addition, thin films with hetero–junction, as seen in the bi–layer design (chapter V), could be formed from the porous TiN films after thermal oxidation, these films should show characteristics of both TiN and TiO_2 (Fig.VI–2 (b)) with thinner layer of intermediary TiON compared to the dense films. This technique should indicate a unique compositional controllability and, thus, we can have a simple method for fabricating nitrogen–doped TiO_2 with controllable crystallinity, optical absorption and chemical composition that can show various visible light responsive activities for optoelectronic and photocatalytic applications.

VI–3) Experimental part

VI–3–1) Films preparation

TiN films were deposited in the RF sputtering reactor (chapter II), using Ti target (99.9%, Neyco), argon as the processing gas and nitrogen as the reactive gas. The TiN deposition parameters were optimized by using plasma diagnostics (chapter II) to ensure the proper film stoichiometry and growth rate. The deposition pressure was controlled by the Ar flow rate in the deposition chamber, fabricating films at p = 2, 3.5, 5, and 14 mtorr with corresponding Ar flow rates of 20, 35, 50, and 140 sccm respectively, and by keeping the pumping velocity constant. The RF power was 200 W, *corresponding to a dc bias voltage of 142 V in argon plasma*, the substrate holder was not biased and not heated.

In order to deposit stoichiometric TiN at a reasonable deposition rate, we chose to deposit each film within the transition region, between the metallic and compound modes (Fig.II–24). In particular, different N_2 flow rates were adjusted for each deposition pressure, in order to work within the same range in the normalized Ti emission lines. Specifically, when there is a low argon flow rate (20 sccm to 35 sccm), the nitrogen flow rate was set between 0.7 to 1 sccm (N_2/Ar=3.5%), for a medium argon flow rate (up to 50 sccm) the nitrogen flow rate was fixed between 1 to 1.5 sccm (N_2/Ar=3 %), and at higher argon flow rates (140 sccm), the nitrogen flow rate was set at 2.5 sccm (N_2/Ar=1.8 %).

Substrates were: Si (101), quartz slides and ITO coated glass. In order to prevent any metal diffusion from the substrate (during the post thermal oxidation process) we did not use any metallic substrate.

VI–3–2) Oxidation of TiN thin films

The previously prepared TiN films were then oxidized simultaneously in a closed furnace under normal air atmosphere. The oxidation temperatures were selected to be 350°C, 450°C, 550°C, 650°C, 750°C, 850°C and 950°C, but here in this chapter we will limit the study for oxidation temperatures in the range of 350°C to 550°C. The oxidation time range was adjusted depending on the oxidation temperature, in order to have the same range of oxidation efficiency.

VI–3–3) Morphology of as deposited TiN thin films

SEM images (top view) are shown in Fig.VI–3 for the resulted TiN thin films deposited at four different working pressures. A network of interconnected titanium nitride columns having mature triangles with sharp & protruding nodules can be seen for all the TiN films. The films deposited at low pressure appeared to be very dense. As the deposition pressure increased, the width of the TiN columns decreased leading to less interconnection between the TiN columns (with a triangular cross section) and higher film porosity. The surface feature of the films deposited at high pressure (14 mtorr) showed that there was an increase in the distance separating the TiN columns, which seemed to extend through the bulk of the film. This could significantly affect the post oxidation kinetics and the resulted film behavior, which will be discussed later In this chapter.

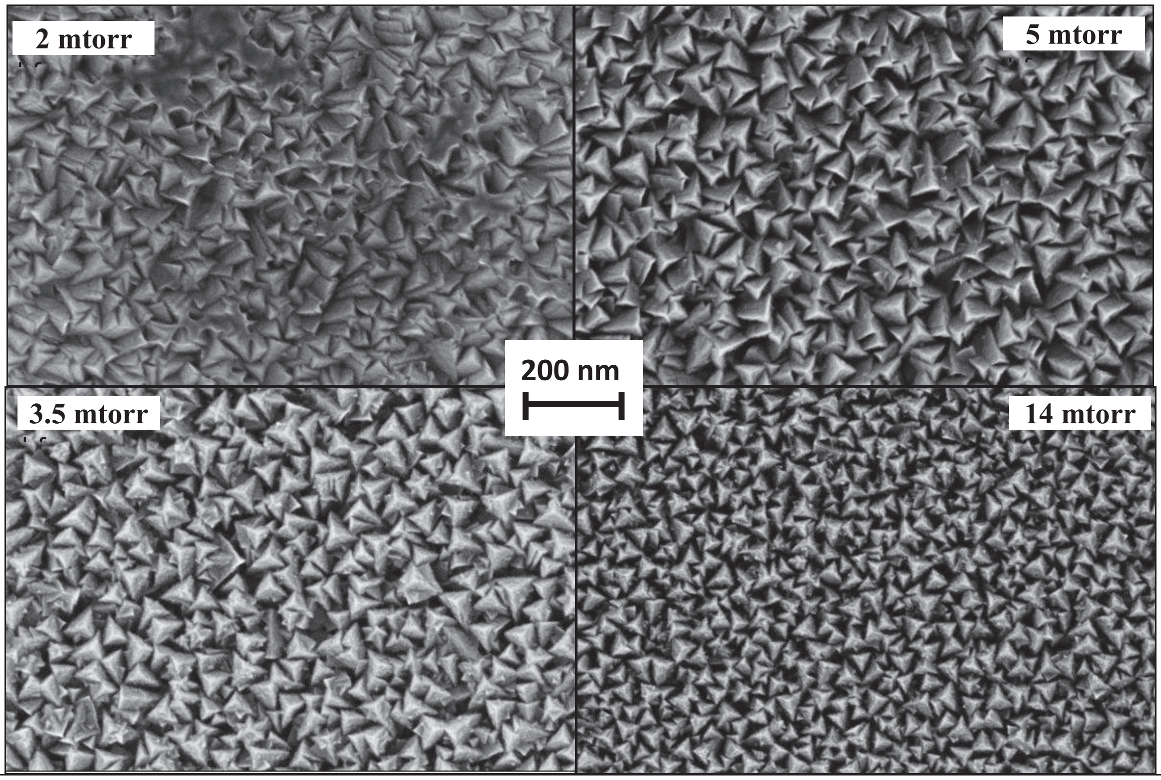

Fig.VI–3: SEM–FEG micrographs of TiN thin films grown at four different pressures 2, 3.5, 5 and 14 mtorr.

The rough porous morphology of these deposited films, without intentional substrate heating, was the typical feature for the TiN films deposited by sputtering in agreement with Thornton structure zone model (annex 4). This model confirmed that when the film was deposited onto a substrate at $T/T_m<0.3$ (where T is the substrate temperature and T_m is the melting point of the thin film material), it was characterized by columns separated by voids, which lead to a porous structure. (T_m=2930 °C for TiN and films were deposited at room temperature)

VI–3–4) Crystal Structure

All of the as–deposited TiN films displayed a very intense peak centered at $2\theta = 36.8^o$, which typically corresponded to the (111) cubic crystal orientation of TiN, as shown in Fig.VI–4 (a). There was also a small peak observed around $2\theta = 43.2^o$, which corresponds to the (200) orientation of TiN. One can observe that there is a clear decrease of the diffraction intensity and a broadening of the TiN (111) peak as the deposition pressure increased from 2 to 14 mtorr. By using the Scherrer equation, one can determine the TiN crystal size, which decreased with the increase of the deposition pressure. The latter observation was consistent with the previous observations of the morphology of the films (Fig.VI–3).

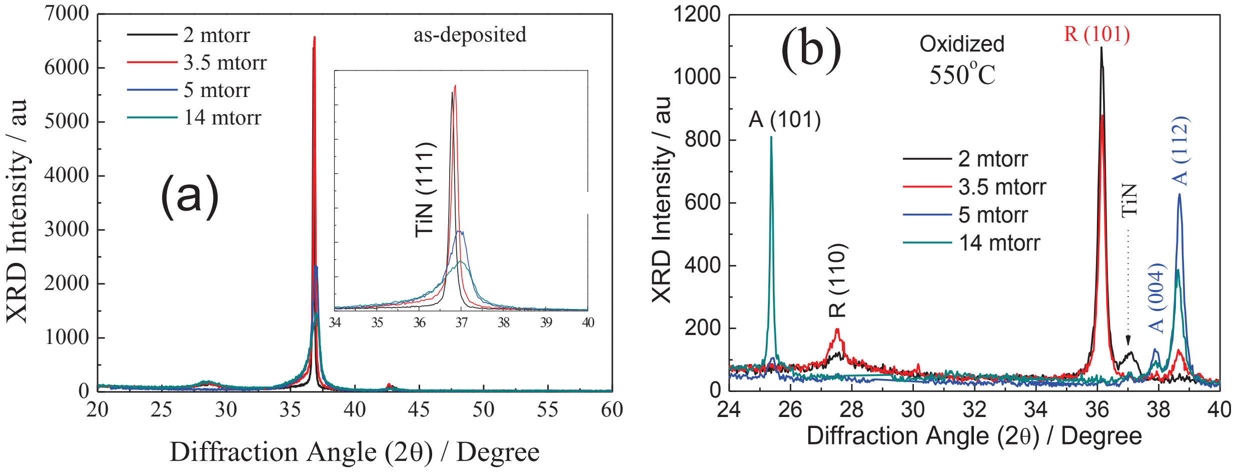

Fig.VI–4: XRD patterns for different films *fabricated at 2, 3.5, 5, and 14 mtorr. (a) the as–deposited TiN thin film, and (b oxidized TiN film at 550^{o}C for 2 hours.*

Fig.VI–4 (b), presents examples of TiN films oxidized at 550°C within 2 hours. Here by analyzing the above results, the following remarks can be made:

1) Oxidation of TiN films prepared at low pressure (2 up to 3.5 mtorr) provide mostly rutile TiO$_2$ phase R(101). No anatase phase could be expected from the oxidation of TiN films prepared at 2 mtorr (very low pressure produces dense films).
2) anatase phase A(112) starts to appear from oxidation of films prepared at 3.5 mtorr, its intensity increases and becomes more dominant (as compared to the rutile phase), as the sputtering pressure increases up to 5 mtorr where the A(101) anatase orientation starts to appear and becomes more dominant as the TiN deposition pressure increases.
3) The anatase phase A(101) is the most dominant from the oxidation of TiN films deposited at 14 mtorr. *This is due to the fact that at high sputtering pressure more porous films are deposited which upon annealing will have more space to develop anatase phase which as mentioned above is characterized by a larger crystal.*

VI–4) TiN oxidation kinetic

<u>VI–4–1) Dense TiN film deposited at 2 mtorr</u>

The films deposited at p = 2 mtorr showed no significant changes when oxidized at 350^{o}C for 24 hours (Fig.VI–5 (a)). The only noticeable difference that was present in the

XRD scans was a small shift ($\Delta 2\theta \approx 0.1^{o} \pm 0.1$) of the TiN(111) peak as the oxidation time increased, as well as a slight decrease in the peak height.

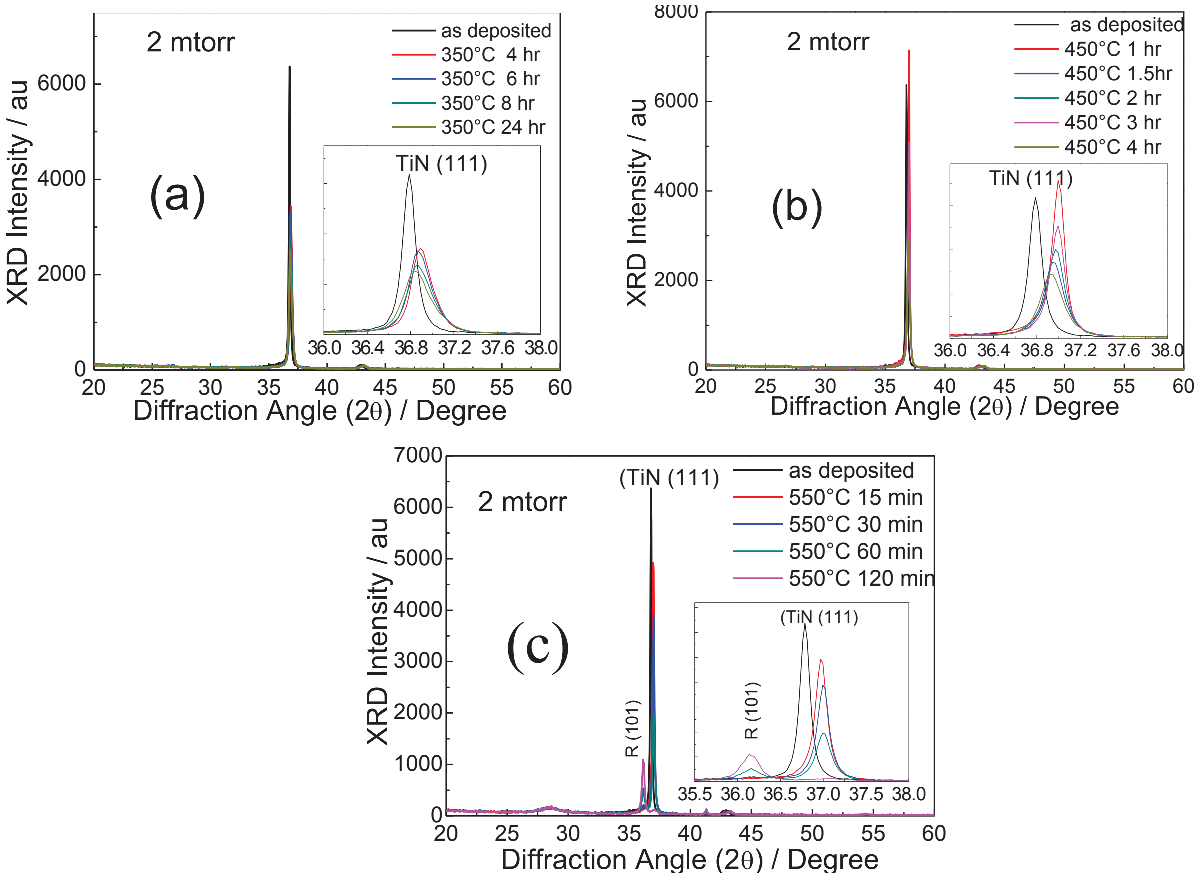

Fig.VI–5 : XRD patterns for TiN thin film deposited at 2 mtorr and oxidized at (a) 350°C, (b) 450°C and (c) 550°C for different times.

The shift decreased with the oxidation time, and after 24 hours the TiN peak at $2\theta = 36.8^{o}$ had shifted to $2\theta = 37.0^{o}$. This shift in the TiN peak can be attributed to an increase in strain on the crystal lattice that was caused by the oxidation process. The strain, however, was not large enough to cause an oxidation in the bulk of this particular film, due to the high density of the coating caused by the low deposition pressure. Similarly, the same film oxidized at 450°C for 24 hours (Fig.VI–5 (b)) didn't go through any noticeable oxidation. Again, a decrease in intensity with peak shift was observed in the TiN peak centered at $2\theta = 36.8^{o}$, with the variance found to be $\Delta 2\theta \approx 0.1^{o} \pm 0.1$. It is clear that for the film deposited at $p = 2$ mtorr, annealing the coatings in the range of 350 to 450°C was not enough to initialize bulk oxidation from TiN to TiO_2 after 24~48 hours of oxidation.

Oxidation at 550°C

However, if the same coating was oxidized at 550°C (Fig.VI–5 (c)), significant changes were observed in the XRD patterns. After 15 and 30 minutes of oxidation at 550°C, a shift in the TiN peak at $2\theta = 36.8^{o}$ was observed, similar to the patterns found after oxidation for several hours at 350°C and 450°C. When the film was oxidized for an hour at 550°C, the intensity of the TiN peak decreased significantly (less than half of its original height), and another peak became observable at $2\theta = 36.15^o$. This new peak corresponded to the (101) orientation of the TiO_2 rutile crystal structure, the intensity of which was still less than the TiN peak after an annealing time of one hour.

After oxidizing this film at 550°C for 2 hours, the rutile peak at $2\theta = 36.15^o$ became much more dominant, and the TiN peak at $2\theta = 36.8^o$ reduced significantly again. It is apparent that for this very dense film deposited at a very low pressure, it was very hard to oxidize TiN to TiO_2. In fact, no significant oxidation was observed below 550°C for a period of one hour. However in the case of this sample, no anatase phase of TiO_2 was observed. These results suggest that the coatings being very dense, makes it too difficult for the anatase phase of TiO_2 to form, and thus only rutile phase which is much smaller than the anatase one can be formed at higher temperatures.

VI–4–2) Dense TiN film deposited at 3.5 mtorr

The TiN film deposited at p = 3.5 mtorr (Fig.VI–6) showed very similar trends to the film deposited at p = 2 mtorr *annealed* at low temperatures *(350°C and 450°C)*, but diverged from these trends at higher temperatures. When this film was oxidized at 350°C *for* 24 hours, no phases of TiO_2 became present. Similar to the other films deposited at a low pressure, only a small shift in the TiN peak centered at $2\theta = 36.8^o$ was observed, with a maximum displacement of $\Delta 2\theta \approx 0.2^o$. When the same TiN film was oxidized at 450°C, for 4 hours, a similar peak shift was observed, again with no distinct TiO_2 phases present (Fig.VI–6 (a)).
When the TiN film is oxidized at 550°C, the trend for the pattern of the XRD scans again diverged from the lower temperature plots (Fig.VI–6 (b)). After oxidation for 15 minutes, only a small peak shift was observed for the TiN peak centered at $2\theta = 36.8^o$. However, after oxidation for 30 minutes, in addition to the TiN peak shift, a small peak at $2\theta = 38.6^o$ was formed which corresponded to the (112) orientation of the anatase phase of TiO_2. This was a unique feature of these coatings (p = 3.5mtorr) as compared to the film deposited at $p = 2$ mtorr, which never showed any anatase phase peaks at any oxidation temperature.

When such a film was oxidized for an hour, the TiN peak decreased significantly and another peak emerged at $2\theta = 36.15^o$, corresponding to the (101) orientation of the rutile phase of TiO_2. The anatase peak at $2\theta = 38.6^o$ remained the same as it was after 30 minutes of oxidation, revealing that the degree of anatase crystallinity did not change, although the relative amount of anatase in the film decreased. After this film was oxidized for 2 hours, the rutile peak at $2\theta = 36.15^o$ became dominant, and the TiN peak disappeared. For this film at these oxidation conditions, it appeared that the TiN film was either completely oxidized to TiO_2, or was almost fully oxidized with only a very small layer of TiN that is undetectable by XRD. Oxidation for 3 hours revealed an identical XRD plot, which indicated that the full oxidation had taken place or the film porosity was not sufficient to allow oxygen diffusion in the bulk.

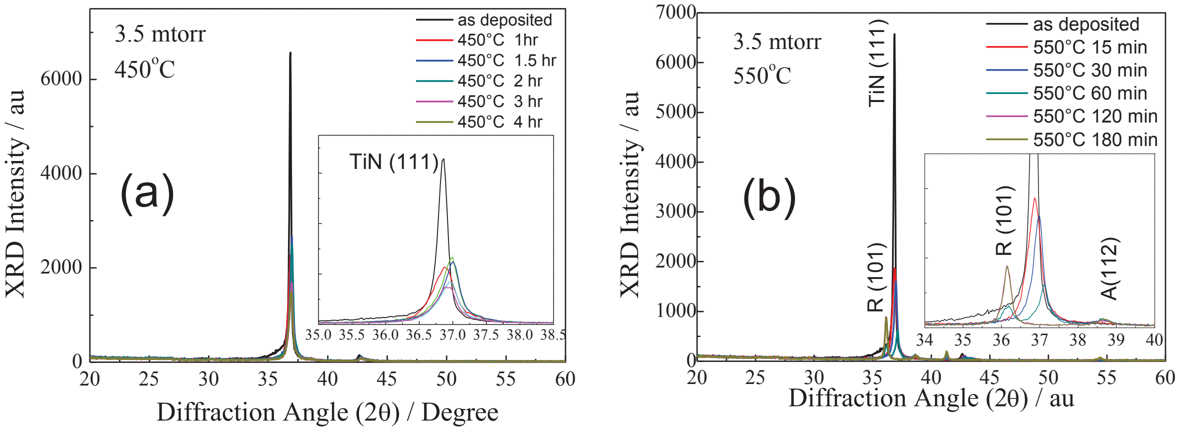

Fig.VI–6: XRD patterns for TiN thin films deposited at 3.5 mtorr and oxidized at (a) 450°C and (b) 550°C, for different times.

It is interesting to note that this film shared both an anatase phase as well as a rutile phase of TiO_2, which is noticeably different from the film deposited at a lower pressure. It is possible that the anatase phase was able to grow, albeit in a very small way, because the film was slightly less dense than the previous film. This density may have provided a more porous surface for the oxygen to be thermally diffused into the material, which may have helped the phase change to anatase.

VI–4–3) TiN film deposited at 5 mtorr

Unlike the two previous films deposited at low pressures, the TiN thin films deposited at p = 5 mtorr exhibited significant changes when oxidized at 350°C. The as–deposited plot showed a very strong and broad peak centered at $2\theta = 36.8^o$, which corresponded to the (111) TiN phase. After oxidation at 350°C for 4 hours (Fig.VI–7 (a)), the TiN peak decreased around 25%, and slightly broadened towards larger angles. After oxidation for 6 hours, the TiN peak again decreased significantly, and was less than half the original peak height. After oxidation of the film for 8 hours at this temperature, a small bump centred at $2\theta = 25.3^o$ began to appear, which corresponded to the (101) orientation of the anatase phase of TiO_2. In addition to the TiN peak becoming much less intense, the overall shape of this peak became much broader at larger angles, which indicated that there was a second peak contributing to the shape.

After oxidation for 12 hours, the TiN peak was again greatly reduced, and a clear stronger peak was visible at $2\theta = 38.6^{\circ}$, which corresponded to the (112) orientation of the anatase phase of TiO_2. Also, the peak centered at $2\theta = 25.3^{\circ}$ became slightly stronger than before. Overall, at this oxidation time and temperature it is clear that the anatase phase of TiO_2 was dominant, while the diagram still showed an appreciable amount of TiN. It is interesting to note that the (112) orientation of TiO_2 shows a stronger peak intensity, making it typically the most dominant peak found for anatase, than the (101) orientation.

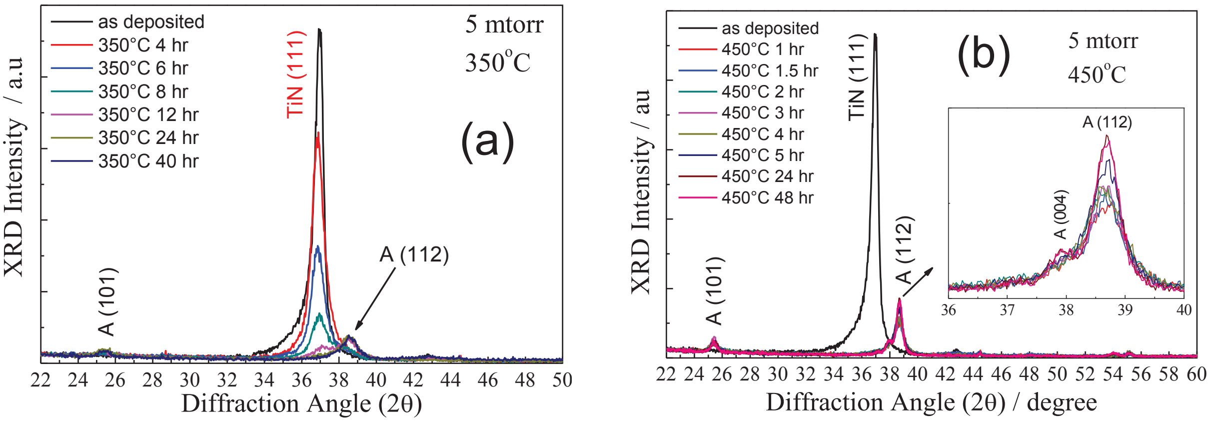

Fig. VI–7: XRD patterns for TiN thin film fabricated at 5 mtorr and oxidized at (a) 350°C, (b) 450°C, for different times.

This indicated that the film deposited at $p = 5$ mtorr had unique qualities, as it oxidized to an unusual phase of TiO_2 when oxidized at $350^{\circ}C$ for several hours. After oxidation for 24 hours, the TiN peak was no longer visible, and the (112) anatase peak was the most intense peak observed. The smaller peak at $2\theta = 25.3^{\circ}$ became slightly taller at this time, but the peak was still much less intense than the (112) peak

Oxidation for 40 hours revealed an identical profile, indicating that the oxidation from TiN to TiO_2 had been completed, leaving a predominantly (112) oriented phase of anatase. The very slow and gradual change from TiN to TiO_2 at this temperature revealed that this film has a controllable crystallinity, and the ratio of TiN to TiO_2 may be controlled very easily, which can be beneficial for many applications.

When the TiN film, deposited at 5 mtorr, was oxidized at $450^{\circ}C$ (Fig. VI–7 (b)), the change from TiN to TiO_2 was more drastic than at $350^{\circ}C$. After one hour of oxidation at $450^{\circ}C$, the XRD pattern showed no peak at $2\theta = 36.8^{\circ}$, suggesting that no TiN was present anymore. In addition, a large peak at $2\theta = 38.6^{\circ}$ was observed, corresponding to the (112) orientation of the anatase phase of TiO_2, and a very small and broad peak also formed at $2\theta = 37.9^{\circ}$, corresponding to the (004) orientation of anatase TiO_2. A smaller peak was also present at $2\theta = 25.3^{\circ}$, corresponding to the (101) orientation of the anatase phase of TiO_2.

When the oxidation time was increased for 48 hours, the peak height at $2\theta = 38.6^{o}$ increased steadily, but the overall shape of the XRD pattern remained the same. This clearly showed that at 450^{o}C, the TiN columns were mostly oxidized to TiO_2 very fast (within an hour), and were stable for 2 days of further oxidation. Again, at this temperature the (112) phase of anatase was significantly more dominant, than the (101) phase, showing a unique preferred orientation.

After oxidation at 550^{o}C, the TiN film showed a very similar trend to the film oxidized at 450^{o}C, suggesting that no new oxidation dynamics were present. The only noticeable difference between oxidation at 550^{o}C compared to 450^{o}C is that the peak at $2\theta = 37.8^{o}$, corresponding to the (004) orientation of anatase is less broad and more pronounced, with a gradual increase in the (112) peak height. No rutile peaks have been detected when the coatings (5 mtorr TiN thin films) went through oxidation up to a temperature of 550°C.

VI–4–4) TiN film deposited at 14 mtorr

When TiN films were deposited at p = 14 mtorr, a very drastic change in the crystallinity during oxidation was observed, which differs dramatically from all of the previous films. At 350^{o}C, the films quickly changed their crystallinity, similar to the films prepared at p = 5 mtorr. However, the dominant orientation that emerged was the (101) anatase phase of TiO_2, as seen by a very tall and narrow peak at $2\theta = 25.3^{o}$ (Fig.VI–8 (a)). Less intense peaks corresponding to the anatase (112) and (200) were also detected at 2θ = 38.6° and 48.2°, respectively. Oxidation at 450^{o}C and 550^{o}C revealed a similar change in crystallinity, as the resulting films demonstrated a strong (101) anatase phase formation. TiN oxidation occurs much faster at these higher temperatures, but gives almost identical XRD spectra (Fig.VI–8 (b)).

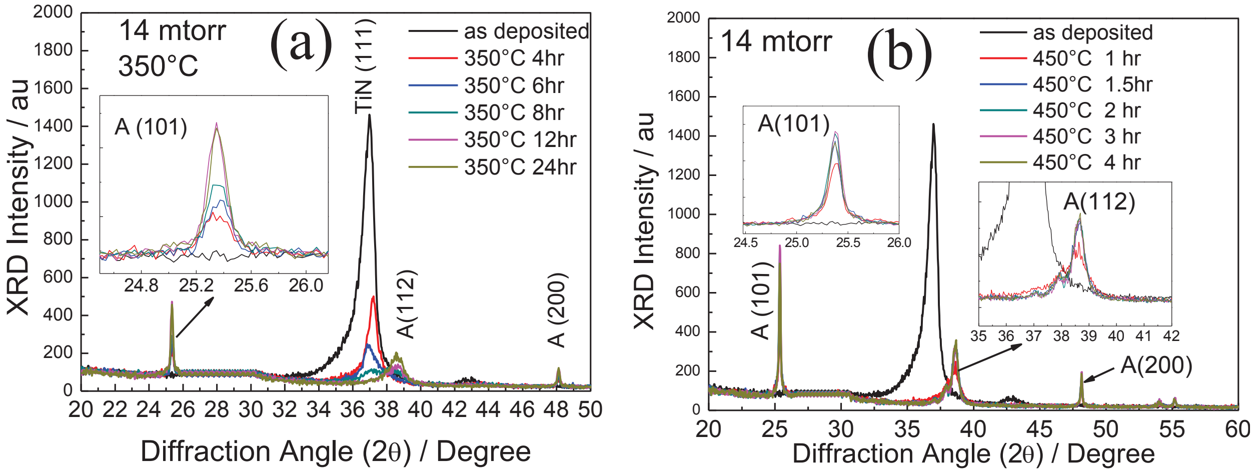

Fig.VI–8: XRD patterns for TiN thin films deposited at 14 mtorr and oxidized at (a) 350°C, (b) 450°C, for different times.

Table VI–1 shows the dominant crystal structure for each film deposited at different pressures for each of the corresponding oxidation temperatures.When changing the TiN deposition pressure, many different orientations and phases of crystalline TiO_2 can be formed after oxidation. Since the oxidation process which the coating deposited at different pressures go through seem to be different and which requires different oxidation times, it was therefore possible to create TiN films, which can oxidize to TiO_2 with different crystal phases, orientations, and concentrations depending on the desired application needs.

Table VI–1: The change in crystal structure for TiN films deposited at different pressures after oxidation at 350°C, 450°C, and 550°C. The numbers in the parentheses represent the dominant crystal orientation, as determined by XRD.

Deposition Pressure	**Oxidation Temperature**		
	350°C	**450°C**	**550°C**
2 mtorr	No change (TiN)	No change (TiN)	TiO_2 rutile (101)
3.5 mtorr	No change (TiN)	No change (TiN)	TiO_2 rutile (101) + anatase (112)
5 mtorr	TiO_2 anatase (112)	TiO_2 anatase (112)	TiO_2 anatase (112)
14 mtorr	TiO_2 anatase (101)	TiO_2 anatase (101)	TiO_2 anatase (101)

VI–5) Crystal size calculation

The crystal size of TiN was estimated by using the Scherrer formula (Eq.III-1) for each of the films before and after oxidation at 350°C, 450°C, and 550°C. The changes in the estimated crystal sizes of the TiN and TiO_2 crystals as a function of oxidation temperature and time are discussed below in details.

VI–5–1) Effect of deposition pressure on the crystal size

Fig.VI–9 presents the ***as–deposited*** TiN crystal size plotted as a function of the deposition pressure. This figure reveals that as the deposition pressure increases from 2 to 5 mtorr, the deposited TiN crystal size decreases significantly from 60 nm to 14 nm, this result is consistent with the SEM–FEG micrographs (Fig.VI–3). In general, thin films deposited at low pressure are denser and have a larger crystal size, while films deposited at higher pressures typically exhibit higher porosity and smaller crystal sizes. This can be explained by the fact that at lower pressures the kinetic energy of the sputtered atoms are higher, which will lead to a higher local temperature of the surface and therefore higher mobility of the species reaching to the surface leading to bigger crystal sizes and higher film density.

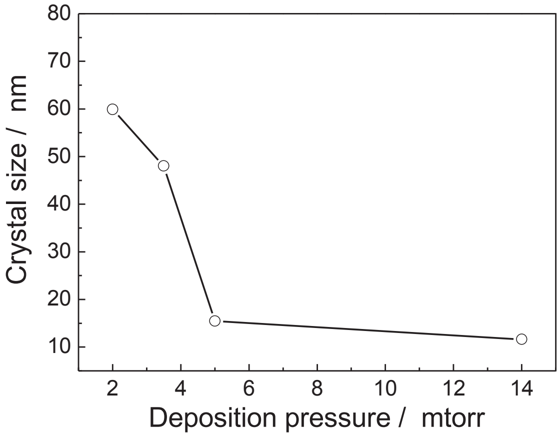

Fig.VI–9: The as–deposited TiN crystal size as a function of the deposition pressure, calculated from the XRD spectra.

TiN Crystal size depends on the deposition pressure. Dense films having bigger crystal size were formed at pressures lower than 5 mtorr, while more porous films having smaller crystal size were formed at higher deposition pressures.

VI–5–2) Dense TiN films deposited at low pressure

Low sputtering deposition pressure (up to 3.5 mtorr) produced dense TiN films, which lead to rutile TiO_2 after thermal oxidation. Fig.VI–10, presents the calculated crystal size of TiN as a function of oxidation time at 350°C, 450°C and 550°C. The crystal size of the rutile TiO_2 is calculated only at 550°C, as this phase appeared only at higher than 550°C.

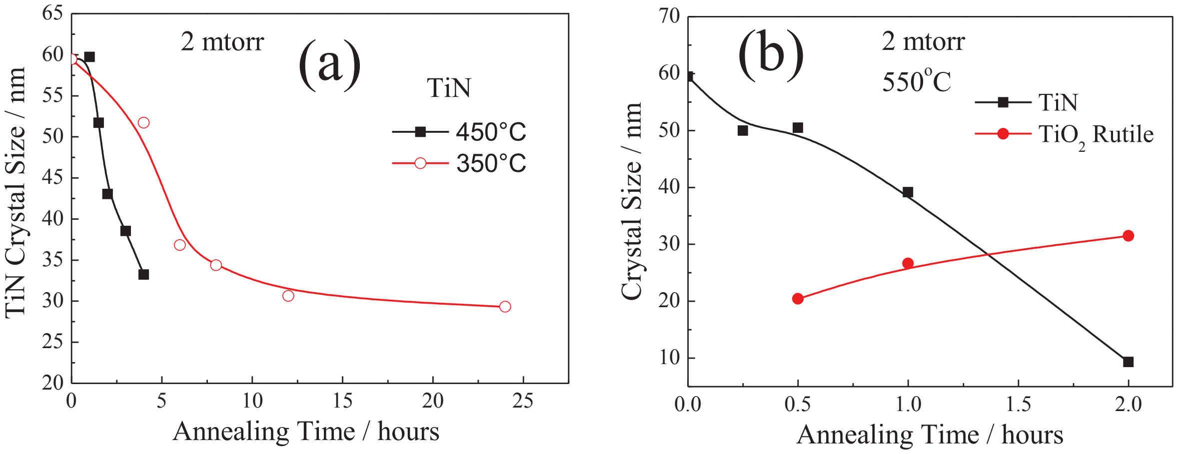

Fig.VI–10: The crystal size of TiN deposited at 2 mtorr as a function of time when oxidized at 350^{o}C and 450^{o}C (a), and the crystal size of TiN and the rutile phase of TiO_2 after oxidation for 2 hours at 550^{o}C (b). TiN was deposited at 2 mtorr.

For the TiN films deposited at *p*= 2 mtorr, the crystal size was estimated using the peak of the (111) cubic phase orientation of TiN, and the (101) rutile phase peak for TiO_2. At low oxidation temperatures (350^{o}C and 450^{o}C), the XRD scans do not reveal any indication of the rutile or anatase phase of TiO_2. However, we were able to detect the presence of TiN during these conditions. As the oxidation time increased, the crystal size of the TiN decreased significantly from roughly 60 nm to 29 nm at 350°C after an annealing time of 12 hours, and at 450°C after an oxidation time of 4 hours.

When this low pressure TiN film was oxidized at 550°C, the TiN crystal size decreased rapidly, and reduced to almost 10 nm after only 3 hours of oxidation. During this high temperature oxidation, the rutile phase of TiO_2 was clearly present after approximately 30 minutes. When the oxidation time was increased, the rutile crystal size also increased, presenting a maximum (33nm) after around 2 hours.

TiN films deposited at p = 3.5 mtorr showed similar characteristics to the film deposited at p = 2 mtorr after oxidation at 350°C and 450°C. As the oxidation time increased, the TiN crystal size decreased, reaching a minimum size of approximately 20 nm after 10 hours of oxidation at 350°C, and after about 4 hours when oxidized at 450°C.

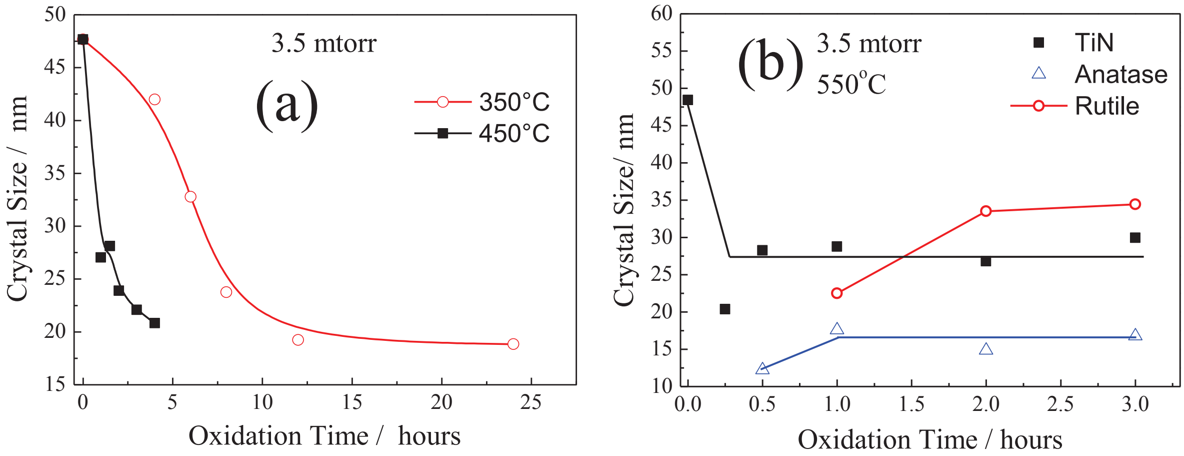

Fig.VI–11: The crystal size of TiN deposited at 3.5 mtorr as a function of time when oxidized at 350°C and 450°C (a), and the crystal size of TiN, the rutile phase of TiO_2, and the anatase phase of TiO_2 after oxidation for 2 hours at 550°C (b).

When this film was oxidized at 550°C, the TiN crystal size again decreased with time. After 30 minutes of oxidation, the anatase phase of TiO_2 was detected. As the oxidation time increased, the anatase crystal size remained close to 17 nm. After an hour of oxidation, the rutile phase of TiO_2 was detected, with a larger crystal size (~22 nm). When the oxidation continued at this temperature, the rutile crystal size grew to approximately 35 nm. *This film showed both the anatase and rutile phases of TiO_2 after thermal oxidation of the resulted TiN film. This could be explained by the fact that the crystal size of TiN decreased since a part of it was transformed to TiO_2, the grain size of which increased with the annealing time.*

VI–5–3) Porous TiN Films deposited at high pressure

The TiN coatings deposited at higher pressures (p = 5~14 mtorr) showed very different crystal growths as compared to the previous two films. In particular, the (112) or

(101) crystal orientation of the anatase phase of TiO$_2$ was observed when oxidation was carried out at 350^{o}C, 450^{o}C, and 550^{o}C, with no traces found of the rutile phase by XRD. Also the TiN peak disappeared when the thermal oxidation was carried out at higher temperatures than 350°C.

Films deposited at 5 mtorr:

The crystal size of the anatase phase of TiO$_2$ is plotted in Fig.VI–12. As the oxidation temperature and time increased, so did the crystal size of the TiO$_2$ anatase crystals. The maximum crystal size for the films deposited at 350^{o}C, 450^{o}C, and 550^{o}C were 15 nm, 24 nm, and 37 nm respectively *which is also logical, as explained above.* Also as the oxidation time increased, the grain size of the new formed crystals should increase in agreement with what reported elsewhere [27–28].

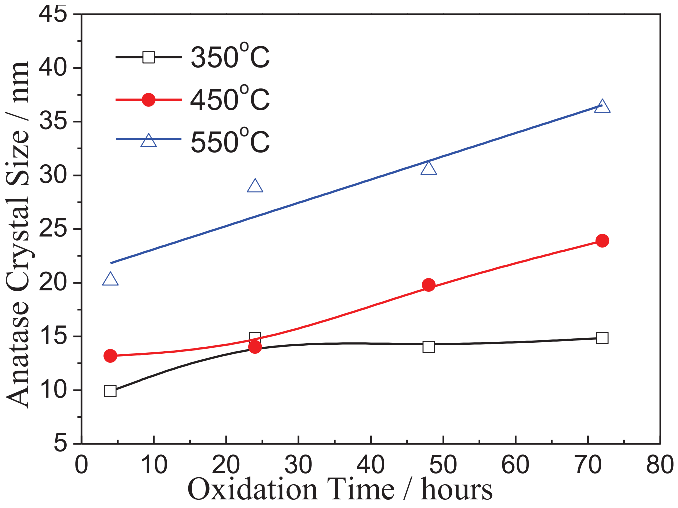

Fig.VI–12: The calculated crystal size of the anatase phase of TiO$_2$ by the (112) orientation peak, as a function of oxidation time at 350^{o}C, 450^{o}C, and 550^{o}C. Initial TiN was deposited at 5 mtorr. Note that, the same time intervals are kept for all the oxidation temperatures.

Films deposited at 14 mtorr:

Fig.VI–13 shows a schematic presentation of one TiN column during the thermal oxidation where d_1 and d_2 are the diameters of TiN and TiO$_2$ columns, respectively. Fig.VI–14 presents the estimated crystal size within the thermal oxidation of TiN film deposited at 14 mtorr. Here the anatase phase (101) of TiO$_2$ was studied, as it was the preferential phase than the anatase (112) orientation. Here also, as the oxidation time increased, so did the anatase crystal size. In addition, the growth in crystal size happened much quicker at higher temperatures (550^{o}C) compared to lower temperatures (350^{o}C). The maximum anatase crystal size estimated was approximately **65 nm** for each of the oxidation temperatures.

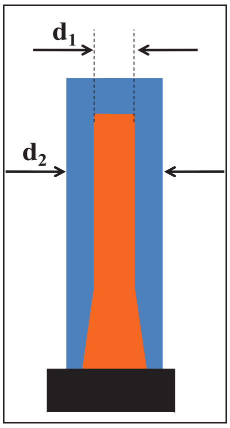

Fig.VI–13: A schematic representation of partially oxidized TiN column (orange color) in the case of porous columnar TiN films shown in Fig.VI–2 (The resulted TiO_2 is in blue color).

It is clear that the deposition pressure played a significant role in the ability of the TiN films to oxidize to TiO_2, as well as the crystal phase and orientation that formed within the TiO_2. In particular, there seems to be a strong correlation between the as–deposited TiN crystal size and the resulting phase of TiO_2 after oxidation. The TiN films deposited at lower pressures formed the rutile phase of TiO_2 after oxidation at high temperatures (550°C), while the films deposited at higher pressures formed the anatase phase more favorable (at low as well as high temperatures). It is apparent that the as–deposited TiN crystal size played a significant role in the development of either rutile or anatase TiO_2 after oxidation.

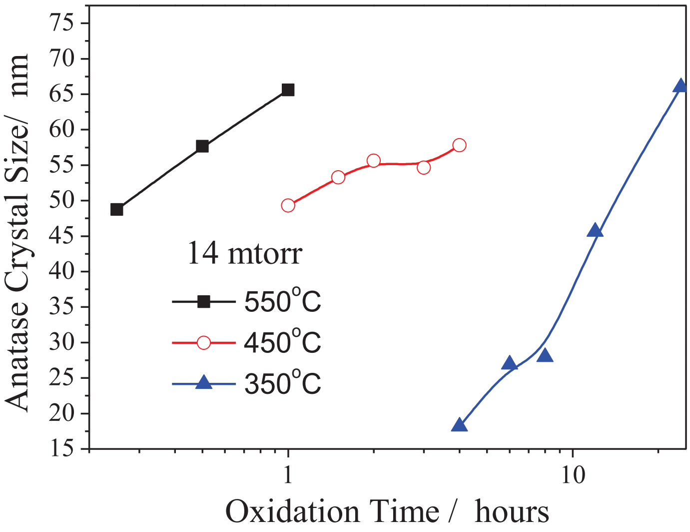

Fig.VI–14: The estimated crystal size of the anatase phase (101) of TiO_2 as a function of oxidation time at different temperatures 350°C, 450°C, and 550°C. TiN film has been deposited at 14 mtorr.

For all the annealing temperatures, as the oxidation time increased, so did the anatase crystal size. In addition, the growth in crystal size of anatase happened much quicker at higher temperatures (550°C) as compared to lower temperatures (350°C).

VI–6) X–ray Photoelectron spectroscopy

The oxidation kinetics has been followed using XPS, here we have restricted to the study on the oxidation of TiN thin films deposited at ***5 mtorr*** then oxidized at 350°C and 450°C. After fitting all the peaks with symmetric Gaussian–Lorentzian deconvoluted peaks, XPS spectrums of N 1s and O 1s core level have been regrouped in Fig.VI–15 and Fig.VI–16 for TiN films oxidized at 350°C and 450°C within different time intervals, respectively. The same spectra for the as deposited TiN films are also presented as a reference at the bottom of Fig.VI–15 (the O1s and N1s trends are discussed in detail in the next two sections).

Table VI–2: Different atomic concentrations, using XPS data, of Ti, O and N species present in the TiN thin films deposited at 5 mtorr then oxidized at 350°C and 450°C for different time intervals. The contribution of each nitrogen sub–species have been presented, as well as the ratio between the two oxygen peaks (N_s: substitutional, N_{ch}: chemisorbed N_i: insertional).

	O1s	**Ti2p**	**N1s**	**N_s 396 eV**	**N_{TiN} 397 eV**	**N_s 398 eV**	**N_{ch} 400 eV**	**N_i 403 eV**	**% O_{532}/O_{530}**
TiN	33.3	41.7	25.0	8.8	12.5	3.7	0.0	0.0	55.9
350ºC for 4hr	48.4	37.9	13.7	4.2	0.0	0.2	1.2	8.1	16.8
350ºC for 6hr	50.1	37.5	12.4	2.9	0.0	0.0	0.5	9.0	16.8
350ºC for 12hr	54.7	36.3	9.0	1.1	0.0	0.0	2.1	5.8	14.6
350ºC for 18hr	56.3	35.9	7.8	1.3	0.0	0.0	3.0	3.5	16.1
350ºC for 24hr	56.8	35.8	7.4	0.6	0.0	0.0	3.3	3.5	15.8
350ºC for 40hr	58.3	35.4	6.3	0.6	0.0	0.0	2.8	2.9	15.6
350ºC for 48hr	59.1	35.2	5.7	0.5	0.0	0.0	2.6	2.6	17.1
350ºC for 72hr	59.7	35.3	5.0	0.0	0.0	0.0	2.3	2.7	18.9
450ºC for 1hr	57.3	35.7	7.0	2.0	0.0	0.0	2.4	2.6	17.7
450ºC for 1.5hr	58.9	35.3	5.8	0.6	0.0	0.0	2.7	2.5	18.9
450ºC for 2hr	60.0	35.0	5.0	0.3	0.0	0.0	2.4	2.3	18.6
450ºC for 3hr	60.3	34.9	4.8	0.4	0.0	0.0	2.3	2.1	12.0
450ºC for 4hr	61.1	34.7	4.2	0.3	0.0	0.0	1.9	2.0	10.6
450ºC for 5hr	61.4	34.8	3.8	0.3	0.0	0.0	1.8	1.7	14.0
450ºC for 24hr	63.7	34.1	2.2	0.4	0.0	0.0	1.0	0.8	17.3
450ºC for 48hr	64.8	33.8	1.4	0.0	0.0	0.0	0.8	0.7	13.9
450ºC for 72hr	65.6	33.6	0.8	0.0	0.0	0.0	0.5	0.3	14.5

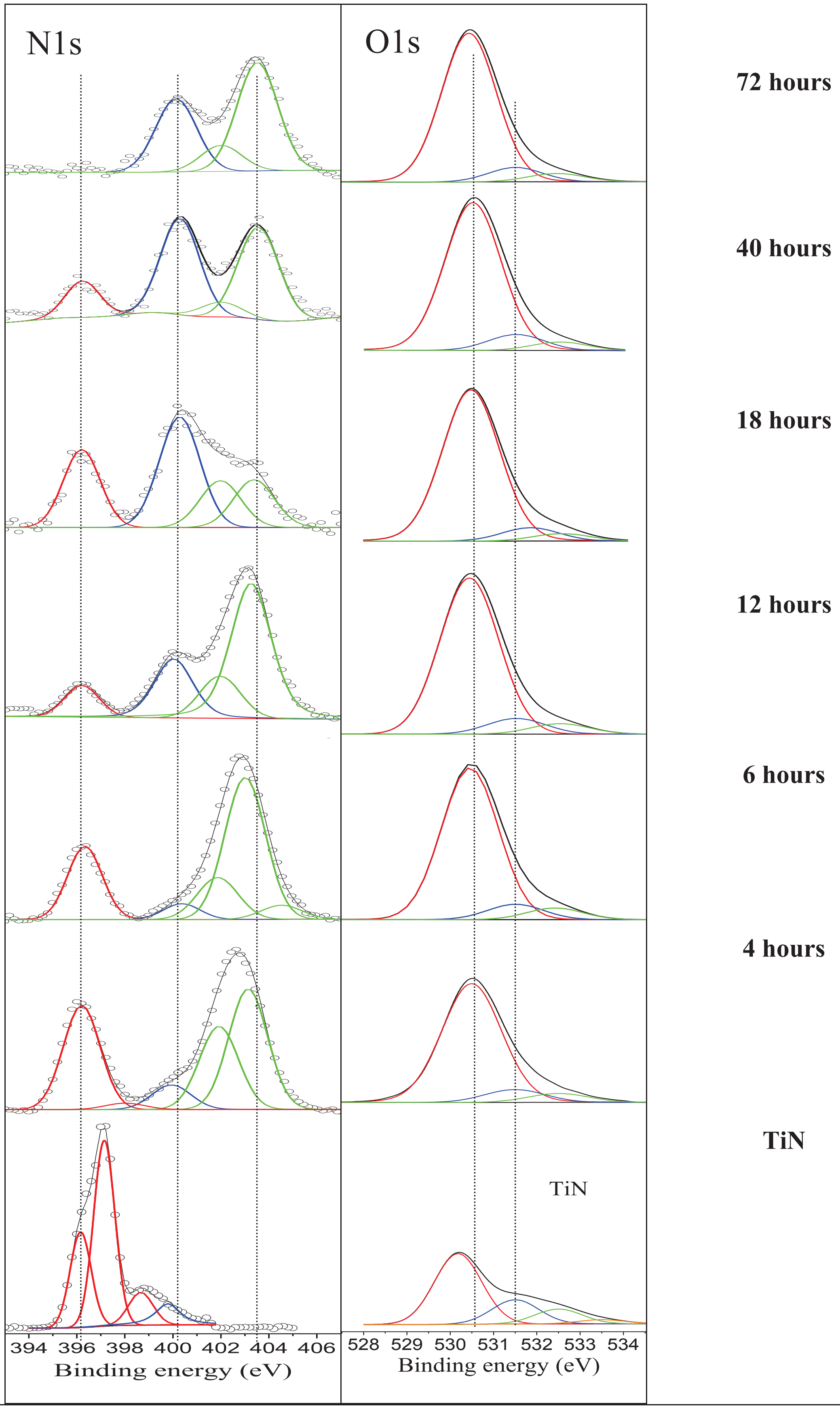

Fig.VI–15 : Deconvolution of N1s and O1s core levels for samples oxidized at ***350°C*** *for different times. Interstitial, chemisorbed and substitutional nitrogen are presented in green, blue and red colors, respectively.*

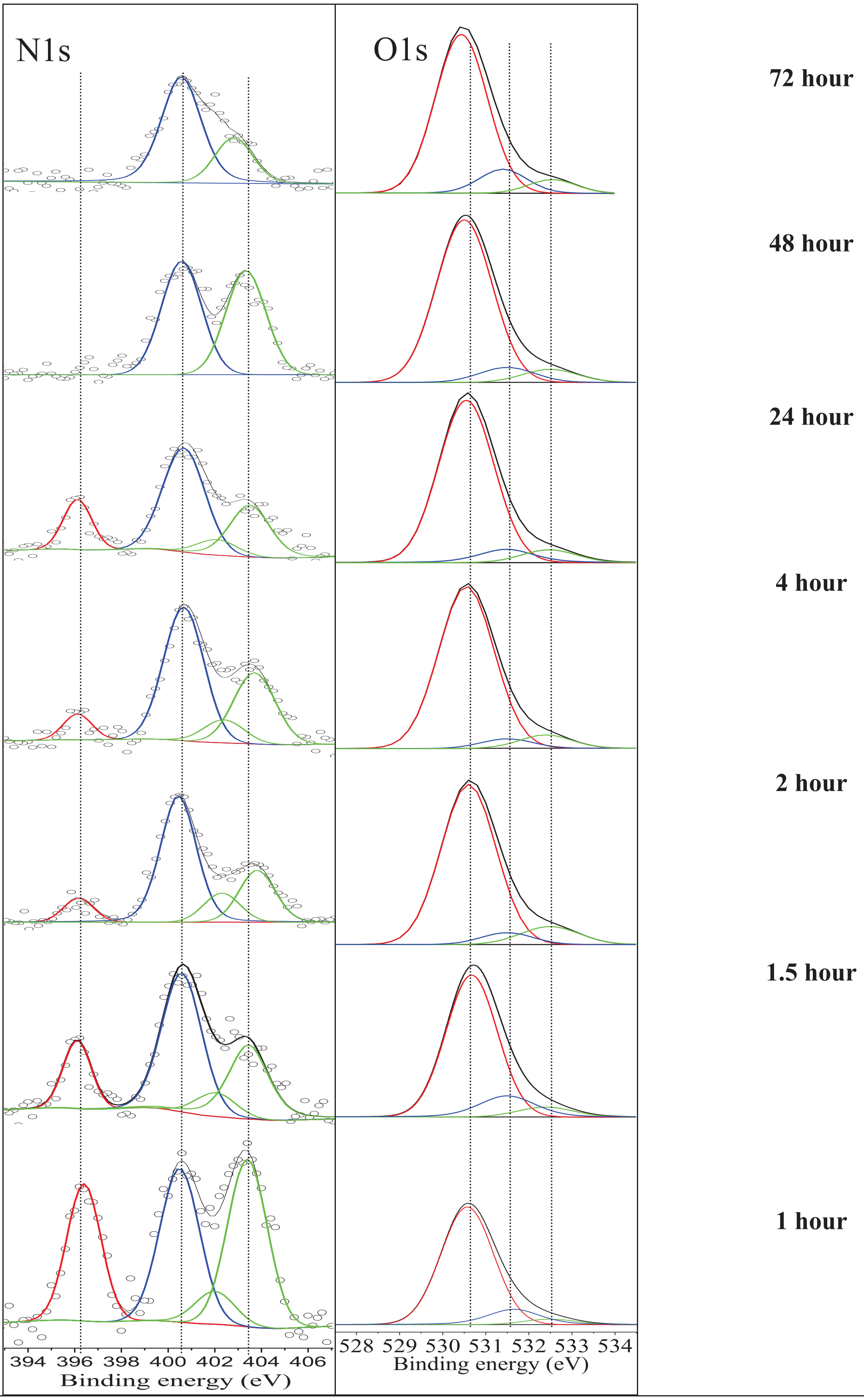

*Fig.VI–16 : Deconvolution of N1s and O1s core levels for samples oxidized at **450°C** for different times. . Interstitial, chemisorbed and substitutional Nitrogen are presented in green, blue and red colors, respectively.*

Atomic concentrations of Ti, O and N species, present in the as-deposited and oxidized TiN thin films, vs oxidation time intervals are presented in Table VI–2 and Fig.VI–17. The contributions of each nitrogen sub–species vs oxidation time are presented in Table V–2 and Fig.VI–18, as well as the ratio between the two Oxygen peaks.

Carbon core level spectra (from surface hydrocarbon contamination) have been used to correct any shift in the binding energies due to surface electrostatic charging. The main C 1s peak has been set at 285 eV and the resulted shift has been used to rescale all the other spectra.

VI–6–1) O1s core level spectra

It is clear that in both oxidation temperatures (350°C and 450°C), O1s core level spectra was deconvoluted into two main peaks located at 530.5 eV and around 532 eV. The former peak is typically assigned to the oxide peak of TiO_2 corresponding to O—Ti—O bonds [16–17], the second peak centered at 532 eV could be deconvoluted into two or even three peaks as follow:

- 531.5 eV corresponds to metal hydroxylation (Ti—OH) [18] due to the presence of –OH groups on the surface of the samples, this contribution could be masked by the C—OH bonds that could have the same BE position, also Ti—N—O could have a contribution in this peak [19][17][13].
- The 532.5 peak could be assigned to Ti—O—N—O contributions [20] due to the interstitial presence of –NO and $–NO_2$ trapped in the lattice of titania which is supported by the N 1s core level spectrum. Also C—O bonds could contribute in this peak as O—C=O or O—C—O.
- O 1s peaks at BE higher than 533 eV have been assigned to the contribution of adsorbed H_2O molecules and the presence of hydrocarbon contaminations (C—O or other C=O bonds) [19][16].

All of these assignments are possible. A light pre–sputtering with argon in the XPS apparatus (just before the acquisition of spectrum to remove C contamination) affected the ratio between the 532 eV and the 530.5 eV peaks without removing the 532 eV peaks. That means that the carbon contamination is not the only reason behind the presence of the secondary shoulder cent at 532 eV. Also, this shoulder is very pronounced in the TiN thin films which contain no Ti—O bonds (Table.VI–2), which supports the presence of the other mentioned secondary species.

The atomic ratio of O/Ti was deduced using the main oxide peak of O 1s (at 530.5 eV) and Ti $2p_{3/2}$. This calculated ratio is about 1.28~1.95 (<2) for the thermally oxidized films, depending on the oxidation time and temperature. In fact, regardless of the doping sites in the lattice of TiO_2, it is difficult to calculate an accurate value of the film stoichiometry (or at least O/Ti) using the oxide peak only at 530.5 eV, as we should consider the other possible Ti bonds such as the hydroxylation of titanium (Ti—OH). However, it is difficult to differentiate the Ti–OH contribution in the shoulder at BE > 531 eV, as explained above, since it is generally screened by the C—OH and –N—O in the O 1s spectra [18].

Looking at the evolution of oxygen concentration with oxidation time (in Fig.VI–17) for both oxidation temperatures of TiN (350°C and 450°C), we can conclude that, for this deposition pressure (5 mtorr), the anatase phase (112) of TiO_2 appeared under these mentioned oxidation temperatures (taking into consideration the above XRD results). The upper thin layer is oxidized to anatase TiO_2 within 10 hours at 350°C and 1.5 hours at 450°C. After this time, the oxidation kinetics becomes slower, probably, due to the slower diffusion of oxygen through the new TiO_2 layer compared to its diffusion through the TiN columns (more porous). RBS and SIMS analysis are more powerful techniques to give a clearer idea about the kinetics of TiN oxidation in the bulk. On the other hand, we note that the area of the main O1s peak increased, while the secondary O1s peak (centered at 532 eV) decreased, with the oxidation time for both of the oxidation temperatures. This is not surprising as at these oxidation temperatures:

- ✓ the diffused oxygen should substitute nitrogen atoms and bond with titanium leading to an increase in the area of the oxide peak of O1s (at 530.5 eV),
- ✓ hydrocarbon compounds were oxidized and desorbed, –OH groups and adsorbed water molecules were also partially desorbed leading to the decrease of the area of the secondary O1s peak (centered at 532 eV).

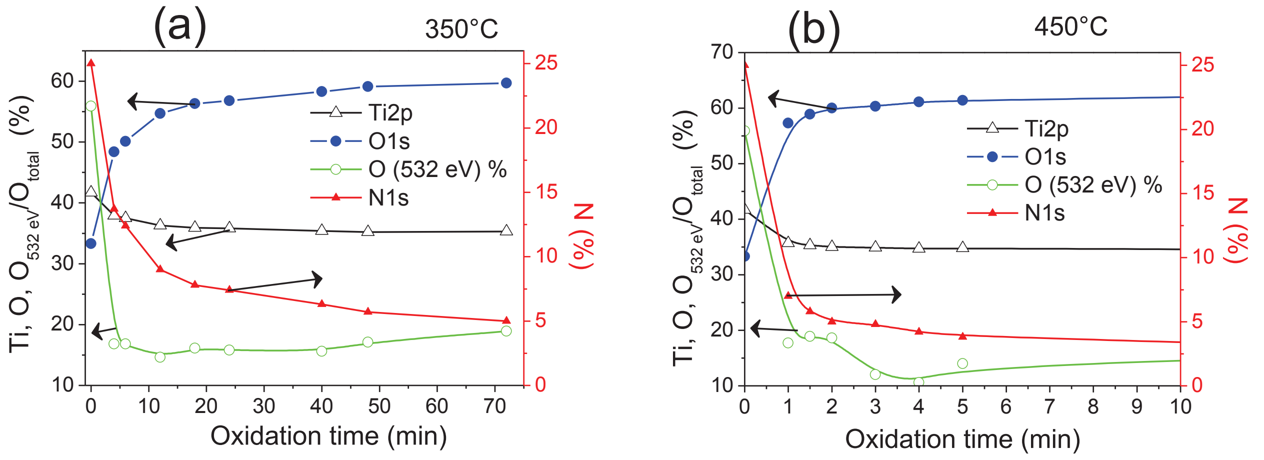

Fig.VI–17: Graphical representation of different atomic concentrations, using XPS data, of Ti, O and N species present in the TiN thin films deposited at 5 mtorr then oxidized at (a) 350°C and (b) 450°C vs oxidation time. Ratio of the secondary oxygen shoulder $O_{532\ eV}/O_{total}$ is presented as well.

The upper layer of porous TiN is oxidized to anatase TiO_2 within 10 hours at 350°C and 1.5 hours at 450°C, after this time, the oxidation kinetics became slower. The O1s spectrum is composed of a main oxide peak centered at 530.5 eV and another secondary peak centered at 532 eV. The last one could be decomposed again to 3 subpeaks corresponding to adsorbed species. The adsorbed species on the surface of the thin films were oxidized and partially desorbed during the oxidation process for both of the oxidation temperatures.

VI–6–2) N1s core level

The different arrangements, concentrations and nature of nitrogen species on the surface layer of the oxidized TiN thin films are presented in Fig.VI–15, Fig.VI–16 and Fig.VI–18. We can distinguish three types of nitrogen species in the resulted network of the N doped titania:

- substitutional nitrogen (**N_s**) (where nitrogen is bonded to titanium) at 396 eV [16][21–22], 398 eV [23–24] and 397 eV [25] as seen in dual gas (paragraph IV-3-3).
- Chemisorbed nitrogen (**N_{ch}**) localized around 400 eV.
- interstitial nitrogen (**N_i**), where N is bonded to one or more O atoms, as NO^-, NO_2^- or NO_3^-, at 401 eV to 404 eV depending on the number of oxygen atoms bonded to each nitrogen species. The binding energy shifts to higher values as the nitrogen is bonded to more oxygen species (more electronegative).

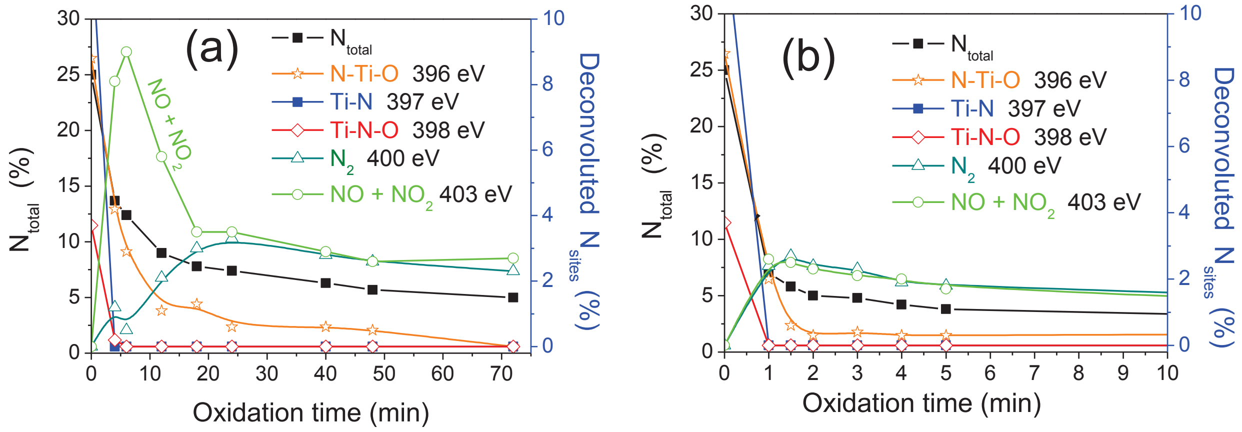

Fig.VI–18: Graphic representation of different nitrogen species present in the TiN thin films deposited at 5 mtorr then oxidized at (a) 350°C and (b) 450°C vs oxidation time, using Table VI–2.

The main difference between nitrogen position here compared to the ones detected in previous deposition methods (in chapter IV and chapter V) is the position of the interstitial nitrogen (oxidized nitrogen species) having Ti—O—N and Ti—O—N—O configurations in the doped TiO_2 lattice. Here, interstitial nitrogen peak, in the oxidized TiN, is located at 403.0 eV and so it is probably attributed to the Ti—NO_2 contributions [22] (i.e. nitrogen atom bonded simultaneously to one titanium and two oxide ions) rather than Ti—NO (at 402 eV) which have been seen previously. Comparing figures.IV–17 and IV–18, we can divide the oxidation process into 2 steps:

- ***First step***: this step has a duration of about 10 hours and 1.5 hours when oxidizing at 350°C and 450°C, respectively. Within this step, the total concentration of nitrogen decreased steadily and at the same rate that of oxygen increased, which is not surprising. But the sub–nitrogen species have different trends, depending on the oxidation time and regardless of the oxidation temperature. The concentration of the interstitial nitrogen N_i (NO_x with $1<x<2$) as well as the chemisorbed species N_{ch} present a fast increase. The increase of these nitrogen sites is probably due to the released nitrogen from the oxidized TiN layers. These released nitrogen species could be partially oxidized and trapped in the new TiO_2 lattice. At the same time, the concentration in substitutional nitrogen sites N_s (such as N—Ti—O, Ti—N—O and Ti—N) decreased with time, due to the oxidation of these bonds following the next *proposed* semi–reaction, where n_1 and n_2 are real numbers:

$$(n_1 + n_2)N_s \xrightarrow{heat,O_2} n_{1.}N_i + n_{2.}N_{ch} \qquad \text{Eq.V–1}$$

- ***Second step***, then the number of interstitial sites decreased again and stabilized around 2% and 1.5% when oxidizing at 350°C and 450°C, respectively. That means that the Ti—N bonds, at the surface of the thin films, were fully oxidized.

During the oxidation of TiN, the total concentration of nitrogen decreased as well as the substitutional nitrogen sites, but not the interstitialones . Interstitial nitrogen sites were mainly in the form of –NO_2 rather than –NO.

VI–6–3) Ti 2p spectrums

For all of the oxidized samples (Fig.VI–19), the Ti 2p spectrum consists of Ti $2p_{3/2}$ and Ti $2p_{1/2}$ contributions located at 459.3 eV and 465.1 eV, respectively.It is noteworthy to mention that a small shift of about 0.1 eV can be considered to be negligible as it is in the same order of magnitude as the step size of the XPS measurements.

Ti $2p_{3/2}$ peaks were located at 458.3 eV for the as-deposited TiN, which is lower than the reported values of such films (around 457eV) [16][25–26]. This means that Ti cations are partially oxidized on the surface which is consistent with the presence of a small oxide peak at 530 eV of O 1s, in the TiN film. Also, maybe a shift in the Fermi level with respect to the core lines (during the XPS measurement due to the bombardment by the incident electron beam) could contribute to this apparent shift of the Ti $2p_{3/2}$ [18].

During the oxidation process, Ti $2p_{3/2}$ peak was located at 459.3 eV and the distance between the Ti $2p_{3/2}$ position and the main oxide O 1s peak (at 530.5 eV) was 71.5±0.1 eV for all the oxidized samples, regardless of the oxidation time. This means that Ti was in its full oxidation state Ti^{4+} [19][16], in the topmost layers of the ***oxidized*** TiN films (analyzed by XPS), from the beginning of the oxidation process, without any oxygen vacancies for all the oxidation temperatures. This is in agreement with the fact that no Ti 3d states near the Fermi level were detected (not presented here, cf also paragraph IV-3-4).

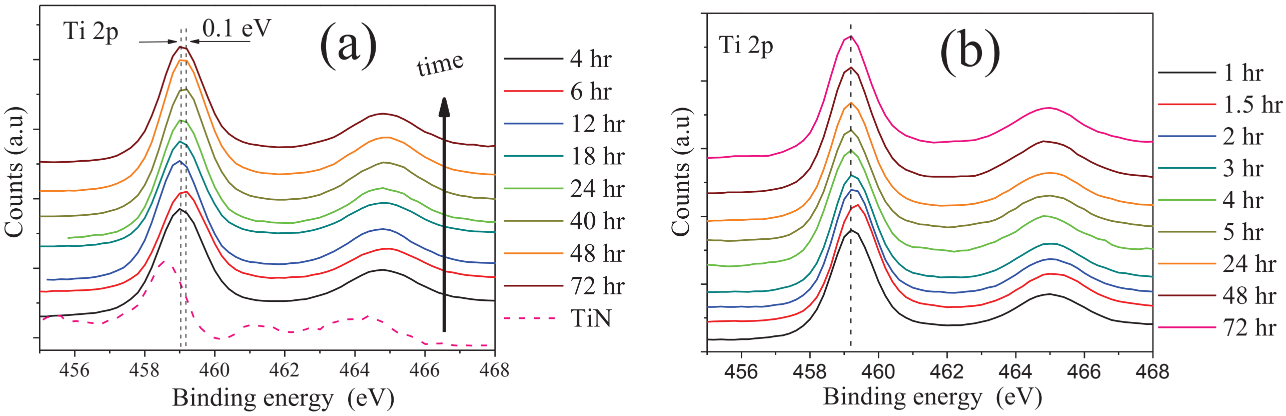

Fig.VI–19: XPS spectrum of Ti 2p, for samples oxidized at a) ***350°C*** *and b)* ***450°C*** *during different time intervals.*

From the beginning of the oxidation process of TiN, Ti was in its full oxidation state. The oxidized layer didn't contain any oxygen vacancies.

VI-6-4) First results of XPS depth profiling:

XPS depth profiling has been used to determine how the oxidation front progresses for the films as a function of annealing time. An example of overlay of the N 1s peak in the depth profiling for the 350°C exposures after 12 hours is shown in Fig.VI–20. The depth profiling results (bulk film composition) for the 5 mtorr deposited films oxidized at 350°C for different annealing times are given in Fig.VI–21.

The as–deposited TiN reference sample exhibited a TiN_x stoichiometry of $TiN_{0.87}$. Upon oxidation, the trend of gradual increase of oxygen concentration (and decrease of N concentration) in the bulk as a function of oxidation time is clear. Interestingly, from Fig.VI–21, it can be seen that regardless of the oxidation time, below the highly oxidized surface region (10–20 nm), the bulk composition of the thin films was invariant as a function of depth. In Fig.VI–20, the N 1s component showed the presence of peaks representative of

TiO_xN_y at the surface, but for all the profiles, below a depth of 10 nm, the N 1s peak shape remained the same, exhibiting a strong peak at 397.1 eV, corresponding to the binding energy of TiN. Hence, for these particular partially oxidized films the TiO_2 layer has a thickness of 10 to 20 nm. Below this layer, there is a bi–phase of TiN/TiO_2 structure, which is again in agreement with the proposed model shown in Fig.VI–2 (b) and Fig.VI-13

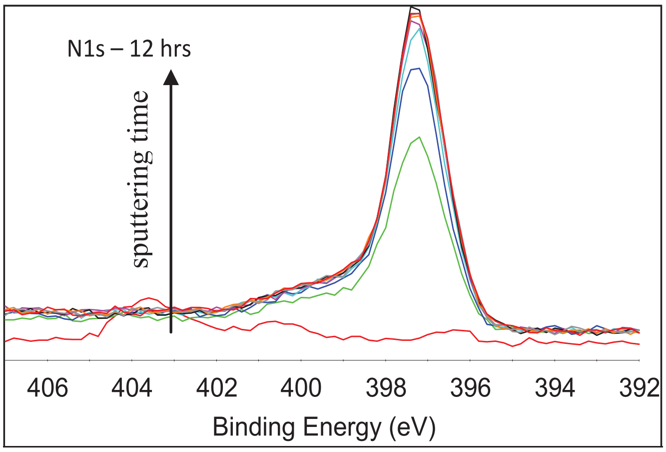

Fig.VI–20: Example of XPS N 1s spectrum for TiN films deposited at 5 mtorr and thermally oxidized at 350°C for 12 hours.

.

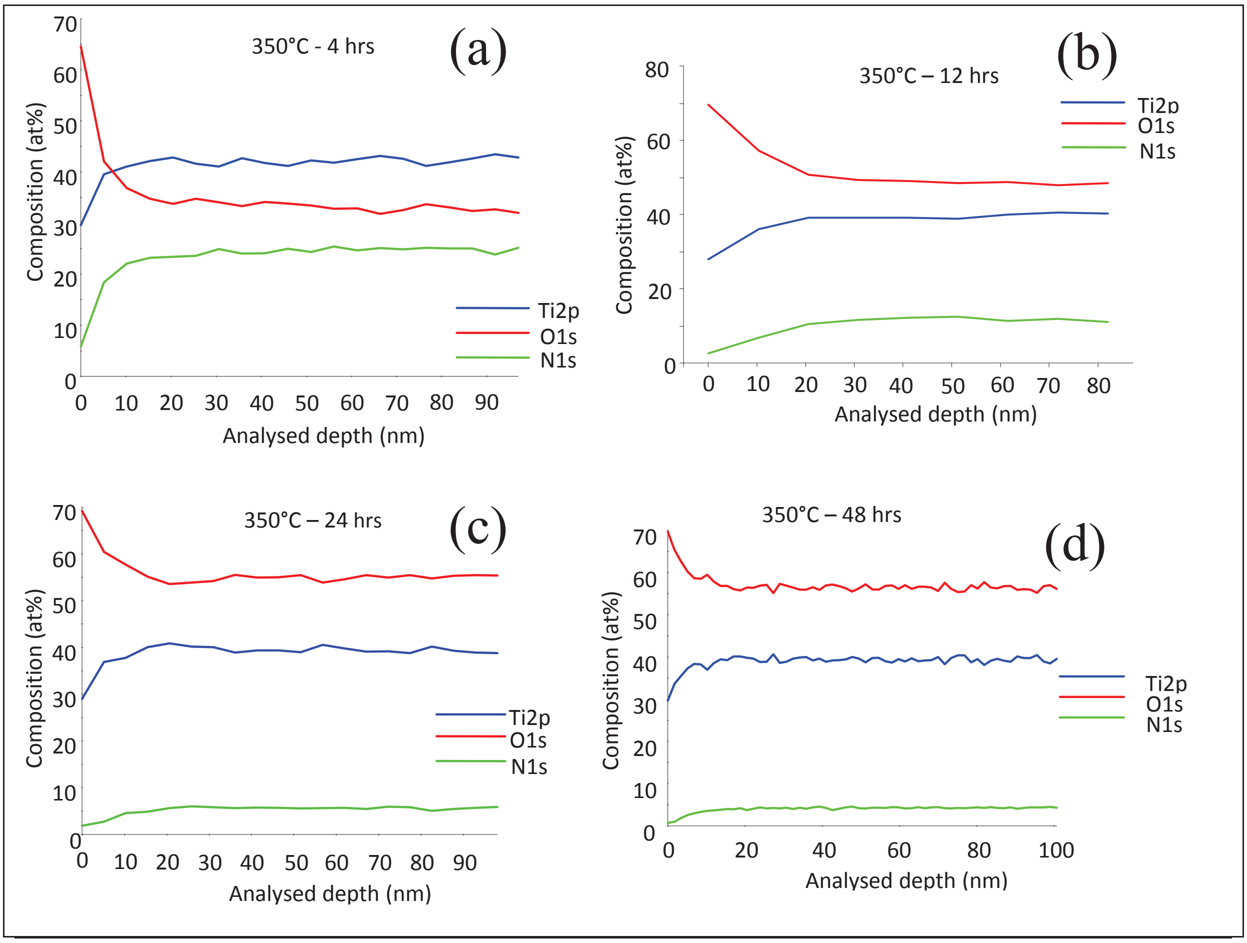

Fig.VI–21: XPS depth profiles for TiN thin films deposited at 5 mtorr and annealed for 4(a), 12(b), 24(c) and 48(d) hours.

When comparing oxygen and nitrogen concentrations in the bulk of the oxidized film (Fig.VI–21 (a), (b), (c) and (d)), it is clear that oxygen concentration increased with the oxidation time, the inverse of what was observed for the nitrogen profile (seeing the concentrations from (a) to (d) in Fig.VI–21). This could be directly correlated to the model in Fig.VI–2 (b) and Fig.VI-13.

VI–7) Optical Properties

VI–7–1) optical absorption

A photograph of oxidized TiN samples is presented in Fig.VI–22, including different deposition pressures, oxidation temperatures and oxidation times.

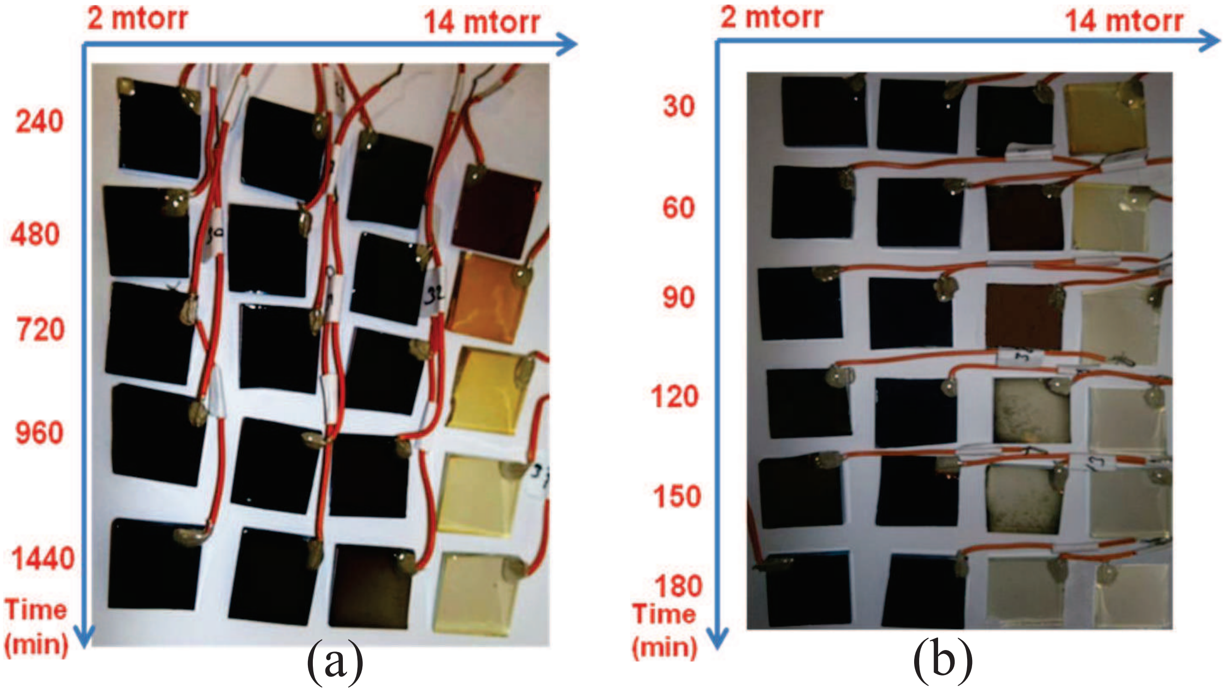

Fig.VI–22: Appearance of different TiN films deposited at 2, 3.5, 5 and 14 mtorr then oxidized at (a) 350°C and (b) 450°C, for different times.

The optical properties of the oxidized TiN films showed a large variance in their spectra, the changes could be directly aligned with the XRD results. The films deposited at p= 2 mtorr and 3.5 mtorr showed no change in their transmission spectra after oxidation at both 350^{o}C and 450^{o}C. This small transmission indicated that the oxidation of these films took place only within the thin layer on the surface, as there is no oxygen diffusion in the bulk, and the films were still mainly composed of TiN.

When the film deposited at p = 5 mtorr was oxidized at 350^{o}C, (Fig.VI–23 (a)), as the oxidation continued, the transmission also increased at higher wavelengths but remained very low for wavelengths below 500 nm, and only achieved a maximum transmission of ~50% after 48 hours of oxidation. After oxidation for 72 hours, the transmission was much higher above 400 nm, and a sharp decrease in transmission due to absorption was seen at 380 nm, corresponding to a band gap energy of 3.2 eV, characteristic of anatase TiO_2. When this film was oxidized at 450°C, the changes in transmission occurred much faster, and the sharp anatase band edge emerged after only 4 hours of oxidation (not shown).

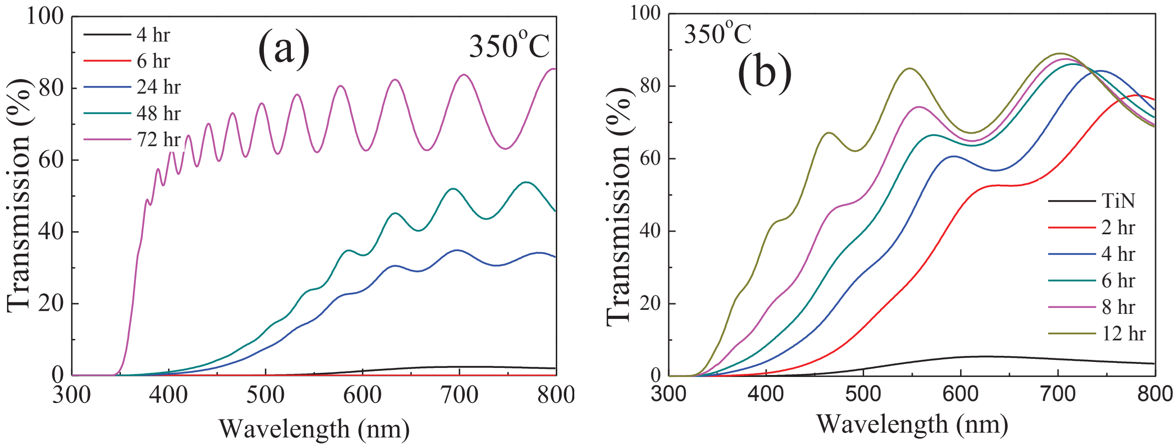

Fig.VI–23: Transmission spectra for the TiN thin films deposited at (a) 5 mtorr and (b) 14 mtorr, oxidized at 350°C.

The as-deposited films at 14 mtorr showed some transmission before any oxidation, seen between 450 nm and 800 nm, with a maximum transmission of ~8%. The oxidation at 350°C for 2 hours showed a large increase in transmission at longer wavelengths, and a gradual decrease down to 450 nm, shown in Fig.VI–23 (b). As the oxidation continued, the absorption edge of the spectra began to shift to lower wavelengths, eventually forming a sharp edge indicative of anatase TiO_2 after 24 hours of oxidation. Oxidation at higher temperatures showed a more drastic change, with the sharp band edge appearing after less than 2 hours and 30 minutes of oxidation at 450°C and at 550°C, respectively (not shown).

VI–7–2) Correlation between structural and optical properties

The films deposited at p = 2 mtorr and 3.5 mtorr showed little change in their crystalline structure and optical transmission when oxidized at low temperatures. However, when the film deposited at p = 2 mtorr was oxidized at 550°C, rutile phases of TiO_2 was observed in the XRD patterns (Table VI–1); but the film deposited at p = 3.5 mtorr showed both rutile and anatase characteristics when oxidized at the same temperature as the anatase phase was able to grow because the film was slightly less dense as compared to the film deposited at 2 mtorr. The decreased density provided more space for anatase formation, which in turn reduced the free space in the lattice (as anatase volume is larger than both TiN and rutile TiO_2), then the anatase growth had to slow down and only rutile continued to grow. Both of films deposited at p = 5 mtorr and 14 mtorr change from TiN to the anatase phase of TiO_2 when oxidized at 350°C, 450°C, and 550°C, with no traces of rutile. However, the film deposited at p = 5 mtorr was transformed to anatase phase with the preferred (112) orientation, while the film deposited at p = 14 mtorr changed to the (101) orientation of anatase. The estimated band gap energies were very similar for both films after oxidation; however their crystal structure was different. The oxidation behavior at 450°C and 550°C occurred very quickly, indicating a more direct transition from TiN to TiO_2, and the chemical reaction may be described by the following equation,

$$2TiN + 2O_2 \rightarrow 2TiO_2 + N_{ch} \quad . \qquad \text{Eq.V–2}$$

However, films deposited at high pressure, oxidized at 350°C showed a much more gradual change from TiN to TiO_2, and their optical, crystalline and chemical properties indicated that an intermediary phase of titanium oxynitride may be formed. At least, there is a two–step reaction to oxidize TiN to titanium oxynitride then to TiO_2, that can be described in the following reactions,

$$TiN + O_2 \rightarrow TiO_xN_y + N_{1-y}O_{2-x} \qquad \text{Eq.V–3}$$

$$TiO_xN_y + O_2 \rightarrow TiO_2 + N_yO_x \qquad \text{Eq.V–4}$$

Equations Eq.V–3 and Eq.V–4 demonstrate how a layer of TiO_xN_y can initially could form on the TiN surface, which then could easily promote the generation of TiO_2. As this oxynitride growth front moved deeper into the film, it still showed the ability to transform into anatase TiO_2. In the low pressure films, this pathway lead to the formation of rutile, while in the high pressure films anatase phase was formed.

The optical properties of the films accurately reflected the change from pure TiN to predominantly TiO_2, indicating that a mixed TiN/TiO_2 structure with or without intermediate N–doped TiO_2 structure (TiO_xN_y), lowered the optical transmission and decreased the band gap (as proposed in Fig.VI-13).

VI–8) Photo electrochemical responses

VI–8–1) Linear sweep voltametry

The setup of photo-electrochemical measurements is presented in (Fig.III-1). Linear sweep voltammograms under white light irradiation of the oxidized TiN films were measured after oxidation at 350°C and 450°C for different time intervals. The photocurrent density as a function of the sweeping bias voltage of samples deposited at 2 mtorr, 3.5 mtorr, 5 mtorr and 14 mtorr are shown in Fig.VI–24 (a), (b) (c) and (d), respectively. Sweeps were conducted from –0.8 V up to 1.0 V/ref. When the biasing voltage increased above 1.2 V a sharp increase in photocurrent was observed, due to the sharp increase in the water splitting reaction. Therefore, for visual clarity we will show the photocurrent generation only between –0.8V and 1.0 V.

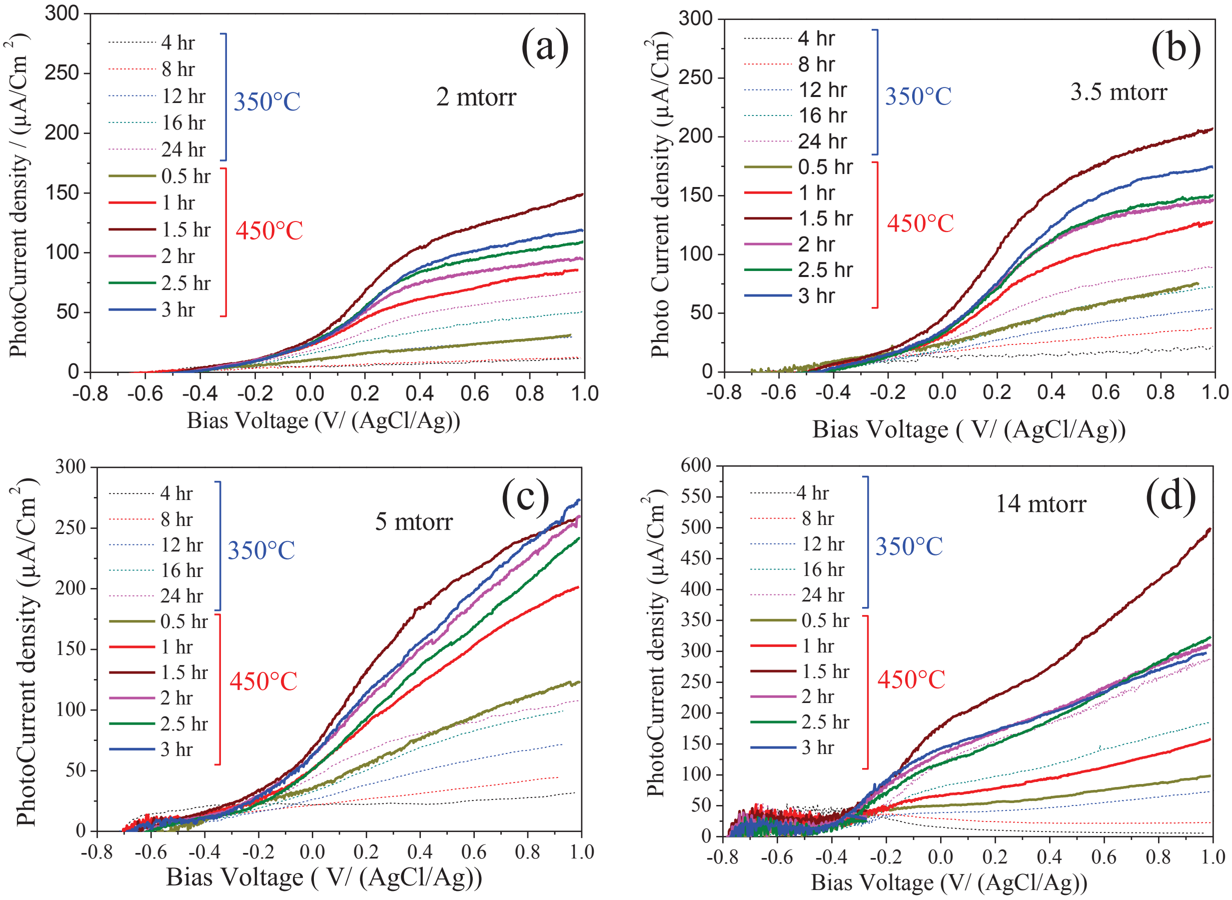

Fig.VI–24: Linear sweep voltammograms under white light irradiation and biasing voltages between –0.8 V to 1.0 V /(AgCl/Ag) , for TiN films prepared at (a) 2 mtorr, (b) 3.5 mtorr, (c) 5 mtorr and (d) 14 mtor, then oxidized at 350°C and 450°C for different times.

The trends for all the deposition pressures seem to be identical with respect to the oxidation temperature and time, although two main trends in the photo–generated current could be observed:

- ✓The maximum photocurrent density, increased as the deposition pressure increased from 2 mtorr to 14 mtorr, this trend will be discussed later (in the next section).
- ✓Samples prepared at lower pressure presented a quasi-stationary plateau for the photo–generated current (Fig.VI-24 (a) and (b)), for biasing voltages higher than 0.4 V/ref. However samples prepared at higher pressures don't present these stationary values on the photocurrent curves , especially in the case of samples prepared at 14 mtorr (Fig.VI-24 (c) and (d)).

To investigate this last remark, the samples were immersed in the electrolyte solution (Na_2SO_4 1 M) for one hour before repeating the sweep measurement of photocurrent, but no change in the measured photocurrent shape was found. This means that the steady increase in the photo generated current, with no stationary plateau, was not due to any change in the adsorption of the electrolyte on the surface of titania. On the other hand, we noted a shift in the Open Circuit Voltage (OCV) from –0.6 V/ref to –0.78 V/ ref as the deposition pressure increased from 2 mtorr to 14 mtorr. Hence, there is a substantial change in the electronic structure of the oxidized TiN films when we increase the deposition pressure from 2 mtorr to 14 mtorr. Therefore the absence of any stationary photocurrent in the high pressure samples was attributed to the increase in the water splitting kinetics at biasing values lower than that of the lower pressure films.

For all of the TiN films deposited at all of the studied pressures and oxidized at 350°C, the photocurrent increased with increasing oxidation time with a maximum photocurrent density observed for the maximum oxidation time of 24 hours. However, for all of the films annealed at 450°C, a maximum photocurrent density was observed after annealing for 1.5 hours, and then the current density began to decrease for further oxidation time.

VI–8–2) Intermittent Photocurrent in potentiostatic configuration

Intermittent photocurrent density measurements were obtained for each of these films witha potentiostatic biasing of 0.5 V/ref (which is positioned in the stationary plateau and before reaching the release wall of O_2), and plotted as a function of time. Intermittent white light current density vs time, of TiN samples deposited at different pressures and oxidized at 350°C and 450°C for different time intervals, are shown in Fig.VI–25. Fig.VI–26 presents the visible light generated current, after the insertion of the UV filter, using the same mentioned samples.

Once again it is seen that after annealing at 350°C, the oxidized TiN films created more photocurrent as the thermal oxidation time increases, with a maximum observed photocurrent of 160 ± 10 $\mu A/cm^2$ for the samples deposited at 14 mtorr. However, when the samples were oxidized at 450°C, a distinct increase in photocurrent was observed, with a maximum current density of 280 ± 7 $\mu A/cm^2$ achieved for the samples deposited at 14 mtorr after 1.5 hours of annealing.

The average photocurrent generated under white light and visible light irradiations, by the oxidized TiN samples, was plotted as a function of annealing time and is shown in Fig.VI–27 and Fig.VI–28. There are several trends which are present in these figures:

Films oxidized at 350°C: From figures.VI–27 (a) and (b), it is clear that as the deposition pressure and/or oxidation time increased, so did the photocurrent density, with a maximum photocurrent of 156 $\mu A/cm^2$ and 9.5 $\mu A/cm^2$ under white light and visible light, for the sample deposited at 14 mtorr and thermally oxidized for 24 hours, respectively. The increase in the photocurrent as a function of the deposition pressure and annealing time was directly related to the oxidation kinetics of each film. Oxidizing the low pressure films (2 and 3.5 mtorr) at 350°C showed no significant structural changes in the XRD plots, and no significant formation of anatase phase.

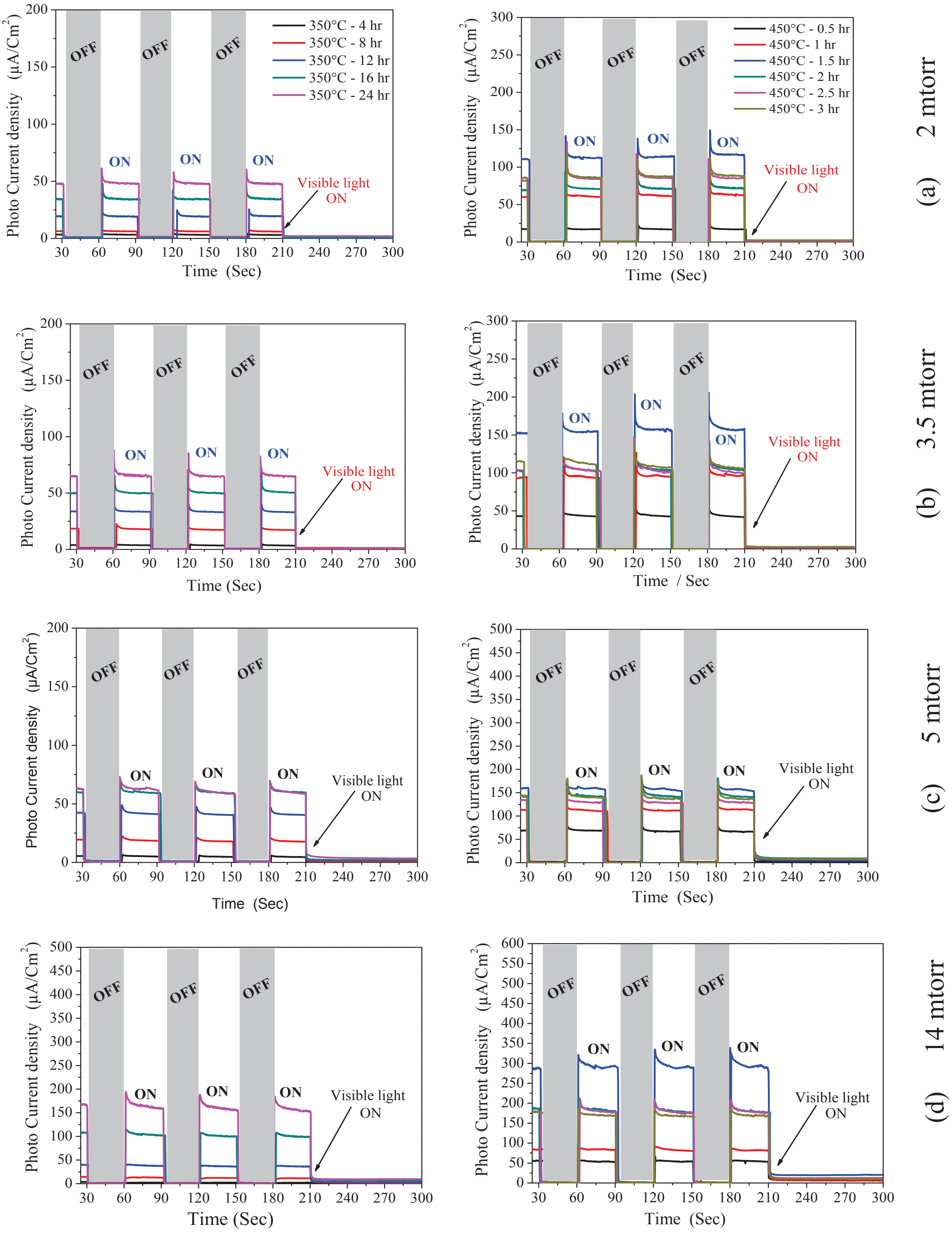

Fig.VI–25: Electrochemical Photocurrent generated at 0.5V/(AgCl/Ag), under intermittent white light/dark irradiations for TiN samples prepared at (a) 2 mtorr, (b) 3.5 mtorr, (c) 5 mtorr and (d) 14 mtorr and oxidized at 350°C (left) and 450°C (right)for different times.

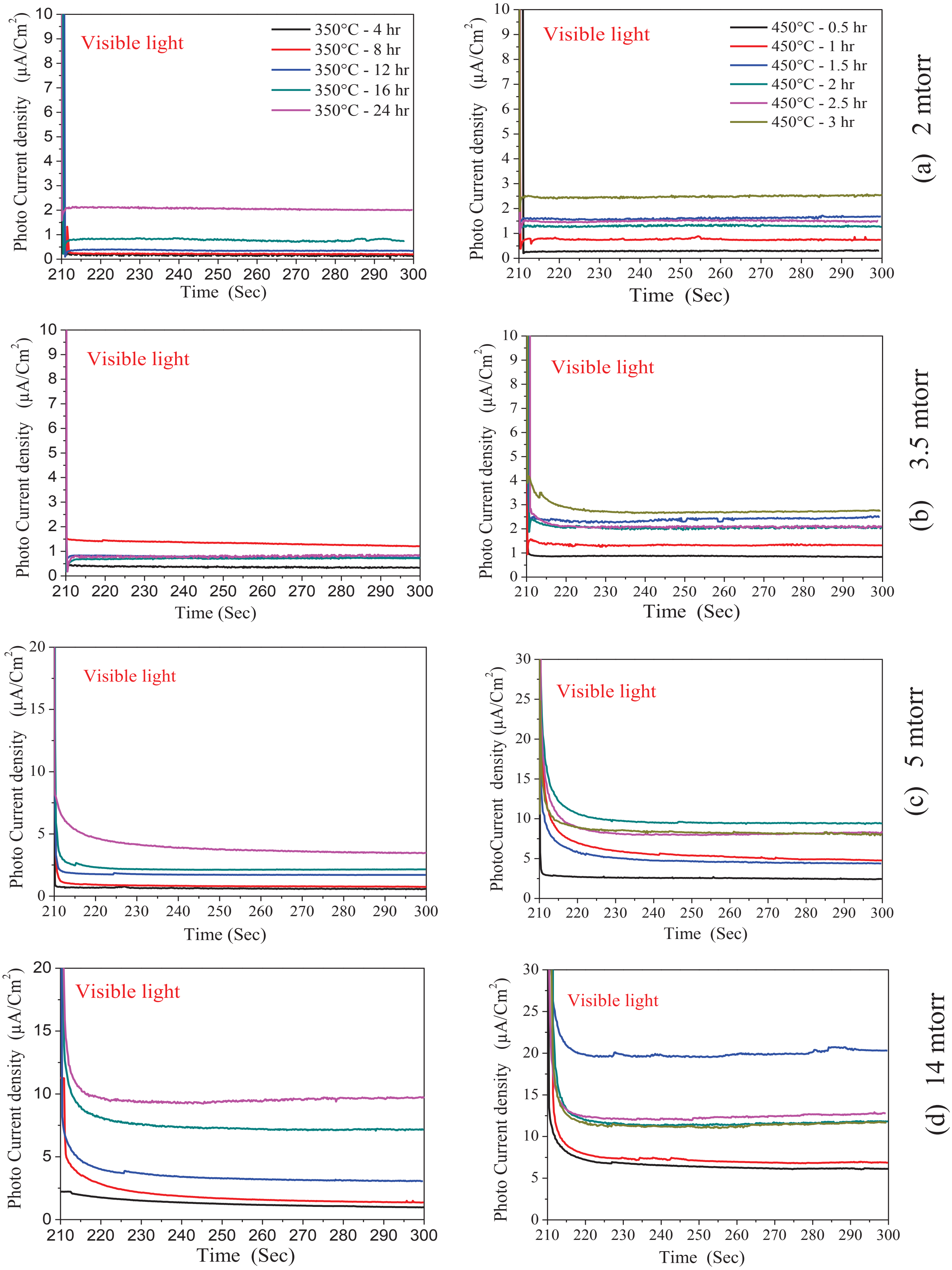

Fig.VI–26: Electrochemical Photocurrent generated at 0.5V/(AgCl/Ag), under visible light irradiations for TiN samples prepared at (a) 2 mtorr, (b) 3.5 mtorr, (c) 5 mtorr and (d) 14 mtorr and oxidized at 350°C (left) and 450°C (right) for different times.

However, the films deposited at higher pressures (5 and 14 mtorr), showed drastic changes in their respective optical and crystalline properties when oxidized at 350°C, and they accordingly showed significantly enhanced photocurrent generation. The films deposited at 5 mtorr and 14 mtorr have preferential (112) and (101) anatase structures, respectively, with optical band gaps within the visible light range when annealing at 350°C. Therefore, the increase in photocurrent for these samples was directly related to their ability to generate photo electrons and holes from the anatase phase of doped titania after the visible light absorption, while the low pressure samples were not.

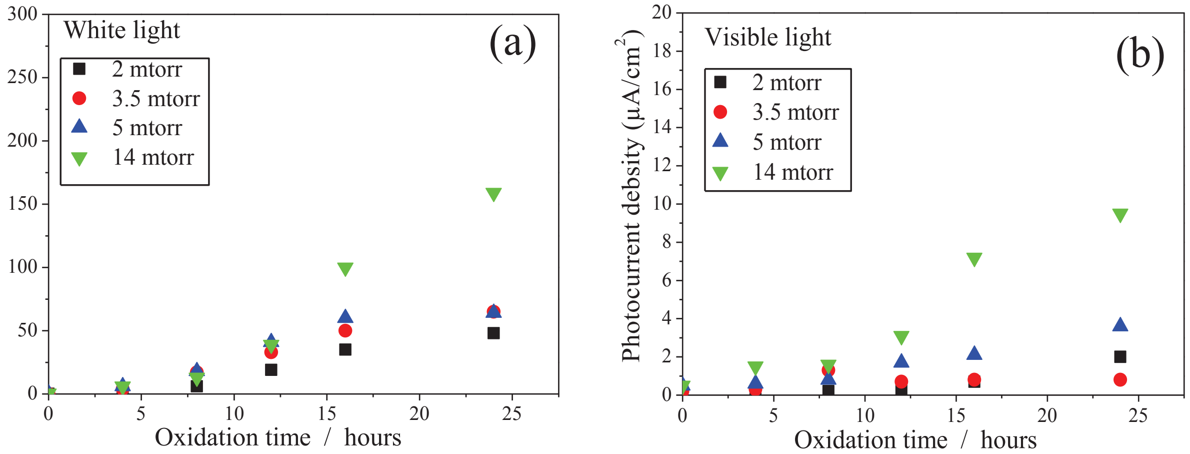

Fig.VI–27: Electrochemical Photocurrent generated at a bias of 0.5V/(AgCl/Ag) for different TiN films oxidized at 350°C vs oxidation time, under (a) white light irradiation and (b) visible light irradiations.

***Films oxidized at 450°C*:** Samples oxidized at 450°C (Fig.VI–28) showed more photocurrent generation as compared to samples oxidized at 350°C. The highest white light and visible light photocurrent density was measured to be 291 μA/cm^2 and 21 μA/cm^2, respectively, for the sample deposited at 14 mtorr, and thermally oxidized for 1.5 hours. The peak in photocurrent generation after only 1.5 hours of annealing was attributed to the change in optical properties of the films. The band gap energy of the films at this oxidation conditions showed the ability to absorb visible light, while annealing for longer times at this temperature steadily decreased the optical absorption. Also, XPS and XRD data revealed that, as we increase the oxidation time of TiN films, there was a relatively fast decrease in the concentration of nitrogen within the oxidized TiN films as well as a steady increase in the anatase crystal size. *There is an optimal compromise between the nitrogen concentration and the anatase crystal size that could lead to the optimal synergic effect of light absorption, charge generation and charge transfer.* These optimal conditions were achieved when oxidizing the TiN films at 450°C for 1.5 hours. Less visible light photons were absorbed when the samples were oxidized longer than 1.5 hours at 450°C.

Remark: It is interesting to note also that the photocurrent generated from samples prepared at lower pressures (2 mtorr and 3.5 mtorr) is mainly from the rutile phase of titania. It has been reported that rutile phase of titania could have some photoactivity but still much lower as compared to the anatase phase due to the higher rate of charge recombination in the rutile when compared to that in the anatase phase.

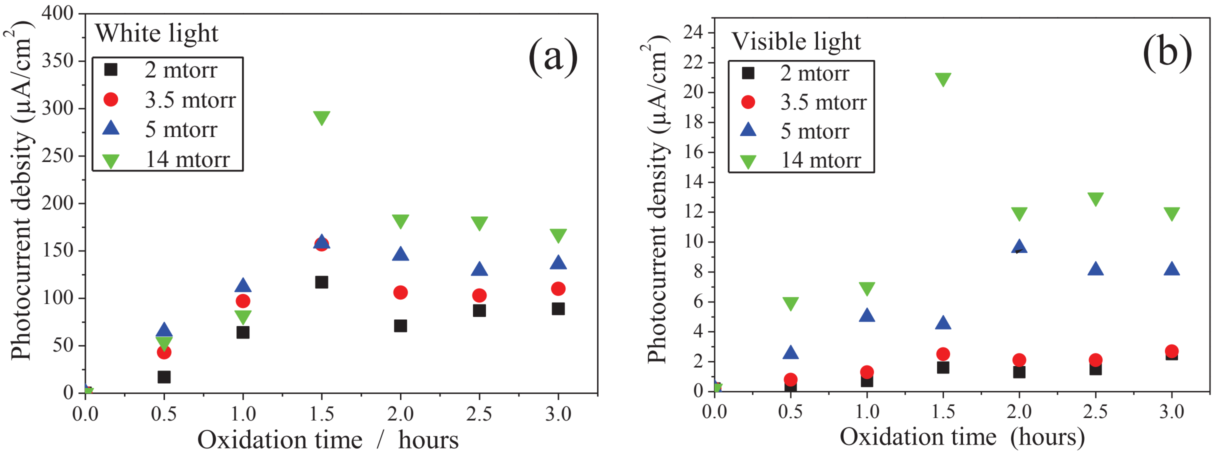

Fig.VI–28: Electrochemical Photocurrent generated at a bias of 0.5V/(AgCl/Ag) for different TiN films oxidized at 450°C vs oxidation time, under (a) white light irradiation and (b) visible light irradiations.

There is an optimal compromise between the nitrogen concentration and the anatase crystal size that could lead to the optimal synergic effect of light absorption, charge generation and charge transfer; achieved when oxidizing the TiN films at 450°C for 1.5 hours (regardless the deposition pressure).

VI–9) Conclusion

This study has shown a simple and versatile method to produce nitrogen doped TiO_2 with various anatase and rutile crystal orientations and nitrogen concentrations via the oxidation of TiN films. The primary step in this process was the deposition of TiN thin films, by RF reactive sputtering at different pressures, which showed very large differences in their as–deposited crystal size and morphology depending on the deposition pressure. When TiN films were oxidized at different temperatures and for different time intervals, significant changes were observed in the crystalline and optical properties of each film, which were unique for each deposition pressure. There was a direct relationship between the as–deposited TiN density as well as its crystal size and the resulting crystal phase and orientation of TiO_2.

There were different diffusion paths along which oxygen can migrate and react within the TiN thin films. The decreasing order of diffusion paths, following the progressive increase in atomic density, could be: (1) along the surface, (2) along voids at column boundaries, (3) along grain boundaries, and (4) through the bulk lattice. Hence, it is found for the more dense films deposited at low pressure, that there was less oxidation in the bulk than for those with a more open columnar structure, deposited at higher pressures.

Rutile phase was found to be more easily formed from the oxidation of dense TiN films having the larger TiN crystal sizes, while the porous TiN films (deposited at higher pressure and having smaller TiN crystal sizes) favored the formation of the anatase crystal phase having a preferential orientation at (112) and (101) when the initial TiN film was deposited at 5 mtorr and 14 mtorr, respectively. Furthermore, it was possible to manipulate the deposition and oxidation conditions in order to obtain films with both the presence of TiO_2 and TiN , indicating the possibility to form thin films having vertical TiO_2/TiN hetero–junctions with controllable optical, crystalline, and compositional properties.

The oxidation of TiN coatings, deposited at higher pressures of 14 mtorr and oxidized at 450°C for 90 minutes, gave the best photo electrochemical activity, under UV (300 $\mu A.cm^{-2}$) as well as visible light irradiations (22 $\mu A.cm^{-2}$), owing to the crystalline structure of the anatase (101) crystal, to the optimal synergic effect of crystal size and photo absorption, and finally to the presence of vertical TiO_2/TiN hetero junctions to reduce the charge recombination. XPS analyses revealed the presence of nitrogen doping in interstitial sites that could contribute to the visible light absorption and charge separation.

This study gave a global understanding of the TiN oxidation process as an effective method to achieve nitrogen doped TiO_2 thin films with a good control of their photo activity and physico–chamical properties. Which, in turn, explained the contradiction previously found in the litterature survey.

References:

[1] C Kwong, W Choy, A Djurisic, P Chui, K Cheng, W Chan, *Nanotechnology*, **15** (2004) 1156–1161

[2] N Sakai, A Fujishima, T Watanabe, K Hashimoto, *The Journal of Physical Chemistry B*, **107** (2003) 1028–1035

[3] W Smith, Y Zhao, Journal of *Physical Chemistry C*, **112** (2008) 19635–19641.

[4] R Asahi, T Morikawa, T Ohwaki, K Aoki, Y Taga, *Science*, **293** (2001) 269–271.

[5] X Jiang, Y Wang, C Pan, *Journal of the American Ceramic Society*, **94** (2011) 4078–4083

[6] Y Lin, Y Tseng, J Huang, C Chao, C Chen, I Wang, *Environmental Science and Technology*, **40** (2006) 1616–1621

[7] T Ihara, M Miyoshi, Y Iriyama, O Matsumoto, S Sugihara, *Applied Catalysis* B: *Environmental*, **42** **(4)** (2003) 403–409.

[8] H Irie, Y Watanabe, K Hashimoto, *Journal of Physical Chemistry B*, **107** (2003) 5483–5486

[9] L Zhu, J Xie, . Cui, J Shen, X Yang, Z Zhang, *Vacuum*, **84**, (2010) 797–802

[10] A Brudnik, M Bucko, M Radecka, A Trenczek–Zajac, K Zakrzewska, *Vacuum*, **82** (2008) 936–941.

[11] D Lee, G Kim, J Lee, Metals and Materials International, **9** (2003) 43–46.

[12] Z. Wu, F. Dong, W. Zhao, S. Guo, Journal of Hazardous Materials, **157**, 57~63 (2008)

[13] A Trenczek–Zajaca, M Radeckaa, K Zakrzewskab, A Brudnikb, E Kusiorb, *Journal of Power Sources*, **194** (2009) 93–103.

[14] A Selloni, *Nature Materials*, **7** (2008) 613–615.

[15] D Wolfe, J Singh, *Journal of Materials Science*, **34** (1999) 2997–3006.

[16] Z Zhang, J Goodall, D Morgan, S Brown, R Clark, J Knowles, N Mordan, J Evans, A Carley, M Bowker, J Darr, *Journal of the European Ceramic Society*, **29** (2009) 2343–2353.

[17] R Sanjinés, H Tang, H Berger,F Gozzo, G Margaritondo, F Lévy, *Journal of Applied Physics*, **75** (6) (1994) 2945–2951.

[18] N Laidani, P Cheyssac, J Perrière, R Bartali, G Gottardi, I Luciu,V Micheli, *Journal of Physics D: Applied Physics*, **43** (2010) 485402 1–11.

[19] S Lee, E Yamasue, K Ishihara, H Okumura, *Applied Catalysis B: Environmental*, **93** (2010) 217–226.

[20] F Peng, Y Liu, H Wang, H Yu, J Yang, *Chinese Journal of Chemical Physics*, **23** (4) (2010) 437–441.

[21] H M Yates, M G Nolan, D W Sheel, M E Pemble, *Journal of Photochemistry and Photobiology A: Chemistry*, **179** (2006) 213–223.

[22] S Hamad, J C Gonza, A Barranco, J P Espino, J Cotrino, *Journal of Physical Chemistry C*, **114** (2010) 22546–22557.

[23] J Suna, L Qiao, S Suna, G Wang, *Journal of Hazardous Materials*, **155** (2008) 312–319.

[24] S Lee, I Cho, D K Lee, D W Kim, T H Noh, C H Kwak, S Park, K S Honga, J K Lee, H S Jung , *Journal of Photochemistry and Photobiology A: Chemistry*, **213** (2010) 129–135.

[25] R Parra, A Arango, P Jose, V Javier, *Dyna,* **163** (2010) 64–74.

[26] M Wong, H Chou, T Yang, *Thin Solid Films*, **494** (2006) 244–249.

[27] Y Sun, K Yan, G Wang, W Guo, T Ma, *Journal of Physical Chemistry C*, **115** (26) (2011) 12844–12849.

[28] A Gonzalez, S Santiago, *Semiconductor Science and Technology*, **22** (2007) 709–716

Conclusion and future work

In this thesis, three different methods to obtain N doped TiO_2 thin films dedicated to photocatalytic activites have been developed using reactive magnetron RF sputtering. The phycico-chemical properties of the deposited films were characterized and their photocatalytic and photoelectrochemical properties were compared. Before and during the deposition plasma diagnostics (OES, Langmuir probe) were performed in order to determine the influence of the process parameters (gas composition, pressure) on the resulting plasma parameters (kTe, ne, V_{dc}) as well as on the characteristics of the deposited films.

By controlling the morphology, the concentration and the incorporation sites of nitrogen in the TiO_2 lattice, the photocatalytic and photoelectrochemical efficiencies of the films can be significantly improved as compared to undoped TiO_2.

For dual gas sputtering, there is a delicate balance between the concentration and the nature of nitrogen doping in TiO_2 that can lead either to improved or deteriorated photo activity. We have shown that there were optimal deposition conditions to maximize the photocatalytic efficiency of N-doped TiO_2 and other conditions to optimize the photo-electrochemical activities. It was found also that the porosity, surface area, crystalline properties, crystal size and the nitrogen doping sites played an important role in the improvement of the photo-activity.

For instance, in homogeneous N doped TiO_2 films prepared by dual gas sputtering (seen in chapter IV), the optimal deposition conditions for the photoelectrochemical efficiency under UV irradiations were 3 mtorr for the deposition pressure and 25% as the fraction of N_2 flow rate in the reactive gas (N_{at}=1%), these samples generated a maximum white light photocurrent density of 567 $\mu A.cm^{-2}$ at 0.5V/(AgCl/Ag). However under visible light irradiation, the optimal fraction of N_2 flow rate in the reactive gas can increase up to 30% (N_{at}=3.3%, maximum visible light photocurrent density of 9 $\mu A.cm^{-2}$ for the same bias). For photocatalytic applications, more porous films deposited at 14 mtorr demonstrated the best photoactivity (NMP degradation within 40 min under UV irradiations with sample having N_{at}=1.8%) as compared to dense films deposited at low pressure.

In chapter V, stacks composed of TiO_2/TiN Bilayers were fabricated and used for the first time for photocatalysis. Such coatings have shown the property to effectively split water when tested in a PEC cell under visible light radiations. The improvement in the structure and performance of the TiO_2/TiN bilayers is directly related to the interfacial area between the two layers, which is in agreement with our theoretical assumptions based on creation of a

Schottky barrier. So far, the optimal deposition conditions for photoelectrochemical and optoelectronic applications are: 18 bilayers with 30% of TiN ratio as compared to TiO_2 thickness (400 µA.cm^{-2} under white light and 23 µA.cm^{-2} in visible). But for photocatalytic applications the optimal deposition conditions are: 9 bilayer with 30% of TiN ratio. Experimentally, we estimate that we can increase the charge separation (between the photo-induced electron-holes) up to 10 times using this design, however, the thickness of each TiN layer should not exceed a limiting value of 16 nm.

Similarly, in chapter VI, various N doped TiO_2 nanostructures were fabricated by oxidizing TiN thin films having different morphologies. These films have shown unique photoelectrochemical properties, and the ability to effectively split water with different efficiencies. The performance of these films depends on the initial TiN porosity (deposition pressure), the oxidation temperature and the oxidation time, the optimal preparation conditions were 14 mtorr, 450°C and 1.5 hours, respectively. These optimal conditions gave rise to white light and visible light photocurrent densities of 300 µA.cm^{-2} and 22 µA.cm^{-2}, respectively.

Nitrogen doping in interstitial sites has shown to be more efficient for photocatalytic applications rather than substitutional ones and this behaviour has been attributed to the enhanced charge separation in the case of interstitial doping sites. However, the synergic effect of substitutional and interstitial nitrogen sites in dense films were more efficient for photoelectrochemical applications, due to good light absorption, good charge transfer in the substitutional doping and good charge separation in the interstitial nitrogen doping.

Each deposition strategy can be applied to obtain functional thin films tailored to one or more applications depending on the activating light source. So far, dense films prepared by dual gas reactive sputtering (at 3 mtorr) gave the best photocurrent generation under UV light (567 µA.cm^{-2} at 0.5V/(AgCl/Ag)) but not under visible light, so it could be dedicated for optoelectronic and photoelectrochemical applications using UV irradiations or at least white light. While porous films (at 14 mtorr) have the best photocatalytic activity but they have low photocurrent generations allowing them to be only useful for photocatalytic applications. Bi-layers gave almost the best photo current generation and memory effect under visible light irradiations (23 µA.cm^{-2} at 0.5V/(AgCl/Ag)) especially with the 18 bilayers; and so far, they gave an interesting photocatalytic activity with 9 bi-layers. These novel stacks are therefore promising candidates as visible light photoactive materials for photocatalysis, PEC and optoelectronic devices. Finally, the thermal oxidation of TiN (deposited at 14 mtorr) is able to produce N doped TiO_2 with best visible light photocurrent generation (as the bi-layers) and good white light activity (as compared to that in the dual gas sputtering) which can be considered as potential candidates for wider applications.

Our approach has been unique in creating multi-layers of TiO_2/TiN nanostructures having controlled crystallinity, visible light absorption and good photoactivity. Also, a good understanding of the kinetics of thermal oxidation of TiN films was developed in order to get TiO_2/TiN hetero-structures with enhanced visible light photo-activity as compared to pure TiO_2 and nitrogen doped TiO_2 having a uniform structure. This study allowed us to have a good overview on the role of the nitrogen doping sites (substitutional and interstitial) in the lattice of doped titania. The photo-performance of the different nanostructures was found to depend on the photoactive surface, the crystal structure of each film, and the percentage of nitrogen as well as its position in the titanium oxide lattice. The unique properties of these nanostructures have a great potential for further improvement of the sputtering process.

There are many perspectives related to this work. In particular, photoluminescence and photo-hall effect measurements can be investigated as an effective way to characterize our films, eventually to detect the energy states of interstitial and substitutional nitrogen sites in the band gap of TiO_2. This could help to understand the deviations between photocatalytic and photoelectrochemical responses of some samples. Also, we have started a new study on the TiO_2/TiN bi-layers by investigating the effect of the pressure on the characteristics and the photo-performance of the deposited films. A promising combination of TiO_2, with AgO oxide in bilayers films (as seen with the bilayers of TiO_2/TiN) could be realized by co-sputtering, in order to improve the charge separation effect. Then the performance of such coatings can be compared to that of homogeneous films of Ag doped TiO_2. AgO oxide could effectively absorb visible light and is expected to act as electron traps, which can extend the life-time of the photo-generated charge carriers. Doping with rare earth elements can be also a very interesting route to investigate for up-conversion materials, in order to produce blue photons from red photons.

By analyzing SEM pictures of some samples, we have detected the presence of nanoparticles (100-300 nm) on the surface of the films. One can make the hypothesis that these nanoparticles are formed in the plasma, and an extensive study using plasma diagnostics could be useful to understand the formation of these nanoparticles, i.e. are they formed due to a sudden variation in total pressure/ due to the partial pressure of the reactive gases, or are they formed due to the sputtering of some clusters from the cathode… etc. The formation of nanoparticles have been extensively studied in PECVD reactors, however there is very little study on particles formed in the case of magnetron sputtering systems.

Conclusion générale

Dans cette thèse, trois différentes méthodes ont été utilisées pour obtenir des couches minces de TiO_2:N photoacitves par pulvérisation réactive magnétron. Les propriétés physicochimiques des films déposés ont été caractérisées ainsi que leurs propriétés photocatalytiques et photoélectrochimiques. La phase plasma a été diagnostiquée (OES, sonde de Langmuir) afin de comprendre l'influence des paramètres du procédés (pression, composition) sur les propriétés du plasma (kTe, ne) ainsi que sur les caractéristiques des films déposés. En contrôlant la morphologie, la concentration et la localisation de l'azote dans la matrice de TiO_2, il a été possible d'améliorer grandement l'efficacité photocatalytique et/ou photoélectrochimique des films comparés au TiO_2 non dopé.

Dans le cas de la pulvérisation dans un milieu plasmagène constitué d'azote et d'oxygène (chapitres 3 et 4), nous avons montré qu'il existe un équilibre délicat entre la localisation de l'azote et sa concentration pouvant conduire aussi bien à une amélioration qu'à une détérioration des propriétés photoactives des films. Nous avons aussi montré qu'il existe des conditions pour optimiser les propriétés photocatalytiques des dépôts et d'autres conditions pour améliorer leurs propriétés photoélectrochimiques. Enfin, nous avons mis en évidence que la porosité, la surface spécifique, la nature et la taille des cristaux jouent aussi un rôle important dans l'amélioration des propriétés photoactives. Par exemple, dans le cas d'un film de TiO_2:N préparé par pulvérisation réactive dans l'azote et l'oxygène, nous avons montré que les conditions optimales pour avoir de bonnes propriétés photoélectrochimiques sous irradiation UV sont une pression de 3 mTorr et une fraction d'azote de 25% par rapport à la totalité de gaz réactifs. Le photocourant maximal mesuré sous éclairement par lumière blanche était de 567 $\mu A.cm^{-2}$ à un potentiel de 0,5 V(AgCl/Ag). Sous éclairement visible, les meilleurs films obtenus ont été préparés à 3 mTorr et 30% d'azote, dans ce cas le photocourant maximal était de 9 $\mu A/cm^{-2}$. En revanche, pour les applications photocatalytiques, les meilleurs films ont été déposés à 14 mTorr donnant lieu à une dégradation totale d'une solution de NMP (dont la concentration initiale est 10 ppm) en 40 min sous éclairement UV.

Dans le chapitre 5, des multicouches de TiO_2/TiN ont été élaborées et utilisées pour la première fois pour la photocatalyse. De tels dépôts ont montré une bonne capacité à dissocier l'eau sous éclairement visible dans une cellule photoélectrochimique. L'amélioration de la structure et des performances des films est directement liés à l'interface entre TiO_2 et TiN, ce qui satisfait avec le modèle des barrières de Schottky. Pour la dissociation de l'eau, les meilleurs dépôts ont été obtenus pour 18 bicouches contenant 30% de TiN (400 $\mu A/cm^2$ en lumière blanche et 23 $\mu A/cm^2$ en lumière visible). Cependant pour la dégradation des polluants, les meilleures couches correspondent à 9 bicouches contenant aussi 30% de TiN. Expérimentalement nous avons montré que les bicouches permettent une séparation des charges environ 10 fois plus efficaces que dans une monocouche et que l'épaisseur des couches de TiN ne doit pas dépasser 16 nm.

De manière similaire, dans le chapitre 6, différentes couches nanostructurées de TiO_2 :N ont été fabriquées par oxydation de couches minces de TiN ayant différentes morphologies. Ces films ont montré d'excellentes propriétés photoélectrochimiques. La performance de tels films dépendent de la porosité initiale de TiN (i.e de la pression de dépôt), de la température et du temps d'oxydation. Les conditions opératoires optimales sont 14 mTorr, 450°C et 1,5 heure respectivement. Ces conditions optimales ont permis d'obtenir des films donnant lieu à des photocourants de 300 µA/cm² et 22 µA/cm² respectivement sous lumière UV et visible.

Nous avons montré que le dopage de l'azote dans les sites interstitiels est plus efficace pour les propriétés photocatalytiques. Ce comportement pourrait être expliqué par la meilleure propriété de séparation de charge dans ce type de dopage. Cependant l'effet synergique du dopage de l'azote dans les sites substitutionnels et interstitiels dans le cas de films denses ont montré être plus efficace pour les applications photoelectrochimiques, grâce à une meilleure absorption de la lumière blanche, à un bon transfert de charge par l'azote substitutionnel et enfin à une bonne séparation des charges avec le dopage de l'azote de type interstitiel.

Chaque stratégie de dépôt entreprise dans cette thèse pourrait être utilisée pour élaborer des couches minces fonctionnelles pour une ou plusieurs applications selon la source de rayonnement envisagée. Les résultats obtenus dans cette thèse ont montré que les films minces denses de TiO_2:N préparés par pulvérisation réactive dans l'azote et l'oxygène (à 3 mtorr) donnent la meilleure génération de photocourant sous UV (567 $\mu A.cm^{-2}$ à 0.5V/(AgCl/Ag)), mais pas sous rayonnement visible. En conséquence ces films seraient intéressants pour les applications optoélectroniques ou photoélectrochimiques utilisant le rayonnement UV ou au moins la lumière blanche. Tandis que les films poreux que nous avons déposé à plus haute pression (14 mTorr) montrent la meilleure activité photocatalytique mais sont caractérisés par un faible photocourant, ce qui implique que l'on peut utiliser ces films uniquement pour les applications photocatalytiques.

Les bicouches, et en particulier les 18 bicouches, ont permis d'obtenir le meilleur photocourant ainsi que l'effet de mémoire sous rayonnement visible (23 $\mu A.cm^{-2}$ à 0.5V/(AgCl/Ag)). Les travaux sur la performance de ces bicouches pour la photocatalyse sont toujours en cours, mais pour le moment les 9 bicouches ont donné les meilleurs résultats. Ces nouveaux empilements de couches sont donc des matériaux très intéressants pour les applications photoactives utilisant la lumière visible.

Enfin, l'oxydation thermique des couches poreuses de TiN déposées à haute pression (14 mTorr) permet d'obtenir des films de TiO_2 :N ayant des propriétés comparables aux multicouches en terme de photocourant dans le visible, et comparables à la pulvérisation réactive dans l'azote et l'oxygène en terme d'activité sous UV. Ainsi, cette voie de fabrication permet de répondre à de plus larges applications.

Le travail original de cette thèse a consisté à élaborer des multicouches de TiO_2/TiN aux propriétés contrôlées. Par ailleurs, une bonne compréhension de la cinétique d'oxydation thermique de TiN a permis d'obtenir des hétérostructures de TiO_2/TiN possédant des propriétés photoactives supérieures aux couches de TiO_2 homogènes, dopées ou non dopées. Ces études ont permis aussi de montrer le rôle de la localisation du dopage à l'azote dans la maille de TiO_2. Ainsi les propriétés uniques de ces films nanostructurés laissent entrevoir de grandes opportunités dans l'amélioration du procédé de pulvérisation.

Ce travail ouvre la voie à de nombreuses perspectives. En particulier, il serait intéressant d'effectuer des mesures de photoluminescence et d'effet Hall sous éclairement afin d'apporter des informations supplémentaires sur la localisaton des niveaux d'énergie de l'azote dans la bande interdite de TiO_2. Ces analyses pourraient permettre de comprendre les différences de comportement des films entre la photocatalyse et la photoélectrolyse de l'eau. Par ailleurs, nous avons débuté une nouvelle étude sur la production de multi-couches en faisant varier la pression, ceci afin d'obtenir un degré de liberté supplémentaire pour améliorer les propriétés photoactives des matériaux. Il serait aussi bien d'envisager la combinaison de TiO_2 avec de l'oxyde d'argent (AgO) en multicouches par co-pulvérisation. En effet, l'oxyde d'argent peut absorber la lumière visible avec une grande efficacité et pourrait piéger les électrons photo-généré par TiO_2 ce qui pourrait prolonger la durée de vie des porteurs de charge photo-générés par le TiO_2. Enfin, on pourrait envisager de doper les couches de TiO_2 avec des terres rares afin de réaliser la conversion de photons rouges (non absorbables) en photons bleus (absorbables par TiO_2).

En analysant certains clichés obtenus au SEM-FEG, nous avons constaté la présence de nanoparticules (100-300 nm) à la surface des films. Ainsi, du point de vue de la caractérisation du plasma, il pourrait être intéressant de réaliser des diagnostics sur les harmoniques de courant ou bien sur la tension d'autopolarisation afin de détecter ou non la formation et la présence de nanoparticules. Ces dernières ont été largement étudiées dans les réacteurs PECVD, mais il excite très peu d'études sur les particules formées dans le cas des réacteurs de pulvérisation cathodique.

Annex 1 : Reviewing of TiO_2 doping in nano particles and thin films*

A1-1) Up conversion luminescence agent

Wang et al. [103] incorporated a compound of $40CdF_2 + 60BaF_2 + 0.8Er2O_3$, (molar ratios) in their TiO_2 powder. This “upconversion” luminescence compound can effectively absorb visible irradiation and then emit into ultraviolet range which could be absorbed efficiently by titania. The photo-catalytic activity of the final mixture has been enhanced by 15 times under visible light irradiation compared with undoped TiO_2 Photo-catalyst, according to the degradation time of acid red B.

A1-2) Ion implantation

Metal and nonmetal implantation (with various transition metal) could be achieved with ions accelerated at high energy (1–200 keV) [22][30] lower energy has been also used [74][90] to implant nitrogen (with 200 eV). When TiO_2 is bombarded with such high energy ions (of metal or nonmetal element) accelerated by high voltage, the ions can be implanted into the lattice without destroying the surface structure of the TiO_2.

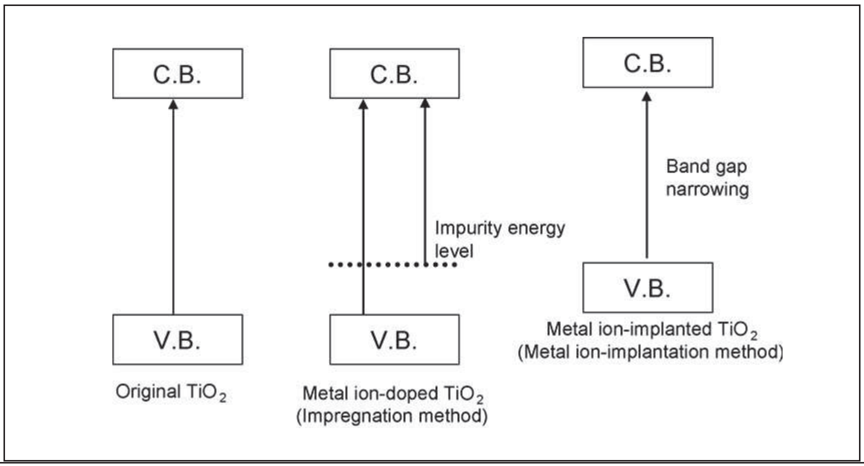

Fig.A1-1: Band structures of TiO_2, chemically ion-doped TiO_2 and physically ion implanted TiO_2.[22]

M Kitano et al. [22] reported a smooth shift of the UV-Vis absorption spectra to visible light regions (up to 600 nm) depending on the kind of metal implanted unlikely to the chemically doped titania which could only exhibit a shoulder absorption in the visible range. This indicates that the band gaps of the physically ion-implanted TiO_2 are much smaller than that of the original TiO_2. The band structures of the original TiO_2, metal doped and ion implanted titania are presented in fig.A1-1.

---

*For the references see chapter I

A1-3) Metal doping

Metallic modifications affect both surface features and chemistry. Doping with these metal ions has shown both positive and negative effects on the photo-catalytic activity of TiO_2. It could delay the photo-generated electron-hole pair recombination (charge separation) and accelerate the photo-excitation and formation of oxidizing species on the surface. But, a number of authors claim that although metal ion doping should decrease the photo-threshold energy of TiO_2, the metal ion may also serve as a recombination center for electrons and holes, thus diminishing the overall activity of the photo-catalyst especially at high doping concentrations [45][118].

Lanthanide metals have the advantage to form complexes with various Lewis bases through the interaction between the f-orbitals of the lanthanide metal and the functional groups of Lewis bases, thus providing an effective adsorbability of organic pollutants on TiO_2 surface. Also they are able to trap conductive band electrons when they are confined to the TiO_2 semiconductor's surface as the case of Nd [104] and Ce [16].

Karvinen et al. [105] have theoretically investigated the role of transition metal dopants in both anatase and rutile TiO_2 models. For anatase TiO_2, the addition of V^{3+},Cr^{3+}, Mn^{3+}, and Fe^{3+} caused significant band gap narrowing; however, no effect was found for the rutile system. Other studies of doping with transition metal ions including Cr [106][45], V [107] Fe [108][116] Pb [109] Cu [110] , Co [111] have been already investigated.

Reports show that there exists a complex photo-activity dependence on the dopant concentration, dopant energy state in the lattice, the d-electron configuration, the distribution of dopants, the electron donor concentration, and the light intensity. Several additional works has been reported on metal doping of TiO_2, but a detailed understanding from a surface science viewpoint has not yet been achieved.

TiO_2 codoping has also been investigated as La/N [36], Ta/N [67], Ag/N [36], B/N [112] as well as composite oxides or semiconductors: PdO/TiON [62], WO_3/TiO_2 [113-114], CdS/TiO_2 and Bi_2S_3/TiO_2 [49] in order to enhance the charge separation in the TiO_2 using the static electrical field generated due to the difference between the conductive band level of TiO_2 and the other loaded semiconductors.

More details on doped TiO_2 could be seen in other references [30] and more in [49].

A1-4) Dye sensitized TiO_2 photo-catalyst

Organic dyes with visible light absorbing are capable of photo-sensitizing TiO_2 semiconductors. The mechanisms involve charge injection from the excited dye molecule into the conduction band of the semiconductor for producing oxidized dye radicals where the dye serves as both a sensitizer and a substrate to be degraded as presented in fig.A1-2. The electron in the conductive band of TiO_2 will reduce the surface of some adsorbed oxidants (like oxygen), to generate active oxidizing spices and radicals ($O_2^{\bullet -}$, $OH^{\bullet}$, $HO_2^{\bullet}$, and H_2O_2) which then will cause the degradation of the pollutant [112][115].

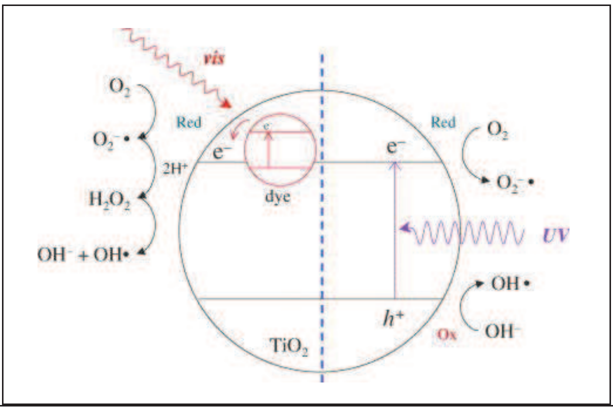

Fig.A1-2: Band structures of dye sensitized TiO_2. The photoactivation mechanism of TiO_2 under UV (right side) and the dye-sensitized activation mechanism under visible light (left side).[115].

The charge transfer depends on the solution in contact with the semiconductor. Panayotov et al. [5] have investigated the charge transfer process on TiO_2-SiO_2 powder material, where the charge transfer from the conduction band to two different adsorbate molecules is compared. There it was found that efficient charge transfer occurs exclusively between the TiO_2 surface and an adsorbate molecule with an electrophilic moiety. No observable charge transfer occurred with a similar molecule but without with the electrophilic moiety.

Annex 2 : Some measured characteristic times of TiO_2

In the next table we can find an example of measured times for primary processes in TiO_2 photo-catalysis from [6].

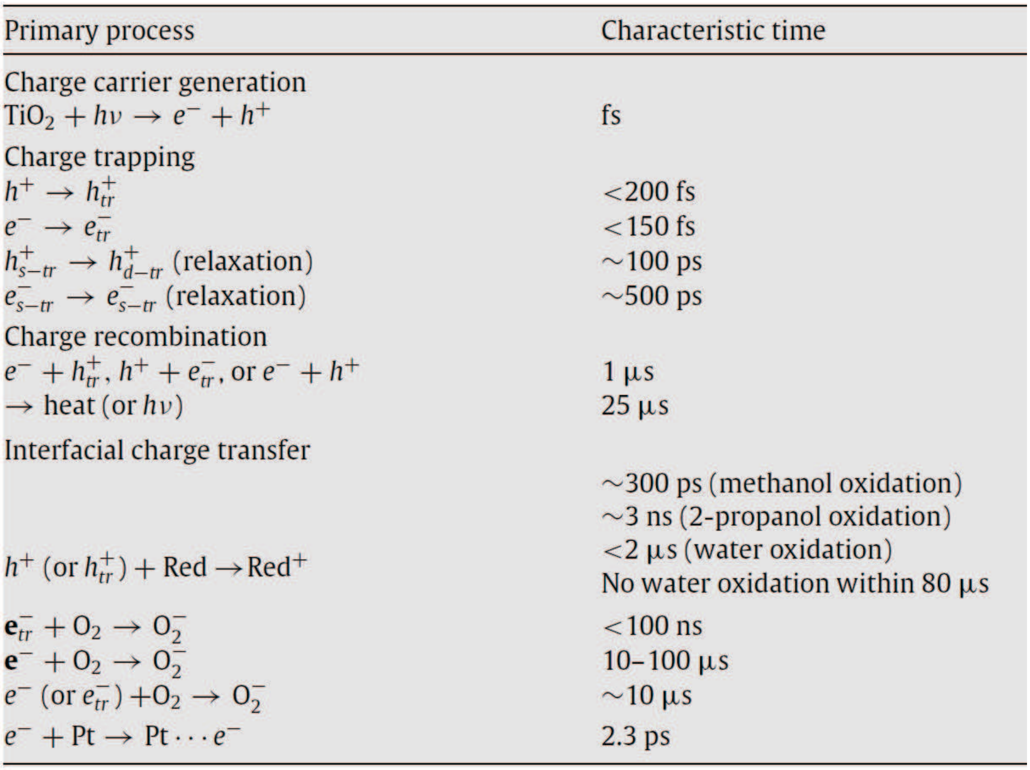

Primary process	Characteristic time
Charge carrier generation	
$TiO_2 + h\nu \rightarrow e^- + h^+$	fs
Charge trapping	
$h^+ \rightarrow h^+_{tr}$	<200 fs
$e^- \rightarrow e^-_{tr}$	<150 fs
$h^+_{s-tr} \rightarrow h^+_{d-tr}$ (relaxation)	~ 100 ps
$e^-_{s-tr} \rightarrow e^-_{s-tr}$ (relaxation)	~ 500 ps
Charge recombination	
$e^- + h^+_{tr}$, $h^+ + e^-_{tr}$, or $e^- + h^+$	1 μs
$\rightarrow$ heat (or $h\nu$)	25 μs
Interfacial charge transfer	
h^+ (or h^+_{tr}) $+$ Red $\rightarrow$ Red$^+$	~ 300 ps (methanol oxidation) ~ 3 ns (2-propanol oxidation) <2 μs (water oxidation) No water oxidation within 80 μs
$\mathbf{e}^-_{tr} + O_2 \rightarrow O_2^-$	<100 ns
$\mathbf{e}^- + O_2 \rightarrow O_2^-$	10–100 μs
e^- (or e^-_{tr}) $+ O_2 \rightarrow O_2^-$	~ 10 μs
$e^- + Pt \rightarrow Pt \cdots e^-$	2.3 ps

Where e^-_{tr} and h^+_{tr} are the trapped electron and hole reached to the surface of the semiconductor.

Annex 3 : Profile of electron and ion densities in capacitive plasma*

We note that outside the sheath, it is possible to assume that ion density in plasma is equal to the electron density. But inside the sheath, electron density decreases very fast and become null at the cathode level.

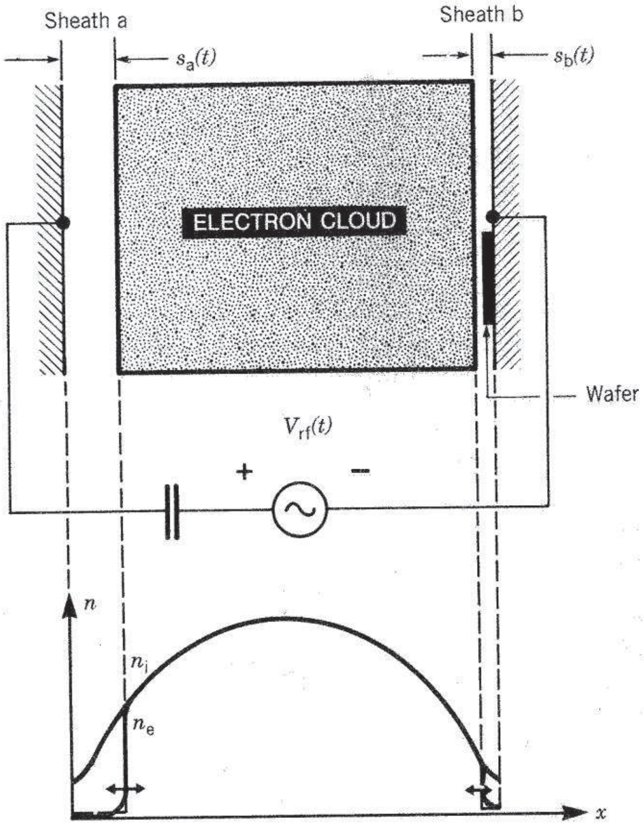

Fig.A3-1: Geometrical variation of electron density ***n**$_e$* *and ion density* ***n**$_i$* *in capacitive plasma, from ref. [38].*

---

*For the references see chapter II

Annex 4 : Film Morphology in sputtering deposition

The morphology of the deposited films can vary depending on the experimental conditions as seen in the Thornton diagram (fig.A4-1). We can recognize three zones as discussed below:

- Zone-1: deposited film is porous and/or amorphous, consisting of trapped crystallites separated by voids. It could result from poor surface mobility, low substrate temperature, low ion energy (low RF or DC bias power) or higher pressures (lower mean free paths).
- "T-zone": this transition zone is characterized with small grain polycrystalline, dense, smooth having a high reflectance. It results from higher surface mobility due to higher substrate temperature or ion energy with higher deposition rate.
- Zone-2: Further increases in surface mobility results in larger columnar grains that have rough surfaces. These rough surfaces lead to poor coverage in later steps.
- Zone-3: Still further increases in surface mobility result in large (non-columnar) grains. These grains can be good for diffusion barriers (less grain boundary diffusion) with large grains, and tend to be more rigid leading to more failures in electrical lines.

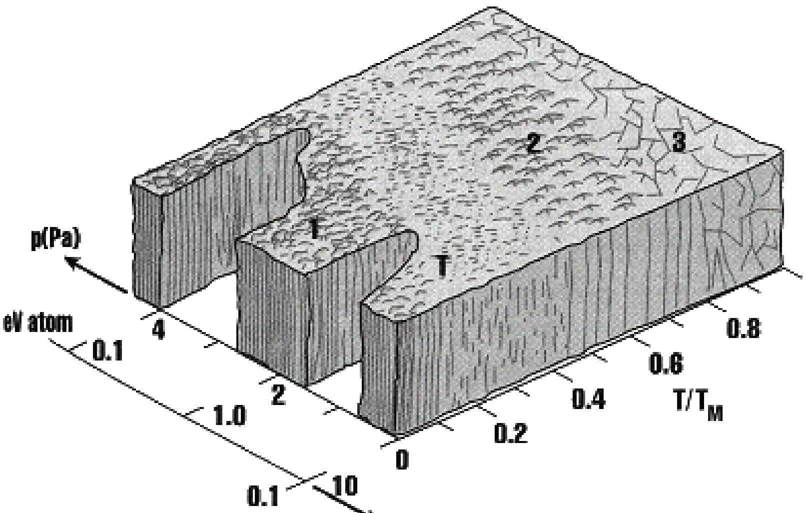

Fig.A4-1: The three zone model of film deposition as proposed by Movchan and Demchishin (after Thornton)

Annex 5 : Peak assignments in XPS spectra *

A5-1) N1s peak assignments

The peak centred around 396±0.2eV has been reported to correspond to substituted nitride or atomic β-N directly bonded to the central Ti cation [17] in N-doped titania [15-16]. To a lesser extent, this peak has also been assigned to the nitrogen triple bond to titanium, N^{3-} (TiN) [20]. Another possible peak for substitutional N could be found around 398 eV, which corresponds to the anionic N^{-} in O—Ti—N bonds [3][26]. The shift in the binding energy to 398 eV (compared to the 396 eV and 397 eV binding energies) might be explained by the fact that, when N atom substitutes the O atom (in the initial O—Ti—O structure), the electron density around N was reduced compared to that in the N–Ti–N structure of TiN crystal, because of the much higher electro-negativity of the O atom [3]. Raut et al., simply, linked this shift to a bonding interaction among N, Ti, and O [14]. All the aforementioned nitrogen peaks will be referred to as ***substitutional*** nitrogen, or N_s.

Peak energies centred around 400 eV could be assigned to molecular chemisorbed N_2 or NO_x [3] located in interstitial sites without any direct linkage to Ti cations, *which could justify the presence of this signal in the non doped TiO_2 samples*. On the other hand, this binding energy has been assigned to an oxynitride of a stoichiometry equivalent to Ti-NO (TiN_xO_{2-x}) [3][9][16], where nitrogen is simultaneously bonded to oxygen and titanium in a defective lattice site (as Ti—N—O local structure). But this last assignment (presence of oxinitride) could be corrected only if it is accompanied with a shift in the Ti 2p signals due to its binding to different chemical species [35]. *The signal at 400 eV has also been detected on the surface of our pure TiO_2 samples, so we assigned this signal to trapped molecular N_2.*

Nitrogen could incorporate in interstitial sites within titania as Ti—O—N or Ti—O—N—O configurations, the electron density of the oxidized nitrogen is lowered compared to that of nitrogen in the N—Ti—O structure, and the binding energy of the 1s electron for oxidized nitrogen (having a positive valence) shifts to a higher energy. Therefore, the N 1s energy level at 402 ± 0.2 eV has been attributed to oxidized nitrogen, which has a configuration of Ti—O—N in the TiO_2 lattice, which will be further referred to as ***interstitial*** nitrogen, or N_i. Lastly, binding energies higher than 402.0 to 403.0 eV have been attributed to Ti—O—N—O or Ti—NO_2 species [16]. Here, nitrogen atom bonds simultaneously to one titanium and two oxide ions in the lattice, so nitrogen is bonded to a more electronegative environment.

**For the references see chapter IV*

A5-2) Carbon contaminations

Several authors have reported hydrocarbon contamination on the surface of thin films [20][40][43]. The narrow spectrum C1s of Carbon could present 2 peaks localized:

- at 282 eV that corresponds to Ti-C bonds.
- at 284 to 285 eV corresponding to C—C bonds.
- at 285.5 to 289 eV corresponding to C—O and C==O compounds.

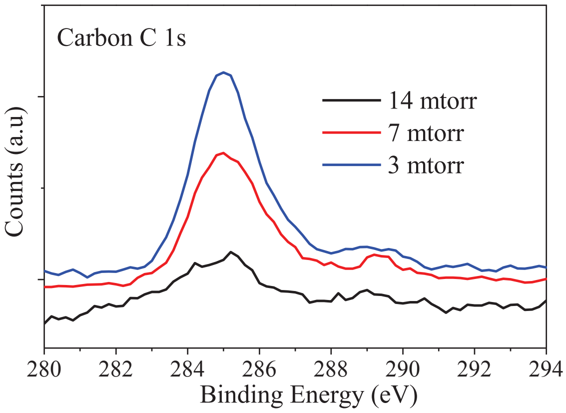

Fig.A5-1: C1s XPS spectrum of pure TiO_2 thin films prepared at different working pressures.

Fig.A5-1 present the XPS spectrum of C 1s corresponding to TiO_2 samples prepared at 3 mtorr, 7 mtorr and 14 mtorr, doped films are found to have the same shape of C1s as pure TiO_2. In our films we found only the second C peaks, which means that the presence of carbon is most probably due to environmental contamination. C—O and C=O compound could also be present in our films which generally was accompanied with O 1s peaks at binding energy higher than 532 eV.

It isuseful to know that many authors report that the use of argon ion sputtering as a means of cleaning the N doped TiO_2 surface (to remove the carbon contamination from the surface) is inappropriate due to the preferential sputtering phenomena which will produce an undesirable changes in the surface composition especially at low nitrogen concentrations [39].

Annex 6 : OES spectra of the white lamp

The Optical Emission Spectra of the white lamp (125 W, PHILIPS) which was used in the photo excitation source for the electrochemical (photocurrent) measurements was measured with and without the insertion of the UV filter(Fig.) One can recognize an emission line in the UV having a wavelength of 365 nm, this UV emission was effectively cut off by the insertion of the UV filter. The other emission lines were all in the visible region, and were present in the spectrum with the UV filter.

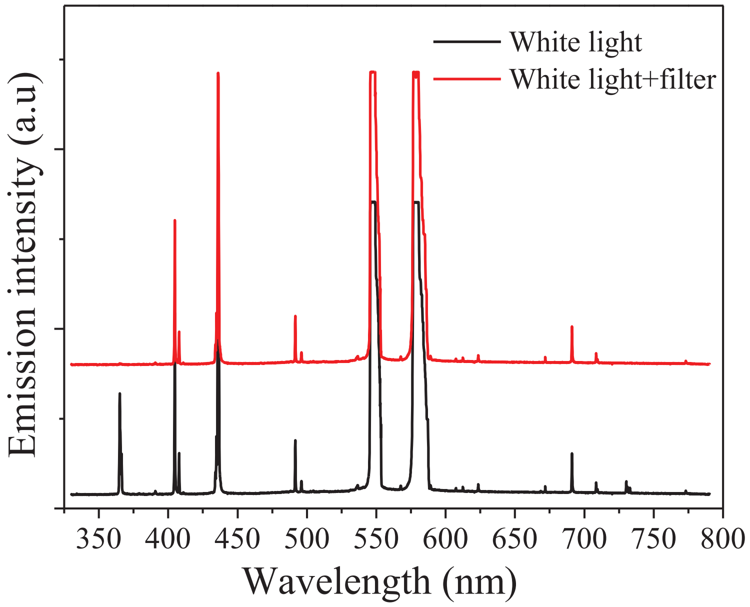

Fig.A6-1: Optical emission spectra of the white lamp which was used in the photocurrent measurement.

List of publications and conferences

Publications

- **H. Fakhouri**, W. Smith, J. Pulpytel, F. Arefi-Khonsari, H. Mortaheb, A. Zolfaghati "Enhancement of NMP Degradation Under UV Light by Nitrogen-doped TiO_2 Thin Films: Effect of Morphology and Substituted Nitrogen Using a Design of Experiment". *Journal of Nano and Electronic Physics*, **3** No1 (2011) 26-40.

- W. Smith, **H. Fakhouri**, J. Pulpytel, F. Arefi-Khonsari "Control of the optical and crystalline properties of TiO_2 in visible-light active TiO_2/TiN bi-layer thin-film stacks" *Journal of Applied Physics*, **111**, (2012) 024301.

- W. Smith, **H. Fakhouri**, S. Mori J. Pulpytel, F. Arefi-Khonsari, "Oxidation Kinetics of TiN Films Deposited by RF Reactive Sputtering at High and Low Pressure", (accepted) Journal *of Physical Chemistry C* (ASAP).

- **H. Fakhouri**, W. Smith, J. Pulpytel, A. Zolfaghati, H. Mortaheb, F. Meshikini, R. Jafari, F. Arefi-Khonsari "Visible Light Water Splitting and Enhanced UV Photocatalysis from Nitrogen Doped TiO_2 Thin Films", (submitted to *Journal of Hazardous Materials*)

- W. Smith, **H. Fakhouri**, R. Grilli, M. Baker, J. Pulpytel, F. Arefi-Khonsari "Control of the Nitrogen Doping State in Dual Gas RF Sputtered TiO_2 Thin Films", (In preparation)

- **H. Fakhouri**, W. Smith, J. Pulpytel, F. Arefi-Khonsari, "Enhanced visible light photoactivity and charge separation in optimized TiO_2/TiN bi-layer thin film" (In preparation).

International conferences

- **H. Fakhouri**, W. Smith, J. Pulpytel, F. Arefi-Khonsari, *Controlling the Properties of TiO_2 in TiO_2/TiN Bi-Layer Thin Films for Photocatalysis and Photocells*. Oral presentation, **EMRS 2011**, Nice, France.

- **H. Fakhouri**, W. Smith, J. Pulpytel, F. Arefi-Khonsari, *Influence of RF reactive sputtering on the nitrogen chemical state in nitrogen doped TiO_2 thin films*. Oral presentation, **MPA 2011**, Alvore, Portugal.

- S. Mori, **H. Fakhouri**, J. Pulpytel, F. Arefi-Khonsari, *Optical and Langmuir probe diagnostics of an Argon plasma in an RF reactive magnetron sputtering system*. 20th International Symposium on Plasma Chemistry, **ISPC20 2011**, Philadelphia, USA.

- W. Smith, **H. Fakhouri**, J. Pulpytel, F. Arefi-Khonsari, *Photoactive TiO_2/TiN Bi-Layer Thin Films Deposited by RF Reactive Sputtering*. 20th International Symposium on Plasma Chemistry, **ISPC20 2011**, Philadelphia, USA.

- W. Smith, **H. Fakhouri**, J. Pulpytel, F. Arefi-Khonsari, *Thermal Oxidation of TiN to TiO_2: Improved Visible Light Photocatalysis and Solar Water Splitting*. 6th International Conference on Surfaces, Coatings, and Nano-structured Materials, **NANOSMAT 2011,** Krakow, Poland.

- W. Smith, **H. Fakhouri**, J. Pulpytel, F. Arefi-Khonsari, *Visible Light Photocatalysis in Nitrogen Doped TiO_2 Films*. **MRS Fall Meeting 2011**, Boston, Massachussetts, USA.